

**UC Berkeley**

**UC Berkeley Electronic Theses and Dissertations**

**Title**

PRECISION TUNING OF SINGLE-METAL SITES ON METAL-ORGANIC FRAMEWORKS FOR CATALYSIS AND GAS ADSORPTION

**Permalink**

<https://escholarship.org/uc/item/33b3d35k>

**Author**

Khoo, Rebecca

**Publication Date**

2022

Peer reviewed|Thesis/dissertation

PRECISION TUNING OF SINGLE-METAL SITES ON METAL-ORGANIC  
FRAMEWORKS FOR CATALYSIS AND GAS ADSORPTION

By

Rebecca Shu Hui Khoo

A dissertation submitted in partial satisfaction of the  
requirements for the degree of

Doctor of Philosophy

in

Chemistry

in the

Graduate Division

of the

University of California, Berkeley

Committee in charge:

Dr. Jian Zhang, Co-Chair

Professor Jeffrey R. Long, Co-Chair

Professor T. Don Tilley

Professor Michael Crommie

Summer 2022

Precision Tuning of Single-Metal Sites on Metal-Organic  
Frameworks for Catalysis and Gas Adsorption

Copyright © 2022

By: Rebecca Shu Hui Khoo

# Abstract

## Precision Tuning of Single-Metal Sites on Metal-Organic Frameworks for Catalysis and Gas Adsorption

By

Rebecca Shu Hui Khoo

Doctor of Philosophy in Chemistry

University of California, Berkeley

Dr. Jian Zhang, Co-chair

Professor Jeffrey R. Long, Co-chair

Metal-organic frameworks (MOFs) are a class of porous crystalline materials created by joining metal ions or clusters, known as nodes, with organic linkers to form a continuous structure. Since the chemical and physical properties of MOFs are highly tunable via the judicious choice of metals and organic linkers, and is further expanded by the possibility for post-synthetic modification, MOFs have over the last decade become a powerful platform for the atomically precise tuning of single-metal sites for applications including gas adsorption and separation, heterogeneous catalysis, and chemical sensing etc. In this dissertation, the post-modification of MOF nodes via installation of transition metal catalytic sites, as well as the exploration of guest-induced phase changes that alter the chemical properties of node single-metal sites are explored.

First, an artificial enzyme mimic on a solid support was synthesized via the post-synthetic insertion of a bis( $\mu$ -oxo)dicopper moiety between the clusters of a Zr-MOF (i.e., **MOF-565**) with a short intercluster distance. Like its parent enzyme, the resulting **MOF-565-Cu<sup>II</sup>** efficiently transfers one oxygen atom from O<sub>2</sub> gas to olefins, forming the monooxygenated epoxide products with high activities and selectivities.

The effect of node type and saturation on the post-synthetic installation of iron on zirconium MOFs was then studied. The unsaturated, 8-connected Zr<sub>6</sub> nodes of **MOF-565**, as well as the Zr<sub>9</sub> nodes of another new MOF, **NPF-520**, were furnished with iron(III) to afford **MOF-565-Fe<sup>III</sup>** and **NPF-520-Fe<sup>III</sup>**, respectively. The visible-light photocatalytic oxidation of toluene to benzaldehyde and/or benzoic acid was then used as a benchmark to compare the Zr-Fe catalysts, both of which demonstrated excellent performance and selectivity under mild reaction conditions.

Finally, the effect of reversible guest-induced phase changes of a novel flexible cobalt MOF, **Co-MOF**, on C<sub>2</sub> gas adsorption, in particular ethylene, was investigated. Two means for phase-transformation were identified: 1) the guest-assisted rotation of an asymmetric linker affecting the coordination number of Co and 2) the opening and closing of the MOF structure by activation and re-solvation, changing the coordination geometry of Co.

# Table of Contents

Table of Contents.....	i
Acknowledgements.....	iii
Chapter 1. Metal-Organic Frameworks: From Design to Application .....	1
1.1 Metal-Organic Frameworks.....	1
1.2 Atomically Precise Metal Sites for Catalysis and Gas Adsorption.....	3
1.3 Node-based Single Metal Sites in MOFs .....	5
1.4 Incorporation of Secondary Single Metal Sites to MOFs .....	7
1.5 Grafting Inorganic Metal Species to Metal Nodes of MOFs .....	10
Chapter 2. Construction of an Artificial Monooxygenase: Stabilization of bis( $\mu$ -oxo)dicopper Cluster in Zr-based Metal Organic Framework via Reticular Chemistry .....	21
2.1 Introduction.....	22
2.2 Synthesis and Structural Characterization of MOF-565.....	25
2.3 Synthesis and Structural Characterization of Binuclear Cu Containing MOF-565-Cu ...	29
2.4 Olefin Epoxidation Catalyzed by MOF-565-Cu.....	33
2.5 Conclusions.....	41
2.6 Materials and Methods.....	42
2.7 References.....	46
2.8 Supporting Information.....	50
Chapter 3. Post-Synthetic Modification of Nodes in Zirconium Metal Organic Frameworks for Photocatalytic Oxidation of Toluene .....	57
3.1 Introduction.....	58
3.2 Synthesis and Structural Characterization of NPF-520 .....	63
3.3 Synthesis and Structural Characterization of MOF-565-Fe.....	66
3.4 Synthesis and Structural Characterization of NPF-520-Fe .....	71
3.5 Photocatalytic Toluene Oxidation by MOF-565-Fe and NPF-520-Fe .....	75
3.6 Mechanism for Photocatalytic Toluene Oxidation by MOF-565-Fe and NPF-520-Fe....	79
3.7 Conclusions.....	84
3.8 Materials and Methods.....	85
3.9 References.....	90

3.10	Supporting Information.....	94
Chapter 4. Reversible Guest-Induced Phase Changes and Selective Ethylene Adsorption in a Flexible-Robust Co-Based Metal Organic Framework .....		103
4.1	Introduction.....	104
4.2	Structural Characterization and Guest-Induced Phase Changes of Co-MOF.....	108
4.3	Ethylene/Ethane/Acetylene Gas Adsorption by Co-MOF .....	122
4.4	Conclusions.....	126
4.5	Materials and Methods.....	127
4.6	References.....	129
4.7	Supporting Information.....	134

## Acknowledgements

First and foremost, I would like to thank my parents, Mr. Peter and Mrs. Samantha Khoo, and my younger brother Derrick. You guys supported me throughout my 7 years in Berkeley even though we were living on opposite sides of the world. The time, effort, and concessions you put in to communicate with me despite the drastically different time zones kept me going, knowing that my family would always be there for me. I love you all.

I am incredibly grateful to my advisor, Dr. Jian Zhang, without whom this PhD would not have been possible. Thank you for taking me as a student when I was in a difficult situation on campus. Your wisdom, guidance and patience were essential in helping me develop as a chemist.

Learning together with my fellow grad students, Christian Fiankor and Yuchen Hu, all the way at the University of Nebraska-Lincoln through fruitful project discussions, collaborations, and literature reviews was a fantastic experience, even though I've only talked to both of you online. I look forward to meeting you in-person someday.

I am also greatly indebted to Dr. Yi Liu and the current and former members of the Liu group, Xinle Li, Chongqing Yang, Bing Sun, Chris Anderson, Matthew Kolaczowski, Songliang Cai, Jun Fan, Lu Huang, Yuli Yin, Ziman Chen, Sizhuo Yang, Harrison Bergman, He Li, and Miao Qi for your valuable help and advice both in lab and every week at group meeting. It was wonderful working together and hanging out with all of you. I'd also like to thank Gabriel Sucich, an undergraduate who spent a summer working with me to make MOFs. The Molecular Foundry staff, especially Liana Klivansky, Teresa Chen, Eric Dailing, Steve Shelton, Tracy Mattox and Anne Pham were instrumental in teaching me the ins-and-outs of working there and ensuring everyone's health and safety. Additionally, I am thankful to all the Foundry users, staff, postdocs, and students I have met over the years, whose experiences in many different fields of science and engineering have broadened my horizons.

I'd like to express my special appreciation for Dr. Simon J. Teat at the Advanced Light Source for showing me the ropes around Beamline 12.2.1, aiding us in getting additional beamtime, diagnosing technical issues at odd hours, and for your invaluable assistance in solving the toughest crystal structures. Many of the single-crystal structures in this dissertation would not exist without you.

My gratitude goes out to my collaborators, Professor Jier Huang, Wenhui Hu, Denan Wang and James Nyakuchena at Marquette University who helped us collect and fit the X-ray absorption data, and Professor Banglin Chen, Yi Xie and Li Ma at the University of Texas at San Antonio for all your aid in gas adsorption experiments.

I also wish to express my appreciation to Professor Jeffrey Long and the entire Long group for helping me transition into grad school and giving me a firm foundation in inorganic chemistry

research. My thanks especially to Alexandre Vincent for conducting the SQUID measurements, and Adrian Huang for helping me collect TGA data at the last minute.

I would not have had the opportunity to study at UC Berkeley if not for my undergraduate research supervisors and mentors, Professor Chorng Haur Sow, Dr. Zhi Han Lim, Professor John Yip and Dr. Van Ha Nguyen at the National University of Singapore, my supervisors as a research assistant at the A\*STAR Institute of Materials Research and Engineering, Professor Andy Hor and Dr. He-Kuan Luo, as well as my intern advisors Dr. Valerio Isoni and Dr. Daniel Kumbang at A\*STAR Institute of Sustainability for Chemicals, Energy and Environment. It was with your support and encouragement that I decided to pursue a career in science.

Finally, surviving grad school would not have been possible without continuous support from my friends. My companion, Kenneth Lim, who insisted on calling me every week despite having to stay up till the wee hours just to make sure I was alright. My roommate of 5 years Zhennan Liu, who endured living together with me and listened to my complaints. My old high school buddies living in the Bay Area, especially Minh Tue Vo Thanh who shared my love of classical music and regularly went to concerts together with me. My neighbor Deborah Mann, who I enjoyed many an evening walk and random conversation with despite the gap between our ages. My friends from undergrad, Emily Chong-Gupta and Kevin Timothy Fridianto, who cheered me on through the hardest times. I might have lost my sanity without you guys.

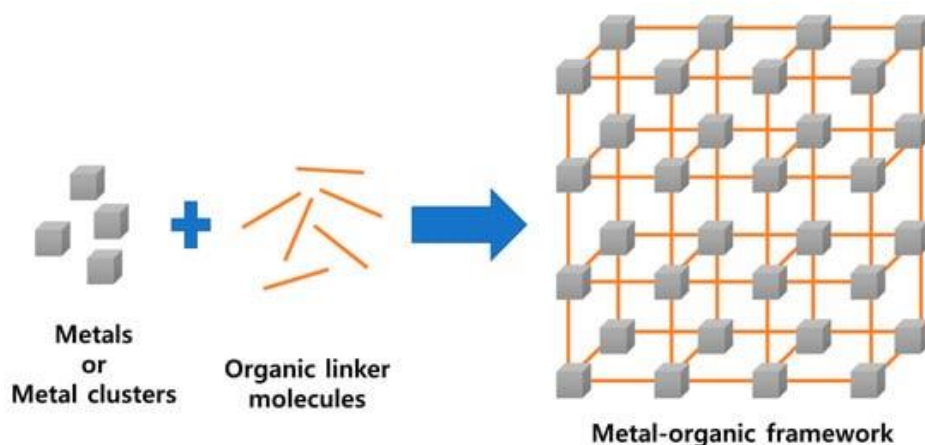
Thank you all so much.



# Chapter 1. Metal-Organic Frameworks: From Design to Application

## 1.1 Metal-Organic Frameworks

For the past two decades, there has been explosive growth in the synthesis, characterization, and study of materials known as metal-organic frameworks (MOFs), a class of porous materials constructed by joining metal ions or clusters, known as nodes, with organic linkers to form continuous 3D structures (Figure 1).<sup>1-5</sup>



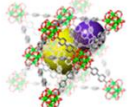
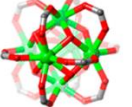
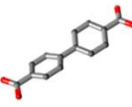
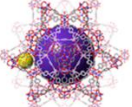
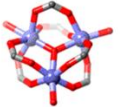
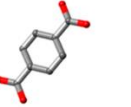
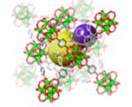
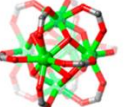
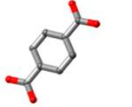
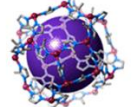

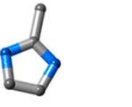
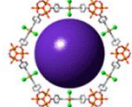
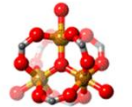
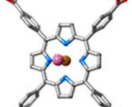
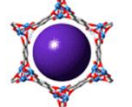
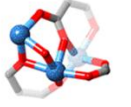
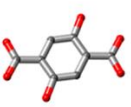
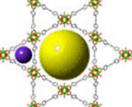
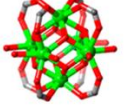
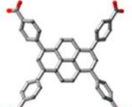
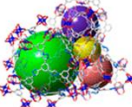
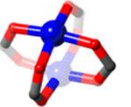
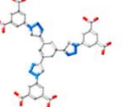
**Figure 1.** Schematic drawing of the formation of metal-organic frameworks (MOFs). Copyright 2020 Polymers.

The flexibility with which the metals and organic linkers can be varied has led to thousands of new MOFs being prepared and studied year on year since the first discovery of **MOF-5** ( $\text{Zn}_4\text{O}(\text{bdc})_3$ , **bdc** = terephthalate)<sup>6</sup> and **HKUST-1** ( $\text{Cu}_3(\text{btc})_2$ , **btc** = 1,3,5-benzenetricarboxylate)<sup>7</sup> in 1999. Metal nodes are most commonly formed from first-row transition metals, Al, Zr, and Hf, although MOFs have been successfully synthesized and reported using nodes based on most metals in the periodic table. Organic linker choices are also highly varied, as any functional group that coordinates to a metal can be utilized, with the only requirement being that it is at least ditopic.

The basic design considerations for MOFs include (1) the choice of linkers with certain rigidity and shapes such as lines, triangles, squares, tetrahedra, and octahedra and (2) the coordination geometry of metal ions or clusters, both of which come together to form unique topologies with differing porosities and chemical environments. Examples of several common MOFs are shown in Figure 2. To date, MOFs with densities as low as  $0.13 \text{ g/cm}^3$ ,<sup>8</sup> pore volumes up to 90% free

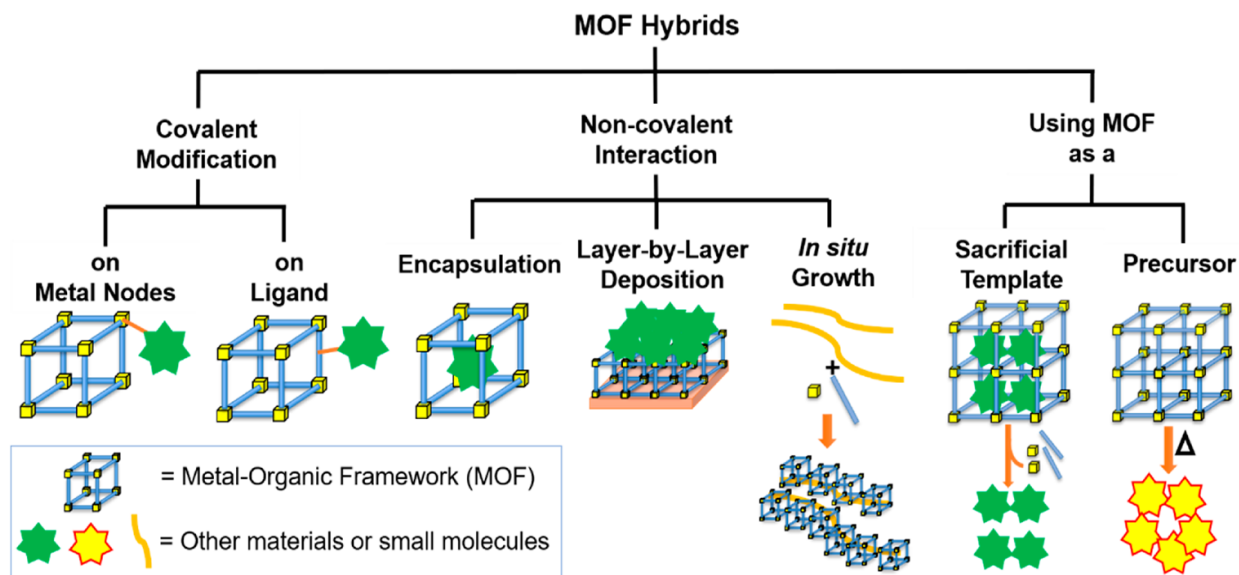
volume,<sup>9</sup> and Brunauer–Emmett–Teller (BET) surface areas greater than 7000 m<sup>2</sup>/g<sup>10</sup> have been reported.

Due to their exceptional porosity and high crystallinity, MOFs have a wide range of potential applications ranging from gas storage and separation,<sup>11-13</sup> chemical sensing,<sup>14</sup> heterogeneous catalysis,<sup>15-16</sup> photocatalysis,<sup>17</sup> bioimaging,<sup>18</sup> drug delivery,<sup>19</sup> proton conduction,<sup>20</sup> water harvesting,<sup>21</sup> and so on.<sup>22</sup>

MOF	Metal Node	Organic Linker	MOF	Metal Node	Organic Linker
 UiO-67	 Zr <sub>6</sub> O <sub>4</sub> (OH) <sub>4</sub>	 BPDC	 Cr-MIL-101	 Cr <sub>3</sub> O(OH) <sub>3</sub>	 BDC
 UiO-66	 Zr <sub>6</sub> O <sub>4</sub> (OH) <sub>4</sub>	 BDC	 ZIF-8	 Zn	 MelM
 PCN-600(M)	 Fe <sub>3</sub> O(OH) <sub>3</sub>	 M-TCPP	 Mg-MOF-74	 MgOH	 BDC-(OH) <sub>2</sub>
 NU-1000	 Zr <sub>6</sub> O <sub>4</sub> (OH) <sub>8</sub> (H <sub>2</sub> O) <sub>4</sub>	 TBAPy	 NU-125	 Cu <sub>2</sub>	 LH <sub>6</sub>

**Figure 2.** Examples of representative MOF structures with their corresponding metal clusters and organic linkers (Zr: green; Fe: yellow; Cr: light purple; Zn: dark red; Mg: blue; Cu: royal blue; C: grey; O: red; N: light blue; Cl: pink). Copyright 2017 Chemistry of Materials.

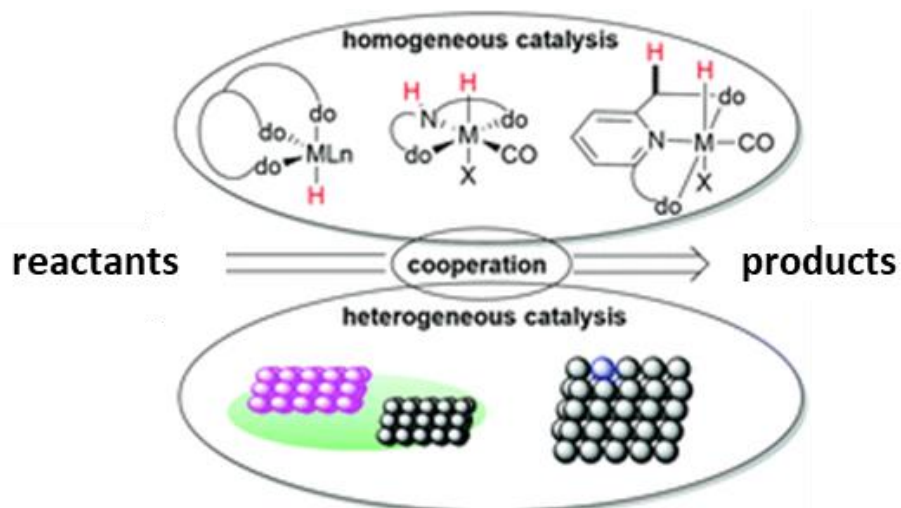
Moreover, post-synthetic modification of MOFs via incorporation and alteration of organic units and metal-organic complexes has emerged as a powerful tool for further varying the chemical reactivity of the porous materials and provide opportunities for designing complex moieties on the atomic level in a highly controlled manner (Figure 3).<sup>23</sup>



**Figure 3.** Summary of methods for post-synthetic modification of MOFs. Copyright 2018 Nature Communications.

## 1.2 Atomically Precise Metal Sites for Catalysis and Gas Adsorption

Transition metal catalyzed chemical transformations are known as key processes in organic synthesis, energy storage, and conversion. Examples of such catalysts include metal nanoparticles and metal complexes (Figure 4).



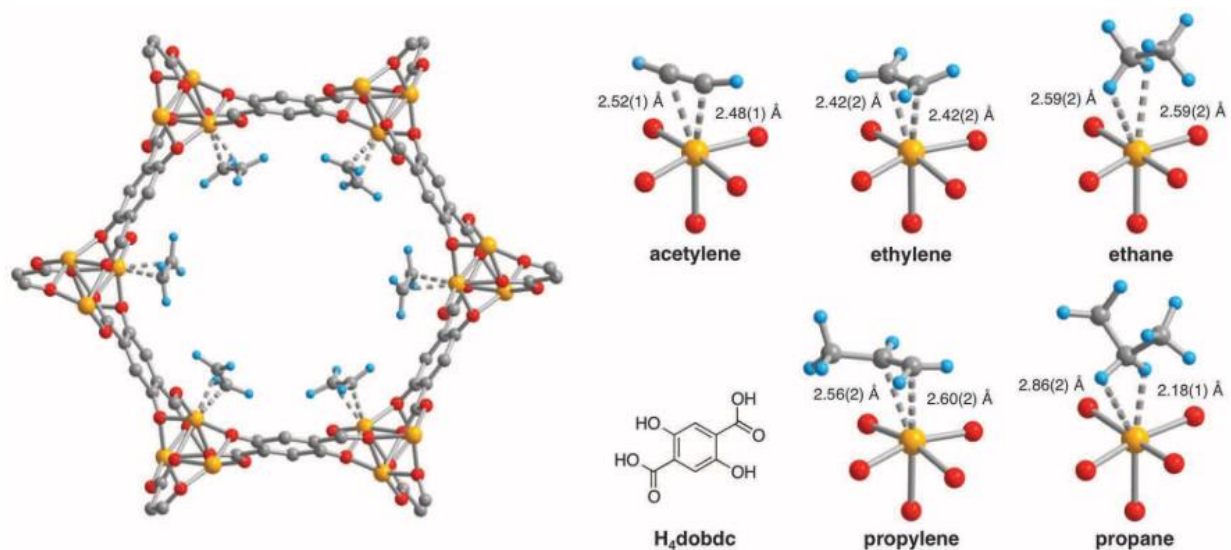
**Figure 4.** Schematic illustrations of homogenous and heterogenous catalysis. Copyright 2021 Chemical Society Reviews.

As a class of conventional heterogeneous catalyst, metal nanoparticles present significant promise in a wide range of catalyzed reactions, with active metal sites located at crystal corners, edges, and facets.<sup>24-26</sup> To normalize the catalytic behaviors and maximize the utilization efficiency of metals, shrinking the particle sizes to maximize surface area to volume ratio is considered one of the more effective methods to significantly boost the catalytic performance by enhancing activity and selectivity; however, catalyst activities by metal loading remain far higher than most homogenous catalysts.

In comparison with the above-mentioned heterogeneous metal nanoparticles, homogenous metal complexes tend to feature greater advantages as a result of their fully exposed, identical, isolated catalytic metal centers in solution.<sup>27-28</sup> However, several fatal flaws, namely, challenges in separation, catalyst recycling, as well as easy deactivation and decomposition cause their prospects in industrial applications to be severely limited.

These problems presented by both homogeneous and traditional heterogeneous metal catalysts have triggered decades of research in the quest for ideal alternatives that would bridge the gap between the two. The goal is to achieve atomically dispersed active single metal sites supported by a large surface area solid support, giving rise to a heterogeneous catalyst with the performance and selectivity of a homogenous catalyst.

In general, the most common method for the facile synthesis of such atomically dispersed single metal sites is to immobilize traditional homogenous metal catalysts directly on the surfaces of heterogeneous supports, including metals, metal oxides, silica, polymers, and macromolecules.<sup>29-32</sup> However, the anchor sites on these materials are often limited and disordered, resulting in non-uniform distribution and complicated intra- and intermolecular interactions between the catalytic sites, surface, and reactants. To address the above issues, high surface-area materials which allow precise control in the construction of catalytic sites are needed. MOFs are one such promising material. Their crystalline frameworks give rise to rigid backbones and permanent porosities, as well as uniform distribution of functionalities that can be precisely modified to produce uniformly distributed, identical, well-dispersed catalytic sites.<sup>33-37</sup> Furthermore, such atomically precise sites show promise in other applications such as gas storage and separation, due in part to the strong coordination of gaseous molecules to unsaturated transition metal sites (Figure 5) as well as intermolecular interactions between gases and MOF surface.<sup>38-39</sup>



**Figure 5.** Coordination of C2 and C3 gases to open metal sites in MOF-74. Copyright 2012 Science.

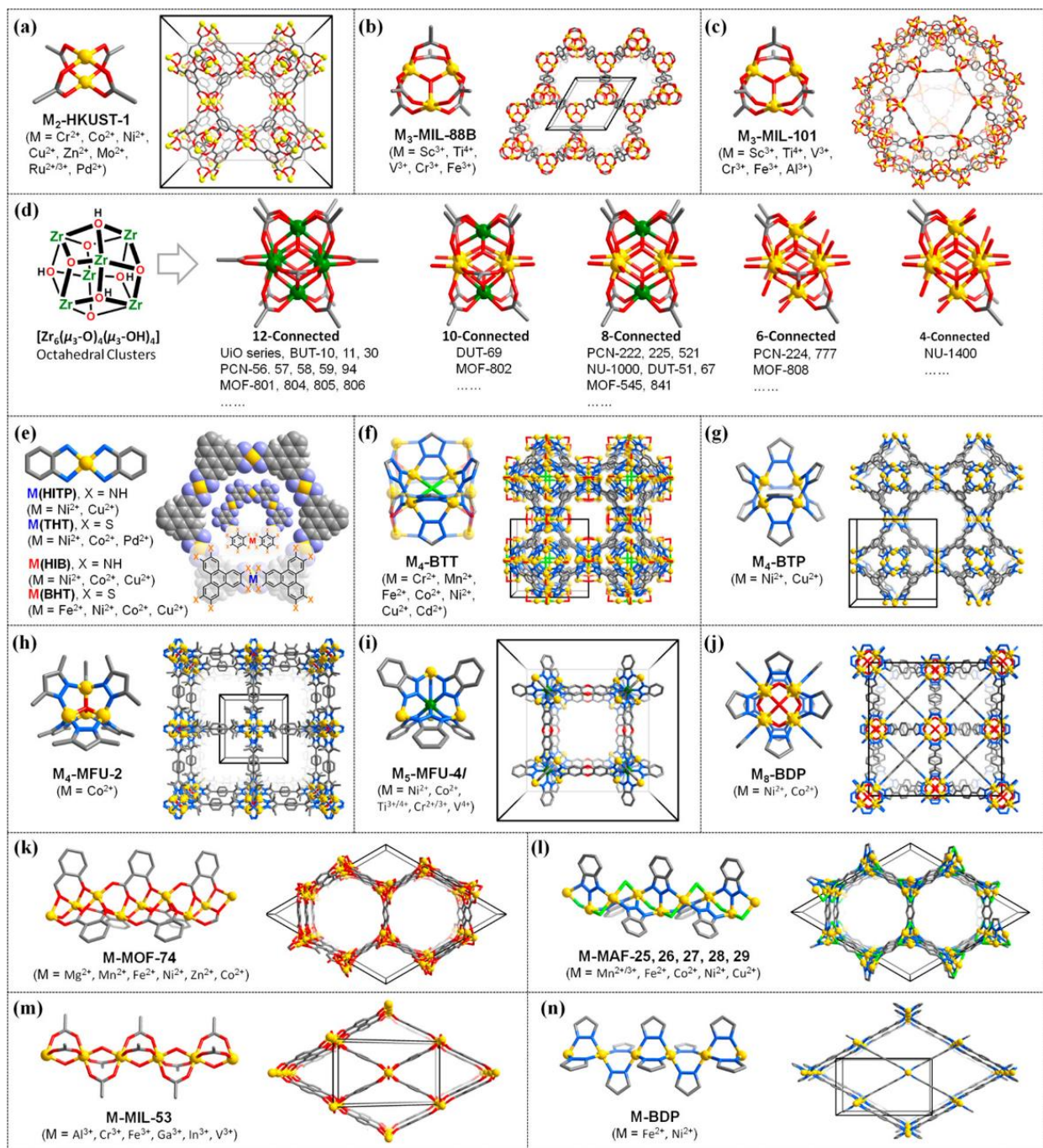
### 1.3 Node-based Single Metal Sites in MOFs

The metal ions in the metal nodes of MOFs are often coordinated not only to the organic linkers, but also to terminal ligands including water and solvent molecules, which can be removed by thermal or vacuum treatments while oftentimes retaining the host framework structures, achieving coordinatively unsaturated metal sites, or open metal sites.<sup>40-42</sup> These open metal sites can then act as anchored points for adsorbing gaseous molecules for storage and separations, or as active catalytic sites. Examples of such nodes include metal paddlewheels as seen in HKUST-1,<sup>43-44</sup> trimeric metal clusters with the formula of  $[M_3(\mu_3-O)(COO)_6(OH)(H_2O)_2]$  as seen in MIL-101,<sup>45</sup> coordinatively unsaturated  $Zr_6$  nodes as seen in PCN-222<sup>46</sup> and MOF-808,<sup>47</sup> and infinite 1D chain nodes as seen in MIL-53 (Figure 6).<sup>48-49</sup>

Unfortunately, in many MOFs such as UiO-66, coordination spheres of the metal nodes are fully/mostly occupied by organic ligands, consequently leading to less possibility for incorporation of extrinsic species. Nonetheless, since all crystals are far from perfect in reality, defect engineering has been used as a powerful approach to expose more active sites at metal nodes, thus significantly boosting the catalytic activities MOFs. However, synthesizing MOFs with well-defined defect structure remains a great challenge at present.<sup>50-52</sup>

Regardless, many MOFs are rendered air or moisture sensitive by the exposure of open metal sites, making them tricky to use in traditional organic catalysis or for reactions that take place in the presence of water or coordinating solvents.<sup>53-54</sup> Additionally, there are limitations to the type of structures that can be formed using different metals, which in turn affects their accessibility to substrates, stability under catalytic conditions, and complexity in rational designing MOFs with certain topologies and functionalities for applications.<sup>55-57</sup> The design and synthesis of MOFs with

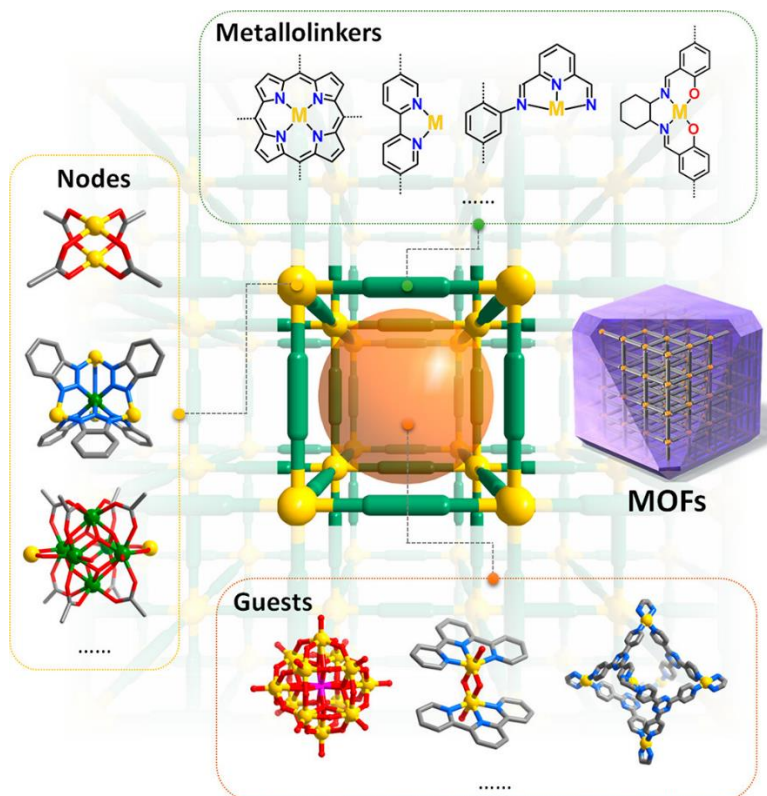
robust yet active open-metal sites are hence still actively ongoing, and a novel example involving a simple flexible cobalt MOF will be described in Chapter 4 of this dissertation.



**Figure 6.** MOFs containing single metal sites for catalysis or gas adsorption. Copyright 2020 Chemical Reviews.

## 1.4 Incorporation of Secondary Single Metal Sites to MOFs

To create MOFs containing single metal sites with desired topologies and porosities, the incorporation of secondary metals during or post-synthesis have been extensively studied.<sup>34, 58-60</sup> To date, several approaches have been employed for such additions, and they can be broadly categorized into three types: 1) coordination of an additional metal to functional groups on the linkers creating metallolinkers,<sup>61-66</sup> 2) node-based single metal sites (from cluster or chemically bonded to cluster),<sup>67-76</sup> and 3) the encapsulation of guests containing metal clusters/moieties into the pores of MOFs (Figure 7).<sup>77-79</sup>

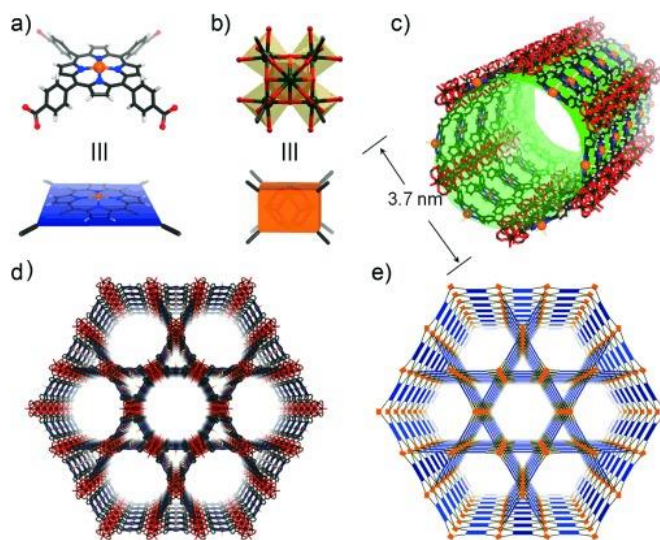


**Figure 7.** Schematic illustration of the three types of single metal-site catalysts based on MOFs. Copyright 2020 Chemical Reviews.

Using the metallolinker approach, many homogeneous metal complexes can be firmly anchored on the MOF linkers to afford heterogeneous catalysts with the same single metal sites as their homogeneous counterparts, effectively bridging the gap between homogeneous and heterogeneous catalysts and affording a way of anchoring active sites onto MOFs with extremely high precision, chemical and physical stability, and even enhancing substrate shape and size selectivities. Moieties that have been introduced in the synthesis of metallolinkers often include

bipyridine, porphyrin, salen, pincer, thiol, and phosphine, all of which are also among the most common ligands used in traditional homogenous catalysis.<sup>61-66</sup>

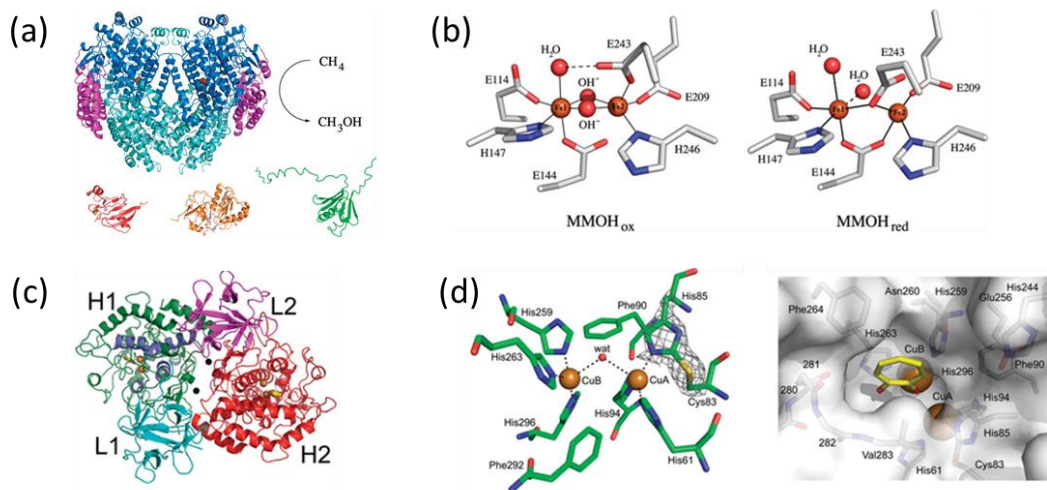
To highlight an example, direct application of iron porphyrins, a well-known moiety in metalloenzymes such as cytochrome P450, as oxidation catalysts in aqueous media is often challenging, largely due to the formation of catalytically inactive dimers and irreversible oxidation of the catalyst itself. To solve the problem, iron porphyrins have been affixed to support materials such as zeolites, nanoparticles, carbon materials, or polymers. Unfortunately, doing so inevitably dilutes the density of active sites. However, in the MOF PCN-222(Fe),<sup>80-81</sup> containing the metallolinker Fe-TCPP (TCPP = tetrakis(4-carboxyphenyl)porphyrin), a highly porous, stable MOF with a high density of iron porphyrin groups maintained at a fixed distance apart from each other was successfully synthesized and reported (Figure 8). The MOF was then shown to act as an effective peroxidase mimic, with catalytic activities and substrate binding affinities surpassing their homogenous analogs.



**Figure 8.** Crystal structure of PCN-222(Fe), with the porphyrin-containing metallolinker Fe-TCPP and an 8-connected  $Zr_6$  cluster. Copyright 2012 Angewandte Chemie International Edition.

On the other hand, cooperative catalysis, in which multiple metal centers work in concert to catalyze a single reaction, also widely exist in nature, notably in enzymes such as the binuclear Fe-containing methane monooxygenase<sup>82-83</sup> and the binuclear Cu-containing tyrosinase (Figure 9),<sup>84-85</sup> which react oxygen gas with methane and phenols respectively under extremely mild conditions. Similarly, through mimicking nature, the synthesis of multinuclear catalysts has emerged as an impressive design strategy that has often resulted in catalysts with higher activities and/or selectivities than their mononuclear analogs.<sup>86-89</sup>





**Figure 9.** (a) Structure of methane monooxygenase and (b) its binuclear Fe active site. Copyright 2011 Accounts of Chemical Research. (c) Structure of mushroom tyrosinase and (d) its binuclear Cu active site. Copyright 2011 Biochemistry.

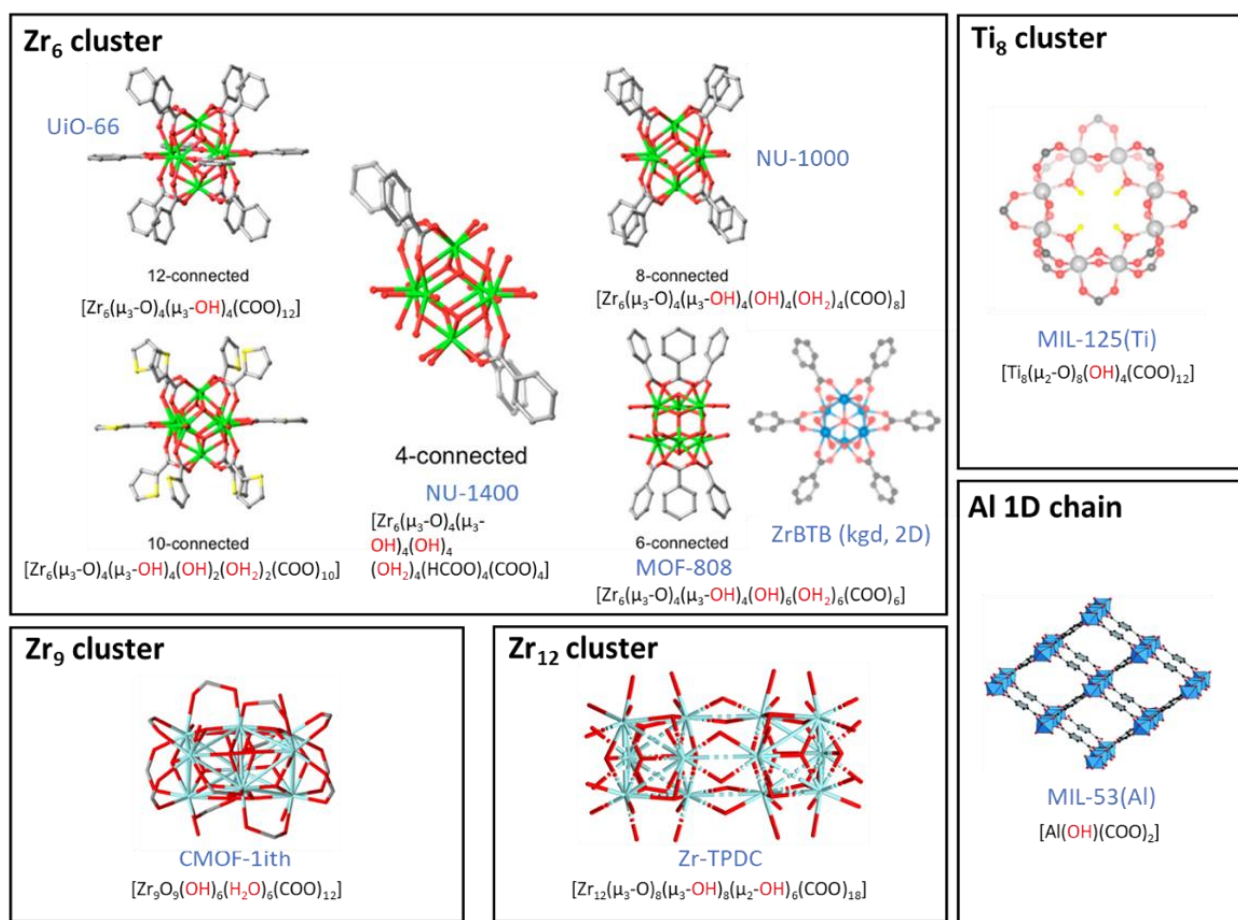
Methods of achieving such cooperative interactions include the design of MOFs with heterobimetallic clusters through controlled synthesis or doping,<sup>90-94</sup> control of metallolinker orientation via synthesis of phases with different topologies,<sup>95</sup> encapsulation of guests that interact with a host framework,<sup>96-97</sup> and grafting or substitution of active metal sites onto the metal nodes of host frameworks,<sup>67-76</sup> all of which have been proven to substantially improve catalytic activity and/or selectivity.

However, in order to preserve the high porosities of MOFs for catalytic applications, retain a high degree of control over the host MOF topology, and allow flexibility in the synthesis of a series of catalysts, the method of grafting catalytically active metal sites onto the nodes of a host framework was chosen as the focus of Chapters 2 and 3 of this dissertation.

As the secondary single metal sites are anchored similarly to traditional metal-oxo supports (metal oxides, silica, alumina),<sup>98-100</sup> which are widely used as heterogeneous catalysts in industrial-scale syntheses, MOFs with  $-OH/-OH_2$  groups on their metal nodes have attracted great interest. Unlike traditional supports with their complex multiple binding modes though, the highly crystalline nature of MOFs with discrete metal-oxo/hydroxo cluster nodes offer a far more well-ordered platform for the atomically precise addition of single metal sites to MOFs, allowing for accurate structural characterization. Furthermore, factors such as pore size and framework topology can be tuned exactly to specification.

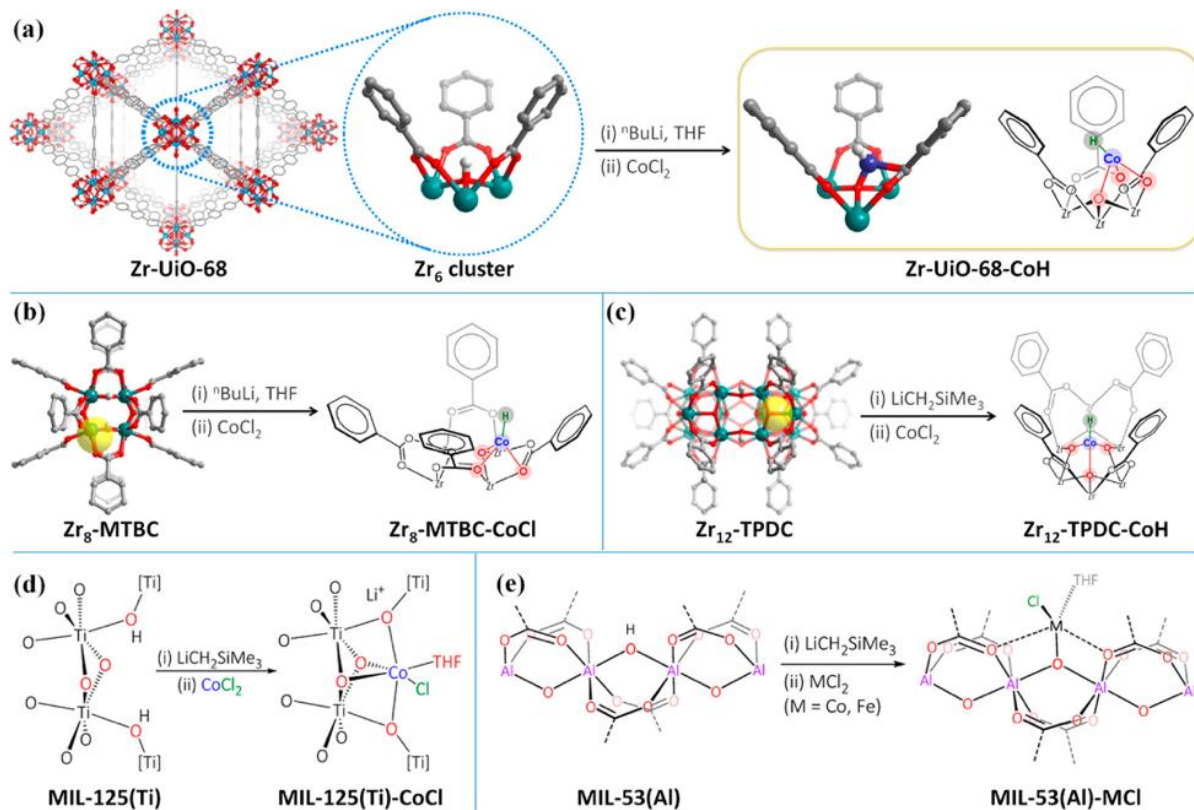
## 1.5 Grafting Inorganic Metal Species to Metal Nodes of MOFs

Many metal nodes in MOFs possess coordinately unsaturated metal clusters with terminal -OH or -OH<sub>2</sub> groups, as well as bridging  $\mu_2$ -OH and  $\mu_3$ -OH groups which can be used as anchors for the grafting of additional metals to the nodes (Figure 10).<sup>67-76</sup> Such grafting of additional metal species has been achieved via chemical deposition<sup>101-104</sup> and vapor-phase atomic layer deposition.<sup>104-106</sup> Of the two methods, chemical deposition is the most popular method to graft single metal-site species on the nodes of MOFs, as no specialized equipment is required, and syntheses can often be conducted at ambient temperature and pressure. MOFs are either directly soaked in a solution of metal salts,<sup>103-104</sup> or the clusters are deprotonated prior to addition of metal salts.<sup>101-102</sup>

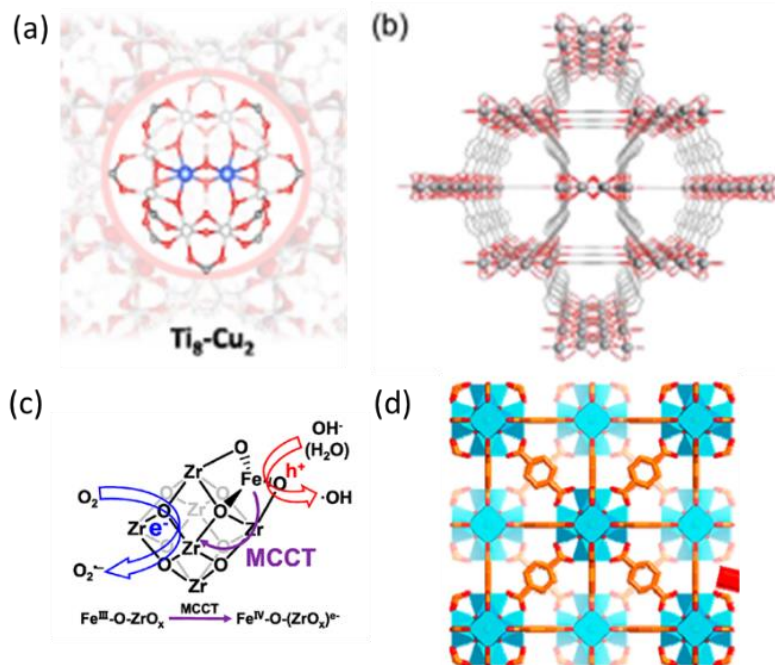


**Figure 10.** Different types of MOF nodes and their cluster formulas. Adapted from 2017-2020 American Chemical Society, 2018 Angewandte Chemie International Edition, 2004 Chemistry-A European Journal.

Generally, only the terminal -OH or -OH<sub>2</sub> groups will be utilized in a direct metal salt solution synthesis, while bases are required to deprotonate bridging  $\mu_2$ -OH and  $\mu_3$ -OH groups.<sup>107-108</sup> The benefit of deprotonation is the creation of additional coordination pockets on the MOF nodes, which help to stabilize the grafted active metal centers. The most commonly used reagents for such deprotonation are alkyllithium reagents, and the method has been developed and applied by the Lin group for the post-synthetic modification of UiO-68, and Zr<sub>12</sub>-TPDC, MIL-125(Ti), and MIL-53(Al), among others (Figure 11).<sup>67-76</sup>



**Figure 11.** Post-synthetic modification of MOFs using alkyllithium bases. Copyright 2016 Springer Nature, 2018-2019 American Chemical Society.



**Figure 12.** (a) Binuclear copper center in (b) MIL-125(Ti). (c) Iron grafted onto a zirconium cluster in (d) UiO-66.

The grafting method has proven to be effective at enhancing synergistic interactions between metals in a framework. Figure 12a and b show a grafted dinuclear copper site reminiscent of the enzyme tyrosinase (refer to Figure 9) into a titanium MOF, MIL-125(Ti), which can be used in catalytic epoxidation and C-H activation of organic substrates.<sup>67</sup> In Figure 12c and d, a proposed metal-to-cluster charge transfer<sup>109-111</sup> upon visible light photoexcitation occurs for the Fe-grafted MOF, UiO-66-Fe.<sup>112</sup> This charge transfer allows the ensemble to act as a redox photocatalyst, oxidizing water to the hydroxyl radical and reducing oxygen gas to the oxide, both reactive oxygen species of which can be utilized for the oxidation of various organic substrates.

The goal of Chapters 2 and 3 is to expand on both ideas and synthesize MOF catalysts with synergistic interactions between the grafted metals, as well as between the metal and node respectively on different MOF platforms and study the factors that affect such synergistic interactions and their influence on the catalytic activities and selectivities of the MOF catalysts.

## 1.6 References

1. Furukawa, H.; Cordova, K. E.; O'Keeffe, M.; Yaghi, O. M., The chemistry and applications of metal-organic frameworks. *Science* **2013**, *341* (6149).
2. Introduction to Metal–Organic Frameworks. *Chem. Rev.* **2012**, *112* (2), 673-674.
3. Zhou, H.-C. J.; Kitagawa, S., Metal–Organic Frameworks (MOFs). *Chem. Soc. Rev.* **2014**, *43* (16), 5415-5418.
4. Griffin, S. L.; Champness, N. R., A periodic table of metal-organic frameworks. *Coord. Chem. Rev.* **2020**, *414*, 213295-213295.
5. Feng, L.; Wang, K. Y.; Willman, J.; Zhou, H. C., Hierarchy in Metal-Organic Frameworks. *ACS Cent Sci* **2020**, *6* (3), 359-367.
6. Yaghi, O. M.; Li, H.; Eddaoudi, M.; O'Keeffe, M., Design and synthesis of an exceptionally stable and highly porous metal-organic framework. *Nature* **1999**, *402* (6759), 276-279.
7. Chui, S. S., A Chemically Functionalizable Nanoporous Material [Cu<sub>3</sub>(TMA)<sub>2</sub>(H<sub>2</sub>O)<sub>3</sub>]<sub>n</sub>. *Science* **1999**, *283* (5405), 1148-1150.
8. Furukawa, H.; Go, Y. B.; Ko, N.; Park, Y. K.; Uribe-Romo, F. J.; Kim, J.; O'Keeffe, M.; Yaghi, O. M., Isoreticular expansion of metal-organic frameworks with triangular and square building units and the lowest calculated density for porous crystals. *Inorg. Chem.* **2011**, *50* (18), 9147-52.
9. Furukawa, H.; Ko, N.; Go, Y. B.; Aratani, N.; Choi, S. B.; Choi, E.; Yazaydin, A. O.; Snurr, R. Q.; O'Keeffe, M.; Kim, J.; Yaghi, O. M., Ultrahigh porosity in metal-organic frameworks. *Science* **2010**, *329* (5990), 424-8.
10. Farha, O. K.; Eryazici, I.; Jeong, N. C.; Hauser, B. G.; Wilmer, C. E.; Sarjeant, A. A.; Snurr, R. Q.; Nguyen, S. T.; Yazaydin, A. O.; Hupp, J. T., Metal-organic framework materials with ultrahigh surface areas: is the sky the limit? *J. Am. Chem. Soc.* **2012**, *134* (36), 15016-21.
11. Qiu, S.; Xue, M.; Zhu, G., Metal-organic framework membranes: from synthesis to separation application. *Chem. Soc. Rev.* **2014**, *43* (16), 6116-40.
12. Banerjee, D.; Simon, C. M.; Elsaidi, S. K.; Haranczyk, M.; Thallapally, P. K., Xenon Gas Separation and Storage Using Metal-Organic Frameworks. *Chem* **2018**.
13. He, Y.; Zhou, W.; Qian, G.; Chen, B., Methane storage in metal-organic frameworks. *Chem. Soc. Rev.* **2014**, *43* (16), 5657-78.
14. Hu, Z.; Deibert, B. J.; Li, J., Luminescent metal-organic frameworks for chemical sensing and explosive detection. *Chem. Soc. Rev.* **2014**, *43* (16), 5815-40.
15. Rogge, S. M. J.; Bavykina, A.; Hajek, J.; Garcia, H.; Olivos-Suarez, A. I.; Sepúlveda-Escribano, A.; Vimont, A.; Clet, G.; Bazin, P.; Kapteijn, F.; Daturi, M.; Ramos-Fernandez, E. V.; Llabrés i Xamena, F. X.; Van Speybroeck, V.; Gascon, J., Metal–organic and covalent organic frameworks as single-site catalysts. *Chem. Soc. Rev.* **2017**.
16. Downes, C. A.; Marinescu, S. C., Electrocatalytic Metal-Organic Frameworks for Energy Applications. *ChemSusChem* **2017**.
17. Jiang, J.; Gandara, F.; Zhang, Y. B.; Na, K.; Yaghi, O. M.; Klemperer, W. G., Superacidity in sulfated metal-organic framework-808. *J. Am. Chem. Soc.* **2014**, *136* (37), 12844-7.
18. Della Rocca, J.; Liu, D.; Lin, W., Nanoscale metal-organic frameworks for biomedical imaging and drug delivery. *Acc. Chem. Res.* **2011**, *44* (10), 957-68.
19. Beyzavi, M. H.; Vermeulen, N. A.; Howarth, A. J.; Tussupbayev, S.; League, A. B.; Schweitzer, N. M.; Gallagher, J. R.; Platero-Prats, A. E.; Hafezi, N.; Sarjeant, A. A.; Miller, J. T.;

- Chapman, K. W.; Stoddart, J. F.; Cramer, C. J.; Hupp, J. T.; Farha, O. K., A Hafnium-Based Metal-Organic Framework as a Nature-Inspired Tandem Reaction Catalyst. *J. Am. Chem. Soc.* **2015**, *137* (42), 13624-31.
20. Ramaswamy, P.; Wong, N. E.; Shimizu, G. K., MOFs as proton conductors--challenges and opportunities. *Chem Soc Rev* **2014**, *43* (16), 5913-32.
21. Kalmutzki, M. J.; Diercks, C. S.; Yaghi, O. M., Metal-Organic Frameworks for Water Harvesting from Air. *Adv Mater* **2018**, e1704304.
22. Furukawa, H.; Cordova, K. E.; O'Keeffe, M.; Yaghi, O. M., The chemistry and applications of metal-organic frameworks. *Science* **2013**, *341* (6149), 1230444.
23. Evans, J. D.; Sumbly, C. J.; Doonan, C. J., Post-synthetic metalation of metal-organic frameworks. *Chem. Soc. Rev.* **2014**, *43* (16), 5933-51.
24. Li, Z.; Xu, Q., Metal-Nanoparticle-Catalyzed Hydrogen Generation from Formic Acid. *Acc. Chem. Res.* **2017**, *50* (6), 1449-1458.
25. Yang, Q.; Xu, Q.; Jiang, H.-L., Metal-organic frameworks meet metal nanoparticles: synergistic effect for enhanced catalysis. *Chem. Soc. Rev.* **2017**, *46* (15), 4774-4808.
26. Liu, L.; Corma, A., Metal Catalysts for Heterogeneous Catalysis: From Single Atoms to Nanoclusters and Nanoparticles. *Chem. Rev.* **2018**, *118* (10), 4981-5079.
27. Shelke, Y. G.; Yashmeen, A.; Gholap, A. V. A.; Gharpure, S. J.; Kapdi, A. R., Homogeneous Catalysis: A Powerful Technology for the Modification of Important Biomolecules. *Chemistry – An Asian Journal* **2018**, *13* (20), 2991-3013.
28. Kumar, A.; Daw, P.; Milstein, D., Homogeneous Catalysis for Sustainable Energy: Hydrogen and Methanol Economies, Fuels from Biomass, and Related Topics. *Chem. Rev.* **2022**, *122* (1), 385-441.
29. Pelletier, J. D. A.; Basset, J.-M., Catalysis by Design: Well-Defined Single-Site Heterogeneous Catalysts. *Acc. Chem. Res.* **2016**, *49* (4), 664-677.
30. Thomas, J. M., The concept, reality and utility of single-site heterogeneous catalysts (SSHCs). *Physical Chemistry Chemical Physics* **2014**, *16* (17), 7647-7661.
31. Yang, X.-F.; Wang, A.; Qiao, B.; Li, J.; Liu, J.; Zhang, T., Single-Atom Catalysts: A New Frontier in Heterogeneous Catalysis. *Acc. Chem. Res.* **2013**, *46* (8), 1740-1748.
32. Wang, A.; Li, J.; Zhang, T., Heterogeneous single-atom catalysis. *Nature Reviews Chemistry* **2018**, *2* (6), 65-81.
33. Zhao, W.; Li, G.; Tang, Z., Metal-organic frameworks as emerging platform for supporting isolated single-site catalysts. *Nano Today* **2019**, *27*, 178-197.
34. Wei, Y. S.; Zhang, M.; Zou, R.; Xu, Q., Metal-Organic Framework-Based Catalysts with Single Metal Sites. *Chem. Rev.* **2020**.
35. Syed, Z. H.; Sha, F.; Zhang, X.; Kaphan, D. M.; Delferro, M.; Farha, O. K., Metal-Organic Framework Nodes as a Supporting Platform for Tailoring the Activity of Metal Catalysts. *ACS Catalysis* **2020**.
36. Corma, A.; García, H.; Llabrés i Xamena, F. X., Engineering Metal Organic Frameworks for Heterogeneous Catalysis. *Chem. Rev.* **2010**, *110* (8), 4606-4655.
37. Jiao, L.; Wang, Y.; Jiang, H.-L.; Xu, Q., Metal-Organic Frameworks as Platforms for Catalytic Applications. *Adv. Mater.* **2018**, *30* (37), 1703663.

38. Li, H.; Li, L.; Lin, R.-B.; Zhou, W.; Zhang, Z.; Xiang, S.; Chen, B., Porous metal-organic frameworks for gas storage and separation: Status and challenges. *EnergyChem* **2019**, *1* (1), 100006.
39. Zhou, D.-D.; Zhang, X.-W.; Mo, Z.-W.; Xu, Y.-Z.; Tian, X.-Y.; Li, Y.; Chen, X.-M.; Zhang, J.-P., Adsorptive separation of carbon dioxide: From conventional porous materials to metal-organic frameworks. *EnergyChem* **2019**, *1* (3), 100016.
40. Cui, Y.; Li, B.; He, H.; Zhou, W.; Chen, B.; Qian, G., Metal-Organic Frameworks as Platforms for Functional Materials. *Acc. Chem. Res.* **2016**, *49* (3), 483-493.
41. Rogge, S. M. J.; Bavykina, A.; Hajek, J.; Garcia, H.; Olivos-Suarez, A. I.; Sepúlveda-Escribano, A.; Vimont, A.; Clet, G.; Bazin, P.; Kapteijn, F.; Daturi, M.; Ramos-Fernandez, E. V.; Llabrés i Xamena, F. X.; Van Speybroeck, V.; Gascon, J., Metal-organic and covalent organic frameworks as single-site catalysts. *Chem. Soc. Rev.* **2017**, *46* (11), 3134-3184.
42. Hall, J. N.; Bollini, P., Structure, characterization, and catalytic properties of open-metal sites in metal organic frameworks. *Reaction Chemistry & Engineering* **2019**, *4* (2), 207-222.
43. Chen, B.; Eddaoudi, M.; Reineke, T. M.; Kampf, J. W.; O'Keeffe, M.; Yaghi, O. M., Cu<sub>2</sub>(ATC)·6H<sub>2</sub>O: Design of Open Metal Sites in Porous Metal-Organic Crystals (ATC: 1,3,5,7-Adamantane Tetracarboxylate). *J. Am. Chem. Soc.* **2000**, *122* (46), 11559-11560.
44. Köberl, M.; Cokoja, M.; Herrmann, W. A.; Kühn, F. E., From molecules to materials: Molecular paddle-wheel synthons of macromolecules, cage compounds and metal-organic frameworks. *Dalton Transactions* **2011**, *40* (26), 6834-6859.
45. Antonio, A. M.; Rosenthal, J.; Bloch, E. D., Electrochemically Mediated Syntheses of Titanium(III)-Based Metal-Organic Frameworks. *J. Am. Chem. Soc.* **2019**, *141* (29), 11383-11387.
46. Jiang, H.-L.; Feng, D.; Liu, T.-F.; Li, J.-R.; Zhou, H.-C., Pore Surface Engineering with Controlled Loadings of Functional Groups via Click Chemistry in Highly Stable Metal-Organic Frameworks. *J. Am. Chem. Soc.* **2012**, *134* (36), 14690-14693.
47. Furukawa, H.; Gándara, F.; Zhang, Y.-B.; Jiang, J.; Queen, W. L.; Hudson, M. R.; Yaghi, O. M., Water Adsorption in Porous Metal-Organic Frameworks and Related Materials. *J. Am. Chem. Soc.* **2014**, *136* (11), 4369-4381.
48. Loiseau, T.; Serre, C.; Huguenard, C.; Fink, G.; Taulelle, F.; Henry, M.; Bataille, T.; Férey, G., A Rationale for the Large Breathing of the Porous Aluminum Terephthalate (MIL-53) Upon Hydration. *Chemistry – A European Journal* **2004**, *10* (6), 1373-1382.
49. Millange, F.; Serre, C.; Férey, G., Synthesis, structure determination and properties of MIL-53as and MIL-53ht: the first C<sub>riii</sub> hybrid inorganic-organic microporous solids: C<sub>riii</sub>(OH)·{O<sub>2</sub>C-C<sub>6</sub>H<sub>4</sub>-CO<sub>2</sub>}·{HO<sub>2</sub>C-C<sub>6</sub>H<sub>4</sub>-CO<sub>2</sub>H}<sub>x</sub>. *Chem. Commun.* **2002**, (8), 822-823.
50. Shearer, G. C.; Chavan, S.; Bordiga, S.; Svelle, S.; Olsbye, U.; Lillerud, K. P., Defect Engineering: Tuning the Porosity and Composition of the Metal-Organic Framework UiO-66 via Modulated Synthesis. *Chem. Mater.* **2016**, *28* (11), 3749-3761.
51. Yuan, L.; Tian, M.; Lan, J.; Cao, X.; Wang, X.; Chai, Z.; Gibson, J. K.; Shi, W., Defect engineering in metal-organic frameworks: a new strategy to develop applicable actinide sorbents. *Chem. Commun.* **2018**, *54* (4), 370-373.
52. He, J.; Li, N.; Li, Z.-G.; Zhong, M.; Fu, Z.-X.; Liu, M.; Yin, J.-C.; Shen, Z.; Li, W.; Zhang, J.; Chang, Z.; Bu, X.-H., Strategic Defect Engineering of Metal-Organic Frameworks for Optimizing the Fabrication of Single-Atom Catalysts. *Adv. Funct. Mater.* **2021**, *31* (41), 2103597.

53. Bachman, J. E.; Kapelewski, M. T.; Reed, D. A.; Gonzalez, M. I.; Long, J. R., M2(m-dobdc) (M = Mn, Fe, Co, Ni) Metal-Organic Frameworks as Highly Selective, High-Capacity Adsorbents for Olefin/Paraffin Separations. *J. Am. Chem. Soc.* **2017**, *139* (43), 15363-15370.
54. Bloch, E. D.; Queen, W. L.; Krishna, R.; Zadrozny, J. M.; Brown, C. M.; Long, J. R., Hydrocarbon Separations in a Metal-Organic Framework with Open Iron(II) Coordination Sites. *Science* **2012**, *335* (6076), 1606-1610.
55. Baumann, A. E.; Burns, D. A.; Liu, B.; Thoi, V. S., Metal-organic framework functionalization and design strategies for advanced electrochemical energy storage devices. *Communications Chemistry* **2019**, *2* (1), 86.
56. Liu, X.; Zhang, L.; Wang, J., Design strategies for MOF-derived porous functional materials: Preserving surfaces and nurturing pores. *Journal of Materiomics* **2021**, *7* (3), 440-459.
57. Bernales, V.; Ortuño, M. A.; Truhlar, D. G.; Cramer, C. J.; Gagliardi, L., Computational Design of Functionalized Metal–Organic Framework Nodes for Catalysis. *ACS Central Science* **2018**, *4* (1), 5-19.
58. Ma, X.; Liu, H.; Yang, W.; Mao, G.; Zheng, L.; Jiang, H. L., Modulating Coordination Environment of Single-Atom Catalysts and Their Proximity to Photosensitive Units for Boosting MOF Photocatalysis. *J. Am. Chem. Soc.* **2021**, *143* (31), 12220-12229.
59. Van Velthoven, N.; Waitschat, S.; Chavan, S. M.; Liu, P.; Smolders, S.; Vercammen, J.; Bueken, B.; Bals, S.; Lillerud, K. P.; Stock, N.; De Vos, D. E., Single-site metal-organic framework catalysts for the oxidative coupling of arenes: Via C-H/C-H activation. *Chemical Science* **2019**, *10* (12), 3616-3622.
60. Lyu, J.; Zhang, X.; Otake, K. I.; Wang, X.; Li, P.; Li, Z.; Chen, Z.; Zhang, Y.; Wasson, M. C.; Yang, Y.; Bai, P.; Guo, X.; Islamoglu, T.; Farha, O. K., Topology and porosity control of metal-organic frameworks through linker functionalization. *Chemical Science* **2019**, *10* (4), 1186-1192.
61. Burgess, S. A.; Kassie, A.; Baranowski, S. A.; Fritzsching, K. J.; Schmidt-Rohr, K.; Brown, C. M.; Wade, C. R., Improved Catalytic Activity and Stability of a Palladium Pincer Complex by Incorporation into a Metal–Organic Framework. *J. Am. Chem. Soc.* **2016**, *138* (6), 1780-1783.
62. Reiner, B. R.; Mucha, N. T.; Rothstein, A.; Temme, J. S.; Duan, P.; Schmidt-Rohr, K.; Foxman, B. M.; Wade, C. R., Zirconium Metal–Organic Frameworks Assembled from Pd and Pt PNNNP Pincer Complexes: Synthesis, Postsynthetic Modification, and Lewis Acid Catalysis. *Inorganic Chemistry* **2018**, *57* (5), 2663-2672.
63. Wei, Y.-L.; Li, Y.; Chen, Y.-Q.; Dong, Y.; Yao, J.-J.; Han, X.-Y.; Dong, Y.-B., Pd(II)-NHDC-Functionalized UiO-67 Type MOF for Catalyzing Heck Cross-Coupling and Intermolecular Benzyne–Benzyne–Alkene Insertion Reactions. *Inorganic Chemistry* **2018**, *57* (8), 4379-4386.
64. Gao, W.-Y.; Chen, Y.; Niu, Y.; Williams, K.; Cash, L.; Perez, P. J.; Wojtas, L.; Cai, J.; Chen, Y.-S.; Ma, S., Crystal Engineering of an nbo Topology Metal–Organic Framework for Chemical Fixation of CO<sub>2</sub> under Ambient Conditions. *Angew. Chem. Int. Ed.* **2014**, *53* (10), 2615-2619.
65. Zhu, J.; Usov, P. M.; Xu, W.; Celis-Salazar, P. J.; Lin, S.; Kessinger, M. C.; Landaverde-Alvarado, C.; Cai, M.; May, A. M.; Slebodnick, C.; Zhu, D.; Senanayake, S. D.; Morris, A. J., A New Class of Metal-Cyclam-Based Zirconium Metal–Organic Frameworks for CO<sub>2</sub> Adsorption and Chemical Fixation. *J. Am. Chem. Soc.* **2018**, *140* (3), 993-1003.
66. Bohnsack, A. M.; Ibarra, I. A.; Bakhmutov, V. I.; Lynch, V. M.; Humphrey, S. M., Rational Design of Porous Coordination Polymers Based on Bis(phosphine)MCl<sub>2</sub> Complexes That Exhibit



High-Temperature H<sub>2</sub> Sorption and Chemical Reactivity. *J. Am. Chem. Soc.* **2013**, *135* (43), 16038-16041.

67. Feng, X.; Song, Y.; Chen, J. S.; Xu, Z.; Dunn, S. J.; Lin, W., Rational Construction of an Artificial Binuclear Copper Monooxygenase in a Metal-Organic Framework. *J. Am. Chem. Soc.* **2021**, *143* (2), 1107-1118.

68. Feng, X.; Song, Y.; Lin, W., Transforming Hydroxide-Containing Metal–Organic Framework Nodes for Transition Metal Catalysis. *Trends in Chemistry* **2020**, *2* (11), 965-979.

69. Song, Y.; Li, Z.; Ji, P.; Kaufmann, M.; Feng, X.; Chen, J. S.; Wang, C.; Lin, W., Metal-Organic Framework Nodes Support Single-Site Nickel(II) Hydride Catalysts for the Hydrogenolysis of Aryl Ethers. *ACS Catalysis* **2019**, *9* (2), 1578-1583.

70. Song, Y.; Chen, J. S.; Li, Z.; Chen, E. Y.; Wang, C.; Lin, W.; Feng, X.; Kaufmann, M., Cobalt-bridged secondary building units in a titanium metal–organic framework catalyze cascade reduction of N-heteroarenes. *Chemical Science* **2018**, *1* (c), 2193-2198.

71. Ji, P.; Song, Y.; Drake, T.; Veroneau, S. S.; Lin, Z.; Pan, X.; Lin, W., Titanium(III)-Oxo Clusters in a Metal-Organic Framework Support Single-Site Co(II)-Hydride Catalysts for Arene Hydrogenation. *J. Am. Chem. Soc.* **2018**, *140* (1), 433-440.

72. Manna, K.; Ji, P.; Lin, Z.; Greene, F. X.; Urban, A.; Thacker, N. C.; Lin, W., Chemoselective single-site Earth-abundant metal catalysts at metal-organic framework nodes. *Nature Communications* **2016**, *7*, 1-11.

73. Manna, K.; Ji, P.; Greene, F. X.; Lin, W., Metal-Organic Framework Nodes Support Single-Site Magnesium-Alkyl Catalysts for Hydroboration and Hydroamination Reactions. *J. Am. Chem. Soc.* **2016**, *138* (24), 7488-7491.

74. Ji, P.; Manna, K.; Lin, Z.; Urban, A.; Greene, F. X.; Lan, G.; Lin, W., Single-Site Cobalt Catalysts at New Zr<sub>8</sub>(μ<sub>2</sub>-O)<sub>8</sub>(μ<sub>2</sub>-OH)<sub>4</sub> Metal-Organic Framework Nodes for Highly Active Hydrogenation of Alkenes, Imines, Carbonyls, and Heterocycles. *J. Am. Chem. Soc.* **2016**, *138* (37), 12234-12242.

75. Feng, X.; Song, Y.; Lin, W., Transforming Hydroxide-Containing Metal–Organic Framework Nodes for Transition Metal Catalysis. *Trends in Chemistry* **2020**, *2* (11), 965-979.

76. An, B.; Li, Z.; Song, Y.; Zhang, J.; Zeng, L.; Wang, C.; Lin, W., Cooperative copper centres in a metal–organic framework for selective conversion of CO<sub>2</sub> to ethanol. *Nature Catalysis* **2020**, *2* (8), 709-717.

77. Zhao, W.; Shi, Y.; Jiang, Y.; Zhang, X.; Long, C.; An, P.; Zhu, Y.; Shao, S.; Yan, Z.; Li, G.; Tang, Z., Fe-O Clusters Anchored on Nodes of Metal-Organic Frameworks for Direct Methane Oxidation. *Angew Chem Int Ed Engl* **2021**, *60* (11), 5811-5815.

78. Yang, Y.; Zhang, X.; Kanchanakungwankul, S.; Lu, Z.; Noh, H.; Syed, Z. H.; Farha, O. K.; Truhlar, D. G.; Hupp, J. T., Unexpected "Spontaneous" Evolution of Catalytic, MOF-Supported Single Cu(II) Cations to Catalytic, MOF-Supported Cu(0) Nanoparticles. *J. Am. Chem. Soc.* **2020**, *142* (50), 21169-21177.

79. Zhang, H.; Liu, X.; Wu, Y.; Guan, C.; Cheetham, A. K.; Wang, J., MOF-derived nanohybrids for electrocatalysis and energy storage: Current status and perspectives. *Chem. Commun.* **2018**, *54* (42), 5268-5288.

80. Feng, D.; Chung, W. C.; Wei, Z.; Gu, Z. Y.; Jiang, H. L.; Chen, Y. P.; Darensbourg, D. J.; Zhou, H. C., Construction of ultrastable porphyrin Zr metal-organic frameworks through linker elimination. *J. Am. Chem. Soc.* **2013**, *135* (45), 17105-17110.

81. Feng, D.; Gu, Z.-Y.; Li, J.-R.; Jiang, H.-L.; Wei, Z.; Zhou, H.-C., Zirconium-Metalloporphyrin PCN-222: Mesoporous Metal–Organic Frameworks with Ultrahigh Stability as Biomimetic Catalysts. *Angew. Chem. Int. Ed.* **2012**, *51* (41), 10307-10310.
82. Tinberg, C. E.; Lippard, S. J., Dioxygen activation in soluble methane monooxygenase. *Acc. Chem. Res.* **2011**, *44* (4), 280-288.
83. Torres Pazmino, D. E.; Winkler, M.; Glieder, A.; Fraaije, M. W., Monooxygenases as biocatalysts: Classification, mechanistic aspects and biotechnological applications. *J. Biotechnol.* **2010**, *146* (1-2), 9-24.
84. Ismaya, W. T.; Rozeboom, H. J.; Weijn, A.; Mes, J. J.; Fusetti, F.; Wichers, H. J.; Dijkstra, B. W., Crystal structure of agaricus bisporus mushroom tyrosinase: Identity of the tetramer subunits and interaction with tropolone. *Biochemistry* **2011**, *50* (24), 5477-5486.
85. Chioccare, F.; Chiodini, G.; Farina, F.; Orlandi, M.; Rindone, B.; Sebastian, R., Synthetic mimics of tyrosinase: catechols from ortho-, meta- and para-substituted phenols and copper(I) complexes. *J. Mol. Catal. A: Chem.* **1995**, *1*, 187-194.
86. Delferro, M.; Marks, T. J., Multinuclear Olefin Polymerization Catalysts. *Chem. Rev.* **2011**, *111* (3), 2450-2485.
87. Zhang, Q.; Guan, J., Mono-/Multinuclear Water Oxidation Catalysts. *ChemSusChem* **2019**, *12* (14), 3209-3235.
88. Fazekas, E.; McIntosh, R. D., Multinuclear catalysts for the ring-opening polymerisation of cyclic esters. In *Organometallic Chemistry: Volume 43*, The Royal Society of Chemistry: 2021; Vol. 43, pp 63-82.
89. Nath, B. D.; Takaishi, K.; Ema, T., Macrocyclic multinuclear metal complexes acting as catalysts for organic synthesis. *Catalysis Science & Technology* **2020**, *10* (1), 12-34.
90. Chen, D.-M.; Zhang, N.-N.; Liu, C.-S.; Jiang, Z.-H.; Wang, X.-D.; Du, M., A Mixed-Cluster Approach for Building a Highly Porous Cobalt(II) Isonicotinic Acid Framework: Gas Sorption Properties and Computational Analyses. *Inorganic Chemistry* **2017**, *56* (5), 2379-2382.
91. Masoomi, M. Y.; Morsali, A.; Dhakshinamoorthy, A.; Garcia, H., Mixed-Metal MOFs: Unique Opportunities in Metal–Organic Framework (MOF) Functionality and Design. *Angew. Chem. Int. Ed.* **2019**, *58* (43), 15188-15205.
92. Caskey, S. R.; Matzger, A. J., Selective Metal Substitution for the Preparation of Heterobimetallic Microporous Coordination Polymers. *Inorganic Chemistry* **2008**, *47* (18), 7942-7944.
93. Wang, Y.; Bredenkötter, B.; Rieger, B.; Volkmer, D., Two-dimensional metal–organic frameworks (MOFs) constructed from heterotrimeric coordination units and 4,4'-biphenyldicarboxylate ligands. *Dalton Transactions* **2007**, (6), 689-696.
94. He, J.; Yu, J.; Zhang, Y.; Pan, Q.; Xu, R., Synthesis, Structure, and Luminescent Property of a Heterometallic Metal–Organic Framework Constructed from Rod-Shaped Secondary Building Blocks. *Inorganic Chemistry* **2005**, *44* (25), 9279-9282.
95. Deria, P.; Gómez-Gualdrón, D. A.; Hod, I.; Snurr, R. Q.; Hupp, J. T.; Farha, O. K., Framework-Topology-Dependent Catalytic Activity of Zirconium-Based (Porphinato)zinc(II) MOFs. *J. Am. Chem. Soc.* **2016**, *138* (43), 14449-14457.
96. Hadjiivanov, K. I.; Panayotov, D. A.; Mihaylov, M. Y.; Ivanova, E. Z.; Chakarova, K. K.; Andonova, S. M.; Drenchev, N. L., Power of Infrared and Raman Spectroscopies to Characterize

Metal-Organic Frameworks and Investigate Their Interaction with Guest Molecules. *Chem. Rev.* **2021**, *121* (3), 1286-1424.

97. Tsumori, N.; Chen, L.; Wang, Q.; Zhu, Q.-L.; Kitta, M.; Xu, Q., Quasi-MOF: Exposing Inorganic Nodes to Guest Metal Nanoparticles for Drastically Enhanced Catalytic Activity. *Chem* **2018**, *4* (4), 845-856.

98. Nguyen, H. G. T.; Mao, L.; Peters, A. W.; Audu, C. O.; Brown, Z. J.; Farha, O. K.; Hupp, J. T.; Nguyen, S. T., Comparative study of titanium-functionalized UiO-66: support effect on the oxidation of cyclohexene using hydrogen peroxide. *Catalysis Science & Technology* **2015**, *5* (9), 4444-4451.

99. Liu, J.-C.; Wang, Y.-G.; Li, J., Toward Rational Design of Oxide-Supported Single-Atom Catalysts: Atomic Dispersion of Gold on Ceria. *J. Am. Chem. Soc.* **2017**, *139* (17), 6190-6199.

100. Thornburg, N. E.; Thompson, A. B.; Notestein, J. M., Periodic Trends in Highly Dispersed Groups IV and V Supported Metal Oxide Catalysts for Alkene Epoxidation with H<sub>2</sub>O<sub>2</sub>. *ACS Catalysis* **2015**, *5* (9), 5077-5088.

101. Feng, X.; Song, Y.; Chen, J. S.; Li, Z.; Chen, E. Y.; Kaufmann, M.; Wang, C.; Lin, W., Cobalt-bridged secondary building units in a titanium metal-organic framework catalyze cascade reduction of N-heteroarenes. *Chemical Science* **2019**, *10* (7), 2193-2198.

102. An, B.; Li, Z.; Song, Y.; Zhang, J.; Zeng, L.; Wang, C.; Lin, W., Cooperative copper centres in a metal-organic framework for selective conversion of CO<sub>2</sub> to ethanol. *Nature Catalysis* **2019**, *2* (8), 709-717.

103. Abdel-Mageed, A. M.; Rungtaweeworanit, B.; Parlinska-Wojtan, M.; Pei, X.; Yaghi, O. M.; Jürgen Behm, R., Highly Active and Stable Single-Atom Cu Catalysts Supported by a Metal-Organic Framework. *J. Am. Chem. Soc.* **2019**, *141* (13), 5201-5210.

104. Otake, K. I.; Ahn, S.; Knapp, J.; Hupp, J. T.; Notestein, J. M.; Farha, O. K., Vapor-Phase Cyclohexene Epoxidation by Single-Ion Fe(III) Sites in Metal-Organic Frameworks. *Inorganic Chemistry* **2021**, *60* (4), 2457-2463.

105. Wang, X.; Zhang, X.; Li, P.; Otake, K. I.; Cui, Y.; Lyu, J.; Krzyaniak, M. D.; Zhang, Y.; Li, Z.; Liu, J.; Buru, C. T.; Islamoglu, T.; Wasielewski, M. R.; Li, Z.; Farha, O. K., Vanadium Catalyst on Isostructural Transition Metal, Lanthanide, and Actinide Based Metal-Organic Frameworks for Alcohol Oxidation. *J. Am. Chem. Soc.* **2020**, *141* (20), 8306-8314.

106. Hackler, R. A.; Pandharkar, R.; Ferrandon, M. S.; Kim, I. S.; Vermeulen, N. A.; Gallington, L. C.; Chapman, K. W.; Farha, O. K.; Cramer, C. J.; Sauer, J.; Gagliardi, L.; Martinson, A. B. F.; Delferro, M., Isomerization and Selective Hydrogenation of Propyne: Screening of Metal-Organic Frameworks Modified by Atomic Layer Deposition. *J. Am. Chem. Soc.* **2020**, 20380-20389-20380-20389.

107. Wang, C.; An, B.; Lin, W., Metal-Organic Frameworks in Solid-Gas Phase Catalysis. *ACS Catalysis* **2019**, *9* (1), 130-146.

108. Manna, K.; Ji, P.; Greene, F. X.; Lin, W., Metal-Organic Framework Nodes Support Single-Site Magnesium-Alkyl Catalysts for Hydroboration and Hydroamination Reactions. *J. Am. Chem. Soc.* **2016**, *138* (24), 7488-7491.

109. Lin, W.; Frei, H., Photochemical CO<sub>2</sub> splitting by metal-to-metal charge-transfer excitation in mesoporous ZrCu(I)-MCM-41 silicate sieve. *J. Am. Chem. Soc.* **2005**, *127* (6), 1610-1.

110. Nakamura, R.; Okamoto, A.; Osawa, H.; Irie, H.; Hashimoto, K., Design of all-inorganic molecular-based photocatalysts sensitive to visible light: Ti(IV)-O-Ce(III) bimetallic assemblies on mesoporous silica. *J. Am. Chem. Soc.* **2007**, *129* (31), 9596-7.
111. Kramar, B. V.; Phelan, B. T.; Sprague-Klein, E. A.; Diroll, B. T.; Lee, S.; Otake, K.-i.; Palmer, R.; Mara, M. W.; Farha, O. K.; Hupp, J. T.; Chen, L. X., Single-Atom Metal Oxide Sites as Traps for Charge Separation in the Zirconium-Based Metal–Organic Framework NDC–NU-1000. *Energy & Fuels* **2021**, *35* (23), 19081-19095.
112. Xu, C.; Pan, Y.; Wan, G.; Liu, H.; Wang, L.; Zhou, H.; Yu, S. H.; Jiang, H. L., Turning on Visible-Light Photocatalytic C-H Oxidation over Metal-Organic Frameworks by Introducing Metal-to-Cluster Charge Transfer. *J. Am. Chem. Soc.* **2019**, *141* (48), 19110-19117.

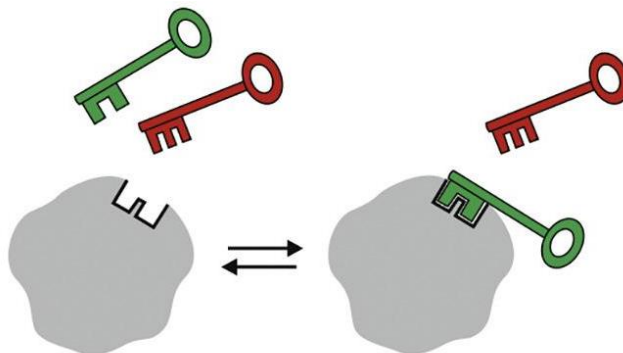
## Chapter 2. Construction of an Artificial Monooxygenase: Stabilization of bis( $\mu$ -oxo)dicopper Cluster in Zr-based Metal Organic Framework via Reticular Chemistry

### Abstract

The creation of artificial enzymes is extensively studied to mimic the structures and functions of their natural analogs. Herein we report the successful synthesis of a chemically and physically stable zirconium metal-organic framework (MOF), **MOF-565**, and the installation of binuclear copper cluster in between its nodes to create a heterogenous artificial enzyme. **MOF-565** has a **csq** topology with closely spaced (3.6 Å), unsaturated nodes containing hydroxide groups that serve as anchors for post-synthetic modification. Upon deprotonation of the hydroxides, metalation of the nodes was conducted to afford the MOF with bis( $\mu$ -oxo)dicopper ( $\text{Cu}^{\text{II}}_2(\mu_2\text{-OH})_2$ ) situated in-between the nodes (**MOF-565-Cu<sup>II</sup>**). The structure of **MOF-565-Cu<sup>II</sup>** was characterized by single-crystal X-ray diffraction, powder X-ray diffraction, inductively coupled plasma-optical emission spectrometry, Fourier-transform infrared spectroscopy, and X-ray absorption spectroscopy. In the presence of coreductant, **MOF-565-Cu<sup>II</sup>** is proved effective at catalyzing the epoxidation of olefins under very mild conditions using  $\text{O}_2$  gas as the oxidant, with activities far surpassing similar mononuclear Cu catalysts.

## 2.1 Introduction

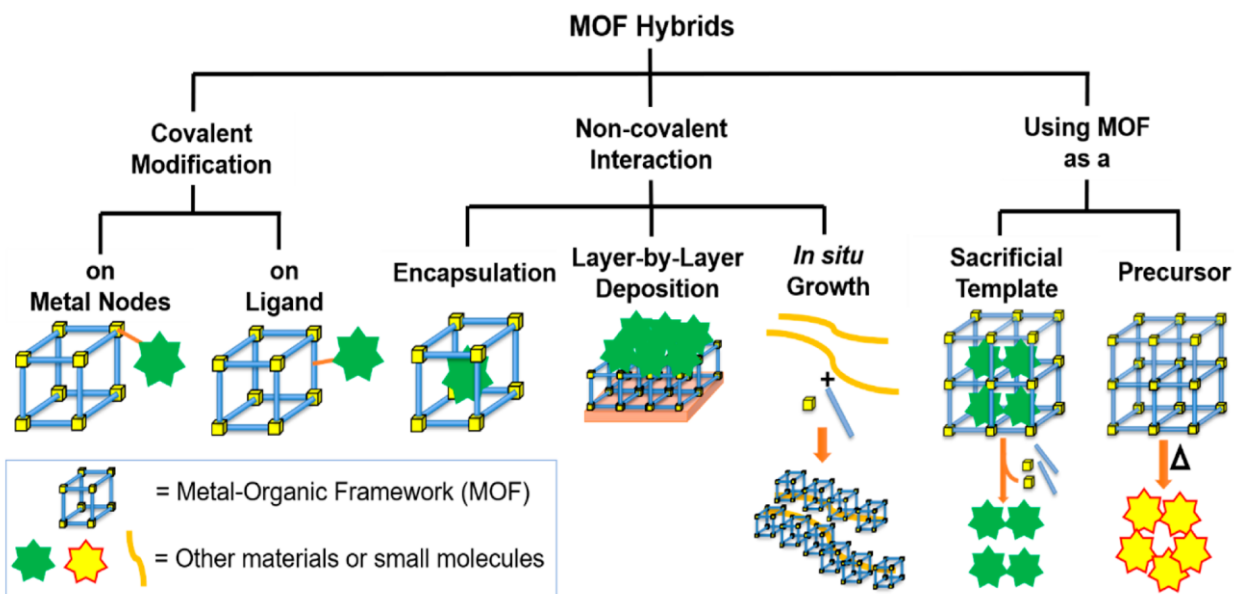
A critical key to designing efficient catalytic systems is the realization of chemical and physical confinement and isolation of reactants, products, and intermediates, as well as catalysts. This is well understood in biocatalysis, in which the correct folding of biomacromolecules such as proteins and membranes creates a binding pocket which dictates the selectivity and activity of enzymes and protects the active center from inhibitors, as well as defines the chemical environment for the catalyzed reaction, analogous to a lock-and-key mechanism (Figure 1).<sup>1-5</sup>



**Figure 1.** Illustration of enzyme lock-and-key mechanism, where grey represents the enzyme, and the red and green keys represent different substrates. Only the green substrate “key” fits into the enzyme “lock”, resulting in high selectivity. Adapted from 2019 Biotechnology Advances.

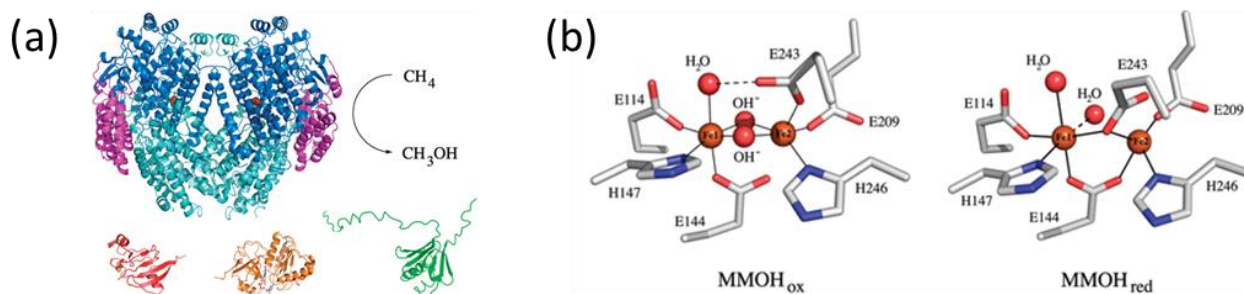
On the contrary, inorganic catalysts such as zeolites relies on the ordered rigid porous molecular-scale confinement to realize their activities and selectivities in chemical catalysis.<sup>6</sup> As an emerging class of porous materials, metal organic frameworks (MOFs) exhibit both crystalline porosity and flexibility and could well bridge enzymes and zeolites. In fact, one of the earliest functions of MOFs was the shape and size selective catalytic cyanylation of aldehydes.<sup>7</sup>

Over the past two decades, the fast pace of MOFs synthesis development drives the rapid expansion of MOF catalysis via three design strategies based on modification of inorganic nodes, organic linker, and pore space (Figure 2).<sup>8-16</sup> Following these approaches, one can not only incorporate and stabilize, but also enable the size-, shape-, regio-, and enantio-selectivity of MOF-based catalysts.<sup>17-24</sup>



**Figure 2.** Summary of methods for post-synthetic modification of MOFs. Copyright 2018 Nature Communications.

One of the targets for bioinspired catalysis is monooxygenases.<sup>25-27</sup> In nature, particulate methane monooxygenase (pMMO), which contains a binuclear Fe active site that selectively activates C-H bonds,<sup>28</sup> is an effective catalyst for methane oxidation to methanol, a holy grail in chemical catalysis (Figure 3). A lot of effort has been casted on construct artificial enzyme mimics in zeolites, including mimics for monooxygenase models such as the binuclear copper species, a multicentered cofactor.<sup>29-34</sup>

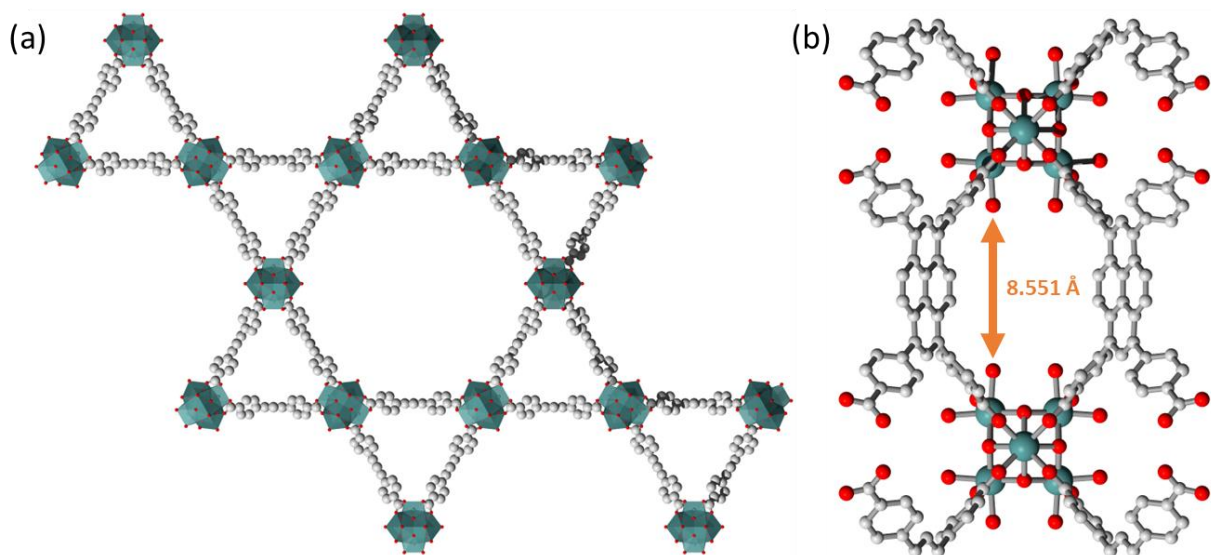


**Figure 3.** Structure of methane monooxygenase and (b) its binuclear Fe active site. Copyright 2011 Accounts of Chemical Research.

Similar design principles have recently been devoted to MOF systems.<sup>35</sup> For instance, MOF-808 was used to install imidazole-based ligands on the  $\text{Zr}_6$  nodes to subsequently metalate with Cu, for which a bis( $\mu$ -oxo)dicopper species was proposed as the probable active site of the catalyst

for N<sub>2</sub>O-promoted methane oxidation to methanol.<sup>36</sup> Another **Zr-MOF**, **NU-1000**, was also used to controllably graft a dicopper species onto the Zr<sub>6</sub> cluster in the hexagonal channels and exhibits selective methane oxidation activity.<sup>37</sup> More recently, Lin and co-workers precisely built a dicopper species inside the hollow center of the octa-nuclear, ring-shaped Ti<sub>8</sub> node of MIL-125-Ti, which is shown to be capable to bind and activate molecular oxygen.<sup>38</sup>

Clearly, previous work has pointed to an effective design strategy by using an oxo/hydroxyl rich region with well-defined position as a template for building artificial monooxygenases. In particular, **Zr-MOFs** with the **csq** topology<sup>39-43</sup> offer an ideal platform to construct binuclear copper monooxygenase. In this structure, each Zr<sub>6</sub> cluster possess two pairs of OH<sup>-</sup>/H<sub>2</sub>O along the *c* axis, and two adjacent clusters thus offer four potential binding sites for metal incorporation. Farha and coworkers have pioneered the post-synthetic modification with transitions metals using **NU-1000**<sup>39</sup> with **csq** topology as the MOF prototype (Figure 4). However, due to the long distance of 8.5 Å between the adjacent clusters, larger multinuclear metal-oxo clusters are often built within the void space, including tetranuclear Ni<sup>44-45</sup> and trinuclear Cu,<sup>46</sup> etc.



**Figure 4.** Structure of **NU-1000** (a) along the *c*-axis and (b) along the (1,2,0) axis with inter-cluster distance.

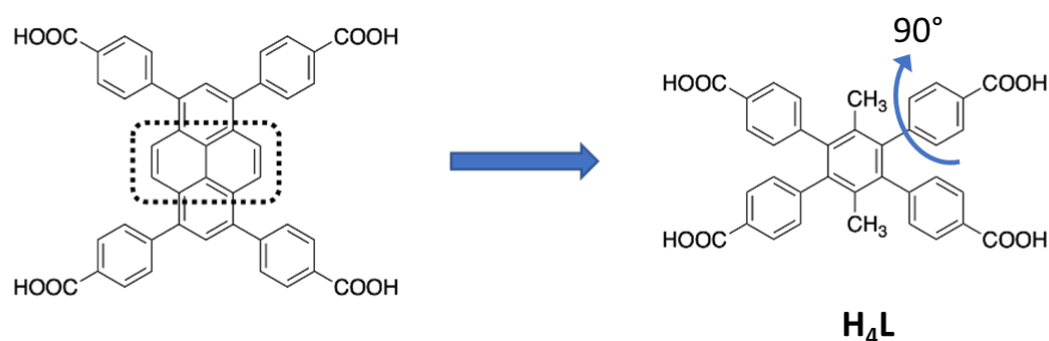
In this chapter, we applied the concept of reticular chemistry and chose a tetratopic ligand with a smaller dimension to reduce the inter-cluster distance to a point where it could ideally host the formation of binuclear, dicopper-oxo clusters. We also demonstrate that the resulting **MOF-565-Cu<sup>II</sup>** consists such dicopper cluster can efficiently catalyze the epoxidation of alkenes.



## 2.2 Synthesis and Structural Characterization of MOF-565

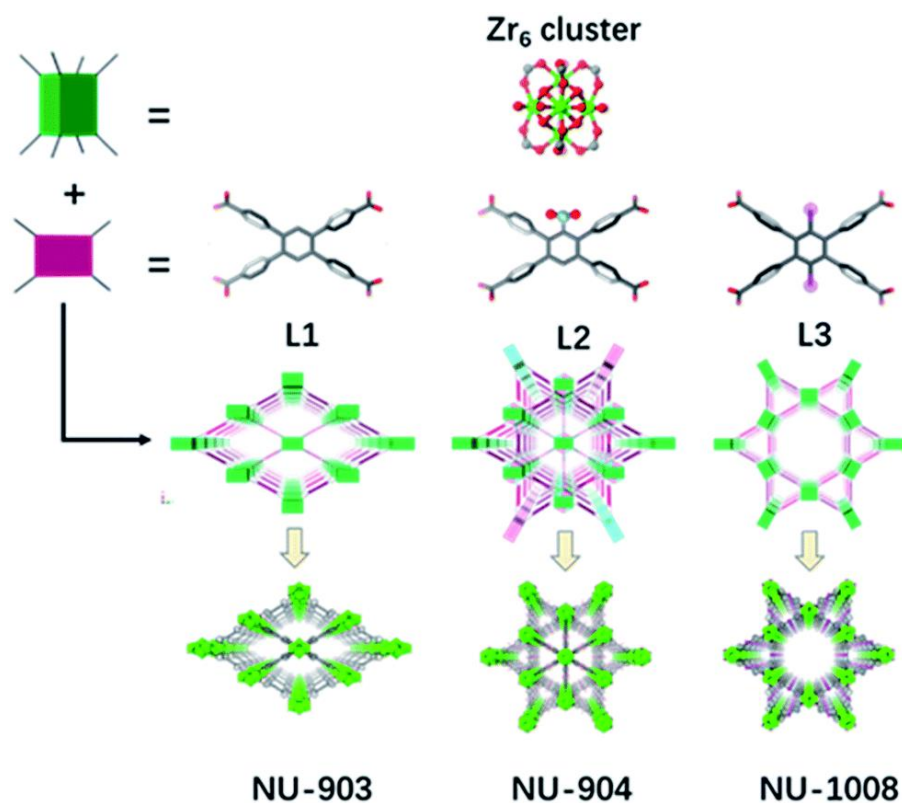
Since the inter-cluster distance, defined as the O–O distance between the two pairs of terminal  $\text{H}_2\text{O}/\text{OH}^-$  groups along the  $c$  axis, of the adjacent  $\text{Zr}_6$  nodes in **NU-1000** of 8.6 Å (Figure 4) is too long to construct a dicopper cluster, it is necessary to reduce the size of the tetratopic ligand along the  $c$  axis to decrease the inter-cluster distance.

One straightforward approach is to replace the pyrene ring with a smaller phenyl ring, which can theoretically reduce the distance by  $\sim 4$  Å, resulting a smaller inter-cluster distance of approximately 4 Å that is more suitable for constructing the desired binuclear copper cluster (Figure 5). Therefore, we chose 1,2,4,5-tetrakis(4-carboxyphenyl)-3,6-dimethyl-benzene, denoted as  $\text{H}_4\text{L}$ , as the organic linker for the synthesis of a new **Zr-MOF** with **csq** topology.



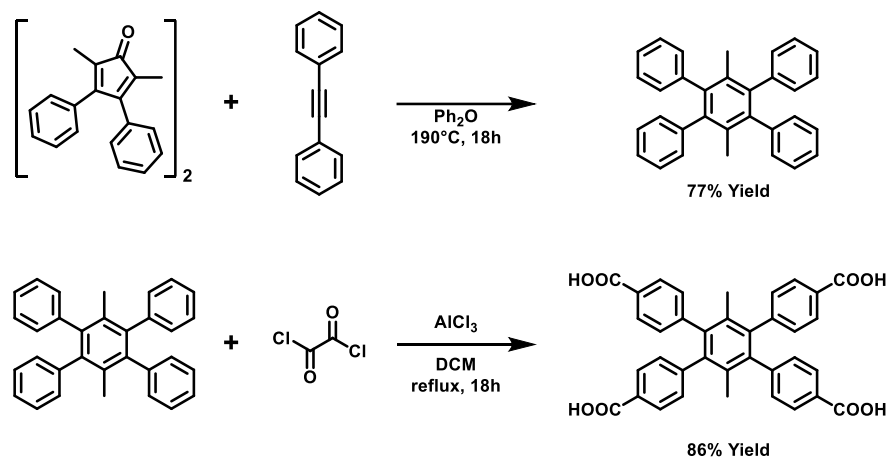
**Figure 5.** Switching to a smaller organic linker and adding methyl groups to enforce a 90° rotation between the central phenyl ring and the four terminal phenyl rings.

Moreover, two methyl groups are incorporated in the central phenyl ring to ensure the proper torsion of the terminal phenyl groups to facilitate the formation of **csq** instead of **scu** or **shp** topology, which are the other common topologies for (4,8)-connected **Zr-MOFs** (Figure 6).<sup>47</sup> Although the reported MOF NU-1008 appears similar to our proposed design, the Br groups on the central ring can be chemically unstable for post-modification and catalysis purposes. Hence, we changed the Br groups to the less reactive methyl groups to avoid the potential chemical transformation.



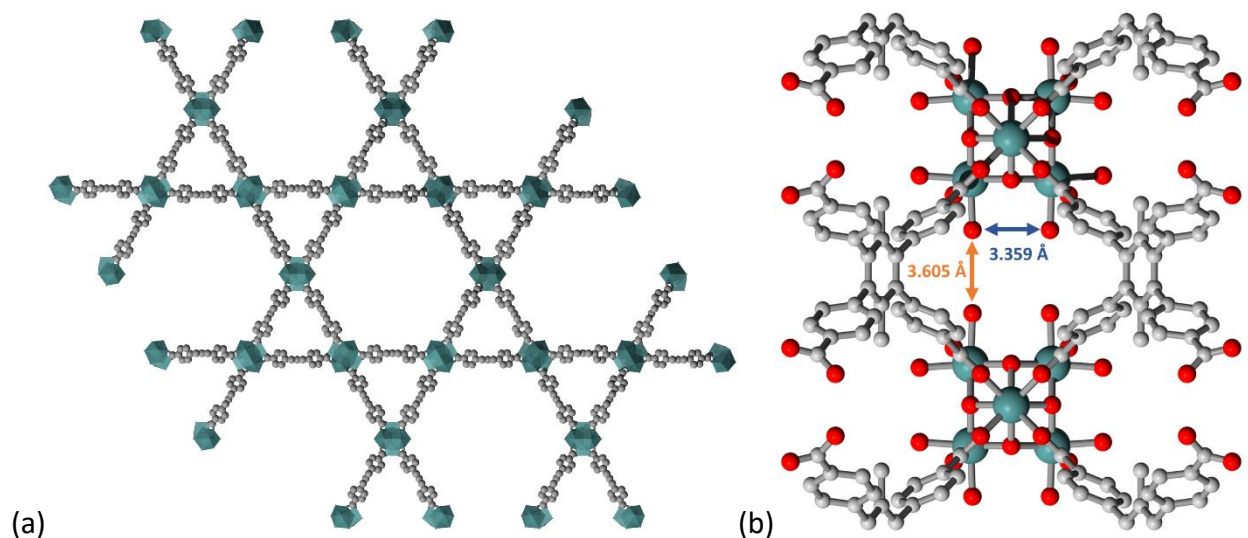
**Figure 6.** Schematic representation of the different topologies for **Zr-MOFs** with tetratopic ligands. **NU-903** (**scu** topology), **NU-904** (**shp** topology), and **NU-1008** (**csq** topology). Copyright 2019 Chemical Science.

The proposed linker **H<sub>4</sub>L** was synthesized following literature procedure (Scheme 1).<sup>48</sup> 2,5-Dimethyl-3,4-diphenylcyclopentadienone and diphenylacetylene were first refluxed in diphenyl ether to produce 1,4-dimethyltetraphenylbenzene in 77% yield. A Friedel-Crafts reaction with aluminum chloride as a catalyst was then conducted to produce **H<sub>4</sub>L** from 1,4-dimethyltetraphenylbenzene and oxalyl chloride in 86% yield. Successful synthesis of **H<sub>4</sub>L** was confirmed by <sup>1</sup>H NMR spectroscopy.



**Scheme 1.** Synthetic scheme of H<sub>4</sub>L.

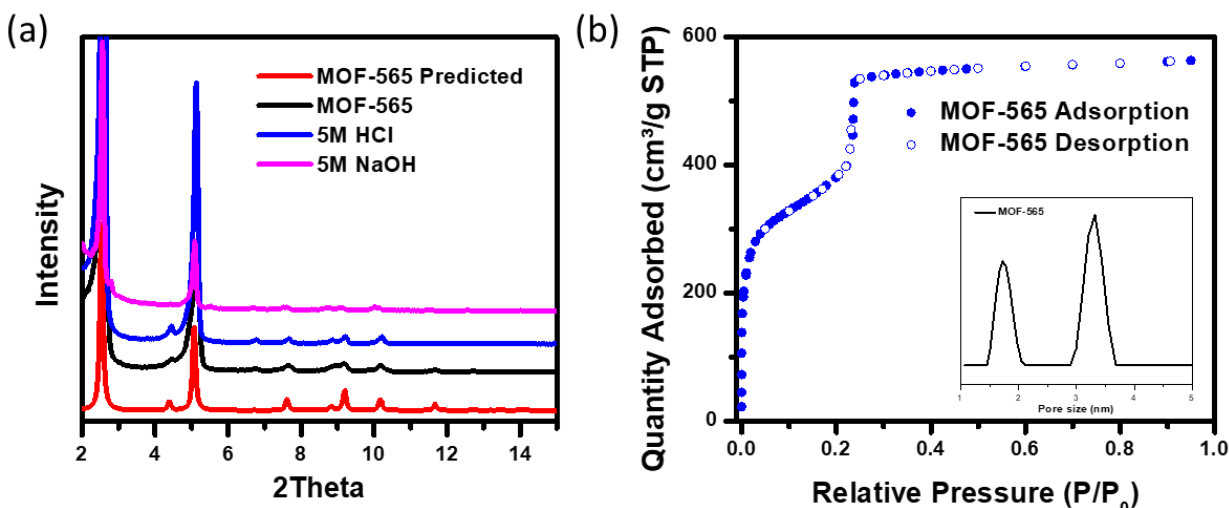
To prepare the Zr-based MOF, a solvothermal synthesis was adopted where ZrCl<sub>4</sub> and H<sub>4</sub>L were reacted in the presence of co-modulating agents, benzoic acid and formic acid, in dimethylformamide (DMF) at 120 °C for 3 days, which yielded hexagonal colorless rod-shaped single crystals, termed as **MOF-565**. Single-crystal X-ray diffraction (sc-XRD) studies at 100 K revealed that **MOF-565** crystallizes in space group *P6/mmm* (no. 191) of the hexagonal system with the lattice parameters  $a = b = 40.212(2)$  Å,  $c = 11.5264(7)$  Å,  $V = 16141.2$  Å<sup>3</sup> (Figure 7 and Table S1). The synthesis generating single crystals was conducted at a 10 mg scale. Importantly, **MOF-565** syntheses can be scaled up to 2 g, only with much smaller crystal sizes. Powder X-ray diffraction patterns confirmed the bulk crystallinity of the MOF sample (*vide infra*, Figure 8a), and thermogravimetric analysis (TGA) revealed the stability of the framework structure up to 520 °C, although the coordinated water on the nodes were lost at 150 °C (Figure S6).



**Figure 7.** Single-crystal structure of **MOF-565** viewed (a) down the *c*-axis (0,0,1 axis) and (b) along the (1,-1,0) axis showing the shorter inter-cluster distance.

As expected, **MOF-565** is indeed a (4,8)-connected net exhibiting the **csq** topology that is built up from 2D Kagome sheets of eight-connected  $[\text{Zr}_6(\mu_3\text{-O})_4(\mu_3\text{-OH})_4(\text{OH})_4(\text{OH}_2)_4]$  nodes bridged by tetra-carboxylate ligands, resulting in the charge-balanced framework formula of  $\text{Zr}_6\text{O}_4(\text{OH})_8(\text{H}_2\text{O})_4\text{L}_2$ . Such connectivity gives rise to a 3D structure with 4 terminal-OH containing (2 -OH and 2 -OH<sub>2</sub>) functional groups pointing into a hexagonal 1D channel of the diameter of 32 Å, with another smaller triangular channel of the diameter of 17 Å. To our delight, **MOF-565** exhibits a close inter-cluster distance of 3.6 Å between the O of the 4 terminal -OH (2 -OH and 2 -OH<sub>2</sub>) on each Zr<sub>6</sub> cluster pointing along the *c* axis, leading to non-porosity between the Kagome sheets. This close node-to-node distance creates a cavity containing two -OH and two -OH<sub>2</sub> groups in a rectangle with the size of 3.6 Å × 3.4 Å, suitable for binding binuclear Cu-oxo cluster in a way like the enzyme monooxygenase.

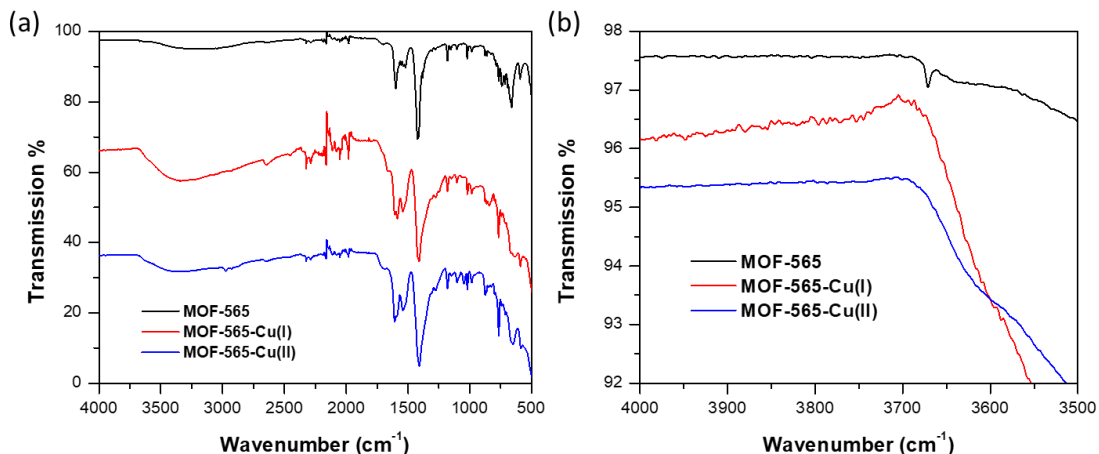
The chemical stability of **MOF-565** was examined by treating the MOF in 5 M hydrochloric acid and 5 M sodium hydroxide aqueous solutions for 24 h at room temperature. As shown in Figure 8a, excellent PXRD patterns remained intact after these treatments, suggesting good stability with no phase transition or framework collapse. After activation under high vacuum at 180°C for 24 h, the permanent porosity of the **MOF-565** was measured by N<sub>2</sub> adsorption isotherms measured at 77 K (Figure 8b). **MOF-565** exhibits a 2-step isotherm, likely a result of the 2 different pore sizes, with a saturated N<sub>2</sub> uptake of 565 cm<sup>3</sup> g<sup>-1</sup> and a Brunauer-Emmett-Teller (BET) surface area of 1347 m<sup>2</sup> g<sup>-1</sup>. This is consistent with the calculated accessible surface area of 1570 m<sup>2</sup>g<sup>-1</sup>. The calculated pore size distribution shows two different pore size with one in the mesopore range, consistent with the crystal structure.



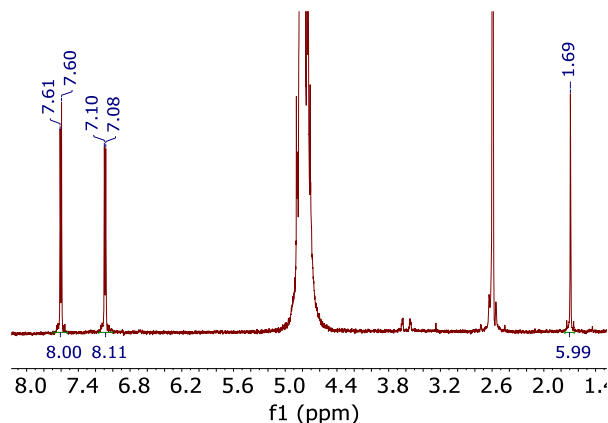
**Figure 8.** (a) PXRD patterns illustrating chemical stability of **MOF-565**. (b) N<sub>2</sub> adsorption and desorption isotherms of **MOF-565** (inset: pore size distribution).

### 2.3 Synthesis and Structural Characterization of Binuclear Cu Containing MOF-565-Cu

Before **MOF-565** can be modified, it must first be pre-treated to exchange the residual capping formate groups on the clusters with reactive terminal -OH and -OH<sub>2</sub> groups. To do this, the **MOF-565** crystals were stirred in a mixture of hydrochloric acid (0.1 M), methanol and water (1:10 ratio) overnight. Next, through deprotonation of the hydroxides with TMSCH<sub>2</sub>Li ((trimethylsilyl)methyl lithium) followed by reaction with Cu(MeCN)<sub>4</sub>BF<sub>4</sub> (tetrakis(acetonitrile)copper(I) tetrafluoroborate) based on a modified literature procedure reported by the Lin group, the Cu species were grafted onto the Zr<sub>6</sub> nodes to afford the copper(I)-modified MOF, **MOF-565-Cu<sup>I</sup>**. The copper(I) was then oxidized by bubbling O<sub>2</sub> through a suspension in CH<sub>3</sub>CN to afford **MOF-565-Cu<sup>II</sup>**. Inductively coupled plasma-optical emission spectrometry (ICP-OES) analysis showed that **MOF-565-Cu<sup>I</sup>** and **MOF-565-Cu<sup>II</sup>** has 4.02 and 4.03 Cu atoms per Zr<sub>6</sub> node, respectively, consistent with the predicted model in which the complete metalation occurs both between the nodes and on the pore-facing terminal hydroxides. Fourier transform infrared spectroscopy (FTIR) confirmed the disappearance of the Zr cluster OH stretch (3670 cm<sup>-1</sup>) upon installation of the Cu moieties (Figure 9b). <sup>1</sup>H NMR spectrum of a digested **MOF-565-Cu<sup>II</sup>** by potassium phosphate confirmed that the linker was unmodified (Figure 10).

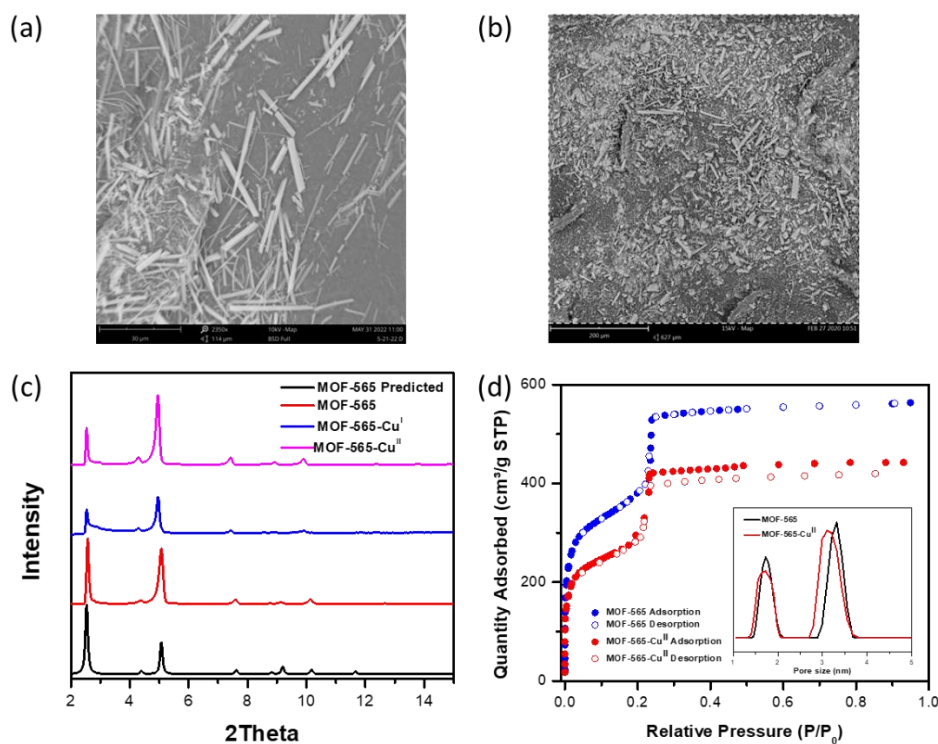


**Figure 9.** FTIR Spectra of **MOF-565**, **MOF-565-Cu<sup>I</sup>**, and **MOF-565-Cu<sup>II</sup>**.



**Figure 10.**  $^1\text{H}$  NMR spectrum of **MOF-565-Cu<sup>II</sup>** treated with potassium phosphate (solvent:  $\text{D}_2\text{O}$ ).

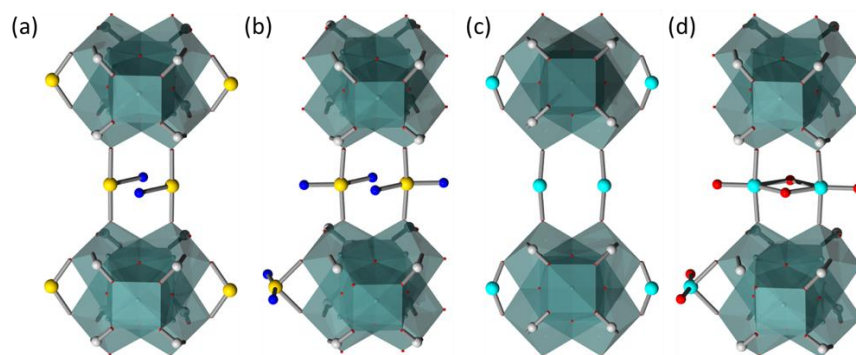
Scanning electron microscope (SEM) images indicate that the Cu-incorporated material maintained the rod-shaped morphology of **MOF-565** (Figures 11a-b). Energy dispersive X-ray spectroscopy (EDS) and X-ray photoelectron spectroscopy (XPS) confirmed the addition of copper (Tables S2-S4, Figures S1-S5), although the EDS and XPS data does not match with ICP likely due to a difference between the bulk and surface exposed metal species.



**Figure 11.** SEM images of **MOF-565** (a) and **MOF-565-Cu<sup>II</sup>** (b). (c) Powder X-ray diffraction patterns and (d)  $\text{N}_2$  adsorption/desorption and pore size distribution of **MOF-565** before and after copper addition.

Powder X-ray diffraction (PXRD) patterns show that the bulk crystallinity was retained throughout the metalation and oxidation processes and the **csq** topology of **MOF-565** remained unchanged during the post-modification (Figure 11c). Thermogravimetric analysis (TGA) showed framework decomposition above 500 °C and 3 steps of mass loss at 70 °C, 220, and 290, likely corresponding to loss of solvent/water and the bis( $\mu$ -O) moiety (Figure S6). Furthermore, installation of Cu reduced the Brunauer-Emmett-Teller (BET) surface area from 1347 m<sup>2</sup> g<sup>-1</sup> for **MOF-565** to 1054 m<sup>2</sup> g<sup>-1</sup> for **MOF-565-Cu<sup>II</sup>**, and the pore size and volume decreased slightly, changed from 32 Å and 17 Å to 30 Å and 16 Å, respectively (Figure 11d).

Single-crystal X-ray diffraction (sc-XRD) after modification was conducted to determine the positions and coordination environments of Cu in **MOF-565-Cu<sup>I</sup>** and **MOF-565-Cu<sup>II</sup>** (Figure 12a and 12c, and Table S1). Two types of Cu were identified, 2 mononuclear Cu per Zr<sub>6</sub> node between the terminal-OH facing the pores and 2 binuclear Cu between two adjacent Zr<sub>6</sub> nodes with a Cu-Cu distance of 2.764 Å. However, the coordination environments of Cu were difficult to determine precisely using only sc-XRD due to diffuse electron clouds and disordered solvent coordination.



**Figure 12.** (a) Single-crystal structure of **MOF-565-Cu<sup>I</sup>** showing two types of Cu: binuclear Cu between the clusters and mononuclear Cu facing the pores. Not all the coordinating solvents were found in the structure. (b) Model of **MOF-565-Cu<sup>I</sup>** used for EXAFS analysis and fitting. (c) Single-crystal structure of **MOF-565-Cu<sup>II</sup>** also showing two types of Cu, but none of the coordinating solvents could be found. (d) Model of **MOF-565-Cu<sup>II</sup>** used for EXAFS analysis and fitting.

To obtain further confirmation of the coordination environment around Cu, extended X-ray absorption fine structure (EXAFS) spectroscopy was conducted assuming a similar coordination environment for both types of Cu. EXAFS (Figure 13a) suggested that the **MOF-565-Cu<sup>I</sup>** model shown in Figure 12b, with 4-coordinate Cu<sup>I</sup> bound to a deprotonated hydroxyl group and water on the Zr<sub>6</sub> cluster, as well as 2 acetonitrile solvent molecules. On the other hand, EXAFS data (Figure 13b) for **MOF-565-Cu<sup>II</sup>** suggested 5-coordinate Cu<sup>II</sup> centers, which, after MOF exposure to oxygen and water, fits well with the bis( $\mu$ -oxo)dicopper species model in Figure 12d, giving a Cu-Cu distance of 3.04 Å.

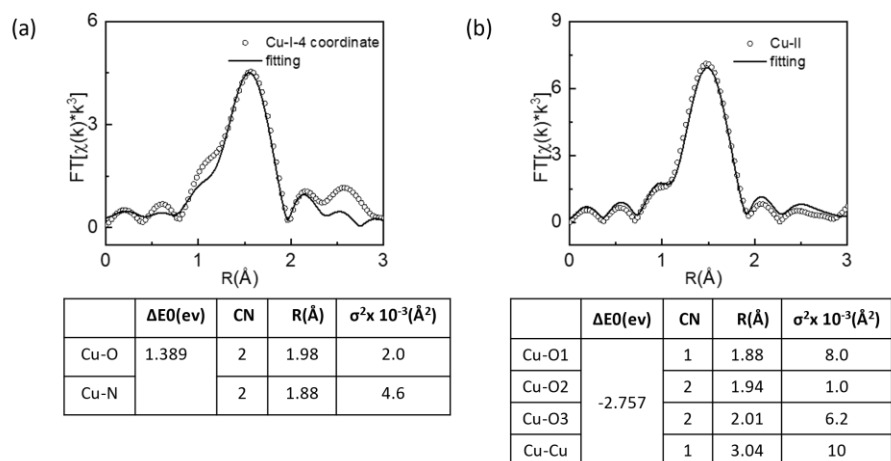
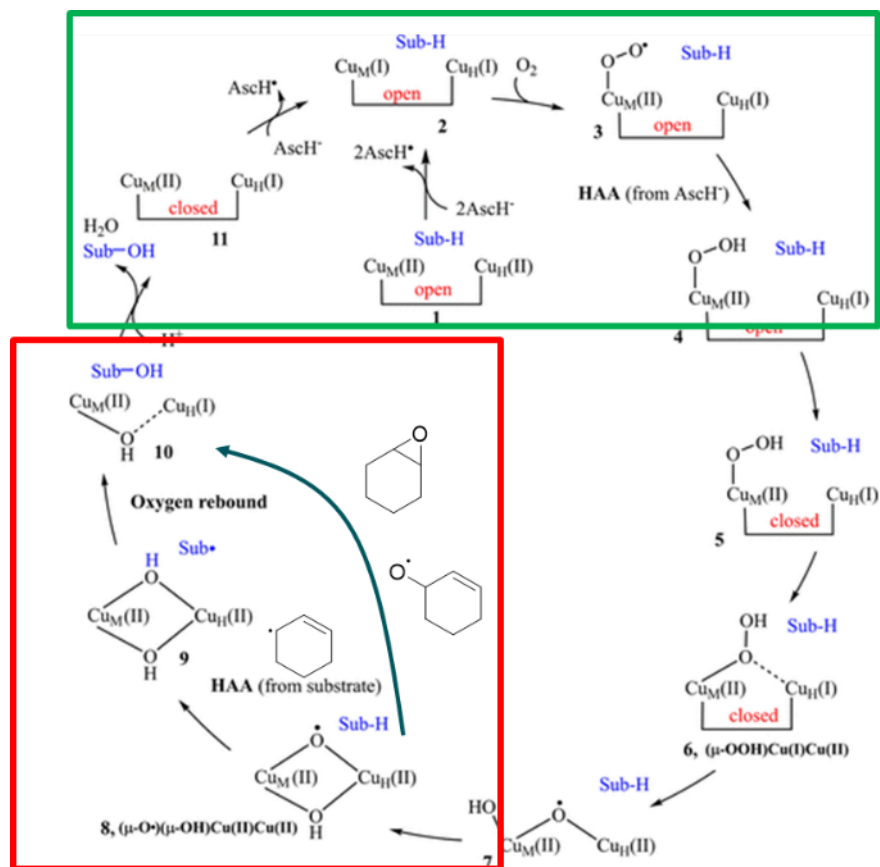


Figure 13. EXAFS fitting of (a) MOF-565-Cu<sup>I</sup> and (b) MOF-565-Cu<sup>II</sup>.



## 2.4 Olefin Epoxidation Catalyzed by MOF-565-Cu

It is known that binuclear Cu centers can efficiently transfer one oxygen atom from O<sub>2</sub> to olefins to form the monooxygenated epoxide product in the presence of co-reductant, following a four-electron process (Figure 14).<sup>49</sup> Thus, **MOF-565-Cu<sup>II</sup>**, with its binuclear Cu centers, was thus tested for catalytic activity for olefin epoxidation.

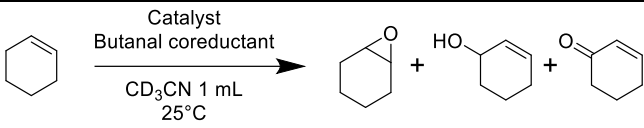


**Figure 14.** Proposed mechanism of substrate oxidation by binuclear copper centers. The red box highlights the substrate oxidation, while the green box highlights the co-reductant cycle (in this case, ascorbic acid, AscH). Adapted from 2019 American Chemical Society.

Cyclohexene was used as a model substrate to screen the reaction conditions for epoxidation (Table 1). In the presence of 0.2 mol % **MOF-565-Cu<sup>II</sup>** (calculated using ICP-OES Cu loading of 4 Cu per Zr<sub>6</sub> node) treatment of cyclohexene with 2 equiv of *n*-butyraldehyde as the coreductant in CH<sub>3</sub>CN under atmospheric pressure O<sub>2</sub> for 18 h at room temperature afforded cyclohexene oxide in 95% conversion and 77% yield (entry 1, Table 1) and along with a small amount of side hydroxylation products 2-cyclohexen-1-ol and 2-cyclohexen-1-one (9% and 6%, respectively).

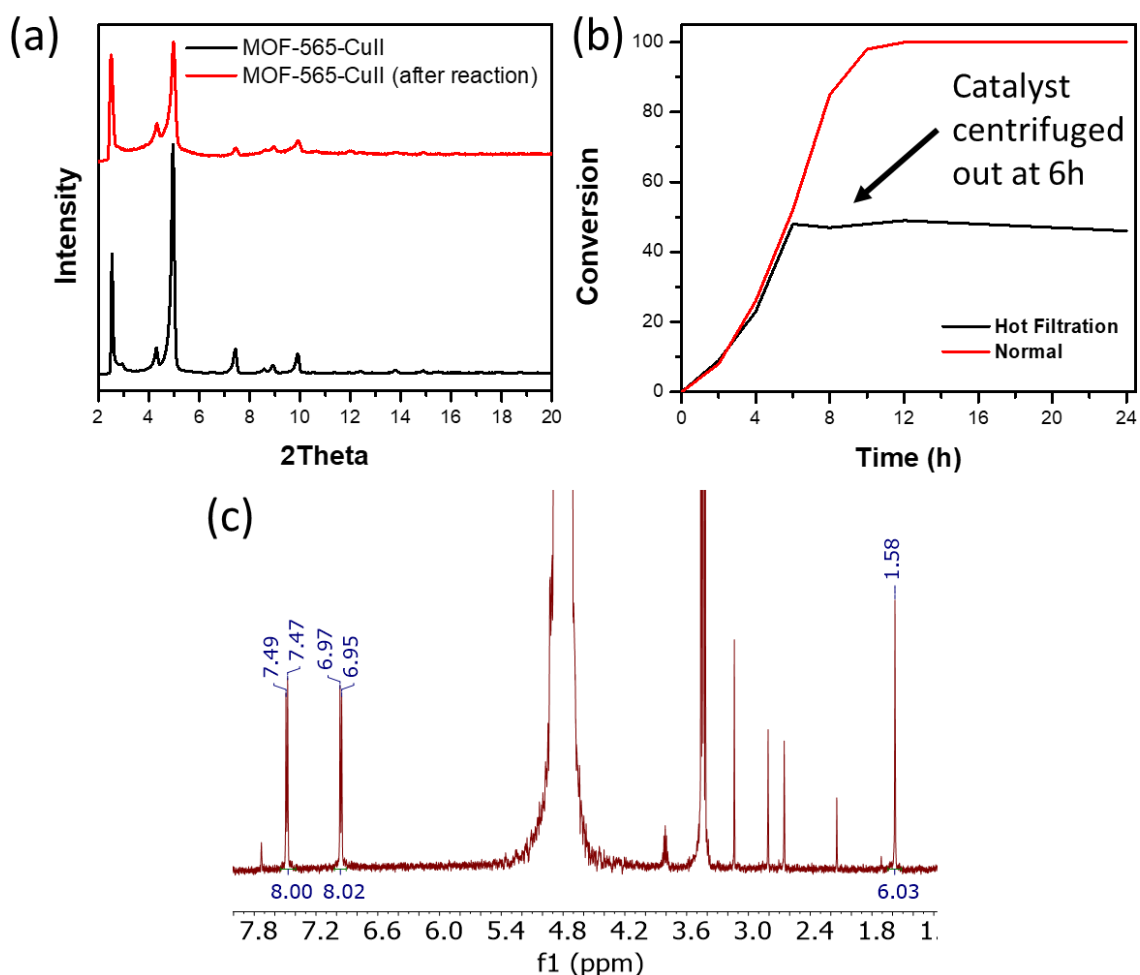
The reaction proceeded, albeit slowly, under air and afforded cyclohexene oxide in 19% yield (entry 4, Table 1). The absence of **MOF-565-Cu<sup>II</sup>**, O<sub>2</sub>, or coreductant prevented the epoxidation reaction from proceeding, affording none or negligible amount of cyclohexene oxide product (entries 5-8, Table 1), whereas the absence of a binuclear Cu center using the homogenous catalyst CuCl<sub>2</sub> and a **MOF-565**-monoCu<sup>II</sup> synthesized with a low Cu loading of 0.71 Cu per Zr<sub>6</sub> node (assumed to have little to no binuclear Cu) led to very low yields (Table 1, entries 9 and 10), demonstrating the important role of binuclear Cu coordination to the metal node in the monooxygenation activity and providing more evidence to support the proposed mechanism in Figure 14.

**Table 1. Epoxidation of Cyclohexene Catalyzed by MOF-565-Cu<sup>II</sup><sup>a</sup>**

					
Entry	Catalyst	Oxidant	<i>t</i> (h)	Conversion <sup>b</sup>	Yield <sup>c</sup>
1	<b>MOF-565-Cu<sup>II</sup></b>	O <sub>2</sub>	12	95	77
2 <sup>d</sup>	<b>MOF-565-Cu<sup>II</sup></b>	O <sub>2</sub>	12	61	51
3	<b>MOF-565-Cu<sup>II</sup></b>	O <sub>2</sub>	18	100	80
4	<b>MOF-565-Cu<sup>II</sup></b>	air	12	21	19
5	<b>MOF-565-Cu<sup>II</sup></b>	N <sub>2</sub>	12	0	-
6 <sup>e</sup>	<b>MOF-565-Cu<sup>II</sup></b>	O <sub>2</sub>	12	0	-
7	<b>MOF-565</b>	O <sub>2</sub>	12	0	-
8	No Catalyst	O <sub>2</sub>	12	0	-
9	CuCl <sub>2</sub>	O <sub>2</sub>	12	6	6
10	<b>MOF-565</b> -monoCu <sup>II</sup> <sup>f</sup>	O <sub>2</sub>	12	19	16

<sup>a</sup>Reaction condition: **MOF-565-Cu<sup>II</sup>** (0.2 mol%), butanal (2 equiv), O<sub>2</sub>, 12 h, 25 °C. <sup>b</sup>Determined by GC-MS analysis. <sup>c</sup>Determined by NMR analysis. <sup>d</sup>0.1mol% **MOF-565-Cu<sup>II</sup>** used. <sup>e</sup>No coreductant. <sup>f</sup>Synthesized using 1 equivalence of Cu instead of excess, ICP-OES indicates a Cu loading of 0.71 Cu per Zr<sub>6</sub> node.

PXRD confirmed the structural integrity of **MOF-565-Cu<sup>II</sup>** after the reaction (Figure 14a). Hot filtration demonstrated that the catalysis is purely heterogeneous and stops occurring when the catalyst is removed halfway during the reaction (Figure 15b). <sup>1</sup>H NMR spectrum of the washed and digested MOF catalyst confirmed that the ligand was intact during the catalytic reaction (Figure 15c).



**Figure 15.** (a) PXRD of **MOF-565-Cu<sup>II</sup>** before and after catalysis, (b) hot filtration at 6h to remove catalyst, (c) NMR of washed and digested **MOF-565-Cu<sup>II</sup>** after catalysis shows intact linker.

Several reaction conditions were also screened for reaction optimization. First, solvents with different polarities and coordination abilities were examined (Table 2). Polar solvents such as acetonitrile and acetone displayed better epoxidation performance compared to non-polar solvents such as hexane. Dichloroethane and dichloromethane gave low conversions, presumably due to a weaker coordination ability compared to acetonitrile and acetone. Methanol and ethanol are not suitable solvents as they are likely susceptible to oxidation. Although water gives a high conversion, the epoxide product selectivity of 46% excludes it as the solvent of choice for the optimized reaction condition, and aggregation of MOF crystals due to its hydrophobicity was observed which likely impacted the activity and selectivity of the reaction.

**Table 2. Epoxidation of Cyclohexene Catalyzed by MOF-565-Cu<sup>II</sup> in Different Solvents**

Entry	Solvent	Conversion <sup>b</sup>	Yield <sup>c</sup>
1	Acetonitrile	92	-
2	Acetonitrile (anhydrous)	97	-
3	Acetonitrile-d <sub>3</sub>	95	77
4	Acetone	99	-
5	Acetone-d <sub>6</sub>	96	70
6 <sup>d</sup>	Water	100	-
7 <sup>d</sup>	D <sub>2</sub> O	100	46
8	Dichloromethane	31	-
9	Dichloroethane	22	-

<sup>a</sup>Reaction condition: **MOF-565-Cu<sup>II</sup>** (0.2 mol%), butanal (2 equiv), O<sub>2</sub>, 12 h, 25 °C. <sup>b</sup>Determined by GC-MS analysis. <sup>c</sup>Determined by NMR analysis. <sup>d</sup>Aggregation of MOF crystals was observed which could have impacted the activity and selectivity.

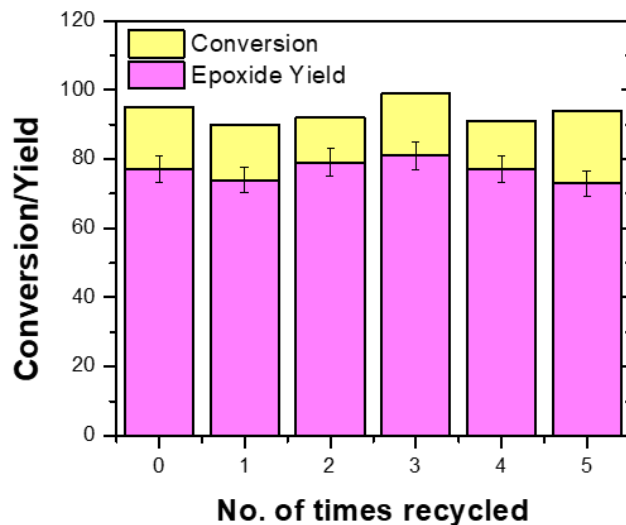
Second, the effect of different coreductants and the amount of coreductant was investigated. Butanal, isobutanal, valeraldehyde, hexanal, and *p*-tolualdehyde were tested, and butanal showed the best performance (Table 3, entries 1-8). The amount of the coreductant butanal was then optimized: with increasing equivalence from 1 to 10 improving the selectivity for the epoxide product up to 97% (Table 3, entries 1, 9-14), but 2 equivalents produced the highest conversion of 95% within a reasonable time of 12 h. When 20 equivalents of butanal was used, the yield of epoxide drastically decreased to 28%. According to the previously proposed mechanism (Figure 14), although excess coreductant likely accelerates the regeneration of Cu<sub>2</sub>(μ-O) active species and reduces the formation of side hydroxylation side products, it also competes with cyclohexene for oxidation, which slows the rate of the reaction and lowers the yield of epoxide product.

**Table 3. Epoxidation of Cyclohexene Catalyzed by MOF-565-Cu<sup>II</sup><sup>a</sup> with Various Coreductants**

Entry	Coreductant	Coreductant Equivalence	Conversion <sup>b</sup>	Yield <sup>c</sup>
1	Butanal	2	95	77
2	Isobutanal	2	77	66
3	Pentanal	2	94	75
4	Hexanal	2	52	45
5	<i>p</i> -Tolualdehyde	2	25	23
6	Water	2	0	0
7	Isopropanol	2	0	0
8	None		0	0
9	Butanal	0.5	22	19
10	Butanal	1	47	40
11	Butanal	5	61	59
12 <sup>d</sup>	Butanal	5	88	84
13	Butanal	10	41	40
14	Butanal	20	28	28

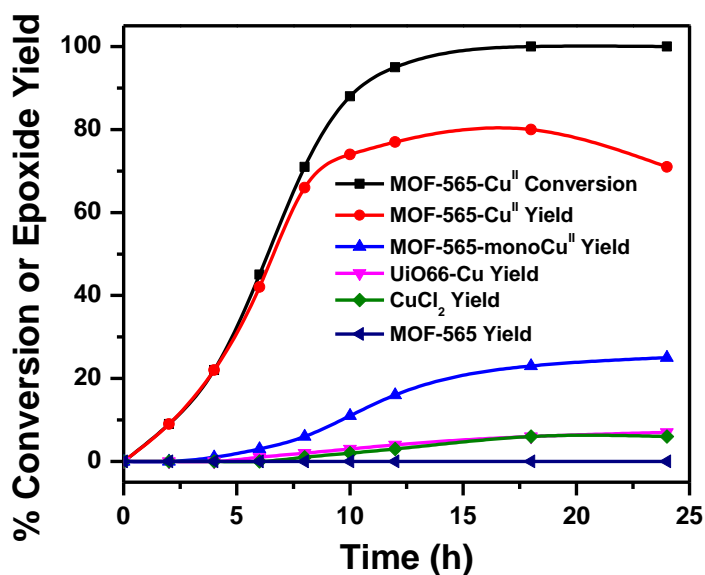
<sup>a</sup>Reaction condition: **MOF-565-Cu<sup>II</sup>** (0.2 mol%), coreductant, O<sub>2</sub>, 12 h, 25 °C. <sup>b</sup>Determined by GC-MS analysis. <sup>c</sup>Determined by NMR analysis. <sup>d</sup>24h.

For the recyclability tests, the reaction mixture was centrifuged to isolate **MOF-565-Cu<sup>II</sup>** after reaction and re-used five times for cyclohexene epoxidation (Figure 16). No significant drop in reactivity was observed during the recycling as the results fall within or close to the standard deviation of 4% based on 8 replicates using freshly prepared **MOF-565-Cu<sup>II</sup>** MOF catalyst (Table S2), and copper leaching was minimal at 1% after five runs, demonstrating the heterogeneous nature of this reaction and the remarkable stability of **MOF-565-Cu<sup>II</sup>** under the catalytic reaction conditions.



**Figure 16.** Catalyst recycling in the epoxidation of cyclohexene.

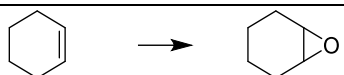

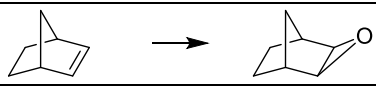
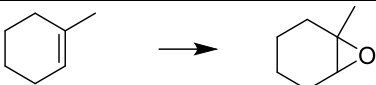
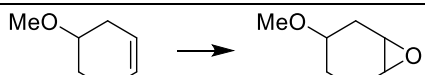
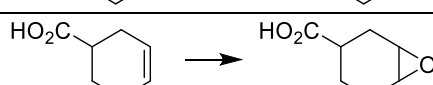
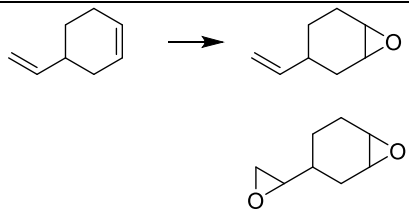
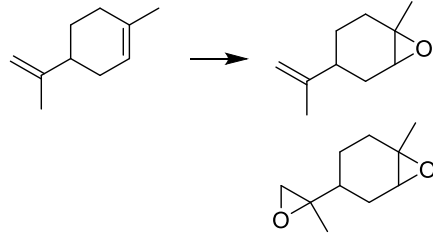

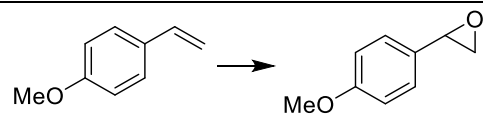
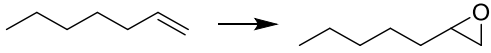
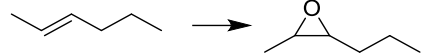
The kinetics of the epoxidation reaction was also studied. As shown in Figure 17, the time-dependent curve shows that **MOF-565-Cu<sup>II</sup>** catalyzed cyclohexene epoxidation occurs efficiently and rapidly with a high conversion of 100% in 18 h, with 80% yield of cyclohexene epoxide. The **MOF-565-monoCu<sup>II</sup>** MOF containing only 0.71 Cu per Zr<sub>6</sub> cluster and assumed to have little to no binuclear Cu, synthesized by using a stoichiometric amount of Cu(MeCN)<sub>6</sub>BF<sub>4</sub>, showed far slower activity with only 25% yield after 24 h even with the same 0.2 mol% Cu loading, demonstrating the importance of the binuclear Cu structure. Similarly, other mononuclear Cu containing controls such as **UiO-66-Cu<sup>50</sup>** and CuCl<sub>2</sub> showed poor activities with a yield below 10% after 24 h.



**Figure 17.** Time dependent conversion and yield of cyclohexene epoxidation catalyzed by **MOF-565-Cu<sup>II</sup>** and various controls.

The substrate scope for **MOF-565-Cu<sup>II</sup>**-catalyzed olefin epoxidation reactions was studied using the optimized conditions. At 0.2 mol % of **MOF-565-Cu<sup>II</sup>**, various olefins from simple alkenes to styrenes were converted to their corresponding epoxides under atmospheric pressure O<sub>2</sub> (Table 4). Good yields of epoxides were obtained with cyclic alkenes with different substituents, even with hindered groups and large substrates (entries 1-4, Table 4). Epoxidation selectivity for the internal alkene was observed for limonene and 4-vinyl-cyclohexene (entries 7-8, Table 4), likely due to the higher reactivity of internal alkenes than terminal alkenes thanks to their more electron-rich nature. Noncyclic alkenes such as styrene derivatives and linear-chain alkenes also underwent epoxidation to afford epoxides in good to excellent yields (entries 9-12, Table 4). A similar preference for the internal alkene was observed between 2-hexene and 1-heptene (entries 11 and 12, Table 4).

Table 4. MOF-565-Cu<sup>II</sup>-Catalyzed Olefin Epoxidation Reactions<sup>a</sup>

Entry	Reaction	t (h)	Conversion <sup>b</sup>	Yield <sup>c</sup>
1		12	95	77
2		12	98	92
3		18	99	93
4		18	100	93
5		24	100	87
6		24	100	75
7		24	100	75:16
8		48	100	87:4
9		48	100	91
10		48	100	82
11		48	90	77
12		12	100	88

<sup>a</sup>Reaction condition: MOF-565-Cu<sup>II</sup> (0.2 mol%), coreductant, O<sub>2</sub>, 12 h, 25 °C. <sup>b</sup>Determined by GC-MS analysis. <sup>c</sup>Determined by NMR analysis.



## 2.5 Conclusions

In this chapter, we demonstrated a novel strategy to construct an artificial monooxygenase by controlling the inter-cluster distance of a **Zr-MOF** via the synthesis and post-modification of **MOF-565-Cu<sup>II</sup>**. This work highlights the potential of MOFs as solid phase supports for the construction of artificial enzymes with uniform and precise active single metal sites as well as high catalytic activities.

**MOF-565** was first designed and then synthesized with the aim of providing a precise binding pocket for the grafting of a binuclear copper species to cooperatively activate O<sub>2</sub> gas. To our elation, the choice of MOF linker H<sub>4</sub>L resulted in a new chemically and physically stable, large-pore **Zr-MOF**, **MOF-565**, with **csq** topology and an inter-cluster distance of 3.6 Å, well-suited for our initial intentions.

The hydroxide groups of the MOF nodes were deprotonated to chemically bond a Cu<sup>I</sup> precursor, which was then oxidized with O<sub>2</sub> to generate the Cu<sup>II</sup>(μ<sub>2</sub>-OH)<sub>2</sub> artificial enzyme between the Zr<sub>6</sub> clusters. The strong oxo-bound ligands and the reticular isolation of the Cu<sub>2</sub> moieties in the MOF led to a chemically and physically robust artificial enzyme for the oxidation of organic substrates under very mild conditions of 1 bar O<sub>2</sub> at room temperature.

**MOF-565-Cu<sup>II</sup>** catalyzed the epoxidation of a broad scope of olefin-containing substrates including cyclic alkenes, linear alkenes, and styrenes with good yields and selectivities despite the large size and steric hindrance in several substrates. **MOF-565-Cu<sup>II</sup>** also efficiently catalyzed the epoxidation of cyclohexene 5 times faster than its mononuclear counterpart, **MOF-565-monoCu<sup>II</sup>**, and more than 10 times faster than other mononuclear Cu containing controls such as **UiO-66-Cu** and CuCl<sub>2</sub>, demonstrating the importance of the binuclear Cu moiety.

Moving forward, **MOF-565-Cu<sup>II</sup>** could be tested for other monooxygenation reactions, including hydroxylation, Baeyer-Villiger oxidation, sulfoxidation, and methane oxidation. Computational studies to further elucidate and provide evidence to support the proposed reaction mechanism would also be crucial to understanding the reactivity and selectivity of the system, as well as factors that will help us improve upon the existing design and structure.

## 2.6 Materials and Methods

**Starting Materials.** All reactions and manipulations were carried out in air inside a fumehood unless otherwise indicated. All starting materials were purchased from Sigma-Aldrich, Combi-Blocks, and TCI (USA) and used without further purification.

**Single Crystal X-ray Diffraction.** Data was collected using synchrotron radiation at the Advanced Light Source, beamline 12.2.1, at Lawrence Berkeley National Laboratory, Berkeley, CA, USA. Indexing was performed using APEX3 (Difference Vectors method). Data integration and reduction were performed using SaintPlus 6.0. Absorption correction was performed by multi-scan method implemented in SADABS. Space groups were determined using XPREP implemented in APEX3. The structure was solved using SHELXT 2018/2 and refined using SHELXL 2018/3 within Olex 2 (full-matrix least-squares on  $F^2$ ). Zr, Cu, C, O, and N atoms were refined with anisotropic displacement parameters and H atoms were placed in geometrically calculated positions and included in the refinement process using riding model with isotropic thermal parameters:  $U_{\text{iso}}(\text{H}) = 1.2U_{\text{eq}}(-\text{CH})$ . The disordered solvent molecules were treated as diffuse using the SQUEEZE procedure implemented in PLATON. Crystal data and refinement details are shown in Table SX. This data can be obtained free of charge from The Cambridge Crystallographic Data Centre via [www.ccdc.cam.ac.uk/data\\_request/cif](http://www.ccdc.cam.ac.uk/data_request/cif).

**Powder X-Ray Diffraction (PXRD) Measurements.** PXRD data were collected by using a Rigaku X-ray diffractometer with Cu  $K\alpha$  radiation at 40 kV and 20 mA.

**$^1\text{H}$  NMR Spectra.**  $^1\text{H}$  spectra were recorded on an AVANCE II 500 (Bruker, Germany).

**Gas Sorption Measurements.** Gas adsorption isotherms were performed on the surface area analyzer ASAP-2020.  $\text{N}_2$  gas adsorption isotherms were measured at 77 K using a liquid  $\text{N}_2$  bath.

**Scanning Electron Microscope.** SEM images and EDS data were collected on a tabletop Phenom ProX equipped with the Element Identification (EID) software package and a specially designed and fully integrated Energy Dispersive Spectrometer (EDS).

**Inductively Coupled Plasma-Optical Emission Spectrometry.** ICP-OES, performed on a Varian ICP-OES 720 Series, was used to quantify the ratio of the MOF metal and the grafted metal. Samples were digested in piranha overnight with stirring and diluted with 2 wt%  $\text{HNO}_3$  before ICP measurement. 1000 ppm zirconium and copper standard solutions (Sigma Aldrich) was used to prepare diluted standards with metal concentrations ranging from 0.1 to 10 ppm.

**Fourier transform infrared (FTIR) Spectra.** FTIR spectra were recorded on the Nicolet iS50 FT-IR system (Thermo Fisher, USA).

**X-ray absorption (XAS).** XAS spectra were measured at the beamline 12BM-B at the Advanced Photon Source in Argonne National Laboratory. The XAS spectra were collected under room temperature with fluorescence mode. The detector was based on 13-element germanium. One

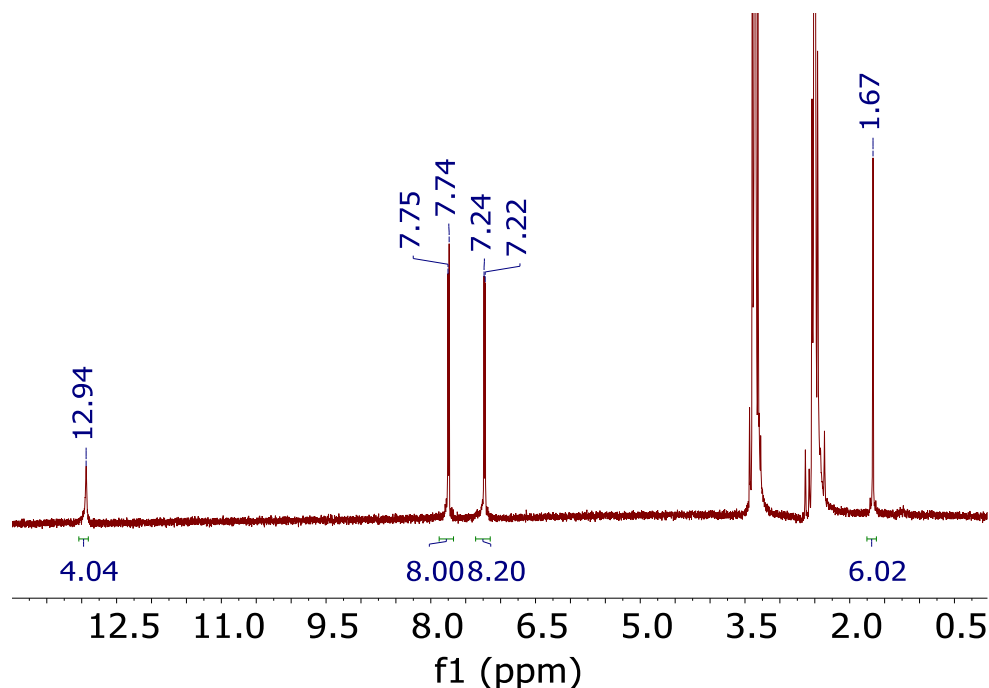
ion chamber is placed before the sample and used as the incident X-ray flux reference signal. There are two ion chambers (second and third chambers) after the sample.

**X-ray Photoelectron Spectroscopy.** A Thermo-Fisher K-Alpha Plus XPS with a monochromatic Al X-Ray source (1.486 eV), energy resolution and spatial resolution of 0.7 eV and 30 mm respectively was used to obtain the quantitative chemical analysis of the MOF surfaces.

## Syntheses of Organic Linker H<sub>4</sub>L, MOF-565 and MOF-565-Cu<sup>II</sup>.

**1,4-dimethyl-2,3,5,6-tetraphenylbenzene.** In a 50 mL round bottom flask, a stirred mixture of 2,5-dimethyl-3,4-diphenylcyclopentadienone (1 g, 1.92 mmol) and diphenylacetylene (1 g, 5.61 mmol) in diphenyl ether 2.5 mL) was heated under reflux for 4h. During this period of time, the mixture changed to deep red and then faded to orange. Slow cooling at room temperature and then at 0°C yielded crystals after 30 min, which were collected by filtration, washed with hexane and dried in an oven, giving 1,4-dimethyl-2,3,5,6-tetraphenylbenzene (1.22 g, 2.97 mmol, 77%) as a light orange solid. <sup>1</sup>H NMR (500 MHz, CDCl<sub>3</sub>): 7.15 (m, 8H), 7.07 (m, 12H), 1.80 (s, 6H).

**H<sub>4</sub>L.** A 50 mL double neck round bottom flask was dried using a heat gun under N<sub>2</sub> flow, where compound 1 (1.06 g, 2.58 mmol) was dissolved in anhydrous CH<sub>2</sub>Cl<sub>2</sub> (20 ml) and placed under N<sub>2</sub> atmosphere on a Schlenk line. The solution was cooled down to 0 °C, then oxalyl chloride (2.5 ml, 25.8 mmol) and AlCl<sub>3</sub> (1.7 g, 12.7 mmol) were added. During the last addition, the color of the solution changed from brown to black. The mixture was stirred for 90 min at 0 °C before additional AlCl<sub>3</sub> (1.5 g, 11.2 mmol) was added and stirred for another 18 h. After this period of time the mixture was transferred in a 50 ml beaker containing ice (25 ml), where light yellow solid was precipitated. The mixture was acidified with 3 M HCl, until pH = 3. The CH<sub>2</sub>Cl<sub>2</sub> was evaporated under vacuum and the solid was collected by filtration, washed with water and dried in an oven overnight. (1.3 g, 2.22 mmol, 86 %). <sup>1</sup>H NMR (500 MHz, DMSO-d<sub>6</sub>): 12.94 (s, 4H), 7.74 (d, 8H), 7.23 (d, 8H), 1.67 (s, 6H).



**MOF-565 (single crystal).** A solution of 500  $\mu$ L DMF, 50  $\mu$ L formic acid, and 14.0 mg ZrCl<sub>4</sub> was added to another solution of 500  $\mu$ L DMF, 850  $\mu$ L formic acid, 120 mg benzoic acid and 6.0 mg of H<sub>4</sub>L in a 4 mL glass vial. The vial was sealed and placed in an isothermal oven at 120°C for 3 days

to form large hexagonal colorless rod crystals (46% crude yield based on **H<sub>4</sub>L**). The MOF was stirred in a 0.1M HCl 10:1 H<sub>2</sub>O:MeOH solution at room temperature overnight to remove the excess formate groups on the clusters, then washed and centrifuged 3 times with 10:1 H<sub>2</sub>O:MeOH, 3 times with acetone, and dried under vacuum at 100°C to give 32% yield based on **H<sub>4</sub>L**.

**MOF-565 (large scale)**. A solution of 50 mL DMF, 5 mL formic acid, and 1.40 g ZrCl<sub>4</sub> was added to another solution of 50 mL DMF, 8.5 μL formic acid, 12 g benzoic acid and 600 mg of **H<sub>4</sub>L** in a 250 mL bottle. The bottle was sealed and placed in an isothermal oven at 120°C for 3 days to form small colorless needles, then washed in a similar manner as the single-crystal MOF sample (28% yield based on **H<sub>4</sub>L**).

1 mg of MOF was digested in D<sub>2</sub>O saturated with K<sub>3</sub>PO<sub>4</sub> at 120°C for 24h for <sup>1</sup>H NMR.

**MOF-565-Cu<sup>I</sup>**. In a N<sub>2</sub>-filled glovebox, TMSCH<sub>2</sub>Li (1.0 M in pentane, 0.2 mL, 20 equiv. w.r.t. Zr<sub>6</sub>) was added dropwise to a cold suspension of **MOF-565** (0.02 mmol Zr<sub>6</sub>) in 20 mL hexanes, and the resultant white suspension was stirred at room temperature for 2 h. The solid was collected through centrifugation and washed with hexanes three times to remove soluble residue. ICP-MS results showed a Li/Zr<sub>6</sub> ratio of 10.9, indicating almost complete lithiation (90%). The resultant **MOF-565-Li** was then transferred to a vial containing 20 mL of Cu(CH<sub>3</sub>CN)<sub>4</sub>BF<sub>4</sub> solution (10 mM) in anhydrous CH<sub>3</sub>CN. After stirring at room temperature for 2 h, the yellow-brown solid was centrifuged and sonicated with CH<sub>3</sub>CN three times. ICP-OES analysis gave a Cu/Zr<sub>6</sub> ratio of 4.0, indicating 4.0 Cu per Zr<sub>6</sub> node.

**MOF-565-Cu<sup>II</sup>**. In a 20 mL vial, **MOF-565-Cu<sup>I</sup>** (50 mg) was dispersed in 10 mL MeCN by sonicating for 10 min. Oxygen was bubbled through overnight at room temperature. The color of the MOF turned from yellow to pale blue, suggesting oxidation of the Cu(I) centers to Cu(II). The resultant **MOF-565-Cu<sup>II</sup>** was washed with CH<sub>3</sub>CN three times. ICP-OES analysis showed a Cu/Zr<sub>6</sub> ratio of 4.0, indicating 4.0 Cu per Zr<sub>6</sub> node.

## 2.7 References

1. Kokkonen, P.; Bednar, D.; Pinto, G.; Prokop, Z.; Damborsky, J., Engineering enzyme access tunnels. *Biotechnol. Adv.* **2019**, *37* (6).
2. Fischer, E., Einfluss der Configuration auf die Wirkung der Enzyme. *Berichte der deutschen chemischen Gesellschaft* **1894**, *27* (3), 2985-2993.
3. Bornscheuer, U. T.; Huisman, G. W.; Kazlauskas, R. J.; Lutz, S.; Moore, J. C.; Robins, K., Engineering the third wave of biocatalysis. *Nature* **2012**, *485* (7397), 185-194.
4. Benkovic, S. J.; Hammes-Schiffer, S., A perspective on enzyme catalysis. *Science* **2003**, *301* (5637), 1196-1202.
5. Sheldon, R. A.; Woodley, J. M., Role of Biocatalysis in Sustainable Chemistry. *Chem Rev* **2018**, *118* (2), 801-838.
6. Li, Y.; Yu, J., Emerging applications of zeolites in catalysis, separation and host-guest assembly. *Nat. Rev. Mater.* **2021**, *6* (12), 1156-1174.
7. Lee, J.; Farha, O. K.; Roberts, J.; Scheidt, K. A.; Nguyen, S. T.; Hupp, J. T., Metal-organic framework materials as catalysts. *Chem. Soc. Rev.* **2009**, *38* (5), 1450-1459.
8. Yoon, M.; Srirambalaji, R.; Kim, K., Homochiral metal-organic frameworks for asymmetric heterogeneous catalysis. *Chem. Rev.* **2012**, *112* (2), 1196-1231.
9. Cohen, S. M., Postsynthetic methods for the functionalization of metal-organic frameworks. *Chem. Rev.* **2012**, *112* (2), 970-1000.
10. Furukawa, H.; Cordova, K. E.; O'Keeffe, M.; Yaghi, O. M., The chemistry and applications of metal-organic frameworks. *Science* **2013**, *341* (6149).
11. Liu, J.; Chen, L.; Cui, H.; Zhang, J.; Zhang, L.; Su, C. Y., Applications of metal-organic frameworks in heterogeneous supramolecular catalysis. *Chem. Soc. Rev.* **2014**, *43* (16), 6011-6061.
12. Huang, Y. B.; Liang, J.; Wang, X. S.; Cao, R., Multifunctional metal-organic framework catalysts: synergistic catalysis and tandem reactions. *Chem. Soc. Rev.* **2017**, *46* (1), 126-157.
13. Dhakshinamoorthy, A.; Li, Z.; Garcia, H., Catalysis and photocatalysis by metal organic frameworks. *Chem. Soc. Rev.* **2018**, *47* (22), 8134-8172.
14. Feng, L.; Wang, K. Y.; Willman, J.; Zhou, H. C., Hierarchy in Metal-Organic Frameworks. *ACS Cent Sci* **2020**, *6* (3), 359-367.
15. Wei, Y. S.; Zhang, M.; Zou, R.; Xu, Q., Metal-Organic Framework-Based Catalysts with Single Metal Sites. *Chem. Rev.* **2020**, *120* (21), 12089-12174.
16. Zhao, M.; Ou, S.; Wu, C. D., Porous metal-organic frameworks for heterogeneous biomimetic catalysis. *Acc. Chem. Res.* **2014**, *47* (4), 1199-1207.
17. Juan-Alcañiz, J.; Gascon, J.; Kapteijn, F., Metal-organic frameworks as scaffolds for the encapsulation of active species: state of the art and future perspectives. *J. Mater. Chem.* **2012**, *22* (20), 10102-10102.
18. Zhao, M.; Yuan, K.; Wang, Y.; Li, G.; Guo, J.; Gu, L.; Hu, W.; Zhao, H.; Tang, Z., Metal-organic frameworks as selectivity regulators for hydrogenation reactions. *Nature* **2016**, *539* (7627), 76-80.
19. Chen, L.; Luque, R.; Li, Y., Controllable design of tunable nanostructures inside metal-organic frameworks. *Chem. Soc. Rev.* **2017**, *46* (15), 4614-4630.
20. Liu, L.; Zhou, T. Y.; Telfer, S. G., Modulating the Performance of an Asymmetric Organocatalyst by Tuning Its Spatial Environment in a Metal-Organic Framework. *J. Am. Chem. Soc.* **2017**, *139* (39), 13936-13943.

21. Huxley, M. T.; Burgun, A.; Ghodrati, H.; Coghlan, C. J.; Lemieux, A.; Champness, N. R.; Huang, D. M.; Doonan, C. J.; Sumbly, C. J., Protecting-Group-Free Site-Selective Reactions in a Metal-Organic Framework Reaction Vessel. *J. Am. Chem. Soc.* **2018**, *140* (20), 6416-6425.
22. Liu, Y.; Shen, Y.; Zhang, W.; Weng, J.; Zhao, M.; Zhu, T.; Chi, Y. R.; Yang, Y.; Zhang, H.; Huo, F., Engineering channels of metal-organic frameworks to enhance catalytic selectivity. *Chem. Commun. (Camb.)* **2019**, *55* (78), 11770-11773.
23. Bauer, G.; Ongari, D.; Tiana, D.; Gaumann, P.; Rohrbach, T.; Pareras, G.; Tarik, M.; Smit, B.; Ranocchiari, M., Metal-organic frameworks as kinetic modulators for branched selectivity in hydroformylation. *Nat Commun* **2020**, *11* (1), 1059-1059.
24. Feng, L.; Yuan, S.; Zhang, L. L.; Tan, K.; Li, J. L.; Kirchon, A.; Liu, L. M.; Zhang, P.; Han, Y.; Chabal, Y. J.; Zhou, H. C., Creating Hierarchical Pores by Controlled Linker Thermolysis in Multivariate Metal-Organic Frameworks. *J. Am. Chem. Soc.* **2018**, *140* (6), 2363-2372.
25. Burton, S. G., Oxidizing enzymes as biocatalysts. *Trends Biotechnol.* **2003**, *21* (12), 543-549.
26. Torres Pazmino, D. E.; Winkler, M.; Glieder, A.; Fraaije, M. W., Monooxygenases as biocatalysts: Classification, mechanistic aspects and biotechnological applications. *J. Biotechnol.* **2010**, *146* (1-2), 9-24.
27. Dong, J.; Fernández-Fueyo, E.; Hollmann, F.; Paul, C. E.; Pesic, M.; Schmidt, S.; Wang, Y.; Younes, S.; Zhang, W., Biocatalytic Oxidation Reactions: A Chemist's Perspective. *Angew. Chem. Int. Ed.* **2018**, *57* (30), 9238-9261.
28. Jasniewski, A. J.; Que Jr, L., Dioxygen Activation by Nonheme Diiron Enzymes: Diverse Dioxygen Adducts, High-Valent Intermediates, and Related Model Complexes. *Chem Rev* **2018**, *118* (5), 2554-2592.
29. Snyder, B. E. R.; Bols, M. L.; Schoonheydt, R. A.; Sels, B. F.; Solomon, E. I., Iron and Copper Active Sites in Zeolites and Their Correlation to Metalloenzymes. *Chem. Rev.* **2018**, *118* (5), 2718-2768.
30. Pappas, D. K.; Martini, A.; Dyballa, M.; Kvande, K.; Teketel, S.; Lomachenko, K. A.; Baran, R.; Glatzel, P.; Arstad, B.; Berlier, G.; Lamberti, C.; Bordiga, S.; Olsbye, U.; Svelle, S.; Beato, P.; Borfecchia, E., The Nuclearity of the Active Site for Methane to Methanol Conversion in Cu-Mordenite: A Quantitative Assessment. *J. Am. Chem. Soc.* **2018**, *140* (45), 15270-15278.
31. Vanelderen, P.; Snyder, B. E. R.; Tsai, M. L.; Hadt, R. G.; Vancauwenbergh, J.; Coussens, O.; Schoonheydt, R. A.; Sels, B. F.; Solomon, E. I., Spectroscopic definition of the copper active sites in mordenite: Selective methane oxidation. *J. Am. Chem. Soc.* **2015**, *137* (19), 6383-6392.
32. Groothaert, M. H.; Smeets, P. J.; Sels, B. F.; Jacobs, P. A.; Schoonheydt, R. A., Selective oxidation of methane by the bis( $\mu$ -oxo)dicopper core stabilized on ZSM-5 and mordenite zeolites. *J. Am. Chem. Soc.* **2005**, *127* (5), 1394-1395.
33. Mahyuddin, M. H.; Shiota, Y.; Staykov, A.; Yoshizawa, K., Theoretical Overview of Methane Hydroxylation by Copper-Oxygen Species in Enzymatic and Zeolitic Catalysts. *Acc. Chem. Res.* **2018**, *51* (10), 2382-2390.
34. Woertink, J. S.; Smeets, P. J.; Groothaert, M. H.; Vance, M. A.; Sels, B. F.; Schoonheydt, R. A.; Solomon, E. I., A  $[\text{Cu}_2\text{O}]^{2+}$  core in Cu-ZSM-5, the active site in the oxidation of methane to methanol. *Proceedings of the National Academy of Sciences of the United States of America* **2009**, *106* (45), 18908-18913.
35. Xue, Q.; Ng, B. K. Y.; Man, H. W.; Wu, T. S.; Soo, Y. L.; Li, M. M.; Kawaguchi, S.; Wong, K. Y.; Tsang, S. C. E.; Huang, B.; Lo, T. W. B., Controlled synthesis of Bi- and tri-nuclear Cu-oxo

nanoclusters on metal-organic frameworks and the structure-reactivity correlations. *Chem. Sci.* **2021**, *13* (1), 50-58.

36. Baek, J.; Rungtaweeworanit, B.; Pei, X.; Park, M.; Fakra, S. C.; Liu, Y.-S.; Matheu, R.; Alshimri, S. A.; Alshihri, S.; Trickett, C. A.; Somorjai, G. A.; Yaghi, O. M., Bioinspired Metal-Organic Framework Catalysts for Selective Methane Oxidation to Methanol. *J. Am. Chem. Soc.* **2018**, jacs.8b11525-jacs.8b11525.

37. Zheng, J.; Ye, J.; Ortuno, M. A.; Fulton, J. L.; Gutierrez, O. Y.; Camaioni, D. M.; Motkuri, R. K.; Li, Z.; Webber, T. E.; Mehdi, B. L.; Browning, N. D.; Penn, R. L.; Farha, O. K.; Hupp, J. T.; Truhlar, D. G.; Cramer, C. J.; Lercher, J. A., Selective Methane Oxidation to Methanol on Cu-Oxo Dimers Stabilized by Zirconia Nodes of an NU-1000 Metal-Organic Framework. *J. Am. Chem. Soc.* **2019**, *141* (23), 9292-9304.

38. Feng, X.; Song, Y.; Chen, J. S.; Xu, Z.; Dunn, S. J.; Lin, W., Rational Construction of an Artificial Binuclear Copper Monooxygenase in a Metal-Organic Framework. *J. Am. Chem. Soc.* **2021**, *143* (2), 1107-1118.

39. Mondloch, J. E.; Bury, W.; Fairen-Jimenez, D.; Kwon, S.; Demarco, E. J.; Weston, M. H.; Sarjeant, A. A.; Nguyen, S. T.; Stair, P. C.; Snurr, R. Q.; Farha, O. K.; Hupp, J. T., Vapor-phase metalation by atomic layer deposition in a metal-organic framework. *J. Am. Chem. Soc.* **2013**, *135* (28), 10294-10297.

40. Morris, W.; Voloskiy, B.; Demir, S.; Gándara, F.; McGrier, P. L.; Furukawa, H.; Cascio, D.; Stoddart, J. F.; Yaghi, O. M., Synthesis, structure, and metalation of two new highly porous zirconium metal-organic frameworks. *Inorg. Chem.* **2012**, *51* (12), 6443-6445.

41. Pang, J.; Yuan, S.; Qin, J.; Liu, C.; Lollar, C.; Wu, M.; Yuan, D.; Zhou, H. C.; Hong, M., Control the Structure of Zr-Tetracarboxylate Frameworks through Steric Tuning. *J. Am. Chem. Soc.* **2017**, *139* (46), 16939-16945.

42. Feng, D.; Gu, Z.-Y.; Li, J.-R.; Jiang, H.-L.; Wei, Z.; Zhou, H.-C., Zirconium-Metalloporphyrin PCN-222: Mesoporous Metal-Organic Frameworks with Ultrahigh Stability as Biomimetic Catalysts. *Angew. Chem. Int. Ed.* **2012**, *51* (41), 10307-10310.

43. Chen, Y.; Hoang, T.; Ma, S., Biomimetic catalysis of a porous iron-based metal-metalloporphyrin framework. *Inorg. Chem.* **2012**, *51* (23), 12600-12602.

44. Platero-Prats, A. E.; League, A. B.; Bernales, V.; Ye, J.; Gallington, L. C.; Vjunov, A.; Schweitzer, N. M.; Li, Z.; Zheng, J.; Mehdi, B. L.; Stevens, A. J.; Dohnalkova, A.; Balasubramanian, M.; Farha, O. K.; Hupp, J. T.; Browning, N. D.; Fulton, J. L.; Camaioni, D. M.; Lercher, J. A.; Truhlar, D. G.; Gagliardi, L.; Cramer, C. J.; Chapman, K. W., Bridging Zirconia Nodes within a Metal-Organic Framework via Catalytic Ni-Hydroxo Clusters to Form Heterobimetallic Nanowires. *J. Am. Chem. Soc.* **2017**, *139* (30), 10410-10418.

45. Platero-Prats, A. E.; Mavrandonakis, A.; Liu, J.; Chen, Z.; Chen, Z.; Li, Z.; Yakovenko, A. A.; Gallington, L. C.; Hupp, J. T.; Farha, O. K.; Cramer, C. J.; Chapman, K. W., The Molecular Path Approaching the Active Site in Catalytic Metal-Organic Frameworks. *J. Am. Chem. Soc.* **2021**, *143* (48), 20090-20094.

46. Ikuno, T.; Zheng, J.; Vjunov, A.; Sanchez-Sanchez, M.; Ortuno, M. A.; Pahls, D. R.; Fulton, J. L.; Camaioni, D. M.; Li, Z.; Ray, D.; Mehdi, B. L.; Browning, N. D.; Farha, O. K.; Hupp, J. T.; Cramer, C. J.; Gagliardi, L.; Lercher, J. A., Methane Oxidation to Methanol Catalyzed by Cu-Oxo Clusters Stabilized in NU-1000 Metal-Organic Framework. *J. Am. Chem. Soc.* **2017**, *139* (30), 10294-10301.



47. Lyu, J.; Zhang, X.; Otake, K. I.; Wang, X.; Li, P.; Li, Z.; Chen, Z.; Zhang, Y.; Wasson, M. C.; Yang, Y.; Bai, P.; Guo, X.; Islamoglu, T.; Farha, O. K., Topology and porosity control of metal–organic frameworks through linker functionalization. *Chemical Science* **2019**, *10* (4), 1186-1192.
48. Angeli, G. K.; Sartsidou, C.; Vlachaki, S.; Spanopoulos, I.; Tsangarakis, C.; Kourtellaris, A.; Klontzas, E.; Froudakis, G. E.; Tasiopoulos, A.; Trikalitis, P. N., Reticular Chemistry and the Discovery of a New Family of Rare Earth (4, 8)-Connected Metal-Organic Frameworks with csq Topology Based on RE<sub>4</sub>(μ<sub>3</sub>-O)<sub>2</sub>(COO)<sub>8</sub> Clusters. *ACS Applied Materials and Interfaces* **2017**, *9* (51), 44560-44566.
49. Wu, P.; Fan, F.; Song, J.; Peng, W.; Liu, J.; Li, C.; Cao, Z.; Wang, B., Theory demonstrated a "Coupled" mechanism for O<sub>2</sub> activation and substrate hydroxylation by binuclear copper monooxygenases. *J. Am. Chem. Soc.* **2019**, *141* (50), 19776-19789.
50. Abdel-Mageed, A. M.; Rungtaweeveranit, B.; Parlinska-Wojtan, M.; Pei, X.; Yaghi, O. M.; Jürgen Behm, R., Highly Active and Stable Single-Atom Cu Catalysts Supported by a Metal-Organic Framework. *J. Am. Chem. Soc.* **2019**, *141* (13), 5201-5210.

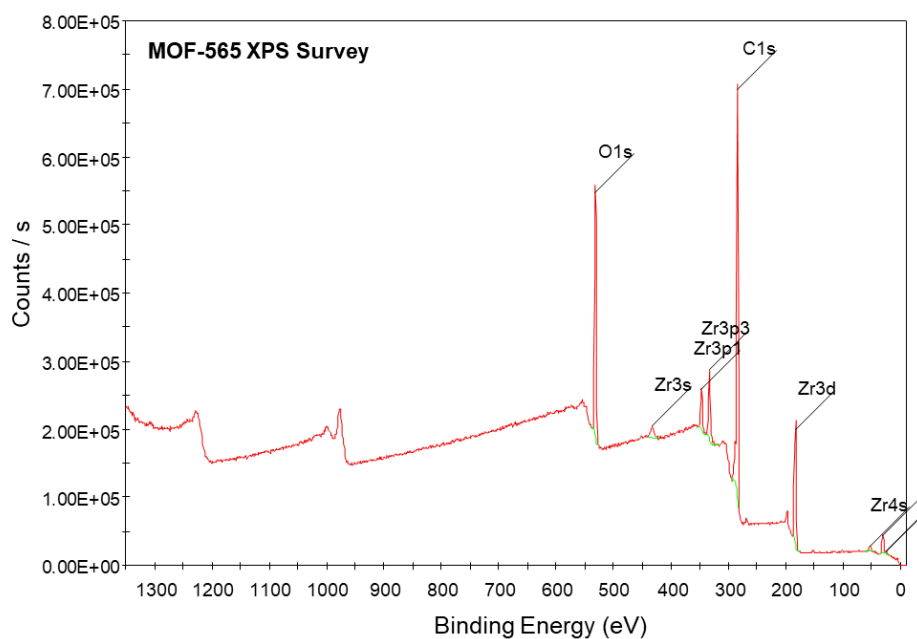
## 2.8 Supporting Information

**Table S1. Crystal data and structural refinement of MOF-565, MOF-565-Cu<sup>I</sup>, and MOF-565-Cu<sup>II</sup>.**

Compound name	MOF-565	MOF-565-Cu <sup>I</sup>	MOF-565-Cu <sup>II</sup>
Empirical formula	C <sub>72</sub> H <sub>56</sub> O <sub>32</sub> Zr <sub>6</sub>	C <sub>72</sub> H <sub>44</sub> Cu <sub>3.53</sub> N <sub>0.37</sub> O <sub>32</sub> Zr <sub>6</sub>	C <sub>72</sub> H <sub>44</sub> Cu <sub>0.87</sub> O <sub>32</sub> Zr <sub>6</sub>
Formula weight (g mol <sup>-1</sup> )	120.24	183.86	2031.93
Temperature (K)	100	100	100
Wavelength (Å)	synchrotron (λ = 0.7288)	synchrotron (λ = 0.7288)	synchrotron (λ = 0.7288)
Crystal system	hexagonal	hexagonal	hexagonal
Space group	P6/mmm	P6/mmm	P6/mmm
a (Å)	40.212(2)	40.065(2)	40.313(2)
b (Å)	40.212(2)	40.065(2)	40.313(2)
c (Å)	11.5264(7)	11.6530(12)	11.4994(9)
α (deg)	90	90	90
β (deg)	90	90	90
γ (deg)	120	120	120
Volume (Å <sup>3</sup> )	16141(2)	16199(2)	16185(2)
Z	3	3	3
Density (calculated) (g/cm <sup>3</sup> )	3.031	3.185	0.625
Absorption Coefficient (mm <sup>-1</sup> )	4.092	8.553	2.66
F(000)	13475	14203	3003
Crystal size (mm <sup>3</sup> )	0.8 × 0.02 × 0.02 mm	0.5 × 0.02 × 0.02 mm	0.34 × 0.02 × 0.02 mm
2θ range for data collection (deg)	3.172 to 55.798	1.204 to 58.138	4.384 to 130.168
Index ranges	-51 ≤ h ≤ 51, -51 ≤ k ≤ 51, -14 ≤ l ≤ 14	-53 ≤ h ≤ 53, -53 ≤ k ≤ 53, -15 ≤ l ≤ 15	-47 ≤ h ≤ 45, -28 ≤ k ≤ 47, -13 ≤ l ≤ 13
Reflections collected	238734	353314	108022
Independent reflections	6696 [R <sub>int</sub> = 0.0758, R <sub>sigma</sub> = 0.0256]	7489 [R <sub>int</sub> = 0.2501, R <sub>sigma</sub> = 0.0746]	5230 [R <sub>int</sub> = 0.2272, R <sub>sigma</sub> = 0.0709]
Completeness to θ (%)	100	100	100
Data/restraints/parameters	6696/0/140	7489/0/149	5230/0/146
Goodness-of-fit on F <sup>2</sup>	1.112	1.032	1.059
Final R indexes [I ≥ 2σ (I)]	R <sub>1</sub> = 0.0370, wR <sub>2</sub> = 0.1164	R <sub>1</sub> = 0.0730, wR <sub>2</sub> = 0.2167	R <sub>1</sub> = 0.0690, wR <sub>2</sub> = 0.1613
Final R indexes [all data]	R <sub>1</sub> = 0.0435, wR <sub>2</sub> = 0.1223	R <sub>1</sub> = 0.0907, wR <sub>2</sub> = 0.2371	R <sub>1</sub> = 0.0997, wR <sub>2</sub> = 0.1865
Largest diff. peak/hole / e Å <sup>-3</sup>	0.69/-0.60	1.86/-1.29	0.72/-1.31

**Table S2. SEM-EDS Elemental Analysis**

<b>Sample</b>	<b>Element Symbol</b>	<b>Atomic Conc.</b>	<b>Weight Conc.</b>
<b>MOF-565</b>	C	70.03	48.77
	O	24.59	22.82
	Zr	5.37	28.41
<b>MOF-565-Cu<sup>II</sup></b>	C	58.91	41.56
	O	27.61	25.94
	Cu	1.41	7.11
	Zr	1.59	8.54



**Figure S1. MOF-565 XPS Survey.**

**Table S3. MOF-565 XPS Element identification and quantification.**

<i>Name</i>	<i>Peak BE</i>	<i>FWHM eV</i>	<i>Area (P) CPS.eV</i>	<i>Atomic %</i>	<i>Q</i>
O1s	531.88	3.32	1257130.11	17.59	1
Zr3s	433.13	5.71	126475.09	3.00	1
Zr3p1	347.01	3.46	226229.37	2.21	1
Zr3p3	333.34	3.61	415224.87	2.08	1
C1s	284.83	2.67	1871865.39	63.31	1
Zr3d	183.50	4.35	741088.25	2.61	1
Zr4s	53.77	3.76	42074.14	6.32	1
Zr4p	31.34	3.69	103569.88	2.89	1

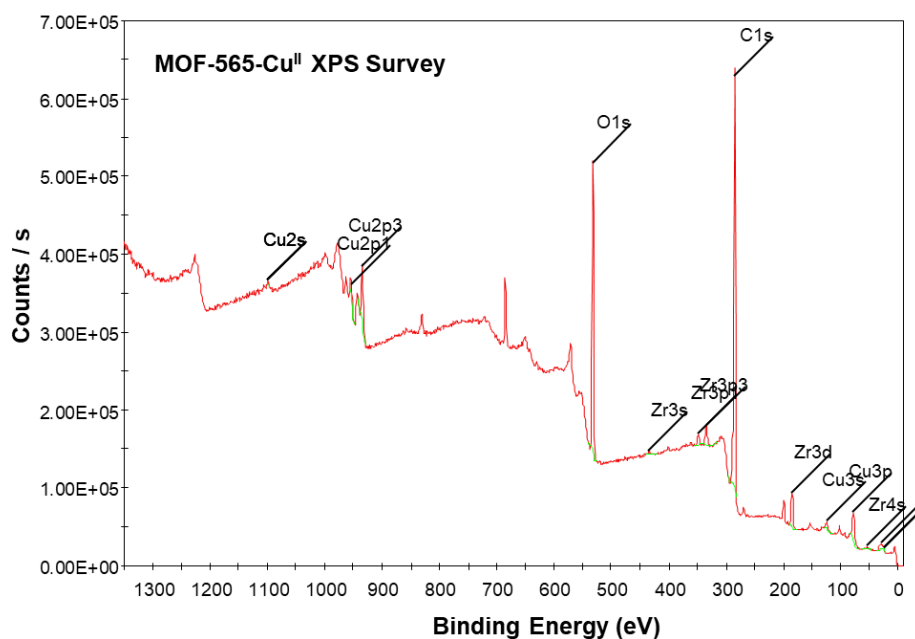
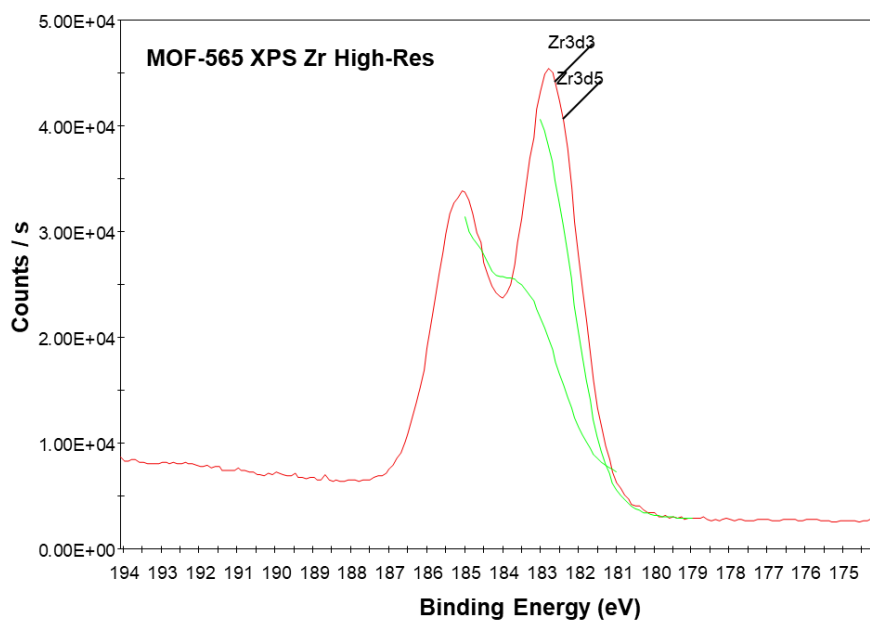


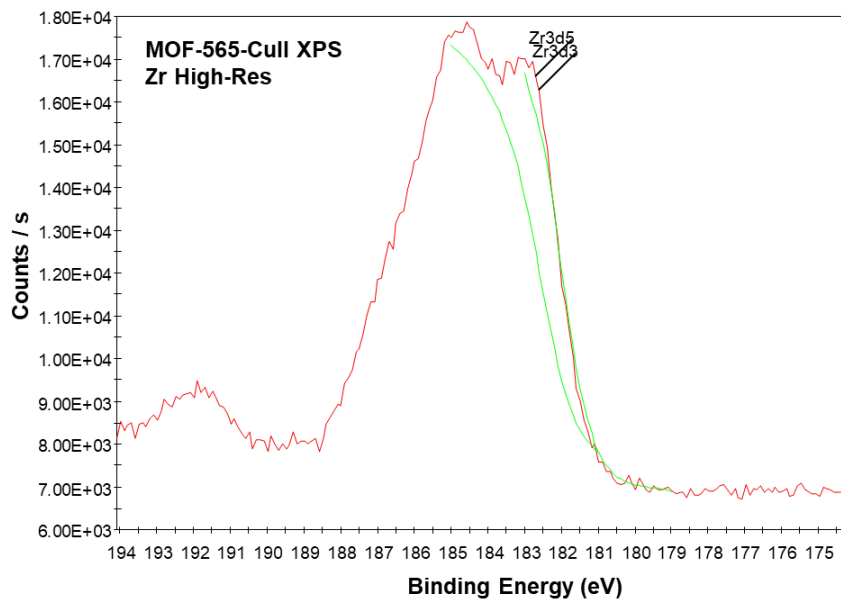
Figure S2. MOF-565-Cu<sup>II</sup> XPS Survey.

Table S4. MOF-565-Cu<sup>II</sup> XPS Element identification and quantification.

<i>Name</i>	<i>Peak BE</i>	<i>FWHM eV</i>	<i>Area (P) CPS.eV</i>	<i>Atomic %</i>	<i>Q</i>
Cu2p1	953.68	2.71	56821.39	0.48	1
Cu2p3	934.17	4.05	302750.48	1.14	1
O1s	532.03	3.25	1241243.15	19.76	1
Zr3s	434.21	1.30	15934.15	0.43	1
Zr3p1	348.18	4.30	57624.85	0.64	1
Zr3p3	334.19	3.94	115927.62	0.66	1
C1s	284.46	1.68	1708167.59	65.72	1
Zr3d	184.27	4.45	198737.95	0.80	1
Cu3s	124.09	4.74	50760.62	2.42	1
Cu3p	77.28	5.02	190771.53	2.80	1
Zr4s	54.27	4.56	20574.36	3.52	1
Zr4p	29.93	6.84	51261.39	1.63	1



**Figure S3. MOF-565 XPS Zr High-Resolution**



**Figure S4. MOF-565-Cu<sup>II</sup> XPS Zr High-Resolution**

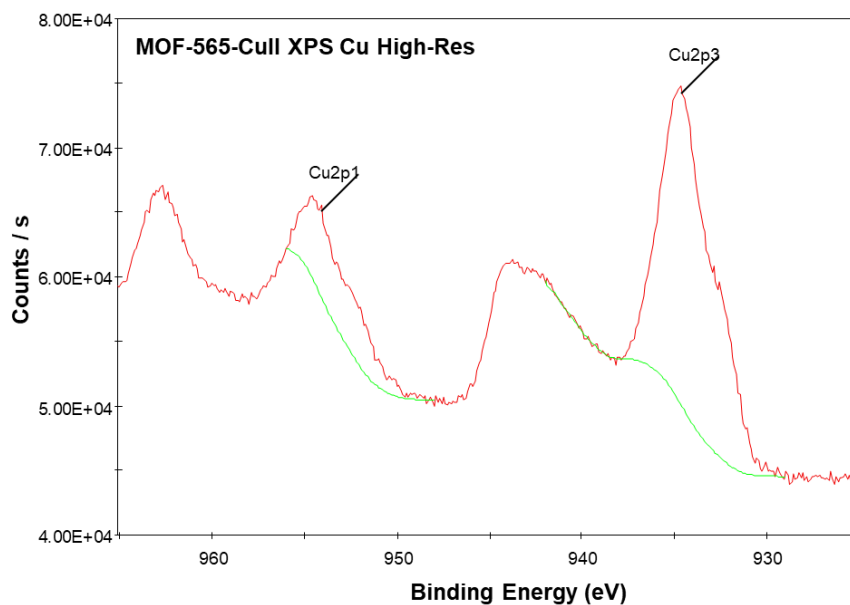


Figure S5. MOF-565-Cu<sup>II</sup> XPS Cu High-Resolution

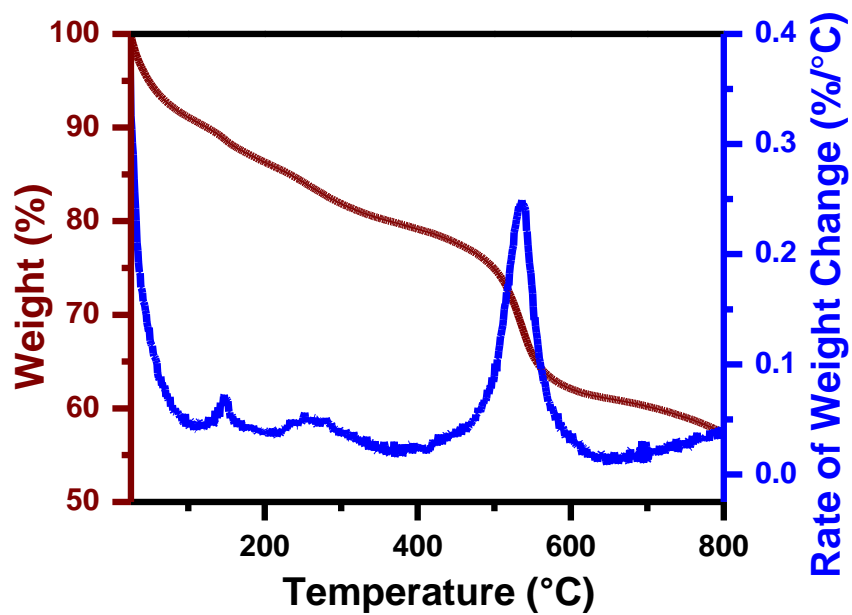


Figure S6. MOF-565 TGA Curve

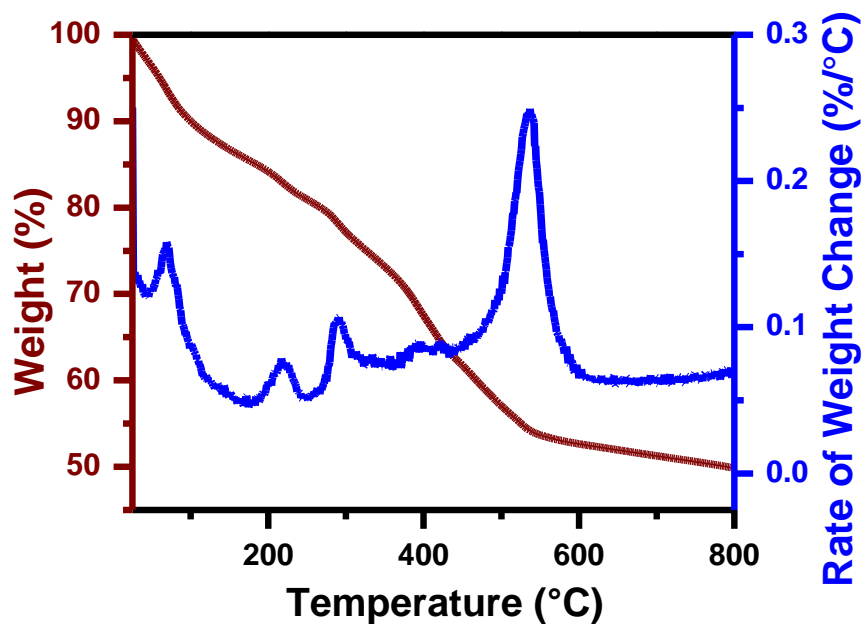


Figure S7. MOF-565-Cu<sup>II</sup> TGA Curve

Table S3. Standard Deviation for Epoxidation of Cyclohexene Catalyzed by MOF-565-Cu<sup>IIa</sup>

Entry	Yield <sup>b</sup>
1	75
2	78
3	72
4	80
5	82
6	78
7	82
8	80
Average	78 ± 4

<sup>a</sup>Reaction condition: **MOF-565-Cu<sup>II</sup>** (0.2 mol%), butanal (2 equiv), O<sub>2</sub>, 12 h, 25 °C. <sup>b</sup>Determined by NMR analysis.



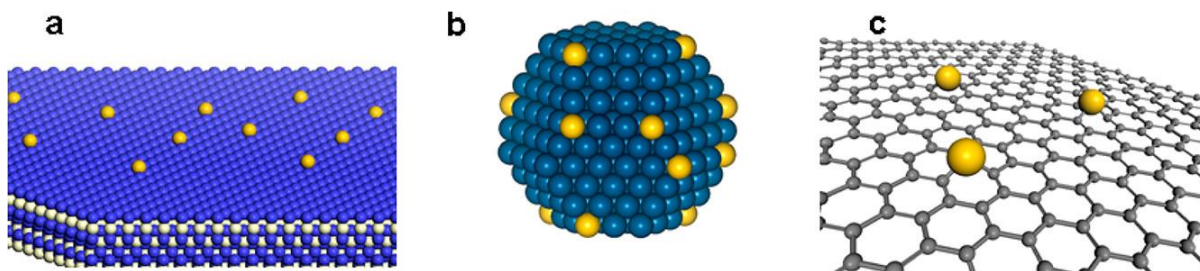
# Chapter 3. Post-Synthetic Modification of Nodes in Zirconium Metal Organic Frameworks for Photocatalytic Oxidation of Toluene

## Abstract

The tailorable chemical and physical properties of metal-organic frameworks (MOFs) make this class of materials highly attractive in the design of photocatalysts. Herein, Fe(III) was furnished onto **MOF-565** with an unsaturated  $Zr_6$  node and **NPF-520** with the rare  $Zr_9$  node to give **MOF-565-Fe<sup>III</sup>** and **NPF-520-Fe<sup>III</sup>**, respectively. A metal-to-cluster charge transfer (MCCT) process is thus generated which enhances the photocatalytic activity of the MOFs for the C-H activation of toluene and its subsequent oxidation under mild conditions, using  $O_2$  gas as the oxidant. Under anhydrous conditions, the photogenerated holes convert toluene to the toluene radical, while the electrons reduce  $O_2$  to  $O_2^{\cdot-}$ , both of which combine to form the eventual product benzaldehyde in 100% selectivity, with **NPF-520-Fe<sup>III</sup>** as the more active catalyst. On the other hand, in the presence of water, **MOF-565-Fe<sup>III</sup>** is the more active catalyst, with the hole instead reacting with water to form the potent hydroxide radical  $\bullet OH$ , resulting in the oxidation of toluene to benzoic acid.

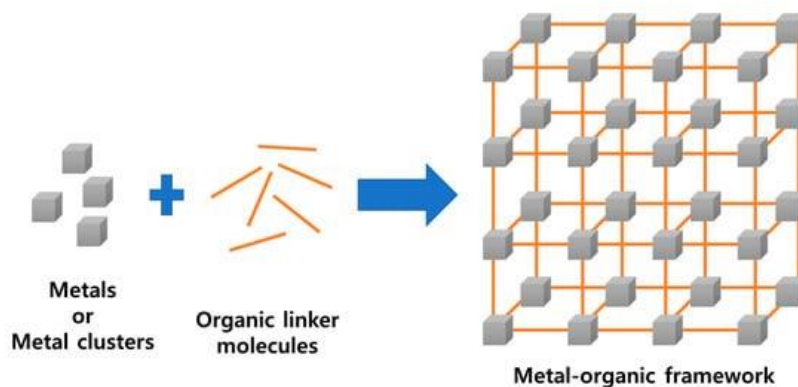
### 3.1 Introduction

Heterogeneous catalysis typically involves reusable solid phase catalysts that are readily separated from the reaction mixture, and has laid the foundation for many applications in daily life ranging from fine chemical production and energy conversion.<sup>1</sup> Typical heterogeneous catalysts are based on solid supports such as metal oxides, zeolites, silica, and alumina that are incorporated with catalytically active metal species.<sup>2-3</sup> The so-called “support effects” state that the binding between metal catalyst and its support significantly affect the selectivity and activity via the coordination mode, geometry, and electronic structures.<sup>4-5</sup> However, elucidation of the structure-activity relationship in most traditional heterogeneous catalysts is a daunting task, due to the difficulty in identifying the active species from the amorphous nature of many solid supports as well as the presence of inhomogeneous binding sites (Figure 1).<sup>6</sup> Moreover, the tunabilities of most common solid supports are quite limited, hampering the establishment of systematic variables for thorough investigation and comparison between different types of supports.



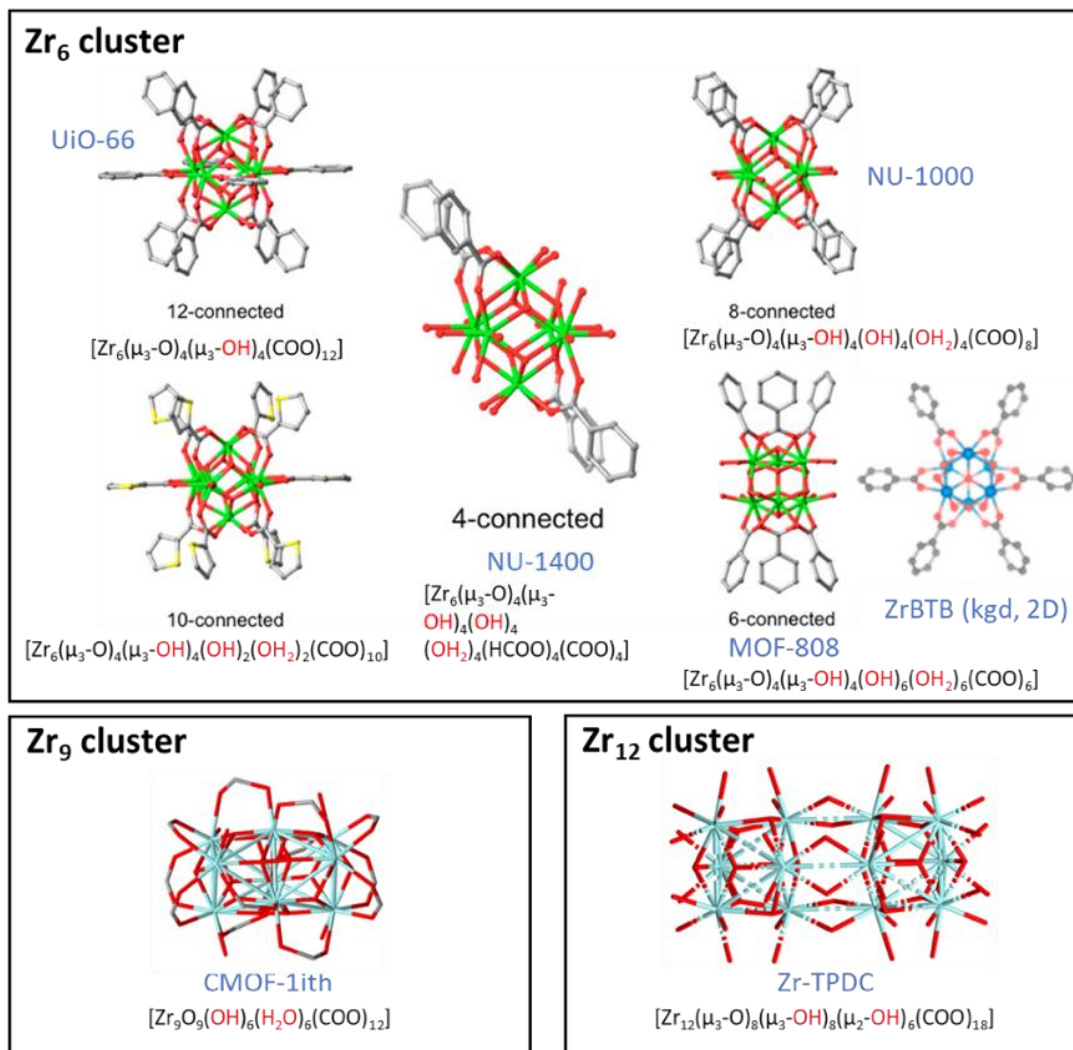
**Figure 1.** Schematic diagram illustrating different types of single-atom metal catalysts (yellow) anchored on (a) metal surface, (b) metal oxide nanoparticle, and (c) graphene supports. The catalytic sites are often randomly spaced, with different modes of binding to the support. Copyright 2013 Accounts of Chemical Research.

Recent advances in organic chemistry and materials chemistry have enabled the chemical properties and porosity of new materials to be accurately controlled on the atomic scale. In this context, metal–organic frameworks (MOFs),<sup>7-11</sup> a class of highly porous crystalline materials that are comprised of organic linkers and inorganic nodes (Figure 2), have rapidly become one of the most attractive classes of solid supports currently under investigation in heterogeneous catalysis.<sup>12-16</sup> Moreover, the periodic spacing of the metal nodes and ligands, as well as the well-ordered pore structures enable the systematic study of the structure-activity relationships of the catalytic reactions.<sup>17-21</sup> In addition, pore sized for MOFs with the same topology can be finely tuned, an important feature for understanding the structure-activity relationships that is not attainable in other solid supports.<sup>22</sup>



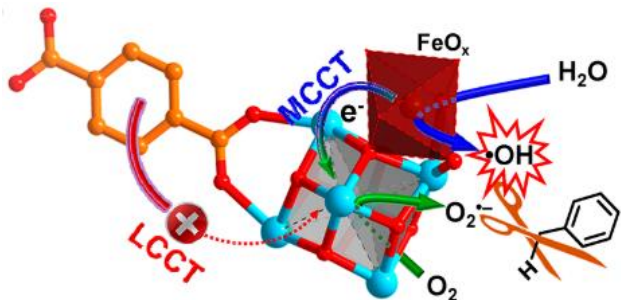
**Figure 2.** Schematic drawing of a metal-organic framework (MOF) structure. Copyright 2020 Polymers.

Zr-based MOFs (Zr-MOFs) in particular are an ideal choice of solid support material due to their outstanding thermal and chemical stability.<sup>23</sup> The terminal and bridging hydroxyl/aqua groups ( $-\text{OH}/\text{H}_2\text{O}$ ) on unsaturated nodes or defect sites can serve as the binding sites for extraneous metal, and their number and availability is controlled by ligand connectivity and Zr nuclearity (Figure 3). The uniform distribution of the metal species with atomic precision can not only prevent aggregation, but also facilitate the structural determination by a variety of spectroscopy methods as well as single-crystal X-ray diffraction (sc-XRD), which further underlines the importance of Zr-MOFs as an ideal model catalyst support.<sup>24-30</sup> To date, diverse MOFs featuring  $\text{Zr}_6$ ,<sup>31-37</sup>  $\text{Zr}_8$ ,<sup>38</sup> and  $\text{Zr}_{12}$ <sup>39</sup> nodes have been widely studied as porous supports for the facile construction of single-site catalysts in heterogeneous catalysis.<sup>39</sup> Unfortunately, in particular to the addition of Fe single-site catalysts on Zr-MOFs, only the fully saturated, 12-connected UiO series and the 8-connected NU-1000 have been reported.<sup>40-42</sup>



**Figure 3.** Different types of Zr-MOF nodes and their cluster formulas. Adapted from 2017-2020 American Chemical Society, 2018 Angewandte Chemie International Edition, 2004 Chemistry-A European Journal.

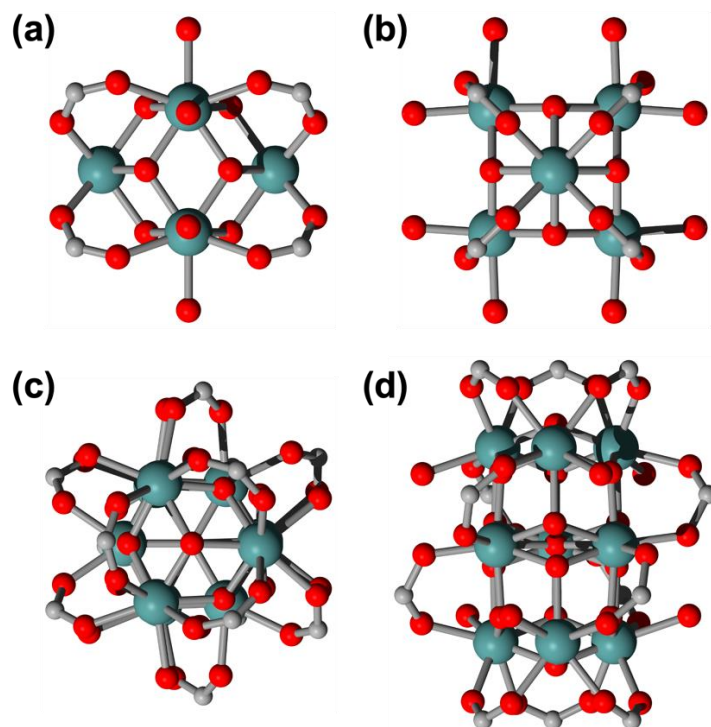
Of these, UiO-66-Fe was found to exhibit considerable activity for the photocatalytic oxidation of toluene (Figure 4).<sup>43</sup> The post-modification strategy used by Jiang and co-workers for the incorporation of Fe<sup>III</sup> onto the Zr-oxo clusters of UiO-66 via microwave-assisted synthesis not only resulted in the creation of catalytic active centers, but also shifted the light absorbance that is attributed to metal-to-cluster or metal-to-metal charge transfer (MCCT) from Fe<sup>III</sup> to the Zr<sub>6</sub> node. It was proposed that the photoinduced charge separation originating from MCCT<sup>44-46</sup> promotes the oxidation of H<sub>2</sub>O to hydroxyl radicals ( $\bullet\text{OH}$ ), which subsequently activates the C–H bonds of toluene in the presence of O<sub>2</sub> and ultimately resulted in the formation of benzoic acid. It should be noted that a cut-off filter at 380 nm was used as the light source to promote the photocatalytic oxidation of toluene.



**Figure 4.** Schematic illustration showing UiO-66-Fe as a photocatalyst for toluene oxidation with water and O<sub>2</sub> gas. Water is oxidized by the hole on Fe, whereas O<sub>2</sub> is reduced by the electron on the cluster.

Besides microwave-assisted synthesis, the incorporation of Fe<sup>III</sup> into Zr-MOFs has also been realized by solvent-assisted synthesis, by which up to 2.2 Fe atoms per Zr<sub>6</sub> node were introduced on NU-1000.<sup>47</sup> The resulting NU-1000-Fe was found to effectively catalyze vapor-phase cyclohexene epoxidation with vaporized hydrogen peroxide.

Hence, we envision that the design space can be further expanded for Zr-MOFs with different Zr ligand connectivity and nuclearity, such as different MOFs with 8-connected **csq** topology as well as Zr-MOFs the newly discovered Zr<sub>9</sub> node.<sup>48-49</sup> The choice of an 8-connected, **csq** topology Zr-MOF was influenced by our interest in synthesizing and characterizing a Zr-MOF with a higher density of Fe single atom sites and fully study the relationship between the coordination mode of Zr<sub>6</sub> node (Figure 5a-b) and the catalytic activity. Similarly, the recently discovered Zr<sub>9</sub> nodes (Figure 5c-d),<sup>48-49</sup> with a node formula of Zr<sub>9</sub>O<sub>9</sub>(OH)<sub>6</sub>(H<sub>2</sub>O)<sub>6</sub> in (4,12)-connected **ith** topology (crystallographic space group *R32*), have terminal -OH/H<sub>2</sub>O groups which can be used as anchors as well as a binding manner of terminal carboxylates which is quite distinct from the Zr<sub>6</sub> clusters. This would likely provide a new local chemical environment that steers the reactivity and connectivity of Fe differently from the Zr<sub>6</sub> nodes, thereby also influencing the catalytic activity and selectivity of the grafted metal.

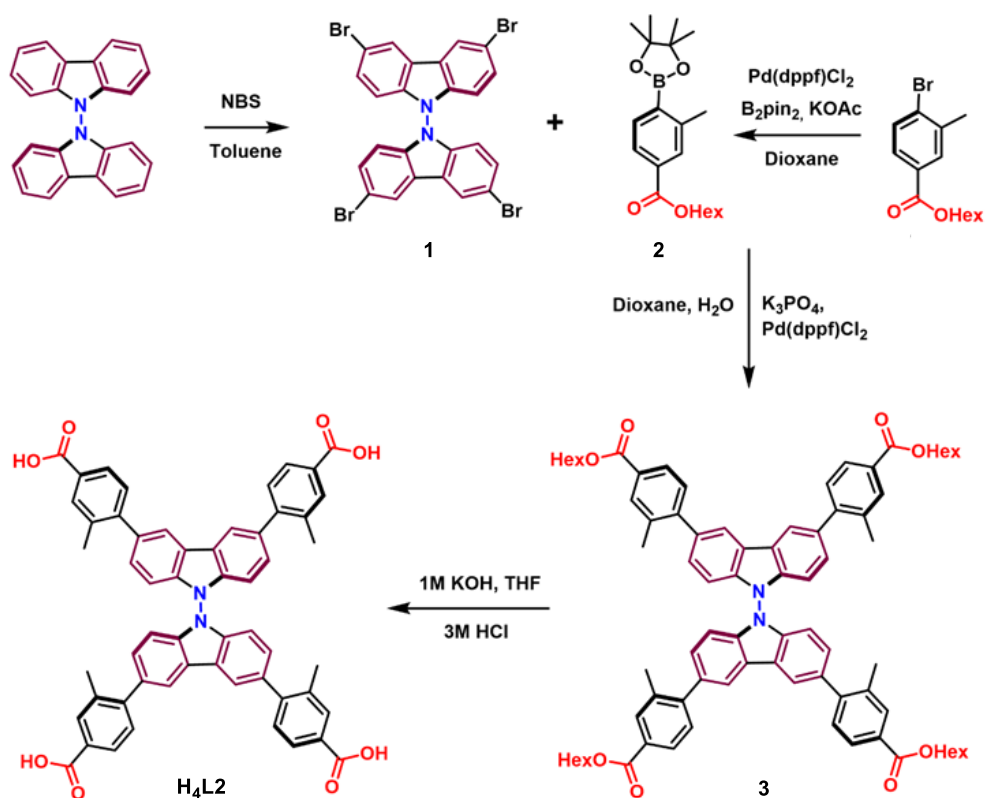


**Figure 5.** (a), (b)  $Zr_6$  node and (c), (d)  $Zr_9$  node viewed at different angles.

Herein, we use **MOF-565**, the 8-connected **csq** topology Zr-MOF described in Chapter 2, and a new (4,12)-connected Zr-MOF with **ith** topology that consists of  $Zr_9$  nodes, **NPF-520** (NPF = Nebraska Porous Framework), as supports for the installation of  $Fe^{III}$  catalytic centers. We then tested the Fe-modified MOFs, **MOF-565-Fe** and **NPF-520-Fe**, for the photocatalytic oxidation of toluene under visible light irradiation.

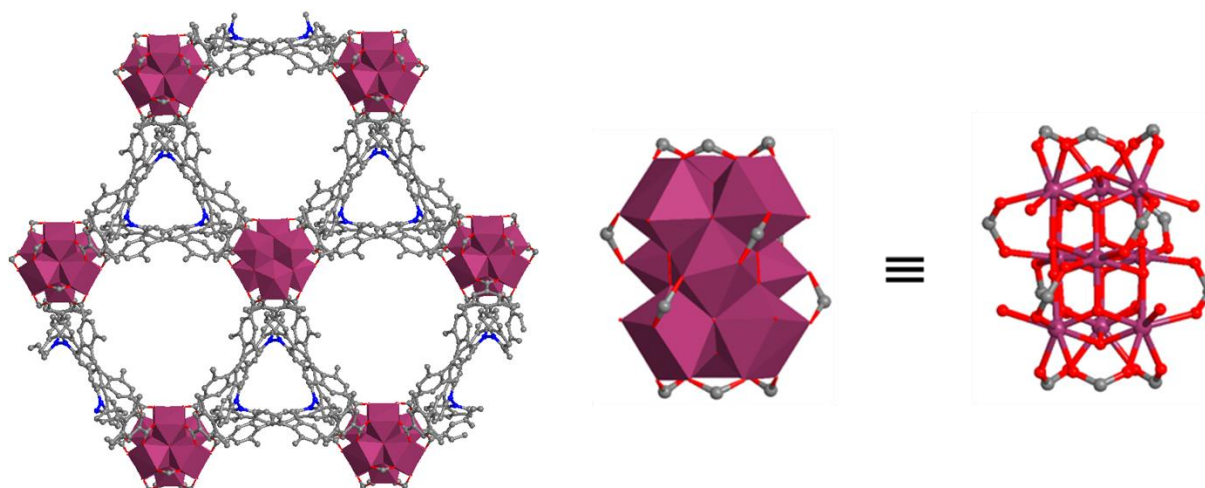
### 3.2 Synthesis and Structural Characterization of NPF-520

The synthesis and characterization of a new MOF with the recently discovered  $Zr_9$  cluster, **NPF-520**, was conducted in collaboration with Christian Fiankor, another student in the Zhang group. The MOF linker  $H_4L_2$  was synthesized via Suzuki coupling of tetrabromobicarbazole (**1**) and hexyl 3-methyl-4-(4,4,5,5-tetramethyl-1,3,2-dioxaborolan-2-yl)benzoate (**2**) to produce the ligand ester (**3**) (Scheme 1). Subsequent hydrolysis in a basic medium yielded  $H_4L_2$ . Colorless trigonal-shaped crystals of **NPF-520** were then obtained by solvothermal reaction of  $ZrCl_4$  and  $H_4L_2$  in the presence of acetic and benzoic acid as co-modulation agents at 120 °C for 48 h.



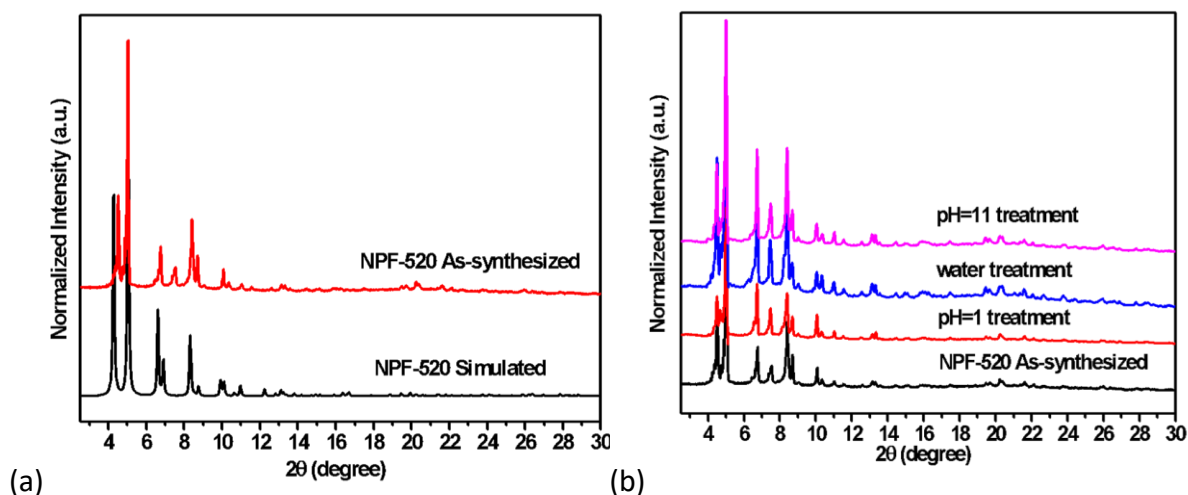
Scheme 1. Synthesis of  $H_4L_2$ .

Single crystal X-ray diffraction studies at 273 K under exposure to solvent vapor revealed that **NPF-520** crystallizes in the trigonal crystal system, in chiral space group  $R32$  with the lattice parameters  $a = b = 35.168 \text{ \AA}$ ,  $c = 28.593 \text{ \AA}$  (Figure 6 and Table S1). Close examination of the zirconium cluster reveals two crystallographic distinct Zr atoms (i.e., Zr1 and Zr2) in each asymmetric unit. Zr1 is bridged by eight oxygen atoms, derived from four  $\mu_3-O^{2-}/OH^-$  groups, as well as three  $L_2$  ligands and a capping  $H_2O$  molecule. Zr2 is bridged by two oxygen atoms emanating from two  $L_2$  ligands and seven  $\mu_3-O^{2-}/OH^-$  groups. Grouped together, six Zr1 and three Zr2 atoms are bound by eight  $\mu_3-O^{2-}/OH^-$  groups, forming the rare  $Zr_9$  nodes.



**Figure 6.** Crystallographic representation of **NPF-520** along the *c*-axis and depiction of  $Zr_9$  node.

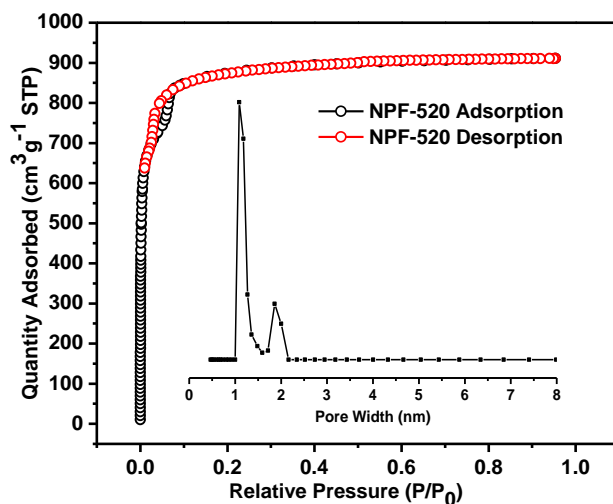
Topologically, each  $Zr_9$  cluster can be described as the face-sharing of two  $Zr_6$  clusters that links 12 tetrahedral ligands, and each tetrahedral ligand is bridged by four  $Zr_9$  clusters to give an extremely rare (4,12)-connected **itb** net.<sup>48, 50</sup> Such interconnection between ligand and  $Zr_9$  node results in a 3D framework with a charge-balanced formula of  $Zr_9O_9(OH)_6(H_2O)_6(L_2)_3$ . The resulting 3D framework contains two types of triangular 1D channels with diameters of 1.2 and 0.4 nm along the *c* axis. PLATON calculations indicate the presence of 66.7% of void space accessible for guest molecules, large enough for small organic substrates to enter.<sup>51</sup> Powder X-ray diffraction (PXRD) patterns of **NPF-520** confirm the bulk phase purity of the as-synthesized sample when compared to the simulated patterns from its corresponding single-crystal structure (Figure 7a).



**Figure 7.** PXRD patterns of **NPF-520** (a) as-synthesized and simulated and (b) at various pH.



The chemical stability of **NPF-520** was examined by treating the MOF in H<sub>2</sub>O, basic (pH = 11), and acidic (pH = 1) conditions after 24 h. As shown in Figure 7b, excellent PXRD patterns remained intact after these treatments, suggesting good stability with no phase transition or framework collapse. After activation using supercritical CO<sub>2</sub> exchange, the permanent porosity of the **NPF-520** was measured by N<sub>2</sub> adsorption isotherms measured at 77 K (Figure 8). **NPF-520** exhibits a typical type I isotherm, with a saturated N<sub>2</sub> uptake of 915 cm<sup>3</sup> g<sup>-1</sup>, a Brunauer–Emmett–Teller surface area (S<sub>BET</sub>) of 3463 m<sup>2</sup> g<sup>-1</sup>, and a pore volume of 1.41 cm<sup>3</sup> g<sup>-1</sup>. This is consistent with the calculated accessible surface area of 2816 m<sup>2</sup> g<sup>-1</sup>.



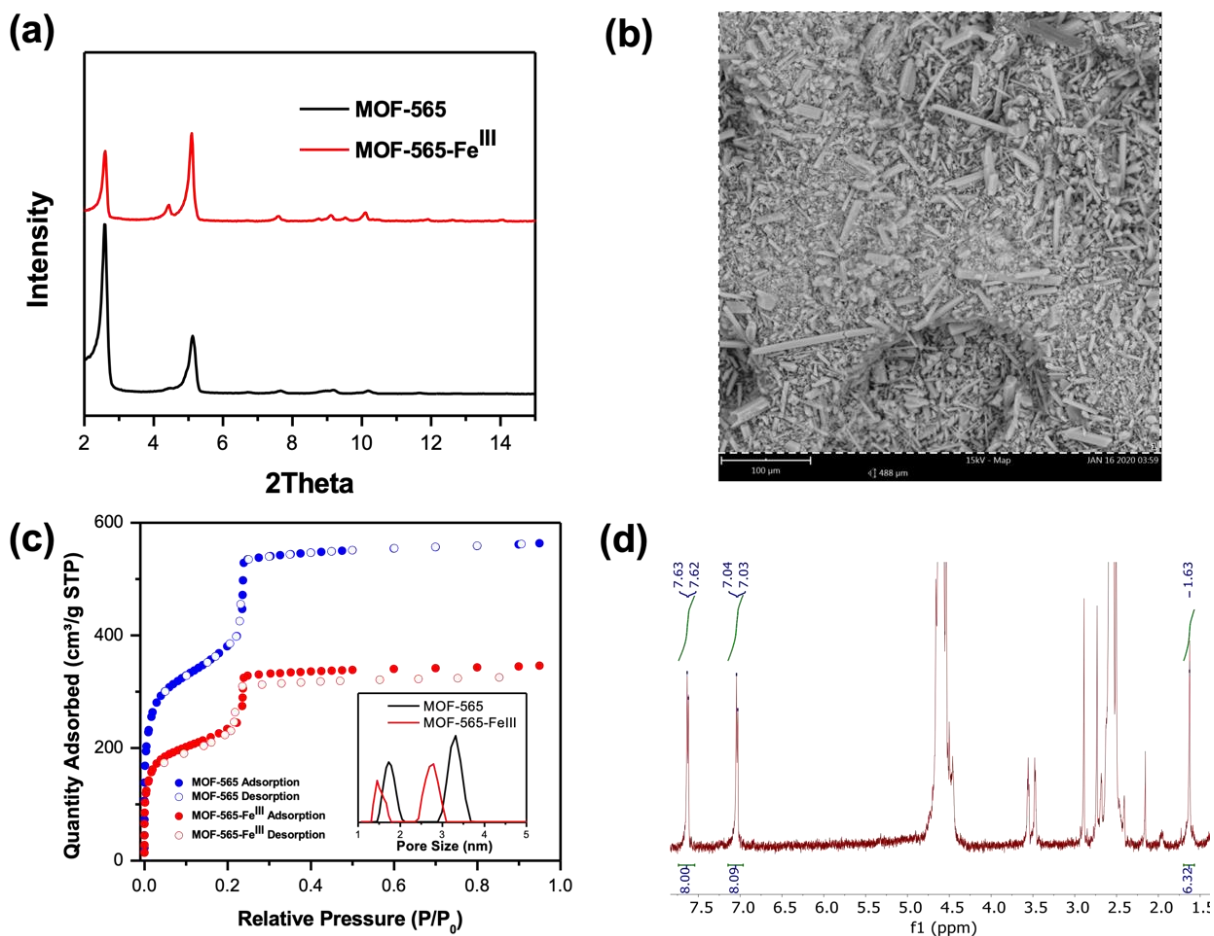
**Figure 8.** Adsorption/desorption isotherms and DFT pore size distribution of **NPF-520**.

### 3.3 Synthesis and Structural Characterization of MOF-565-Fe

In order to increase the loading of Fe<sup>III</sup> compared to previous work using the solvent or microwave assisted methods, we adopted the deprotonation-assisted metalation strategy developed by Lin and coworkers, which was found to be able achieve a maximum loading of 4 Fe atoms per Zr<sub>6</sub> node in UiO-68<sup>52</sup> and 4 Cu atoms per Zr<sub>6</sub> node in **MOF-565** (Chapter 2).

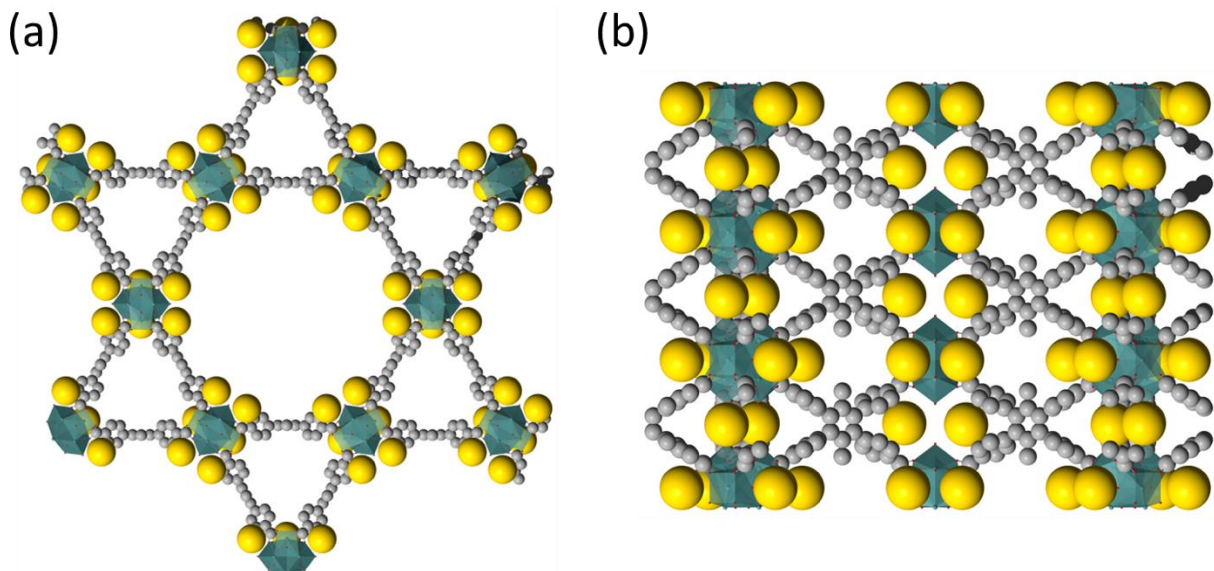
Before **MOF-565** can be modified, it was first pre-treated to exchange the residual capping unreactive formate groups on the clusters with reactive terminal -OH and -OH<sub>2</sub> groups by stirring in a mixture of hydrochloric acid (0.1 M), methanol and water (1:10 ratio) overnight. The hydroxide groups were then deprotonated using TMSCH<sub>2</sub>Li ((trimethylsilyl)methyl lithium) in hexane followed by reaction with anhydrous FeCl<sub>2</sub> (iron(II) chloride) or FeCl<sub>3</sub> (iron(III) chloride) in acetonitrile to afford the iron(II)- and iron(III)-modified MOFs, **MOF-565-Fe<sup>II</sup>** and **MOF-565-Fe<sup>III</sup>**.

Inductively coupled plasma-optical emission spectrometry (ICP-OES) analysis showed that **MOF-565-Fe<sup>II</sup>** and **MOF-565-Fe<sup>III</sup>** has 4.02 and 3.85 Fe atoms per Zr<sub>6</sub> node, respectively, suggesting that the maximum loading of Fe is similar to UiO-68. Unfortunately, **MOF-565-Fe<sup>II</sup>** oxidized instantly upon exposure to air and was too unstable for other characterizations. Powder X-ray diffraction (PXRD) studies showed that bulk crystallinity of **MOF-565-Fe<sup>III</sup>** was retained throughout the metalation and oxidation processes (Figure 9a) and the crystal morphology was retained as needles as seen by SEM imaging (Figure 9b). Installation of Fe centers reduced the Brunauer-Emmett-Teller (BET) surface area from 1347 m<sup>2</sup>/g for **MOF-565** to 911 m<sup>2</sup>/g for **MOF-565-Fe<sup>III</sup>**, while the pore sizes shrunk (Figure 9c). <sup>1</sup>H NMR dspectrum of **MOF-565-Fe<sup>III</sup>** digested with potassium phosphate in D<sub>2</sub>O confirmed that the linker was unmodified (Figure 9d). Energy dispersive X-ray spectroscopy (EDS) and X-ray photoelectron spectroscopy confirmed the addition of iron, although the EDS (Table S2) and XPS data (Figures S4, S6, S7) does not match with ICP likely due to a difference between the bulk and surface exposed metal sites.



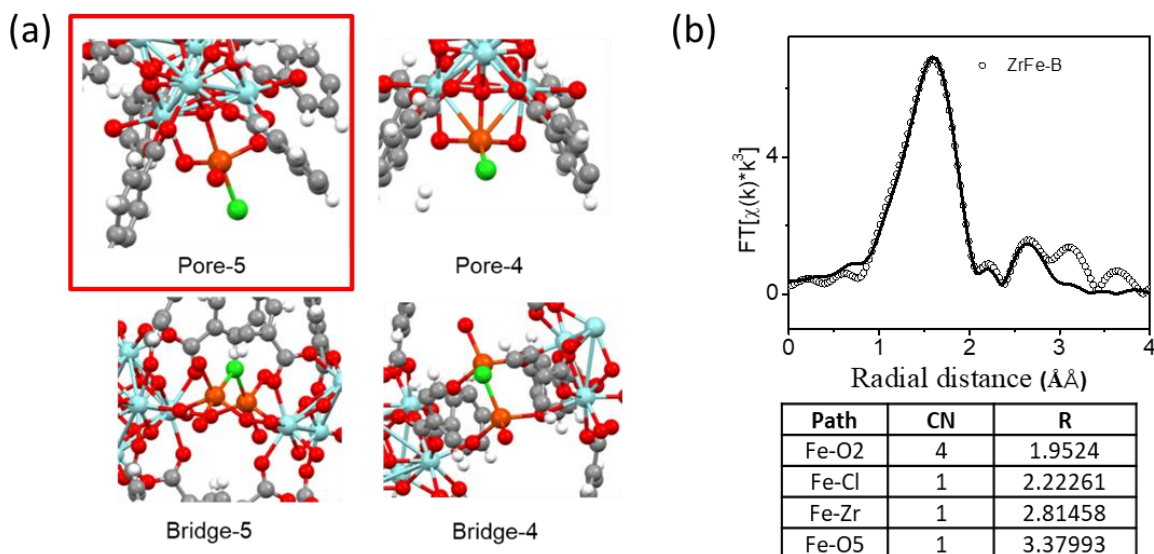
**Figure 9.** (a) PXRD of **MOF-565** and **MOF-565-Fe<sup>III</sup>**. (b) SEM image of **MOF-565-Fe<sup>III</sup>**. (c) N<sub>2</sub> adsorption/desorption and pore sizes of **MOF-565** and **MOF-565-Fe<sup>III</sup>**. (d) <sup>1</sup>H NMR spectrum of **MOF-565-Fe<sup>III</sup>** digested in K<sub>3</sub>PO<sub>4</sub>/D<sub>2</sub>O showing the unmodified linker along with various solvent impurities.

Single-crystal X-ray diffraction (sc-XRD) study after modification was conducted to determine the Fe positions and coordination environments in **MOF-565-Fe<sup>III</sup>** (Figure 10). Unfortunately, we could only identify the regions of electron density where the installed Fe, and likely its coordinated Cl atom were located. As the distances between the terminal hydroxyl/water on the cluster and the center of the electron densities ranged from 3-3.8 Å, which is too long for an Fe-O bond (approximately 2 Å), we surmised that the electron density was not that of an Fe atom but rather a result of disordered complexes involving Fe, Cl and coordinated solvent molecules. A similar observation was made for the reported Fe-modified NU-1000,<sup>42</sup> but no clarification was given about the unusually long bond distance or further structural characterization conducted.



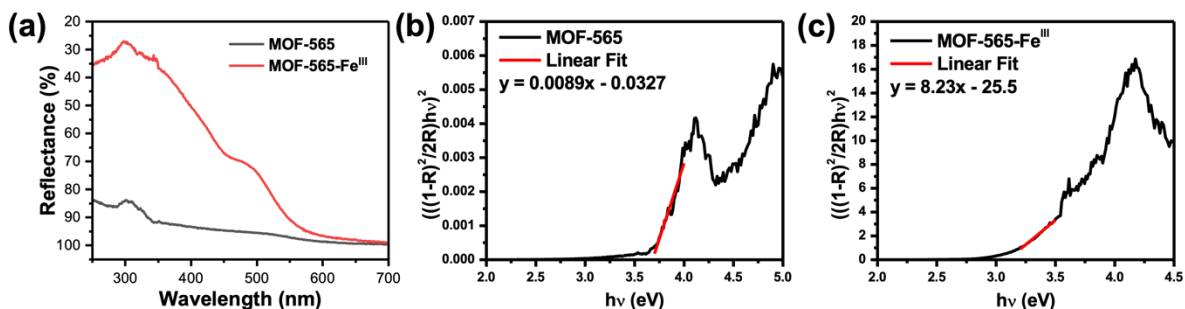
**Figure 10.** Single-crystal structure of **MOF-565-Fe<sup>III</sup>** viewed down the (a) *c*-axis and (b) *a*-axis. Yellow spheres indicate regions of electron density and the most likely locations of the installed Fe atoms.

To better study the structure of the installed Fe atoms, Fe K-edge X-ray absorption near-edge structure (XANES) and extended X-ray absorption fine structure (EXAFS) spectroscopy were conducted, and the results fitted to various models constructed based on common coordination modes and geometries of Fe atoms, while taking to account the positions of electron densities found in the single crystal structure. In total, 4 models were created and fitted: 1) Pore-5: 5-coordinate trigonal bipyramidal, 2) Pore-4: 4-coordinate tetrahedral Fe, 3) Bridge-5: 5-coordinate trigonal bipyramidal Fe coordinated in between 2 nodes, and 4) Bridge-4: 4-coordinate tetrahedral Fe coordinated in between 2 nodes (Figure 11a). The Pore-5 model was found to provide the best fit for the EXAFS data (Figure 11b), confirming that Fe is 5-coordinate with a trigonal bipyramidal geometry, and bound to O/OH<sub>2</sub>/μ<sub>3</sub>-O on the node as well as free Cl<sup>-</sup>/OH<sub>2</sub>. Unlike **MOF-565-Cu<sup>I</sup>** in Chapter 2, Fe does not prefer to coordinate between 2 nodes.



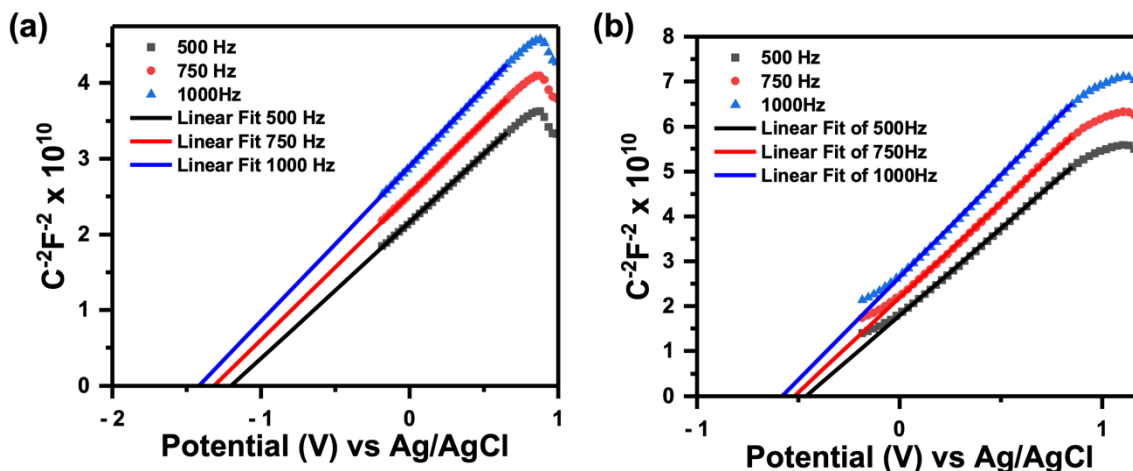
**Figure 11.** (a) Models for Fe coordination to the Zr<sub>6</sub> node of **MOF-565**. (b) EXAFS fitting using the Pore-5 model. All Fe-O bonds were assumed to be identical.

The electronic structure of **MOF-565** before and after Fe<sup>III</sup> incorporation was also studied. The UV-vis spectrum shows a red-shift and an enhanced visible light absorption after installation of Fe<sup>III</sup> (Figure 12a), consistent with the yellow color of the material after the modification. The band gaps estimated from the Tauc plots of **MOF-565** and **MOF-565-Fe<sup>III</sup>** are 3.67 eV and 3.09 eV, respectively (Figure 12b and c).



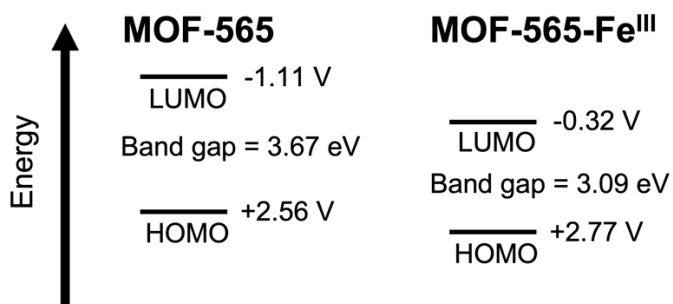
**Figure 12.** (a) UV-visible reflectance spectrum. (b) Tauc plot for **MOF-565**. (c) Tauc plot for **MOF-565-Fe<sup>III</sup>**.

In order to determine the band edge, Mott-Schottky plots were recorded for **MOF-565** and **MOF-565-Fe<sup>III</sup>**. The positive slopes of the linear Mott-Schottky plots of both MOFs at different frequencies indicate the n-type characteristics of semiconductor nature (Figure 13). The LUMO energy levels were determined from the average of 3 X-intercepts at 500-1000 Hz, with the values of -1.31 V and -0.52 V vs Ag/AgCl (i.e., -1.11 V and -0.32 V vs NHE) for **MOF-565** and **MOF-565-Fe<sup>III</sup>**, respectively.<sup>53</sup>



**Figure 13.** Mott-Schottky plots for (a) **MOF-565** and (b) **MOF-565-Fe<sup>III</sup>**.

Combined with the band gaps estimated by Tauc plots, the energy diagrams are depicted in Figure 14, which suggest that the incorporation of Fe<sup>III</sup> lowers both the HOMO and LUMO energy levels and shrinks the band gap by 0.58 eV. From a thermodynamic perspective, both MOFs have the capability for water oxidation ( $E_{\text{OH}^{\bullet}/\text{OH}^-} = 1.89$  V vs NHE;  $E_{\text{O}_2/\text{H}_2\text{O}} = 1.23$  V vs NHE) as well as O<sub>2</sub> reduction ( $E_{\text{O}_2/\text{O}_2^{\bullet-}} = -0.16$  V),<sup>54</sup> but only **MOF-565-Fe<sup>III</sup>** has a band gap that falls within the visible light range (1.7-3.1 eV). The band gap of 3.09 eV for **MOF-565-Fe<sup>III</sup>** is also comparable to the previously reported Fe-UiO-66 (3.02 eV).<sup>43</sup>

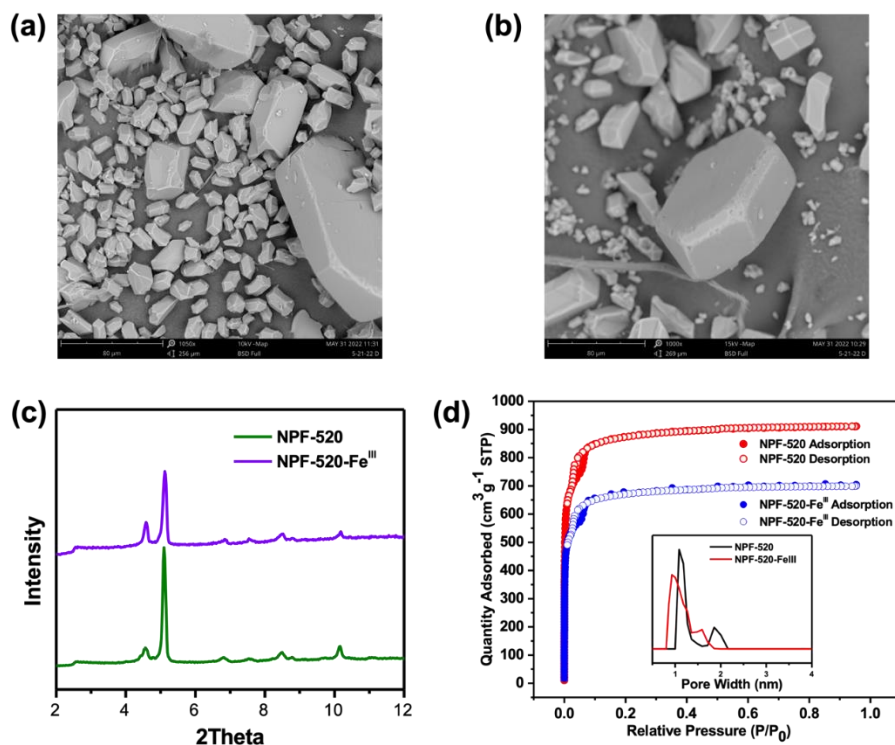


**Figure 14.** Energy level diagram for **MOF-565** and **MOF-565-Fe<sup>III</sup>**.

### 3.4 Synthesis and Structural Characterization of NPF-520-Fe

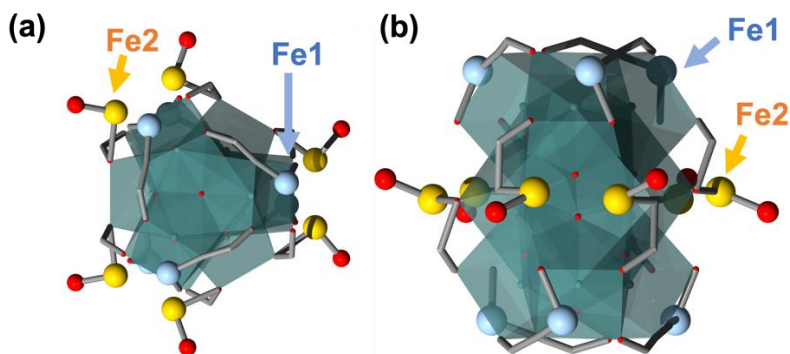
**NPF-520** was pre-treated and modified using the same method described for **MOF-565-Fe** to afford the iron(II)- and iron(III)-modified MOFs, **NPF-520-Fe<sup>II</sup>** and **NPF-520-Fe<sup>III</sup>**. Interestingly, inductively coupled plasma-optical emission spectrometry (ICP-OES) analysis showed that **NPF-520-Fe<sup>II</sup>** and **NPF-520-Fe<sup>III</sup>** has 0.15 and 3.14 Fe atoms per Zr<sub>9</sub> node, respectively, suggesting that Fe<sup>II</sup> does not bind as well to the Zr<sub>9</sub> cluster as Fe<sup>III</sup>. Unfortunately, like **MOF-565-Fe<sup>II</sup>**, **NPF-520-Fe<sup>II</sup>** also oxidized instantly upon exposure to air and was too unstable for other characterizations.

SEM images confirmed that the block morphology of **NPF-520** (Figure 15a) was retained upon installation of Fe (Figure 15b). Powder X-ray diffraction (PXRD) patterns showed that bulk crystallinity of **NPF-520-Fe<sup>III</sup>** was retained throughout the metalation process (Figure 15c). Installation of Fe centers reduced the Brunauer-Emmett-Teller (BET) surface area from 3463 m<sup>2</sup>/g for **NPF-520** to 2511 m<sup>2</sup>/g for **NPF-520-Fe<sup>III</sup>** and reduced the pore size from 1.9 Å and 1.1 Å to 1.6 Å and 0.9 Å (Figure 15d). <sup>1</sup>H NMR spectrum of **NPF-520-Fe<sup>III</sup>** digested with sulfuric acid in D<sub>2</sub>O confirmed that the linker was unmodified (Figure S1). Energy dispersive X-ray spectroscopy (EDS) and X-ray photoelectron spectroscopy confirmed the addition of iron, although the EDS (Table S2) and XPS data (Figures S5, S8, S9) does not match with ICP likely due to a difference between the bulk and surface exposed metal sites.



**Figure 15.** SEM images of (a) **NPF-520** and (b) **NPF-520-Fe<sup>III</sup>**. (c) Powder X-ray diffraction patterns and (d) adsorption/desorption isotherms and pore size distribution of **NPF-520** and **NPF-520-Fe<sup>III</sup>**.

Single-crystal X-ray diffraction (sc-XRD) analyses was conducted to obtain the structural insights into the incorporated Fe<sup>III</sup> species in **NPF-520-Fe<sup>III</sup>** (Figure 16). After refinement of the framework structure of **NPF-520**, the residual electron density was calculated to identify the location and occupancy of Fe. There are two crystallographically distinct Fe sites (i.e., Fe1 and Fe2) in each asymmetric unit.



**Figure 16.** Single-crystal structure of **NPF-520-Fe<sup>III</sup>** viewed down the (a) *c*-axis and (b) *b*-axis. Fe1 atoms are colored yellow and Fe2 blue to differentiate between the two types of Fe.

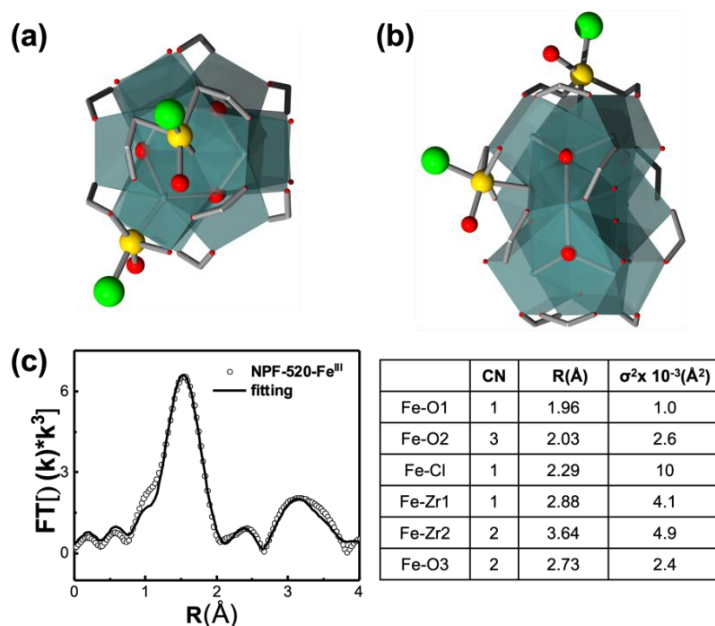
The Fe1 site is located inside the two corners of the trigonal bipyramidal cage and coordinated to the Zr<sub>9</sub> node through  $\mu_3$ -bridging oxygen (O5, 2.52 Å) and carboxylate oxygens (O7/O8, 2.97 Å and 3.03 Å). The Fe2 site sits in the triangular pore and coordinates to the Zr<sub>9</sub> node through terminal oxygen (O6, 2.51 Å), carboxylate oxygen (O2, 2.62 Å), and  $\mu_3$ -bridging oxygens (O3, 3.41 and 3.50 Å). The total occupancies of the Fe sites are 1.15 (Fe1) and 1.66 (Fe2) per Zr<sub>9</sub> node, which corresponds to a total iron content of 2.81 Fe/Zr<sub>9</sub>, consistent with the ICP-OES data (3.1 Fe/Zr<sub>9</sub>). The location of Cl<sup>-</sup> could not be determined, likely due to severe disorder and low occupancy.

The relatively long Fe-O distances (2.5~3.5 Å) suggest a weak interaction between Fe and the Zr node at the solvated state during which the sc-XRD data was collected. Thus, although sc-XRD is helpful to reveal the general location and occupancy, more investigation needs to be done to elucidate the local coordination of Fe.

X-ray absorption spectroscopy (XAS) was thus used to probe the coordination environment of the incorporated Fe atoms in **NPF-520-Fe<sup>III</sup>**. A dominant peak at 1.47 Å is observed in the Fourier-transformed extended X-ray absorption fine structure (FT-EXAFS) spectrum (Figure 17c). No apparent peaks corresponding to the close Fe-Fe bond are present, consistent to the fact the multiple Fe2 sites are the result of symmetry generation instead of a real close Fe-Fe contact. The extended X-ray absorption fine structure (EXAFS) regions were best fit to the model in Figure 17a and 17b, which gives an average coordination number of 5 for Fe. The first-shell coordination environment around Fe can be attributed to Fe-O/Cl bonding with a bond distance of 2.00 Å and

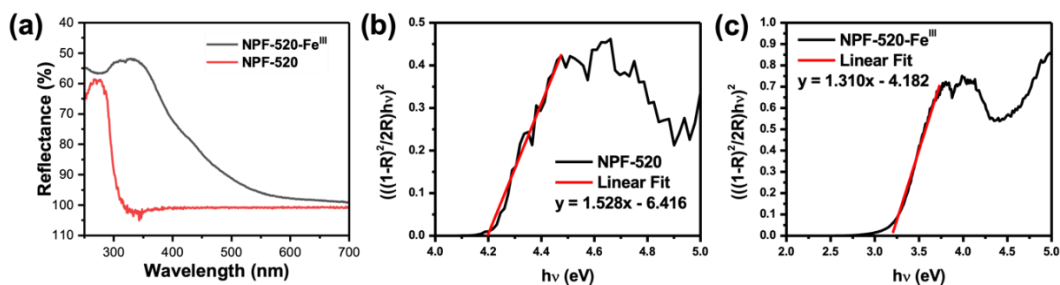


2.29 Å respectively, consistent with a structural model in which Fe1 is coordinated with two carboxylate oxygens, one  $\mu_3$ -bridging oxygen, one chloride, and one oxygen from water or hydroxide, and Fe2 is coordinated with one carboxylate oxygen, one terminal oxygen, one  $\mu_3$ -bridging oxygen, one chloride, and one oxygen from water or hydroxide (Figure 17a and b).



**Figure 17.** Model used for EXAFS fitting viewed (a) down the *c*-axis and (b) along the (1,-1,0) plane. (c) EXAFS data and fitted parameters.

The electronic structure of **NPF-520** before and after the incorporation of Fe<sup>III</sup> was also studied. UV-vis spectra show a red-shift and an enhanced visible light absorption after modification of Fe<sup>III</sup> (Figure 18a), consistent with light yellow color of the material after the modification. The band gaps estimated from the Tauc plots of **NPF-520** and **NPF-520-Fe<sup>III</sup>** are 4.20 eV and 3.19 eV respectively (Figure 18b and c).



**Figure 18.** (a) UV-vis reflectance spectra of **NPF-520** and **NPF-520-Fe<sup>III</sup>**. (b) Tauc plot for **NPF-520**. (c) Tauc plot for **NPF-520-Fe<sup>III</sup>**.

The positive slopes of the linear Mott-Schottky plots of **NPF-520** and **NPF-520-Fe<sup>III</sup>** at different frequencies indicate the n-type characteristics of semiconductor nature (Figure 19). The LUMO energy levels were determined from the intersection with the values of -0.77 V and -0.42 V vs Ag/AgCl (i.e., -0.58 V and -0.23 V vs NHE) for **NPF-320** and **NPF-320-Fe<sup>III</sup>**, respectively.<sup>53</sup>

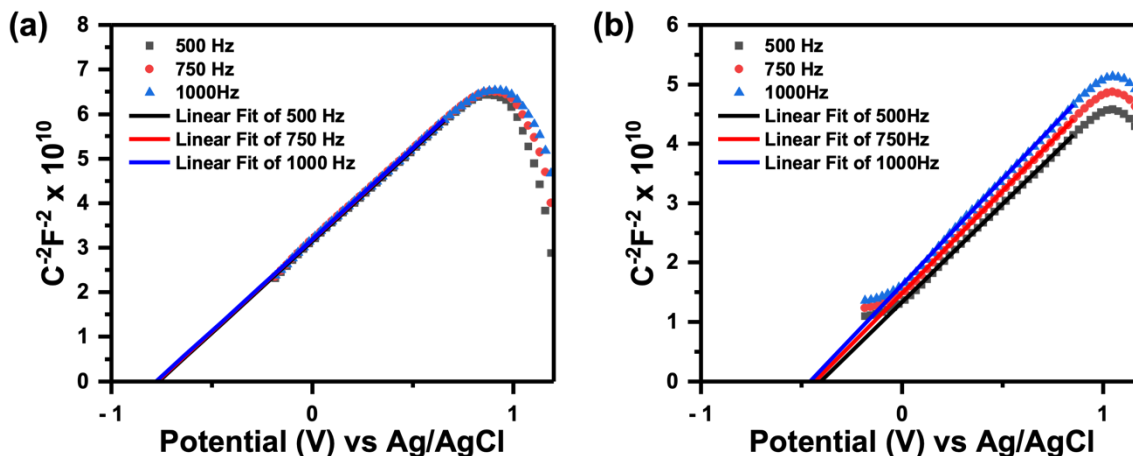


Figure 19. Mott-Schottky plots for (a) **NPF-520** and (b) **NPF-520-Fe<sup>III</sup>**.

Combined with the band gaps estimated by Tauc plots, the energy diagrams are depicted in Figure 20, which suggest that the incorporation of Fe<sup>III</sup> lowers the LUMO energy level while raising the HOMO energy level, resulting in the band gap decreasing from 4.20 eV to 3.19 eV. From a thermodynamic perspective, both MOFs have the capability for water oxidation ( $E_{\bullet\text{OH}/\text{OH}^-} = 1.89$  V vs NHE;  $E_{\text{O}_2/\text{H}_2\text{O}} = 1.23$  V vs NHE) as well as O<sub>2</sub> reduction ( $E_{\text{O}_2/\text{O}_2^{\bullet-}} = -0.16$  V),<sup>54</sup> but only **NPF-520-Fe<sup>III</sup>** has a band gap that falls close to the visible light range (1.7-3.1 eV). The band gap of 3.19 eV for **NPF-520-Fe<sup>III</sup>** is also comparable to the previously reported Fe-UiO-66 (3.02 eV) and **MOF-565-Fe** (3.09 eV).<sup>43</sup>

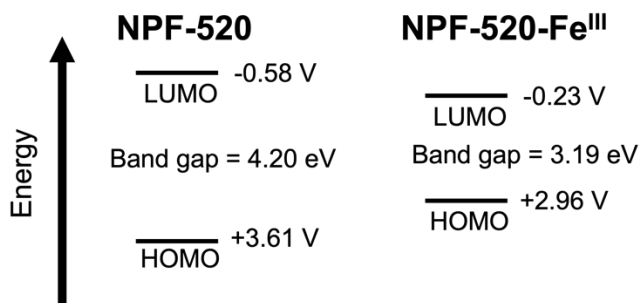


Figure 20. Energy level diagram for **MOF-565** and **MOF-565-Fe<sup>III</sup>**.

### 3.5 Photocatalytic Toluene Oxidation by MOF-565-Fe and NPF-520-Fe

UiO-66 with grafted Fe atoms on the  $Zr_6$  nodes is known to exhibit considerable activity for the photocatalytic oxidation of toluene (Figure 4, early part of chapter).<sup>43</sup> Hence, we tested **MOF-565-Fe<sup>III</sup>** and **NPF-520-Fe<sup>III</sup>** for the same reaction.

Under visible light irradiation from a blue LED photoreactor (395 nm), toluene oxidation was first carried out in the presence of 5 mol% **NPF-520-Fe<sup>III</sup>** or 1 mol% **MOF-565-Fe<sup>III</sup>** photocatalyst and O<sub>2</sub> (1 atm). To our delight, the **NPF-520-Fe<sup>III</sup>** reaction gave 100% conversion in 8 h with exclusive selectivity to benzaldehyde (entry 1, Table 1), which suggests that the absence of water prevents the complete oxidation to benzoic acid. Continuing to run the reaction for another 16 h still does not produce any detectable benzoic acid. Similarly, **MOF-565-Fe<sup>III</sup>** under the same conditions catalyzed toluene oxidation to benzaldehyde selectively (entry 9, Table 1), but with a much lower conversion of 54% after 8 h.

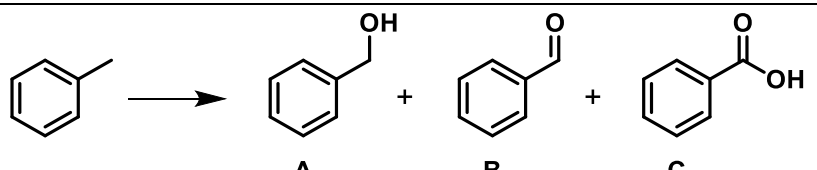
Upon the introduction of 20  $\mu$ L water into the reaction mixture benzoic acid started to emerge (6% and 100%, entries 3 and 10 for **NPF-520-Fe<sup>III</sup>** and **MOF-565-Fe<sup>III</sup>** respectively, Table 1). Complete benzoic acid selectivity for **NPF-520-Fe<sup>III</sup>** was achieved by increasing the amount of water to 100  $\mu$ L (entry 4, Table 1). The photocatalytic activity of **MOF-565-Fe<sup>III</sup>** with water added was so high, the amount of catalyst was reduced, and the substrate concentration increased (entries 10 and 11, Table 1).

To further benchmark the catalytic activity of **NPF-520-Fe<sup>III</sup>**, we synthesized two Fe<sup>III</sup>-dope Zr-MOFs, UiO-66-Fe<sup>III</sup> (1.1 Fe per  $Zr_6$  node) and UiO-69-Fe<sup>III</sup> (1.2 Fe per  $Zr_6$  node), as the comparison following the literature procedure reported by the Lin group for UiO-68-Fe.<sup>52</sup> It was noted that both UiO materials exhibited inferior activities compared to **MOF-565-Fe<sup>III</sup>** and **NPF-520-Fe<sup>III</sup>** under similar reaction conditions (entries 18-21, Table 1), suggesting that metalation of an unsaturated node containing terminal -OH/OH<sub>2</sub> groups result in higher photocatalytic activity.

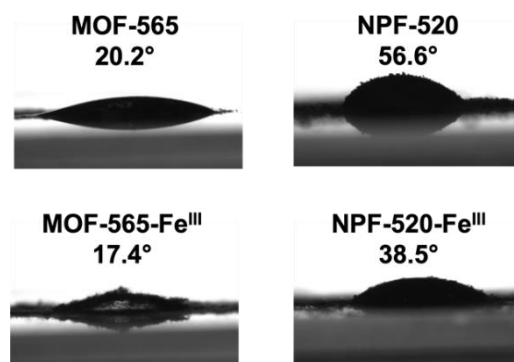
One possible reason for this is the presence of water already coordinated to the nodes, which speeds up the reaction compared to a fully saturated node where water has to diffuse into the pores of the MOF. Another possible reason is the increased exposure of the Fe single atom site to the substrates without the steric hindrance of the ligands on a fully saturated node.

Interestingly, **NPF-520-Fe<sup>III</sup>** demonstrated higher activity under anhydrous conditions than **MOF-565-Fe<sup>III</sup>**, while the photocatalytic activities were the other way round when water is present (entries 1, 3, 9, 10, Table 1). We surmise that the hydrophobicities of the MOFs might play a role in this preference, as **NPF-520-Fe<sup>III</sup>** is a lot more hydrophobic than **MOF-565-Fe<sup>III</sup>** based on water contact angle (Figure 21), which might result in a faster reaction under anhydrous conditions and slower reaction in the presence of water. At the same time, since the band gaps and HOMO/LUMO energies are relatively similar, the cause for the reactivity difference between these two MOFs should be not be a thermodynamic effect.

**Table 1. Toluene Oxidation under Different Conditions**

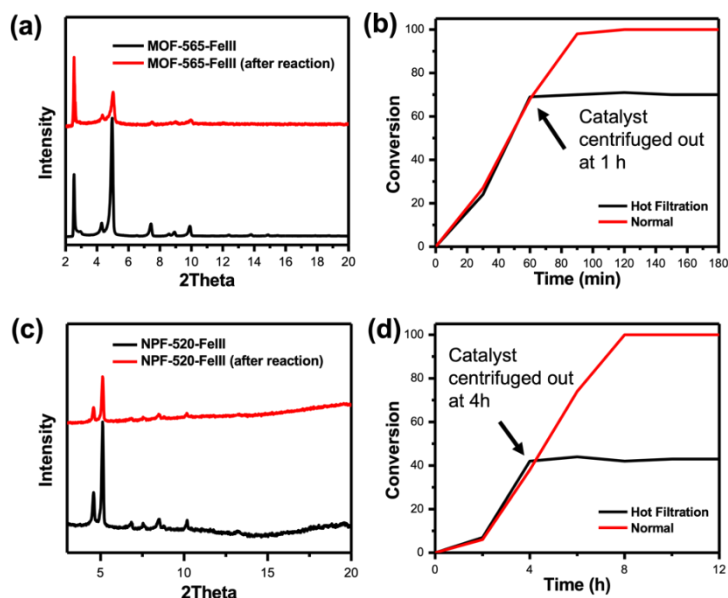
					
Entry	Catalyst	H <sub>2</sub> O/ $\mu$ L	t/h	Conversion <sup>c</sup>	Selectivity <sup>c</sup> (A/B/C)
1 <sup>a</sup>	NPF-520-Fe <sup>III</sup>	0	8	100	0/100/0
2 <sup>a</sup>		0	24	100	0/100/0
3 <sup>a</sup>		20	8	41	0/94/6
4 <sup>a</sup>		100	6	100	0/0/100
5 <sup>ad</sup>		0	8	0	-
6 <sup>ad</sup>		100	6	0	-
7 <sup>a</sup>	NPF-520	0	12	0	-
8 <sup>a</sup>		100	12	0	-
9 <sup>a</sup>	MOF-565-Fe <sup>III</sup>	0	8	54	0/100/0
10 <sup>b</sup>		20	3	100	0/0/100
11 <sup>b</sup>		100	0.5	100	0/0/100
12 <sup>bd</sup>		0	3	0	-
13 <sup>bd</sup>		100	3	0	-
14 <sup>b</sup>	MOF-565	0	12	0	-
15 <sup>b</sup>		100	12	0	-
16 <sup>a</sup>	FeCl <sub>3</sub>	0	12	0	-
17 <sup>a</sup>		100	12	0	-
18 <sup>a</sup>	UiO-66-Fe <sup>III</sup>	0	12	0	-
19 <sup>a</sup>	UiO-69-Fe <sup>III</sup>	0	12	4	0/100/0
20 <sup>a</sup>		100	12	6	0/36/64
21 <sup>a</sup>		100	12	12	0/18/82

<sup>a</sup>Reaction conditions: 5  $\mu$ L toluene, 1 mL MeCN, 5 mol% catalyst (based on Fe<sup>III</sup>), 395 nm blue LED photoreactor, 1 atm O<sub>2</sub>. <sup>b</sup>Reaction conditions: 10  $\mu$ L toluene, 1 mL MeCN, 1 mol% catalyst (based on Fe<sup>III</sup>), 395 nm blue LED photoreactor, 1 atm O<sub>2</sub>. <sup>c</sup>Determined by GC/GC-MS using a standard curve with 1  $\mu$ L chlorobenzene internal reference. <sup>d</sup>without O<sub>2</sub>.



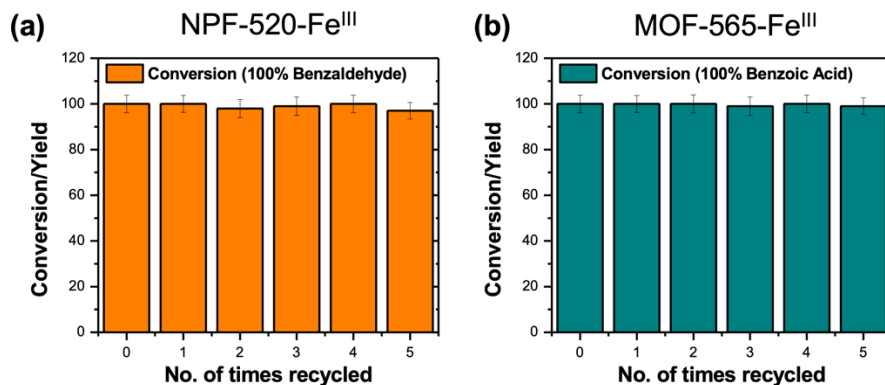
**Figure 21.** Wetting contact angles of **MOF-565** and **NPF-520** with and without Fe.

As expected, the reaction does not proceed in the absence of O<sub>2</sub> (entries 5, 6, 12, and 13, Table 1), and the unmodified **MOF-565**, **NPF-520**, and FeCl<sub>3</sub> show no catalytic activity under the same reaction conditions (entries 7, 8, 14-17, Table 1), confirming the importance of MCCT upon Fe doping for the photoactivity. PXRD patterns confirmed that the MOF structure and crystallinity was retained after the reaction (Figure 22a and 22c), and hot filtration experiments demonstrate that the oxidation catalysis occurs heterogeneously (Figure 22b and 22d) as the reaction ceased to proceed once the catalyst was removed. The ligands also do not undergo hydroxylation as indicated by the <sup>1</sup>H NMR spectrum of **MOF-565-Fe<sup>III</sup>** digested by K<sub>3</sub>PO<sub>4</sub> in D<sub>2</sub>O and **NPF-520-Fe<sup>III</sup>** digested by D<sub>2</sub>SO<sub>4</sub> in d<sub>6</sub>-DMSO (Figures S2 and S3).



**Figure 22.** (a) PXRD patterns of **MOF-565-Fe<sup>III</sup>** before and after catalysis (20  $\mu$ L water). (b) Hot filtration of **MOF-565-Fe<sup>III</sup>**. (c) PXRD patterns of **NPF-520-Fe<sup>III</sup>** before and after catalysis (anhydrous). (d) Hot filtration of **NPF-520-Fe<sup>III</sup>**.

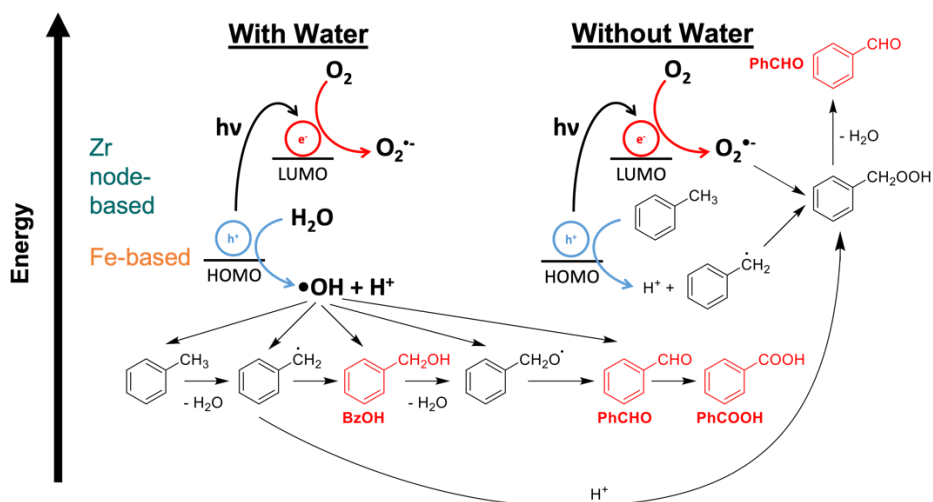
ICP-OES data indicate minor iron leaching (<1%) after the first run, but the iron content remains stable after the next 4 repetitions at room temperature (Table S3). However, leaching is severe when the catalytic reaction is heated to 50 °C in the photoreactor (5-8%). Regardless, the photocatalytic activity of the MOFs is well maintained within five consecutive runs at room temperature (Figure 23).



**Figure 23.** Catalyst recycling for (a) **NPF-520-Fe<sup>III</sup>** under anhydrous conditions and (b) **MOF-565-Fe<sup>III</sup>** with 20  $\mu$ L of water added.

### 3.6 Mechanism for Photocatalytic Toluene Oxidation by MOF-565-Fe and NPF-520-Fe

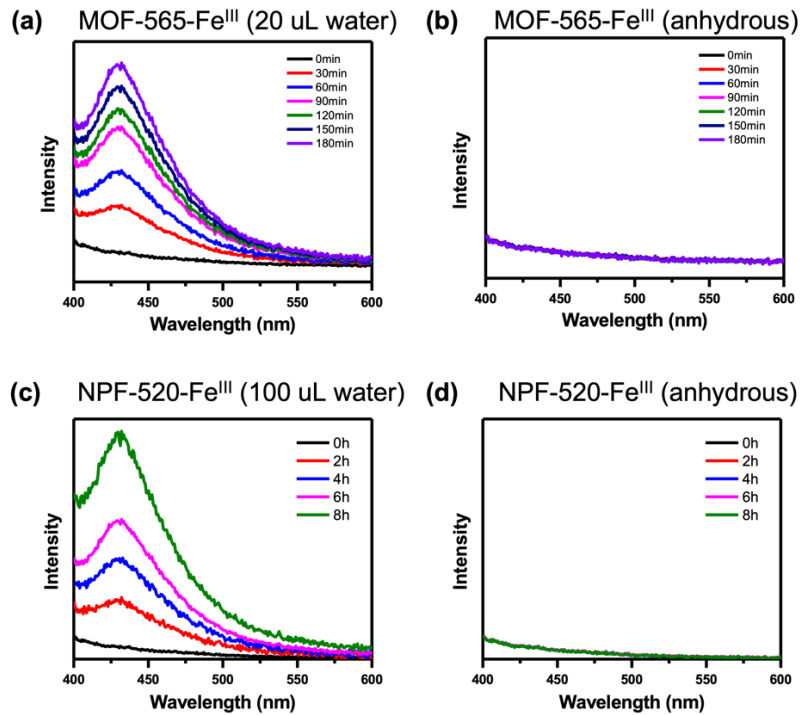
Based on the MMCT process proposed by the Jiang group,<sup>43</sup> we proposed a mechanism for the photocatalytic oxidation of toluene both in the presence of water and under anhydrous conditions (Figure 24). When water is present, the photoexcited hole is transferred to a water molecule, resulting in the formation of the hydroxyl radical  $\bullet\text{OH}$  and a proton,  $\text{H}^+$ . The photoexcited electron then reacts with  $\text{O}_2$  to form superoxide,  $\text{O}_2^{\bullet-}$ . From there, the generated reactive oxygen species (ROS),  $\bullet\text{OH}$  and  $\text{O}_2^{\bullet-}$ , can react with toluene and its partially oxidized derivatives to form benzyl alcohol (**BzOH**), benzaldehyde (**PhCHO**), and benzoic acid (**PhCOOH**).



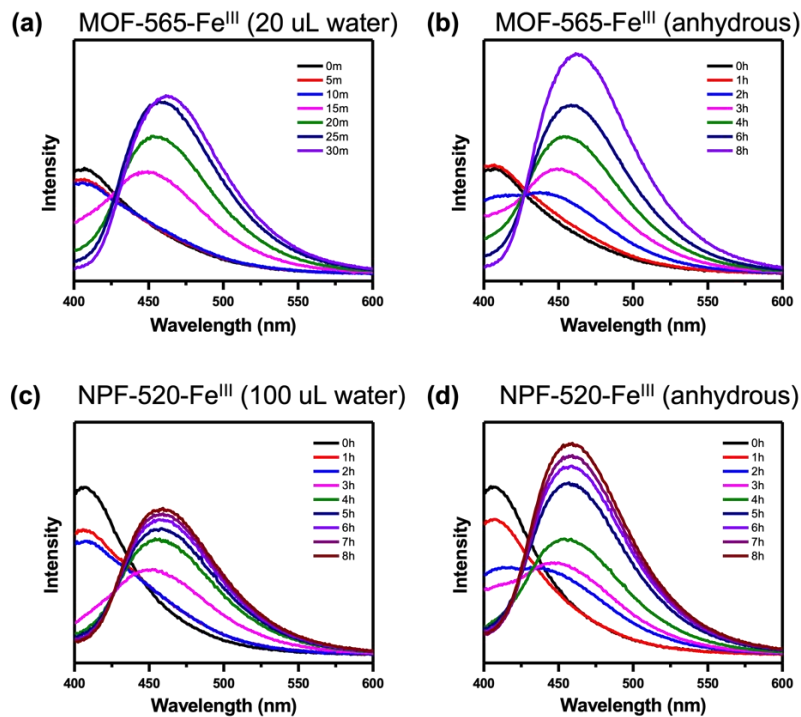
**Figure 24.** Proposed mechanism for the photocatalytic oxidation of toluene in the presence of water and under anhydrous conditions.

On the other hand, in the absence of water, the photoexcited hole can only react with toluene to form the toluene radical and a proton, which then combines with  $\text{O}_2^{\bullet-}$  to form benzaldehyde. The superoxide does not further react with benzaldehyde to form the fully oxidized product, benzoic acid, resulting in selectivity for the aldehyde product, which is observed in all cases when the photooxidation reaction is conducted under anhydrous conditions.

Since the photocatalytic reaction produces ROS such as the hydroxyl radical  $\bullet\text{OH}$  and superoxide  $\text{O}_2^{\bullet-}$ , the presence of these ROS can be detected using certain fluorescent compounds as substrates instead of toluene, such as terephthalic acid (BDC) for  $\bullet\text{OH}$  and luminol for  $\text{O}_2^{\bullet-}$ .<sup>55</sup> As expected, under anhydrous conditions, no  $\bullet\text{OH}$  was produced (Figure 25), confirming our proposed reaction mechanism where water reacts with the photoexcitation-generated hole to produce  $\bullet\text{OH}$ . On the other hand,  $\text{O}_2^{\bullet-}$  is produced whether water is present or not, confirming that  $\text{O}_2$  gas is indeed the electron acceptor.



**Figure 25.** Fluorescence of oxidized BDC with time. Peak appears at 425 nm as BDC is oxidized by hydroxyl radical  $\bullet\text{OH}$ .



**Figure 26.** Fluorescence of luminol with time. Peak shifts from 410 nm to 460 nm as luminol is oxidized by superoxide  $\text{O}_2^{\bullet-}$ .



Radical quenchers such as 2-methylfuran (singlet oxygen  $^1\text{O}_2$ ), 1,4-diazabicyclo[2.2.2]octane (DABCO,  $^1\text{O}_2$ ), 2,2,6,6-Tetramethylpiperidine 1-oxyl (TEMPO, all radicals) were also used to help identify the ROS species involved in the reaction.<sup>55</sup> According to Table 2, the addition of 2-methylfuran and DABCO did not affect the photocatalytic reaction at all, suggesting that singlet oxygen is not involved in the mechanism for both Fe-modified MOFs. On the other hand, TEMPO completely quenched the reaction, highlighting the importance of radical species in the photocatalysis.

Besides the radical quenchers, addition of sacrificial electron or hole donors were added to the reaction mixture to confirm if the oxidation was hole or electron driven, and while the sacrificial electron donor triethylamine completely quenched the reaction, the reaction proceeded in the presence of hole donor  $(\text{NH}_4)_2\text{Ce}(\text{NO}_3)_6$ , suggesting that the photooxidation is hole-driven.

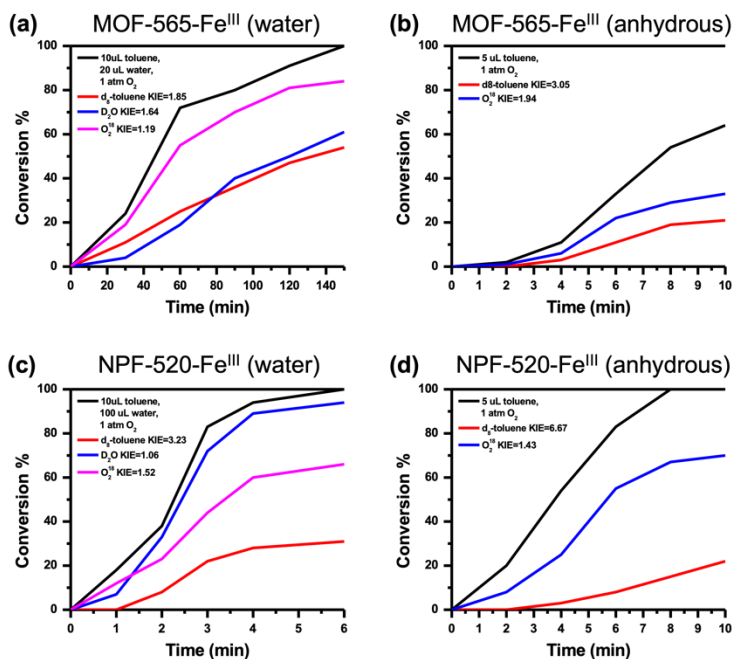
Finally, hydrogen peroxide ( $\text{H}_2\text{O}_2$ ) was used to check if the Fenton reaction is the main force driving the reaction. As expected, the Fenton reaction is not the dominant reaction driving the toluene oxidation, as the conversion in the presence of  $\text{H}_2\text{O}_2$  is minimal.

**Table 2. Photocatalytic toluene oxidation in the presence of quenching agents.**

Entry	Catalyst	Additive	Conversion <sup>c</sup>	Selectivity <sup>c</sup> (A/B/C)
1 <sup>a</sup>	<b>NPF-520-Fe<sup>III</sup></b>	2-methylfuran	100	0/0/100
2 <sup>a</sup>		DABCO	100	0/0/100
3 <sup>a</sup>		TEMPO	0	-
4 <sup>a</sup>		triethylamine	0	-
5 <sup>a</sup>		$(\text{NH}_4)_2\text{Ce}(\text{NO}_3)_6$	73	6/91/3
6 <sup>ad</sup>		$\text{H}_2\text{O}_2$	4	0/100/0
7 <sup>b</sup>	<b>MOF-565-Fe<sup>III</sup></b>	2-methylfuran	100	0/0/100
8 <sup>b</sup>		DABCO	100	0/0/100
9 <sup>b</sup>		TEMPO	0	-
10 <sup>b</sup>		triethylamine	0	-
11 <sup>b</sup>		$(\text{NH}_4)_2\text{Ce}(\text{NO}_3)_6$	50	5/85/10
12 <sup>bd</sup>		$\text{H}_2\text{O}_2$	12	0/100/0

<sup>a</sup>Reaction conditions: 5  $\mu\text{L}$  toluene, 1 mL MeCN, 5 mol% catalyst (based on Fe<sup>III</sup>), 395 nm blue LED photoreactor, 8 h, 1 atm O<sub>2</sub>. <sup>b</sup>Reaction conditions: 10  $\mu\text{L}$  toluene, 1 mL MeCN, 1 mol% catalyst (based on Fe<sup>III</sup>), 395 nm blue LED photoreactor, 3 h, 1 atm O<sub>2</sub>. <sup>c</sup>Determined by GC/GC-MS using a standard curve with 1  $\mu\text{L}$  chlorobenzene internal reference. <sup>d</sup>1 atm N<sub>2</sub> instead of O<sub>2</sub>.

Finally, the kinetic isotope effect (KIE) was studied to determine the rate-limiting step in the photooxidation of toluene (Figure 27). KIE refers to the change in the reaction rate when one or more of the reactant atoms is replaced by its isotope, and reactions tend to be slowed when heavier isotopes are used, due to an increase in the amount of energy needed to break the bond. A KIE significantly larger or smaller than 1 indicates an isotope effect, whereas a KIE of 1 shows that there is no effect, likely because the bond breaking does not affect the reaction kinetics, or the bond is not broken at all during the reaction.



**Figure 27.** Kinetic plots and KIE of toluene oxidation by **MOF-565-Fe<sup>III</sup>** and **NPF-520-Fe<sup>III</sup>** in the presence of water and under anhydrous conditions.

In all cases, switching toluene to deuterated toluene demonstrated the largest KIE (1.85-6.67), meaning that the C-H bond activation is the rate-limiting step regardless of the photocatalyst used or the reaction conditions. When water is present in the reaction, **MOF-565-Fe<sup>III</sup>** exhibited a much larger KIE than **NPE-520-Fe<sup>III</sup>** even with 5 times less water added (Figure 27a and 27c), demonstrating that water has a much larger impact on the reaction rate for **MOF-565-Fe<sup>III</sup>**. This brings us back to our proposal that the hydrophobicity of the MOF plays a huge role in the photocatalytic oxidation of toluene, and the hydrophilic **MOF-565-Fe<sup>III</sup>** toluene oxidation depends much more on hole-to-water oxidation to the hydroxy radical than **NPE-520-Fe<sup>III</sup>**.

In the absence of water, hole-to-toluene oxidation instead occurs to produce the toluene radical, which then reacts with ROS such as superoxide to form benzaldehyde. As expected, Figure 27b and 27d show that under anhydrous conditions, the rate-limiting effect of toluene is

even greater than with water present, with KIE of 3.05 and 6.67 versus 1.85 and 3.23 for **MOF-565-Fe<sup>III</sup>** and **NPF-520-Fe<sup>III</sup>**, respectively.

Finally, although O<sup>18</sup><sub>2</sub> shows a KIE of more than 1 for all reactions, indicating that O-O bond breaking is crucial to the reaction, especially under anhydrous conditions, it is not the predominant rate-limiting step.

### 3.7 Conclusions

In summary, we report the successful synthesis and characterization of a new Zr-MOF, **NPF-520**, containing the recently discovered  $Zr_9$  node, using a tetrahedral bicarbonate linker. The  $Zr_9$  nodes of this MOF, along with  $Zr_6$  nodes in **MOF-565** that was shown in Chapter 2, were used as supports for the installation of Fe single atom sites.

The installation of  $Fe^{III}$  onto **MOF-565** and **NPF-520** supports using a base-assisted method gave rise to **MOF-565- $Fe^{III}$**  and **NPF-520- $Fe^{III}$**  respectively. In both MOFs,  $Fe^{III}$  was found to coordinate strongly to the nodes in a 5-coordinate trigonal pyramidal geometry, utilizing the terminal -OH/ $OH_2$  groups on the nodes, the bridging  $\mu_3-O$ , and the O on the linker carboxylates as anchors.

The addition of  $Fe^{III}$  single atom sites gave rise to a metal-to-cluster charge transfer (MCCT) transition, which has a band gap within the visible light range, and upon visible light irradiation, catalyzed the photooxidation of toluene both in the presence of water and under anhydrous conditions. In particular, the reaction under anhydrous conditions produced exclusively benzaldehyde, which is commonly used as food flavoring and as precursors to many other organic compounds of industrial importance.

An investigation of the photocatalysis then revealed the presence of the ROS  $\bullet OH$  and  $O_2^{\bullet -}$ , which react with toluene to form its oxidized products, mainly benzaldehyde and benzoic acid depending on whether water is absent or present, respectively. Furthermore, we showed that neither  $^1O_2$  nor  $H_2O_2$  were responsible for the excellent catalytic activity, and that the process is mainly hole-driven, with the C-H bond breaking of toluene being the rate-limiting step.

Moving forward, we are interested in the anchoring of different metals onto MOF supports, in particular **NPF-520** with its  $Zr_9$  node, and investigating the difference in chemical and physical properties arising from the different Zr clusters. Varying the saturation of the  $Zr_6$  node is yet another interesting direction to pursue in the pursuit of the optimal heterogeneous catalysts for industrial, environmental, and biomedical applications.

### 3.8 Materials and Methods

**Starting Materials.** All reactions and manipulations were carried out in air inside a fumehood unless otherwise indicated. All starting materials were purchased from Sigma-Aldrich, Combi-Blocks, and TCI (USA) and used without further purification.

**Single Crystal X-ray Diffraction.** Data was collected using synchrotron radiation at the Advanced Light Source, beamline 12.2.1, at Lawrence Berkeley National Laboratory, Berkeley, CA, USA. Indexing was performed using APEX3 (Difference Vectors method). Data integration and reduction were performed using SaintPlus 6.0. Absorption correction was performed by multi-scan method implemented in SADABS. Space groups were determined using XPREP implemented in APEX3. The structure was solved using SHELXT 2018/2 and refined using SHELXL 2018/3 within Olex 2 (full-matrix least-squares on  $F^2$ ). Zr, Cu, C, O, and N atoms were refined with anisotropic displacement parameters and H atoms were placed in geometrically calculated positions and included in the refinement process using riding model with isotropic thermal parameters:  $U_{iso}(H) = 1.2U_{eq}(-CH)$ . The disordered solvent molecules were treated as diffuse using the SQUEEZE procedure implemented in PLATON. Crystal data and refinement details are shown in Table SX. This data can be obtained free of charge from The Cambridge Crystallographic Data Centre via [www.ccdc.cam.ac.uk/data\\_request/cif](http://www.ccdc.cam.ac.uk/data_request/cif).

**Powder X-Ray Diffraction (PXRD) Measurements.** PXRD data were collected by using a Rigaku X-ray diffractometer with Cu  $K\alpha$  radiation at 40 kV and 20 mA.

**$^1H$  NMR Spectra.**  $^1H$  spectra were recorded on an AVANCE II 500 (Bruker, Germany).

**Gas Sorption Measurements.** Gas adsorption isotherms were performed on the surface area analyzer ASAP-2020.  $N_2$  gas adsorption isotherms were measured at 77 K using a liquid  $N_2$  bath.

**Scanning Electron Microscope.** SEM images and EDS data were collected on a tabletop Phenom ProX equipped with the Element Identification (EID) software package and a specially designed and fully integrated Energy Dispersive Spectrometer (EDS).

**Inductively Coupled Plasma-Optical Emission Spectrometry.** ICP-OES, performed on a Varian ICP-OES 720 Series, was used to quantify the ratio of the MOF metal and the grafted metal. Samples were digested in piranha overnight with stirring and diluted with 2 wt%  $HNO_3$  before ICP measurement. 1000 ppm zirconium and iron standard solutions (Sigma Aldrich) was used to prepare diluted standards with metal concentrations ranging from 0.1 to 10 ppm.

**Fourier transform infrared (FTIR) Spectra.** FTIR spectra were recorded on the Nicolet iS50 FT-IR system (Thermo Fisher, USA).

**UV-visible Spectroscopy.** UV-visible diffuse reflectance data were taken using a Cary 5000 spectrometer with an internal diffuse reflectance accessory.

**X-ray absorption (XAS).** XAS spectra were measured at the beamline 12BM-B at the Advanced Photon Source in Argonne National Laboratory. The XAS spectra were collected under room temperature with fluorescence mode. The detector was based on 13-element germanium. One ion chamber is placed before the sample and used as the incident X-ray flux reference signal. There are two ion chambers (second and third chambers) after the sample.

**Contact angle.** A Kudos DropMeter A-200 was used to collect the images for contact angle measurement. 5  $\mu$ L of water was gently placed on a glass slide with a thin layer of MOF formed by drop casting, and then drying in air overnight.

**Photoluminescence.** A Quantaaurus-QY Plus UV-NIR absolute PL quantum yield spectrometer was used to measure the fluorescence spectra. Equivalent 100  $\mu$ L volumes of sample were removed from the ongoing reaction using a syringe, then diluted to 1 mL and filtered through a syringe filter before measurement.

**X-ray Photoelectron Spectroscopy.** A Thermo-Fisher K-Alpha Plus XPS with a monochromatic Al X-Ray source (1.486 eV), energy resolution and spatial resolution of 0.7 eV and 30 mm respectively was used to obtain the quantitative chemical analysis of the MOF surfaces.

## Synthesis.

**1,4-Dimethyl-2,3,5,6-tetraphenylbenzene.** In a 50 mL round bottom flask, a stirred mixture of 2,5-dimethyl-3,4-diphenylcyclopentadienone (1 g, 1.92 mmol) and diphenylacetylene (1 g, 5.61 mmol) in diphenyl ether (2.5 mL) was heated under reflux for 4h. During this period of time, the mixture changed to deep red and then faded to orange. Slow cooling at room temperature and then at 0°C yielded crystals after 30 min, which were collected by filtration, washed with hexane and dried in an oven, giving 1,4-dimethyl-2,3,5,6-tetraphenylbenzene (1.22 g, 2.97 mmol, 77%) as a light orange solid. <sup>1</sup>H NMR (500 MHz, CDCl<sub>3</sub>): 7.15 (m, 8H), 7.07 (m, 12H), 1.80 (s, 6H).

**H<sub>4</sub>L.** A 50 mL double neck round bottom flask was dried using a heat gun under N<sub>2</sub> flow, where compound 1 (1.06 g, 2.58 mmol) was dissolved in anhydrous CH<sub>2</sub>Cl<sub>2</sub> (20 ml) and placed under N<sub>2</sub> atmosphere on a Schlenk line. The solution was cooled down to 0 °C, then oxalyl chloride (2.5 ml, 25.8 mmol) and AlCl<sub>3</sub> (1.7 g, 12.7 mmol) were added. During the last addition, the color of the solution changed from brown to black. The mixture was stirred for 90 min at 0 °C before additional AlCl<sub>3</sub> (1.5 g, 11.2 mmol) was added and stirred for another 18 h. After this period of time the mixture was transferred in a 50 ml beaker containing ice (25 ml), where light yellow solid was precipitated. The mixture was acidified with 3 M HCl, until pH = 3. The CH<sub>2</sub>Cl<sub>2</sub> was evaporated under vacuum and the solid was collected by filtration, washed with water and dried in an oven overnight. (1.3 g, 2.22 mmol, 86 %). <sup>1</sup>H NMR (500 MHz, DMSO-d<sub>6</sub>): 12.94 (s, 4H), 7.74 (d, 8H), 7.23 (d, 8H), 1.67 (s, 6H).

**MOF-565 (single crystal).** A solution of 500 μL DMF, 50 μL formic acid, and 14.0 mg ZrCl<sub>4</sub> was added to another solution of 500 μL DMF, 850 μL formic acid, 120 mg benzoic acid and 6.0 mg of H<sub>4</sub>L in a 4 mL glass vial. The vial was sealed and placed in an isothermal oven at 120°C for 3 days to form large hexagonal colorless rod crystals (46% crude yield based on H<sub>4</sub>L). The MOF was stirred in a 0.1M HCl 10:1 H<sub>2</sub>O:MeOH solution at room temperature overnight to remove the excess formate groups on the clusters, then washed and centrifuged 3 times with 10:1 H<sub>2</sub>O:MeOH, 3 times with acetone, and dried under vacuum at 100°C to give 32% yield based on H<sub>4</sub>L.

**MOF-565 (large scale).** A solution of 50 mL DMF, 5 mL formic acid, and 1.40 g ZrCl<sub>4</sub> was added to another solution of 50 mL DMF, 8.5 μL formic acid, 12 g benzoic acid and 600 mg of H<sub>4</sub>L in a 250 mL bottle. The bottle was sealed and placed in an isothermal oven at 120°C for 3 days to form small colorless needles, then washed in a similar manner as the single-crystal MOF sample (28% yield based on H<sub>4</sub>L).

1 mg of MOF was digested in D<sub>2</sub>O saturated with K<sub>3</sub>PO<sub>4</sub> at 120°C for 24h for <sup>1</sup>H NMR.

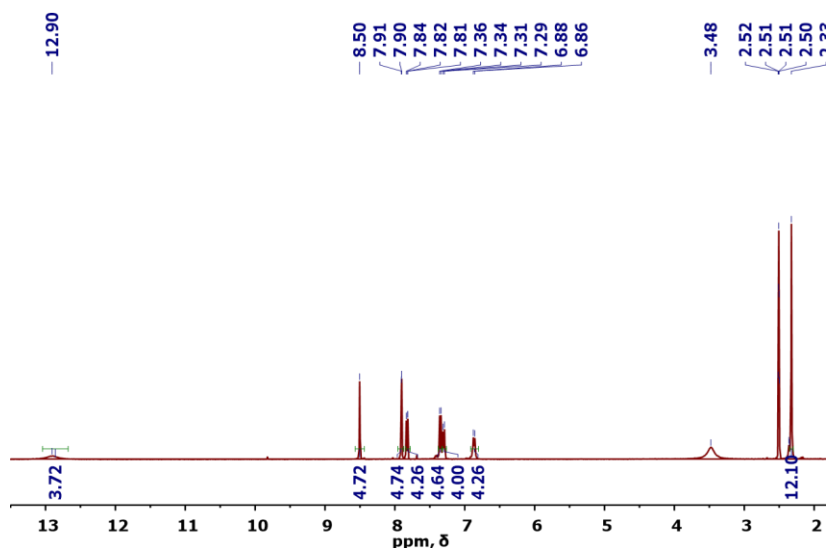
**3,3',6,6'-tetrabromo-N,N'-bicarbazole (1).** Synthesized according to literature without modification.<sup>56</sup>

**Hexyl 3-methyl-4-(4,4,5,5-tetramethyl-1,3,2-dioxaborolan-2-yl)benzoate (2).** Synthesized according to literature without modification,<sup>57</sup> with the exception that hexyl 4-bromo-3-

methylbenzoate was used as the starting material.  $^1\text{H}$  NMR (400 MHz,  $\text{CDCl}_3$ )  $\delta$  7.89 – 7.76 (m, 3H), 4.33 (t,  $J$  = 6.7 Hz, 2H), 2.60 (s, 3H), 1.84 – 1.73 (m, 2H), 1.51 – 1.32 (m, 18H), 0.92 (dd,  $J$  = 9.7, 4.5 Hz, 3H).

**Tetrahexyl 4,4',4'',4'''-([9,9'-bicarbazole]-3,3',6,6'-tetrayl)tetrakis(3-methylbenzoate) (3).** Compound **1** (2.5 g, 3.86 mmol),  $\text{K}_3\text{PO}_4$  (9.8 g, 46.3 mmol), compound **2**, (8.0 g, 23.1 mmol) and  $\text{Pd}(\text{dppf})\text{Cl}_2$  (0.282 g, 0.38 mmol) were charged in a 250 mL 2-neck round bottom flask equipped with a magnetic stir bar. Dioxane (90 mL) and water (15 mL) was added, and the mixture was degassed by sparging with argon for 35 min. The flask was capped and heated to  $95^\circ\text{C}$  under inert atmosphere for 72 h. After cooling down to room temperature, the reaction mixture was extracted into chloroform (150 mL  $\times$  2) and washed with brine (100 mL). The organic fractions were collected, dried with  $\text{MgSO}_4$ , concentrated and subject to column chromatography ( $\text{CH}_2\text{Cl}_2$ : Hexanes = 9:1). The fractions were concentrated and dried under vacuum to afford compound **5** as an off-white solid (3.7 g, yield: 79%).  $^1\text{H}$  NMR (400 MHz,  $\text{CDCl}_3$ )  $\delta$  8.19 (d,  $J$  = 1.2 Hz, 1H), 8.02 (s, 1H), 7.97 (dd,  $J$  = 7.9, 1.5 Hz, 1H), 7.45 (d,  $J$  = 8.0 Hz, 1H), 7.40 (dd,  $J$  = 8.4, 1.6 Hz, 1H), 7.14 (d,  $J$  = 8.3 Hz, 1H), 4.37 (t,  $J$  = 6.7 Hz, 2H), 2.44 (s, 3H), 1.81 (dd,  $J$  = 14.7, 6.9 Hz, 2H), 1.55 – 1.44 (m, 2H), 1.43 – 1.34 (m, 5H), 0.99 – 0.88 (m, 4H).

**4,4',4'',4'''-([9,9'-bicarbazole]-3,3',6,6'-tetrayl)tetrakis(3-methylbenzoic acid) ( $\text{H}_4\text{L}_2$ ).** Compound **3** (3 g, 2.48 mmol) was dissolved in 100 mL of THF to which 100 mL of 1 M KOH was added. The resulting suspension was stirred under reflux for 48 h. After cooling down to room temperature, the organic solvent was removed in vacuo. The aqueous phase was reprecipitated with 5 M HCl until pH = 2 was reached. The precipitate was filtered, washed with 200 mL of  $\text{H}_2\text{O}$  and dried under vacuum to give  $\text{H}_4\text{L}$  as a colorless solid (1.8 g, yield: 83%).  $^1\text{H}$  NMR (400 MHz, DMSO)  $\delta$  12.90 (s, 4H), 8.50 (s, 5H), 7.90 (d,  $J$  = 1.3 Hz, 5H), 7.84 – 7.78 (m, 4H), 7.35 (d,  $J$  = 7.9 Hz, 5H), 7.30 (d,  $J$  = 8.5 Hz, 4H), 6.87 (d,  $J$  = 8.2 Hz, 4H), 2.34 (d,  $J$  = 10.1 Hz, 12H).



$^1\text{H}$  NMR Spectrum of  $\text{H}_4\text{L}_2$ .



**NPF-520.**  $\text{ZrCl}_4$  (5.5 mg), and acetic acid (170  $\mu\text{L}$ ) were ultrasonically dissolved in 1 mL DMF in a 1-dram vial. The clear solution was heated in an 80°C oven. After 1 h, **H4L2** (3 mg), added and sonicated for 5 min. The mixture was heated in a 120°C oven for 24 h. After slowly cooling down to room temperature, colorless trigonal-shaped crystals were present at the bottom of the vial.

**MOF-565-Fe.** In a  $\text{N}_2$ -filled glovebox,  $\text{TMSCH}_2\text{Li}$  (1.0 M in pentane, 0.2 mL, 20 equiv. w.r.t.  $\text{Zr}_6$ ) was added dropwise to a cold suspension of **MOF-565** (0.02 mmol  $\text{Zr}_6$ ) in 20 mL hexanes, and the resultant white suspension was stirred at room temperature for 2 h. The solid was collected through centrifugation and washed with hexanes three times to remove soluble residue. ICP-MS results showed a  $\text{Li}/\text{Zr}_6$  ratio of 10.9, indicating almost complete lithiation (90%). The resultant **MOF-565-Li** was then transferred to a vial containing 20 mL of  $\text{FeCl}_3$  solution (10 mM) in anhydrous  $\text{CH}_3\text{CN}$ . After stirring at room temperature for 2 h, the yellow solid was centrifuged and sonicated with  $\text{CH}_3\text{CN}$  three times. ICP-OES analysis gave a  $\text{Fe}/\text{Zr}_6$  ratio of 4.0, indicating 4.0 Fe per  $\text{Zr}_6$  node.

**NPF-520-Fe.** **NPF-520-Fe** was synthesized using the same method as **MOF-565-Fe**. ICP-OES analysis gave a  $\text{Fe}/\text{Zr}_9$  ratio of 3.2, indicating 3.2 Fe per  $\text{Zr}_9$  node.

### 3.9 References

1. Schlogl, R., Heterogeneous catalysis. *Angew. Chem. Int. Ed.* **2015**, *54* (11), 3465-520.
2. Ma, Z.; Zaera, F., *Heterogeneous Catalysis by Metals*. John Wiley & Sons, Ltd: 2006.
3. Rothenberg, G., *Catalysis : concepts and green applications*. Wiley-VCH: Weinheim, 2008.
4. Comotti, M.; Li, W. C.; Spliethoff, B.; Schuth, F., Support effect in high activity gold catalysts for CO oxidation. *J. Am. Chem. Soc.* **2006**, *128* (3), 917-24.
5. Zhang, S.; Chen, L.; Qi, Z.; Zhuo, L.; Chen, J. L.; Pao, C. W.; Su, J.; Somorjai, G. A., Insights into the Mechanism of n-Hexane Reforming over a Single-Site Platinum Catalyst. *J. Am. Chem. Soc.* **2020**, *142* (39), 16533-16537.
6. Yang, X. F.; Wang, A.; Qiao, B.; Li, J.; Liu, J.; Zhang, T., Single-atom catalysts: A new frontier in heterogeneous catalysis. *Acc. Chem. Res.* **2013**, *46* (8), 1740-1748.
7. Furukawa, H.; Cordova, K. E.; O'Keeffe, M.; Yaghi, O. M., The chemistry and applications of metal-organic frameworks. *Science* **2013**, *341* (6149), 1230444.
8. Cook, T. R.; Zheng, Y. R.; Stang, P. J., Metal-organic frameworks and self-assembled supramolecular coordination complexes: comparing and contrasting the design, synthesis, and functionality of metal-organic materials. *Chem. Rev.* **2013**, *113* (1), 734-77.
9. Zhou, H. C.; Kitagawa, S., Metal-organic frameworks (MOFs). *Chem. Soc. Rev.* **2014**, *43* (16), 5415-8.
10. Li, B.; Wen, H. M.; Cui, Y.; Zhou, W.; Qian, G.; Chen, B., Emerging Multifunctional Metal-Organic Framework Materials. *Adv. Mater.* **2016**, *28* (40), 8819-8860.
11. Islamoglu, T.; Goswami, S.; Li, Z.; Howarth, A. J.; Farha, O. K.; Hupp, J. T., Postsynthetic Tuning of Metal-Organic Frameworks for Targeted Applications. *Acc. Chem. Res.* **2017**, *50* (4), 805-813.
12. Zhu, L.; Liu, X. Q.; Jiang, H. L.; Sun, L. B., Metal-Organic Frameworks for Heterogeneous Basic Catalysis. *Chem Rev* **2017**, *117* (12), 8129-8176.
13. Wang, C.; An, B.; Lin, W., Metal–Organic Frameworks in Solid–Gas Phase Catalysis. *ACS Catal.* **2018**, 130-146.
14. Dhakshinamoorthy, A.; Li, Z.; Garcia, H., Catalysis and photocatalysis by metal organic frameworks. *Chem. Soc. Rev.* **2018**, *47* (22), 8134-8172.
15. Bavykina, A.; Kolobov, N.; Khan, I. S.; Bau, J. A.; Ramirez, A.; Gascon, J., Metal-Organic Frameworks in Heterogeneous Catalysis: Recent Progress, New Trends, and Future Perspectives. *Chem Rev* **2020**, *120* (16), 8468-8535.
16. Liu, J.; Goetjen, T. A.; Wang, Q.; Knapp, J. G.; Wasson, M. C.; Yang, Y.; Syed, Z. H.; Delferro, M.; Notestein, J. M.; Farha, O. K.; Hupp, J. T., MOF-enabled confinement and related effects for chemical catalyst presentation and utilization. *Chem Soc Rev* **2022**, 1045-97.
17. Pattengale, B.; Yang, S.; Ludwig, J.; Huang, Z.; Zhang, X.; Huang, J., Exceptionally Long-Lived Charge Separated State in Zeolitic Imidazolate Framework: Implication for Photocatalytic Applications. *J. Am. Chem. Soc.* **2016**, *138* (26), 8072-5.
18. Wang, X.; Zhang, X.; Li, P.; Otake, K. I.; Cui, Y.; Lyu, J.; Krzyaniak, M. D.; Zhang, Y.; Li, Z.; Liu, J.; Buru, C. T.; Islamoglu, T.; Wasielewski, M. R.; Li, Z.; Farha, O. K., Vanadium Catalyst on Isostructural Transition Metal, Lanthanide, and Actinide Based Metal-Organic Frameworks for Alcohol Oxidation. *J. Am. Chem. Soc.* **2019**, *141* (20), 8306-8314.

19. Babucci, M.; Guntida, A.; Gates, B. C., Atomically Dispersed Metals on Well-Defined Supports including Zeolites and Metal-Organic Frameworks: Structure, Bonding, Reactivity, and Catalysis. *Chem Rev* **2020**, *120* (21), 11956-11985.
20. He, X.; Looker, B. G.; Dinh, K. T.; Stubbs, A. W.; Chen, T.; Meyer, R. J.; Serna, P.; Román-Leshkov, Y.; Lancaster, K. M.; Dincă, M., Cerium(IV) Enhances the Catalytic Oxidation Activity of Single-Site Cu Active Sites in MOFs. *ACS Catal.* **2020**, *10* (14), 7820-7825.
21. Chen, C.; Alalouni, M. R.; Dong, X.; Cao, Z.; Cheng, Q.; Zheng, L.; Meng, L.; Guan, C.; Liu, L.; Abou-Hamad, E.; Wang, J.; Shi, Z.; Huang, K. W.; Cavallo, L.; Han, Y., Highly Active Heterogeneous Catalyst for Ethylene Dimerization Prepared by Selectively Doping Ni on the Surface of a Zeolitic Imidazolate Framework. *J. Am. Chem. Soc.* **2021**, *143* (18), 7144-7153.
22. Ockwig, N. W.; Delgado-Friedrichs, O.; O'Keeffe, M.; Yaghi, O. M., Reticular chemistry: occurrence and taxonomy of nets and grammar for the design of frameworks. *Acc. Chem. Res.* **2005**, *38* (3), 176-82.
23. Bai, Y.; Dou, Y.; Xie, L. H.; Rutledge, W.; Li, J. R.; Zhou, H. C., Zr-based metal-organic frameworks: design, synthesis, structure, and applications. *Chem. Soc. Rev.* **2016**, *45* (8), 2327-67.
24. Otake, K. I.; Cui, Y.; Buru, C. T.; Li, Z.; Hupp, J. T.; Farha, O. K., Single-Atom-Based Vanadium Oxide Catalysts Supported on Metal-Organic Frameworks: Selective Alcohol Oxidation and Structure-Activity Relationship. *J. Am. Chem. Soc.* **2018**, *140* (28), 8652-8656.
25. Hackler, R. A.; Pandharkar, R.; Ferrandon, M. S.; Kim, I. S.; Vermeulen, N. A.; Gallington, L. C.; Chapman, K. W.; Farha, O. K.; Cramer, C. J.; Sauer, J.; Gagliardi, L.; Martinson, A. B. F.; Delferro, M., Isomerization and Selective Hydrogenation of Propyne: Screening of Metal-Organic Frameworks Modified by Atomic Layer Deposition. *J. Am. Chem. Soc.* **2020**, 20380-20389.
26. Yang, Y.; Zhang, X.; Kanchanakungwankul, S.; Lu, Z.; Noh, H.; Syed, Z. H.; Farha, O. K.; Truhlar, D. G.; Hupp, J. T., Unexpected "Spontaneous" Evolution of Catalytic, MOF-Supported Single Cu(II) Cations to Catalytic, MOF-Supported Cu(0) Nanoparticles. *J. Am. Chem. Soc.* **2020**, *142* (50), 21169-21177.
27. Ma, X.; Liu, H.; Yang, W.; Mao, G.; Zheng, L.; Jiang, H. L., Modulating Coordination Environment of Single-Atom Catalysts and Their Proximity to Photosensitive Units for Boosting MOF Photocatalysis. *J. Am. Chem. Soc.* **2021**, *143* (31), 12220-12229.
28. Ye, G.; Wang, H.; Chen, W.; Chu, H.; Wei, J.; Wang, D.; Wang, J.; Li, Y., In Situ Implanting of Single Tungsten Sites into Defective UiO-66(Zr) by Solvent-Free Route for Efficient Oxidative Desulfurization at Room Temperature. *Angew Chem Int Ed Engl* **2021**, *60* (37), 20318-20324.
29. Zhao, W.; Shi, Y.; Jiang, Y.; Zhang, X.; Long, C.; An, P.; Zhu, Y.; Shao, S.; Yan, Z.; Li, G.; Tang, Z., Fe-O Clusters Anchored on Nodes of Metal-Organic Frameworks for Direct Methane Oxidation. *Angew Chem Int Ed Engl* **2021**, *60* (11), 5811-5815.
30. Chen, Y.; Ahn, S.; Mian, M. R.; Wang, X.; Ma, Q.; Son, F. A.; Yang, L.; Ma, K.; Zhang, X.; Notestein, J. M.; Farha, O. K., Modulating Chemical Environments of Metal-Organic Framework-Supported Molybdenum(VI) Catalysts for Insights into the Structure-Activity Relationship in Cyclohexene Epoxidation. *J. Am. Chem. Soc.* **2022**, *144* (8), 3554-3563.
31. Nguyen, H. G. T.; Schweitzer, N. M.; Chang, C.-Y.; Drake, T. L.; So, M. C.; Stair, P. C.; Farha, O. K.; Hupp, J. T.; Nguyen, S. T., Vanadium-Node-Functionalized UiO-66: A Thermally Stable MOF-Supported Catalyst for the Gas-Phase Oxidative Dehydrogenation of Cyclohexene. *ACS Catalysis* **2014**, *4* (8), 2496-2500.

32. Yuan, S.; Chen, Y. P.; Qin, J.; Lu, W.; Wang, X.; Zhang, Q.; Bosch, M.; Liu, T. F.; Lian, X.; Zhou, H. C., Cooperative Cluster Metalation and Ligand Migration in Zirconium Metal-Organic Frameworks. *Angew. Chem. Int. Ed.* **2015**, *54* (49), 14696-700.
33. Yang, D.; Odoh, S. O.; Borycz, J.; Wang, T. C.; Farha, O. K.; Hupp, J. T.; Cramer, C. J.; Gagliardi, L.; Gates, B. C., Tuning Zr<sub>6</sub> Metal–Organic Framework (MOF) Nodes as Catalyst Supports: Site Densities and Electron-Donor Properties Influence Molecular Iridium Complexes as Ethylene Conversion Catalysts. *ACS Catal.* **2015**, *6* (1), 235-247.
34. Manna, K.; Ji, P.; Greene, F. X.; Lin, W., Metal-Organic Framework Nodes Support Single-Site Magnesium-Alkyl Catalysts for Hydroboration and Hydroamination Reactions. *J. Am. Chem. Soc.* **2016**, *138* (24), 7488-91.
35. Li, Z.; Peters, A. W.; Bernales, V.; Ortuno, M. A.; Schweitzer, N. M.; DeStefano, M. R.; Gallington, L. C.; Platero-Prats, A. E.; Chapman, K. W.; Cramer, C. J.; Gagliardi, L.; Hupp, J. T.; Farha, O. K., Metal-Organic Framework Supported Cobalt Catalysts for the Oxidative Dehydrogenation of Propane at Low Temperature. *ACS Cent Sci* **2017**, *3* (1), 31-38.
36. Zheng, J.; Ye, J.; Ortuno, M. A.; Fulton, J. L.; Gutierrez, O. Y.; Camaioni, D. M.; Motkuri, R. K.; Li, Z.; Webber, T. E.; Mehdi, B. L.; Browning, N. D.; Penn, R. L.; Farha, O. K.; Hupp, J. T.; Truhlar, D. G.; Cramer, C. J.; Lercher, J. A., Selective Methane Oxidation to Methanol on Cu-Oxo Dimers Stabilized by Zirconia Nodes of an NU-1000 Metal-Organic Framework. *J. Am. Chem. Soc.* **2019**, *141* (23), 9292-9304.
37. Platero-Prats, A. E.; Mavrandonakis, A.; Liu, J.; Chen, Z.; Chen, Z.; Li, Z.; Yakovenko, A. A.; Gallington, L. C.; Hupp, J. T.; Farha, O. K.; Cramer, C. J.; Chapman, K. W., The Molecular Path Approaching the Active Site in Catalytic Metal-Organic Frameworks. *J. Am. Chem. Soc.* **2021**, *143* (48), 20090-20094.
38. Ji, P.; Manna, K.; Lin, Z.; Urban, A.; Greene, F. X.; Lan, G.; Lin, W., Single-Site Cobalt Catalysts at New Zr<sub>8</sub>(μ<sub>2</sub>-O)<sub>8</sub>(μ<sub>2</sub>-OH)<sub>4</sub> Metal-Organic Framework Nodes for Highly Active Hydrogenation of Alkenes, Imines, Carbonyls, and Heterocycles. *J. Am. Chem. Soc.* **2016**, *138* (37), 12234-42.
39. An, B.; Li, Z.; Song, Y.; Zhang, J.; Zeng, L.; Wang, C.; Lin, W., Cooperative copper centres in a metal–organic framework for selective conversion of CO<sub>2</sub> to ethanol. *Nature Catalysis* **2019**, *2* (8), 709-717.
40. Manna, K.; Ji, P.; Lin, Z.; Greene, F. X.; Urban, A.; Thacker, N. C.; Lin, W., Chemoselective single-site Earth-abundant metal catalysts at metal-organic framework nodes. *Nature Communications* **2016**, *7*, 1-11.
41. Xu, C.; Pan, Y.; Wan, G.; Liu, H.; Wang, L.; Zhou, H.; Yu, S. H.; Jiang, H. L., Turning on Visible-Light Photocatalytic C-H Oxidation over Metal-Organic Frameworks by Introducing Metal-to-Cluster Charge Transfer. *J. Am. Chem. Soc.* **2019**, *141* (48), 19110-19117.
42. Otake, K. I.; Ahn, S.; Knapp, J.; Hupp, J. T.; Notestein, J. M.; Farha, O. K., Vapor-Phase Cyclohexene Epoxidation by Single-Ion Fe(III) Sites in Metal-Organic Frameworks. *Inorganic Chemistry* **2021**, *60* (4), 2457-2463.
43. Xu, C.; Pan, Y.; Wan, G.; Liu, H.; Wang, L.; Zhou, H.; Yu, S. H.; Jiang, H. L., Turning on Visible-Light Photocatalytic C-H Oxidation over Metal-Organic Frameworks by Introducing Metal-to-Cluster Charge Transfer. *J. Am. Chem. Soc.* **2019**, *141* (48), 19110-19117.
44. Lin, W.; Frei, H., Photochemical CO<sub>2</sub> splitting by metal-to-metal charge-transfer excitation in mesoporous ZrCu(I)-MCM-41 silicate sieve. *J. Am. Chem. Soc.* **2005**, *127* (6), 1610-1.

45. Nakamura, R.; Okamoto, A.; Osawa, H.; Irie, H.; Hashimoto, K., Design of all-inorganic molecular-based photocatalysts sensitive to visible light: Ti(IV)-O-Ce(III) bimetallic assemblies on mesoporous silica. *J. Am. Chem. Soc.* **2007**, *129* (31), 9596-7.
46. Kramar, B. V.; Phelan, B. T.; Sprague-Klein, E. A.; Diroll, B. T.; Lee, S.; Otake, K.-i.; Palmer, R.; Mara, M. W.; Farha, O. K.; Hupp, J. T.; Chen, L. X., Single-Atom Metal Oxide Sites as Traps for Charge Separation in the Zirconium-Based Metal-Organic Framework NDC-NU-1000. *Energy & Fuels* **2021**, *35* (23), 19081-19095.
47. Otake, K. I.; Ahn, S.; Knapp, J.; Hupp, J. T.; Notestein, J. M.; Farha, O. K., Vapor-Phase Cyclohexene Epoxidation by Single-Ion Fe(III) Sites in Metal-Organic Frameworks. *Inorg. Chem.* **2021**, *60* (4), 2457-2463.
48. Jiang, H.; Zhang, W.; Kang, X.; Cao, Z.; Chen, X.; Liu, Y.; Cui, Y., Topology-Based Functionalization of Robust Chiral Zr-Based Metal-Organic Frameworks for Catalytic Enantioselective Hydrogenation. *J. Am. Chem. Soc.* **2020**, *142* (21), 9642-9652.
49. Gong, W.; Arman, H.; Chen, Z.; Xie, Y.; Son, F. A.; Cui, H.; Chen, X.; Shi, Y.; Liu, Y.; Chen, B.; Farha, O. K.; Cui, Y., Highly Specific Coordination-Driven Self-Assembly of 2D Heterometallic Metal-Organic Frameworks with Unprecedented Johnson-type (J51) Nonanuclear Zr-Oxocarboxylate Clusters. *J. Am. Chem. Soc.* **2021**, *143* (2), 657-663.
50. Furukawa, H.; Gandara, F.; Zhang, Y. B.; Jiang, J.; Queen, W. L.; Hudson, M. R.; Yaghi, O. M., Water adsorption in porous metal-organic frameworks and related materials. *J. Am. Chem. Soc.* **2014**, *136* (11), 4369-81.
51. Spek, A. L., Single-crystal structure validation with the program PLATON. *J. Appl. Crystallogr.* **2003**, *36* (Copyright (C) 2012 American Chemical Society (ACS). All Rights Reserved.), 7-13.
52. Manna, K.; Ji, P.; Lin, Z.; Greene, F. X.; Urban, A.; Thacker, N. C.; Lin, W., Chemoselective single-site Earth-abundant metal catalysts at metal-organic framework nodes. *Nat. Commun.* **2016**, *7*, 12610.
53. Yuan, S.; Qin, J. S.; Xu, H. Q.; Su, J.; Rossi, D.; Chen, Y.; Zhang, L.; Lollar, C.; Wang, Q.; Jiang, H. L.; Son, D. H.; Xu, H.; Huang, Z.; Zou, X.; Zhou, H. C., [Ti<sub>8</sub>Zr<sub>2</sub>O<sub>12</sub>(COO)<sub>16</sub>] Cluster: An Ideal Inorganic Building Unit for Photoactive Metal-Organic Frameworks. *ACS Cent Sci* **2018**, *4* (1), 105-111.
54. Schwarz, H. A.; Dodson, R. W., Equilibrium between hydroxyl radicals and thallium(II) and the oxidation potential of hydroxyl(aq). *J. Phys. Chem.* **2002**, *88* (16), 3643-3647.
55. Nosaka, Y.; Nosaka, A. Y., Generation and Detection of Reactive Oxygen Species in Photocatalysis. *Chem. Rev.* **2017**, *117* (17), 11302-11336.
56. Kundu, S.; Behera, B.; Giri, A.; Saha, N.; Patra, A., N,N'-bicarbazole-benzothiadiazole-based conjugated porous organic polymer for reactive oxygen species generation in live cells. *Chem. Commun.* **2021**, *57* (56), 6875-6878.
57. Gómez-Gualdrón, D. A.; Colón, Y. J.; Zhang, X.; Wang, T. C.; Chen, Y.-S.; Hupp, J. T.; Yildirim, T.; Farha, O. K.; Zhang, J.; Snurr, R. Q., Evaluating topologically diverse metal-organic frameworks for cryo-adsorbed hydrogen storage. *Energy Environ. Sci.* **2016**, *9* (10), 3279-3289.

### 3.10 Supporting Information

**Table S1. Crystal data and structural refinement of MOF-565, MOF-565-Fe, and NPF-520-Fe.**

Compound name	NPF-520	MOF-565-Fe	NPF-520-Fe
Empirical formula	C <sub>171</sub> H <sub>129</sub> N <sub>6</sub> O <sub>45</sub> Zr <sub>9</sub>	C <sub>72</sub> H <sub>44</sub> Fe <sub>1.6</sub> O <sub>32</sub> Zr <sub>6</sub>	C <sub>171</sub> H <sub>129</sub> Fe <sub>3.12</sub> N <sub>6</sub> O <sub>47.52</sub> Zr <sub>9</sub>
Formula weight (g mol <sup>-1</sup> )	3808.77	211.54	3803.89
Temperature (K)	273(2)	100	273(2)
Wavelength (Å)	synchrotron (λ = 0.7288)	synchrotron (λ = 0.7288)	synchrotron (λ = 0.7288)
Crystal system	trigonal	trigonal	trigonal
Space group	R32	P-3	R32
a (Å)	35.168(9)	40.1904(13)	34.510(4)
b (Å)	35.168(9)	40.1904(13)	34.510(4)
c (Å)	28.593(12)	11.5148(6)	28.659(4)
α (deg)	90	90	90
β (deg)	90	90	90
γ (deg)	120	120	120
Volume (Å <sup>3</sup> )	30625(21)	16107.6(13)	29559(7)
Z	3	3	3
Density (calculated) (g/cm <sup>3</sup> )	0.620	2.857	0.641
Absorption Coefficient (mm <sup>-1</sup> )	0.271	5.8	0.397
F(000)	5751.0	12838	5668
Crystal size (mm <sup>3</sup> )	0.3 × 0.3 × 0.3 mm	0.5 × 0.02 × 0.02 mm	0.3 × 0.3 × 0.2 mm
2θ range for data collection (deg)	2.004 to 57.292	2.078 to 61.76	2.018 to 54.194
Index ranges	-46 ≤ h ≤ 44, -45 ≤ k ≤ 46, -34 ≤ l ≤ 37	-56 ≤ h ≤ 56, -56 ≤ k ≤ 56, -16 ≤ l ≤ 16	-43 ≤ h ≤ 43, -43 ≤ k ≤ 43, -35 ≤ l ≤ 35
Reflections collected	100902	404424	186025
Independent reflections	16078 [R <sub>int</sub> = 0.1060, R <sub>sigma</sub> = 0.0748]	31446 [R <sub>int</sub> = 0.1799, R <sub>sigma</sub> = 0.0944]	13409 [R <sub>int</sub> = 0.1421, R <sub>sigma</sub> = 0.0712]
Completeness to θ (%)	100	100	100
Data/restraints/parameters	16078/293/340	31446/0/527	13409/0/341
Goodness-of-fit on F <sup>2</sup>	1.079	1.1	1.057
Final R indexes [I ≥ 2σ (I)]	R <sub>1</sub> = 0.1172, wR <sub>2</sub> = 0.2981	1.1	R <sub>1</sub> = 0.0851, wR <sub>2</sub> = 0.2229
Final R indexes [all data]	R <sub>1</sub> = 0.1857, wR <sub>2</sub> = 0.3863	R <sub>1</sub> = 0.1231, wR <sub>2</sub> = 0.2687	R <sub>1</sub> = 0.1241, wR <sub>2</sub> = 0.2775
Largest diff. peak/hole / e Å <sup>-3</sup>	4.94/-2.42	4.46/-1.73	2.67/-1.07

**Table S2. SEM-EDS Elemental Analysis**

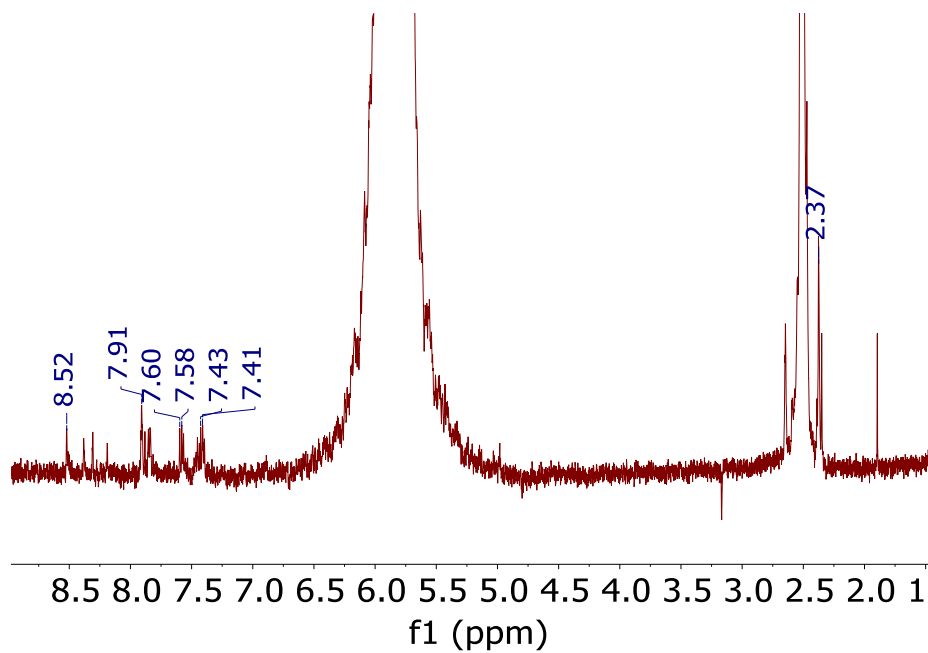
<b>Sample</b>	<b>Element Symbol</b>	<b>Atomic Conc.</b>	<b>Weight Conc.</b>
<b>MOF-565</b>	C	70.03	48.77
	O	24.59	22.82
	Zr	5.37	28.41
<b>MOF-565-FeIII</b>	C	65.25	50.12
	O	30.74	31.46
	Zr	2.37	13.83
	Fe	0.67	2.38
	Cl	0.98	2.21
<b>NPF-520</b>	C	66.02	47.49
	O	16.41	15.72
	N	12.8	10.73
	Zr	4.77	26.06
<b>NPF-520-FeIII</b>	C	75.07	52.47
	O	18.42	17.15
	Zr	4.7	24.94
	Fe	1.44	4.68
	Cl	0.37	0.76

**Table S3. Catalyst Recycling and Leaching**

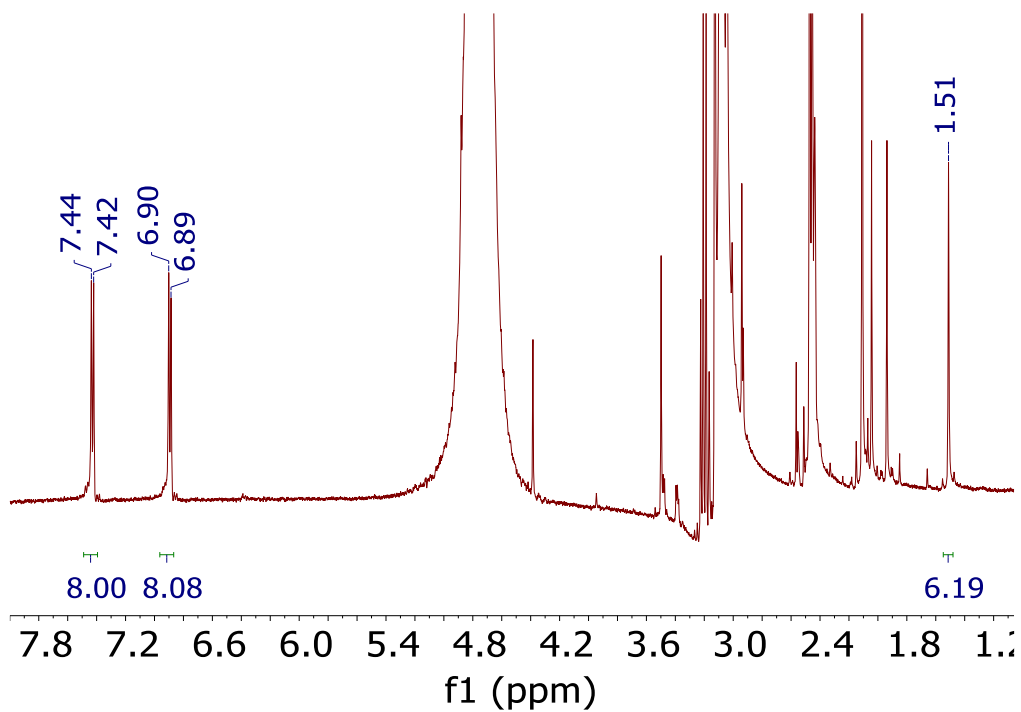
Entry	Catalyst	Times Recycled	Conversion <sup>c</sup>	Fe/Zr <sub>6</sub> Ratio (ICP-OES)
1 <sup>b</sup>	MOF-565-Fe <sup>III</sup>	0	100	3.85
2 <sup>b</sup>	MOF-565-Fe <sup>III</sup>	1	100	3.82
3 <sup>b</sup>	MOF-565-Fe <sup>III</sup>	2	100	3.82
4 <sup>b</sup>	MOF-565-Fe <sup>III</sup>	3	99	3.81
5 <sup>b</sup>	MOF-565-Fe <sup>III</sup>	4	100	3.81
6 <sup>b</sup>	MOF-565-Fe <sup>III</sup>	5	99	3.81
7 <sup>bd</sup>	MOF-565-Fe <sup>III</sup>	6	100	3.55
8 <sup>a</sup>	NPF-520-Fe <sup>III</sup>	0	100	3.14
9 <sup>a</sup>	NPF-520-Fe <sup>III</sup>	1	100	3.10
10 <sup>a</sup>	NPF-520-Fe <sup>III</sup>	2	98	3.10
11 <sup>a</sup>	NPF-520-Fe <sup>III</sup>	3	99	3.09
12 <sup>a</sup>	NPF-520-Fe <sup>III</sup>	4	100	3.11
13 <sup>a</sup>	NPF-520-Fe <sup>III</sup>	5	97	3.09
13 <sup>ad</sup>	NPF-520-Fe <sup>III</sup>	6	92	2.98

<sup>a</sup>Reaction conditions: 5 μL toluene, 1 mL MeCN, 5 mol% catalyst (based on Fe<sup>III</sup>), 395 nm blue LED photoreactor, 8 h, 1 atm O<sub>2</sub>. <sup>b</sup>Reaction conditions: 10 μL toluene, 1 mL MeCN, 1 mol% catalyst (based on Fe<sup>III</sup>), 395 nm blue LED photoreactor, 2 h, 1 atm O<sub>2</sub>. <sup>c</sup>Determined by GC/GC-MS using a standard curve with 1 uL chlorobenzene internal reference. <sup>d</sup>Heated to 50°C in the photoreactor.

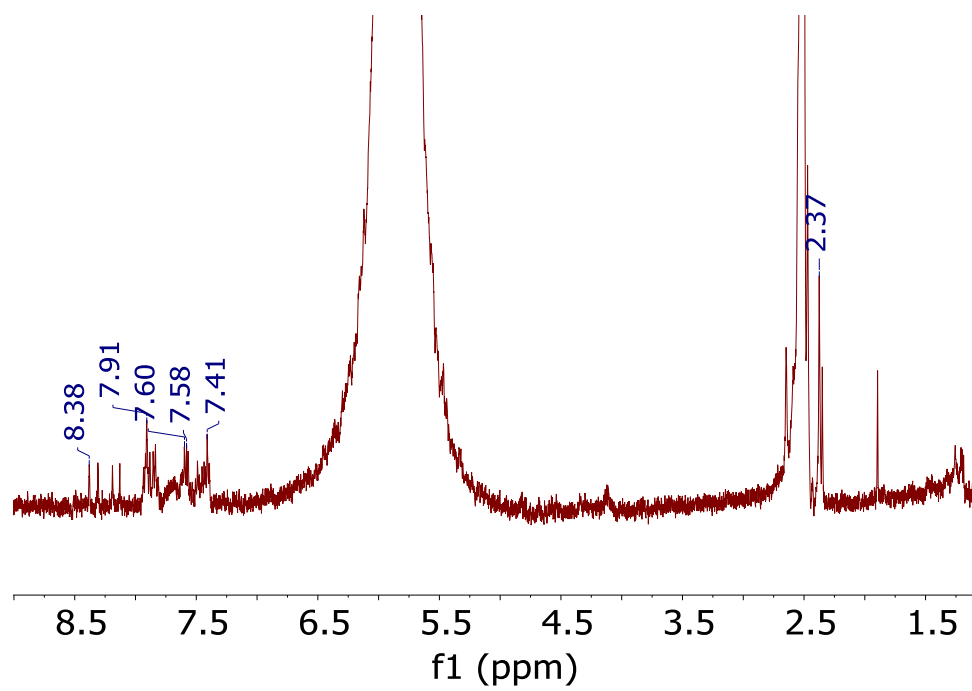




**Figure S1.**  $^1\text{H}$  NMR of as-synthesized **NPF-520-Fe<sup>III</sup>**, digested in  $\text{D}_2\text{SO}_4/\text{d}_6\text{-DMSO}$ .



**Figure S2.**  $^1\text{H}$  NMR of **MOF-565-Fe<sup>III</sup>** after catalysis, digested in  $\text{K}_3\text{PO}_4/\text{D}_2\text{O}$ .



**Figure S3.** <sup>1</sup>H NMR of **NPF-520-Fe<sup>III</sup>** after catalysis, digested in D<sub>2</sub>SO<sub>4</sub>/d<sub>6</sub>-DMSO.

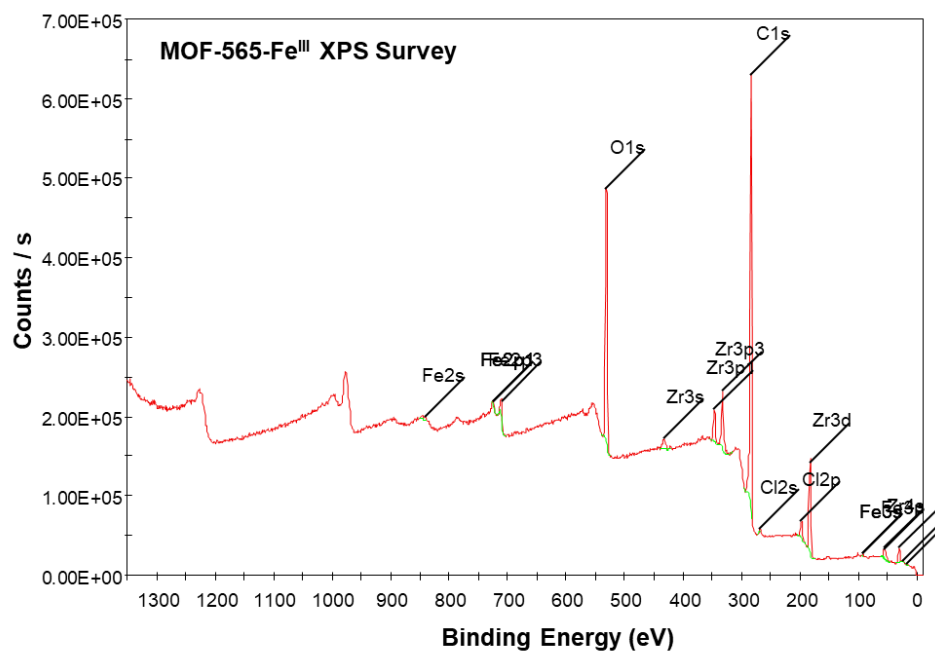


Figure S4. MOF-565-Fe<sup>III</sup> XPS Survey.

Table S4. MOF-565-Fe<sup>III</sup> XPS element identification and quantification.

<i>Name</i>	<i>Peak BE</i>	<i>FWHM eV</i>	<i>Area (P) CPS.eV</i>	<i>Atomic %</i>	<i>Q</i>
Fe2s	841.36	2.05	29266.12	0.50	1
Fe2p3	710.82	3.58	79509.46	0.39	1
O1s	531.74	3.56	1223151.79	17.69	1
Zr3s	433.38	5.17	88946.19	2.18	1
Zr3p1	346.96	3.45	150092.26	1.51	1
Zr3p3	333.21	3.52	299640.72	1.55	1
C1s	284.47	1.65	1715571.83	59.98	1
Cl2s	269.31	0.96	5788.63	0.13	1
Cl2p	198.24	3.64	79268.03	0.96	1
Zr3d	183.37	4.38	499049.29	1.82	1
Fe3p	55.58	2.67	53121.48	1.09	1
Zr4s	55.66	4.38	63190.00	9.83	1
Zr4p	31.23	3.58	63446.34	1.83	1
O2s	24.39	0.00	1386.82	0.36	1
Cl3s	16.74	0.21	690.31	0.19	1

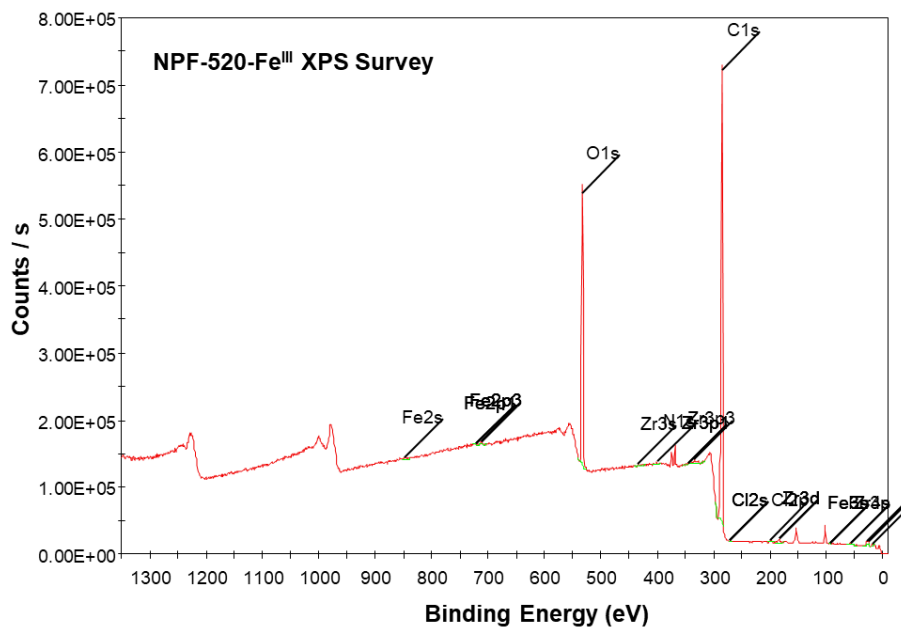
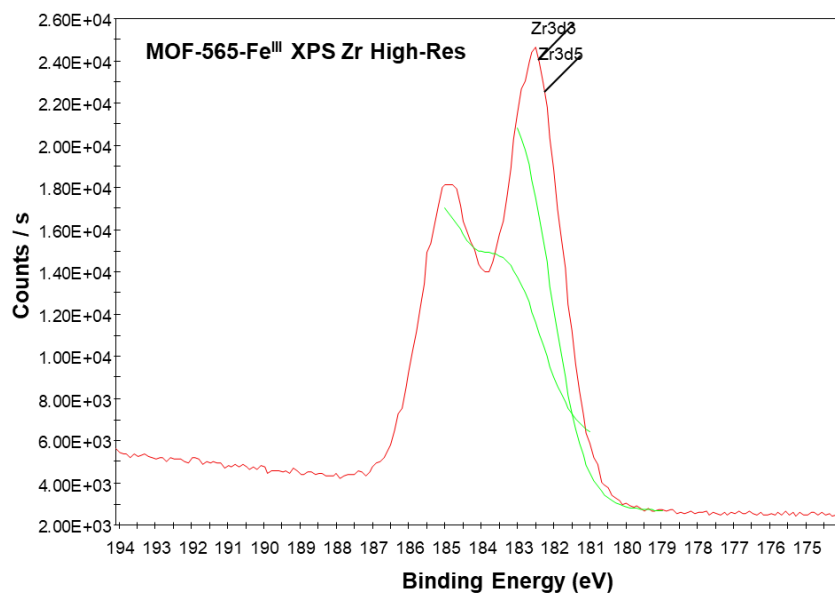


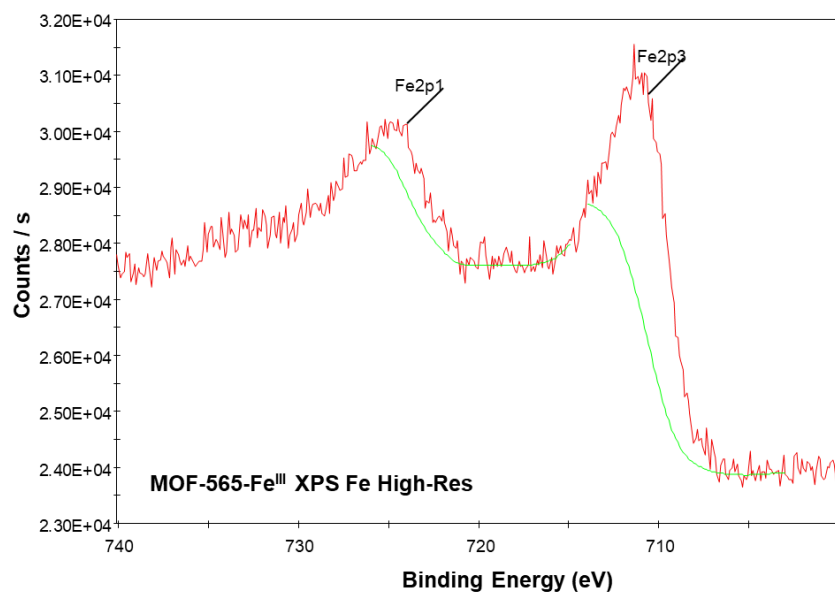
Figure S5. MOF-565-Fe<sup>III</sup> XPS Survey.

Table S5. NPF-520-Fe<sup>III</sup> XPS element identification and quantification.

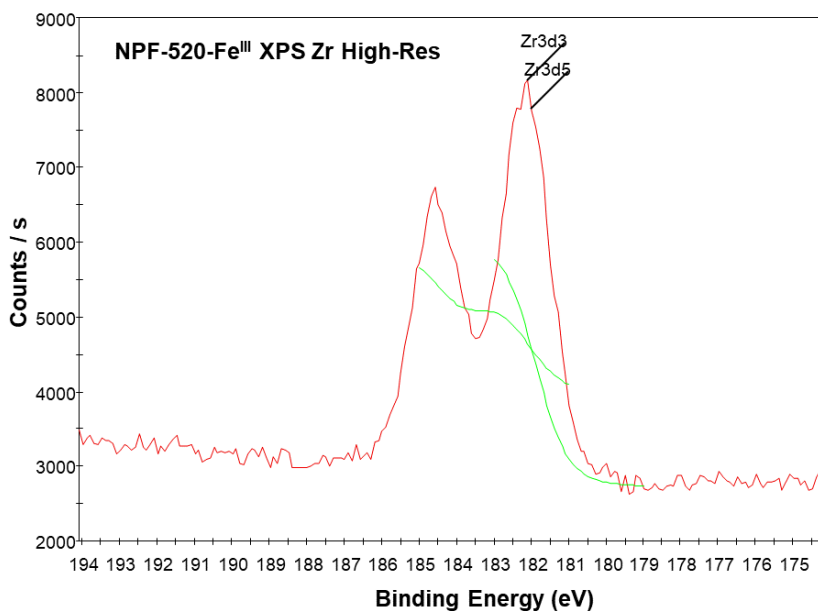
Name	Peak BE	FWHM eV	Area (P) CPS.eV	Atomic %	Q
Fe2s	846.35	3.19	8609.25	0.15	1
O1s	532.28	3.09	1295095.71	19.04	1
Zr3s	433.30	2.70	9198.50	0.23	1
N1s	400.01	0.86	6760.23	0.15	1
Zr3p3	333.09	2.07	38174.58	0.20	1
C1s	284.88	2.70	2166815.58	76.97	1
Cl2p	198.76	1.03	9833.30	0.12	1
Fe3p	55.95	2.63	6582.39	0.14	1
Zr4s	56.02	3.29	8317.71	1.31	1
Zr4p	26.98	4.36	22474.52	0.66	1
Cl3s	16.66	2.40	3696.25	1.02	1



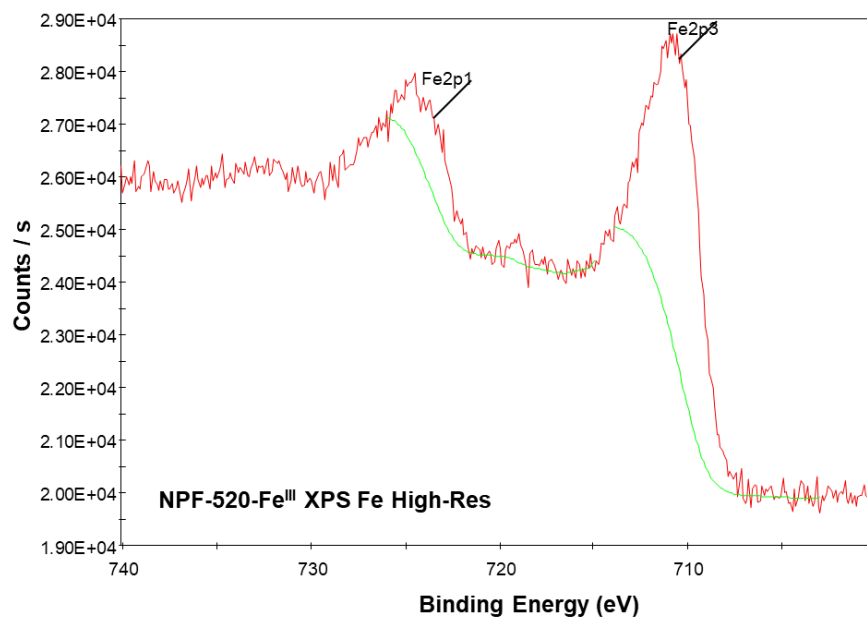
**Figure S6. MOF-565-Fe<sup>III</sup> XPS Zr High-Resolution**



**Figure S7. MOF-565-Fe<sup>III</sup> XPS Fe High-Resolution**



**Figure S8. NPF-520-Fe<sup>III</sup> XPS Zr High-Resolution**



**Figure S9. NPF-520-Fe<sup>III</sup> XPS Fe High-Resolution**

## Chapter 4. Reversible Guest-Induced Phase Changes and Selective Ethylene Adsorption in a Flexible-Robust Co-Based Metal Organic Framework

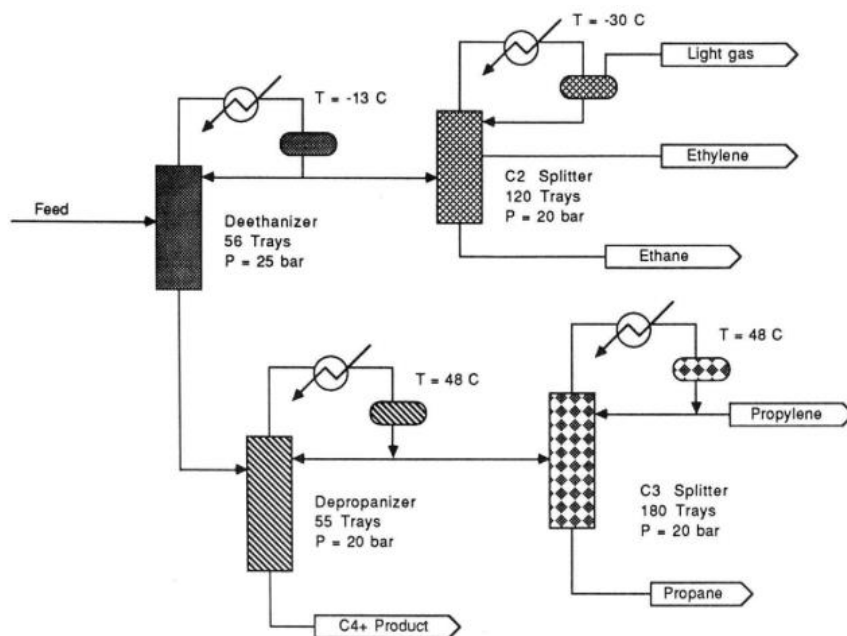
### Abstract

A novel flexible-robust metal-organic framework, **Co-MOF**, exhibiting reversible guest-induced phase changes and selective ethylene adsorption has been successfully synthesized and characterized by single-crystal X-ray diffraction, powder X-ray diffraction, Fourier-transform infrared spectroscopy, UV-visible spectroscopy, thermogravimetric analyses, and magnetometry. We propose that the 3-amino-4-hydroxybenzoic acid linker rotates when exposed to guests such as dimethylformamide and methanol, resulting in different coordination number (4-, 5-, and 6-coordinate) and geometries (tetrahedral, trigonal bipyramidal, square pyramidal, octahedral) for the Co nodes. Moreover, **Co-MOF** is flexible, collapsing upon activation under heating and vacuum to give the closed phase. This gives rise to 6 phases in total: **Co-MOF-DMF**, **Co-MOF-DA**, **Co-MOF-MeOH**, **Co-MOF-MA**, **Co-MOF-46**, **Co-MOF-46A**. The conditions for each phase change and its reversibility were studied, and the **Co-MOFs** tested for adsorption of C<sub>2</sub> gases. Interestingly, **Co-MOF-DMF** showed ethylene adsorption properties characteristic of materials with open metal sites while remaining selective for ethylene over acetylene and ethane, and the closed phase **Co-MOF-DA** and **Co-MOF-MA** displayed greater adsorption capacity for ethylene over the desolvated open phase **Co-MOF-46**, suggesting cooperative packing interactions during the phase opening.

## 4.1 Introduction

With a global production capacity of exceeding 170 million tons per year,<sup>1</sup> ethylene ( $C_2H_4$ ) is one of the most important chemical feedstocks in petrochemical industries and agriculture for its production of polymers and high-value organic chemicals including polyethylene, polypropylene, poly(vinyl chloride), and ethanol.<sup>2-3</sup> The primary industrial method for producing  $C_2H_4$  is steam cracking (or thermal decomposition) of ethane ( $C_2H_6$ ) and liquidized petroleum gas.<sup>4</sup>

Since steam crackers do not yield pure  $C_2H_4$  (>99.95%), the impurities (mostly  $C_2H_6$ ) must be removed from  $C_2H_4/C_2H_6$  mixtures especially for manufacturing plastics.<sup>4</sup> This is usually accomplished by heat-driven cryogenic distillation through repeated distillation–compression cycles under harsh conditions (typically at 5–28 bar and 180–258 K)<sup>5</sup> to produce commercial polymer-grade  $C_2H_4$  (Figure 1).<sup>6-7</sup>



**Figure 1.** Conventional cryogenic distillation process for ethylene/ethane and propylene/propane mixtures from a steam cracking feed. Copyright 1993 American Chemical Society.

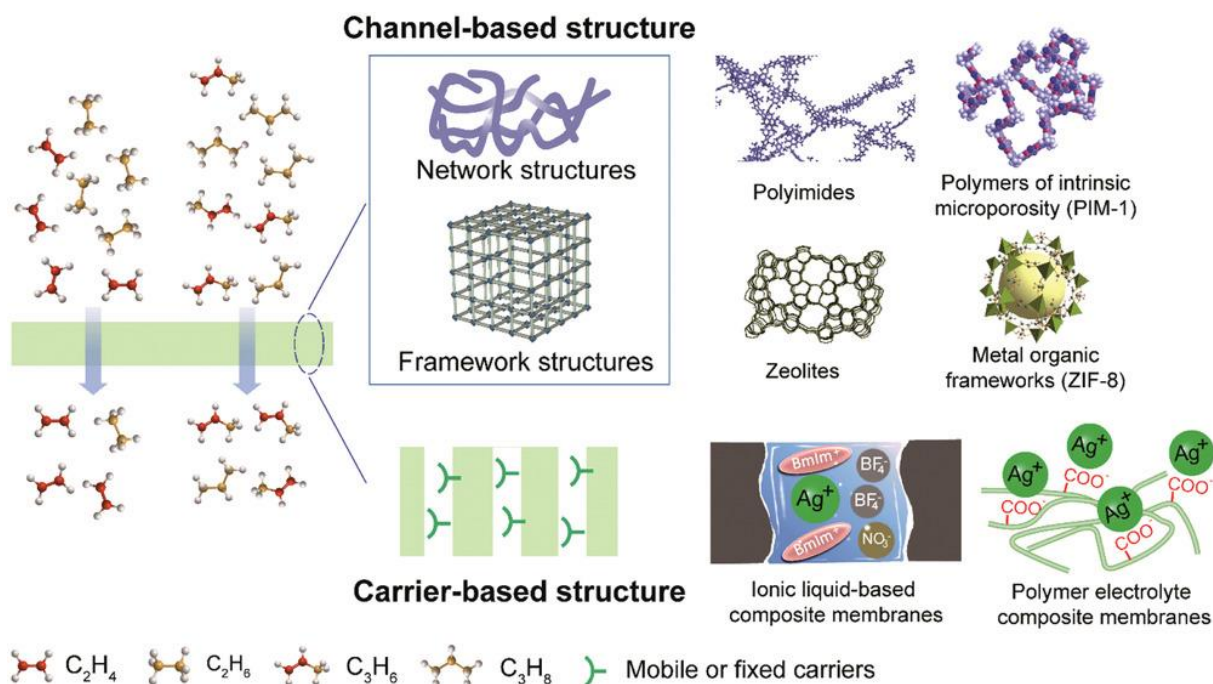
However, cryogenic distillation is extremely energy intensive as it requires the use of a large distillation tower (120–180 trays) for high reflux ratios due to the similar kinetic diameter, boiling point and other physicochemical properties of  $C_2H_4$  and  $C_2H_6$  (Table 1).<sup>8</sup> Indeed, the total energy used for such separation is estimated to be about 7.3 GJ per tonne of  $C_2H_4$ .<sup>9</sup> To avoid such a high consumption of energy, it is urgent to explore alternative technologies and materials that can efficiently separate and purify  $C_2H_4$  under mild conditions with low-energy consumption.<sup>10-11</sup>



**Table 1. Physical properties of C<sub>2</sub> and C<sub>3</sub> olefins and paraffins.**

Component	Boiling point (K)	Critical temperature (K)	Kinetic diameter (nm)	Polarizability × 10 <sup>25</sup> (cm)	Dipole moment × 10 <sup>18</sup> (esu cm)
Ethylene	169.5	282.3	0.423	42.5	0
Ethane	184.5	305.3	0.442	44.3	0
Propylene	225.5	364.9	0.468	62.6	0.366
Propane	231.1	369.8	0.506	63.3	0.084

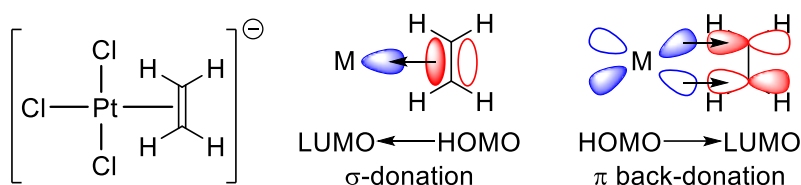
Among techniques with lower energy requirements and operating costs, the adsorptive separation process based on porous solid materials have risen to prominence.<sup>12-22</sup> Utilizing the differences of the molecular geometry and physical properties, porous materials can exhibit differential adsorption for various components of the mixture. Conventional solid adsorptive materials, such as polymer membranes, zeolites,<sup>23-25</sup> alumina,<sup>26</sup> mesoporous silica,<sup>27</sup> and carbon-based materials,<sup>28-31</sup> have been explored for the C<sub>2</sub>H<sub>4</sub>/C<sub>2</sub>H<sub>6</sub> separation (Figure 2).<sup>32</sup> However, except for a few chemisorbents,<sup>33</sup> conventional porous materials are not satisfactory in separation processes of industrial demand due to poor adsorption selectivity and low capacity as well as the lack of any recognition mechanism.<sup>34</sup>



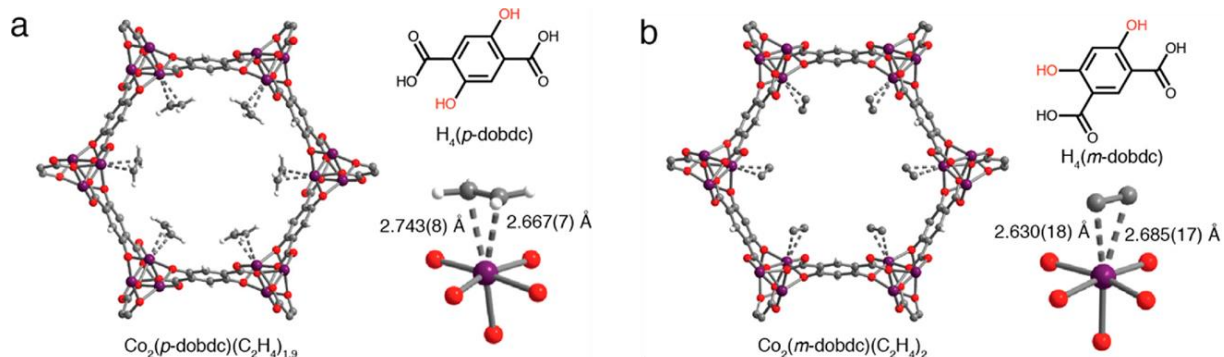
**Figure 2.** Examples of various porous materials and membranes that were explored for ethylene/ethane and propylene/propane separations. Copyright 2020 Wiley.

In this context, metal–organic frameworks (MOFs) with structural diversity, tunable pore characteristics, designable pore sizes, and high pore volumes have in recent years emerged as promising adsorbents to address the challenge of gas separation,<sup>35-42</sup> especially the separation of C<sub>2</sub>H<sub>4</sub> from C<sub>2</sub>H<sub>6</sub>.<sup>43-54</sup> In principle, incorporation of functional sites into MOFs can enhance binding interaction for polar hydrocarbons, while precise control over the pore sizes can exclude larger molecules, both resulting in improved separation performance. However, the separation of C<sub>2</sub>H<sub>4</sub> and C<sub>2</sub>H<sub>6</sub> is extremely challenging due to their similar physical properties and molecular size (3.28 × 4.18 × 4.84 Å<sup>3</sup> for C<sub>2</sub>H<sub>4</sub> and 3.81 × 4.08 × 4.82 Å<sup>3</sup> for C<sub>2</sub>H<sub>6</sub>).<sup>55</sup>

Currently, most MOFs used for C<sub>2</sub>H<sub>6</sub>/C<sub>2</sub>H<sub>4</sub> separation are mainly C<sub>2</sub>H<sub>4</sub>-selective MOFs.<sup>56-57</sup> This is because the design strategies for C<sub>2</sub>H<sub>4</sub>-selective MOFs are relatively straightforward, that is, the introduction of highly polar binding centers like open metal sites (OMSs)<sup>56-67</sup> and Ag<sup>I</sup>/Cu<sup>I</sup> metal ions<sup>68-70</sup> to exploit the strong binding affinity of C<sub>2</sub>H<sub>4</sub> to metals via the C=C double bond, a phenomenon that has been known since the discovery of Zeise’s salt, or potassium trichloro(ethylene)platinate(II), in 1831 (Figure 3).<sup>71</sup> This approach takes advantage of the larger quadrupole moment of C<sub>2</sub>H<sub>4</sub> (C<sub>2</sub>H<sub>4</sub>: 1.50 × 10<sup>-26</sup> esu cm<sup>2</sup>, C<sub>2</sub>H<sub>6</sub>: 0.65 × 10<sup>-26</sup> esu cm<sup>2</sup>) and the presence of π electrons,<sup>72</sup> which render its stronger interactions with metal sites/clusters via σ-donation and π back-donation.



**Figure 3.** Structure of Zeise’s salt and orbital model of a metal to C=C bond.

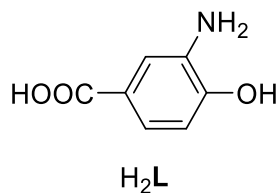


**Figure 4.** Single-crystal X-ray structures for (a) **Co-MOF-74** and (b) **Co<sub>2</sub>(*m*-dobdc)**. Purple, red, gray, and white spheres represent Co, O, C, and H atoms, respectively. Copyright 2017 American Chemical Society.

Unfortunately, many materials with exposed OMS are highly air- and/or moisture sensitive, due to the even higher affinity of these sites to water, oxygen, and other gases in the atmosphere. This becomes a problem when these “poisons” are present in the feed gas from a cracker stream, as the materials then

become deactivated and inactive. Several well-known examples depicted in Figure 4 are the MOF-74 series<sup>73</sup> ( $M_2(p\text{-dobdc})$ ,  $M = \text{Mg, Mn, Fe, Co, Ni, Zn}$ ;  $p\text{-dobdc}^{4-} = 2,5\text{-dioxido-1,4-benzenedicarboxylate}$ ) and the structural isomer  $M_2(m\text{-dobdc})$  series<sup>74</sup> ( $M = \text{Mg, Mn, Fe, Co, Ni}$ ;  $m\text{-dobdc}^{4-} = 4,6\text{-dioxido-1,3-benzenedicarboxylate}$ ), both of which use coordinatively unsaturated  $M^{II}$  sites to effectively polarize and adsorb ethylene preferentially over ethane, but must be handled under  $N_2$  atmospheres.

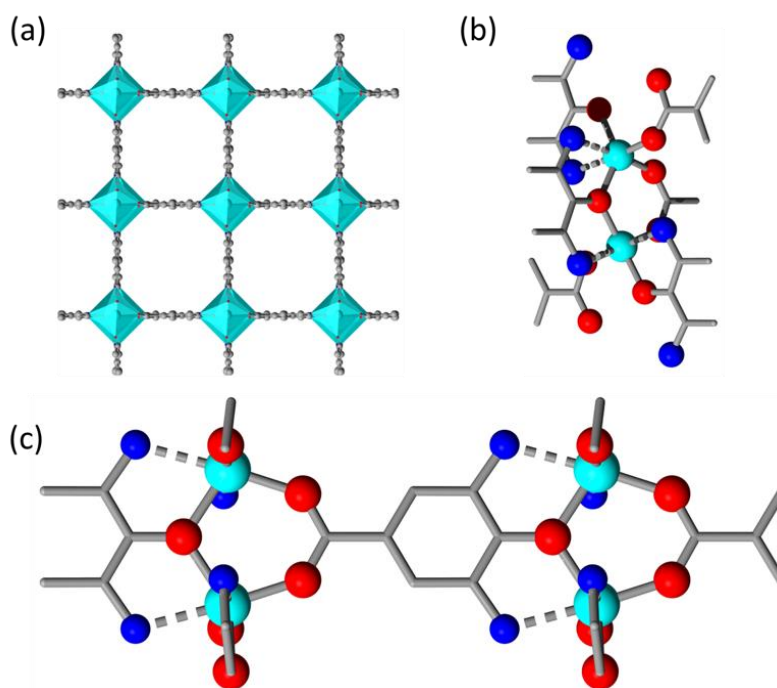
In order to design a MOF with air-stable OMS, we hypothesize that alteration of the nature of the coordination bond might contribute to the stabilization of a 5-coordinate single metal site, as well as increase the electron density of the d-orbital to enhance binding affinity to alkenes. Henceforth we chose a commercially available ligand  $H_2L$  ( $L = 3\text{-amino-4-hydroxybenzoic acid}$ , Figure 5) that features an *ortho*-aminophenol to form a highly robust Co-based MOF (**Co-MOF**). This ligand features a phenolic oxygen and amino group as the unconventional binding site to metals.



**Figure 5.** Structure of ligand  $H_2L$ .

## 4.2 Structural Characterization and Guest-Induced Phase Changes of Co-MOF

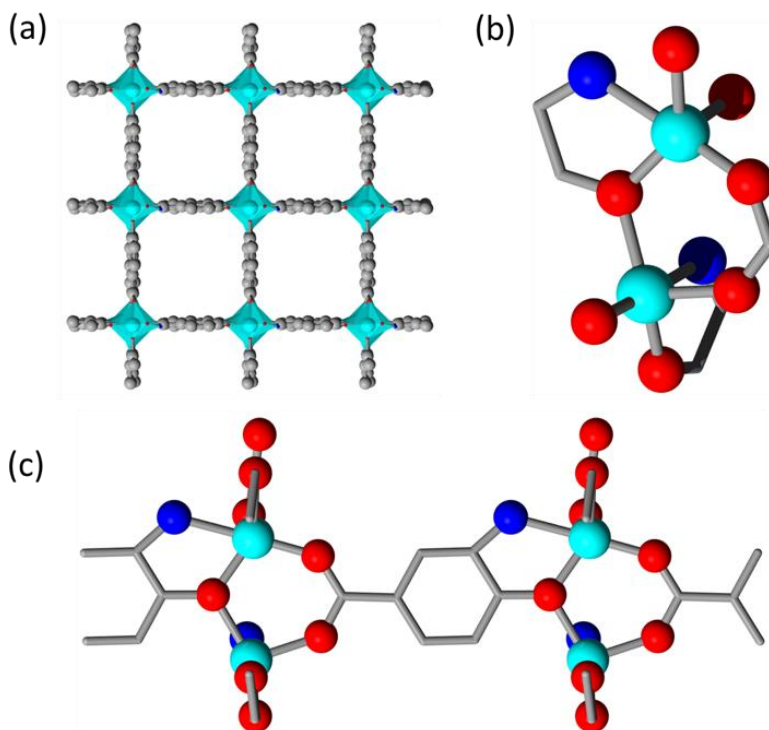
Single-crystals of **Co-MOF** were readily obtained from a solvothermal reaction of  $\text{Co}(\text{NO}_3)_2 \cdot 6\text{H}_2\text{O}$  (cobalt(II) nitrate hexahydrate) and  $\text{H}_2\text{L}$  in *N,N*-dimethylformamide (DMF) and water at 125 °C for 48 h, giving a yield based on the ligand of 73%. Single-crystal X-ray diffraction (sc-XRD) studies of the as-synthesized MOF, labeled **Co-MOF-DMF**, at 100 K revealed that it has a formula of  $[\text{CoL}]$  and crystallizes in space group  $P4_122/P4_322$  (no. 91/95) of the tetragonal system with the lattice parameters  $a = b = 9.100(8)$  Å,  $c = 13.1449(9)$  Å,  $V = 1088.72$  Å<sup>3</sup> (Figure 6), with crystals in both chiral space groups present in the mixture as well as large twinned crystals containing both chiralities.



**Figure 6.** Single-crystal structure of **Co-MOF-DMF** viewed (a) down the  $c$ -axis, (b) along the  $(1,1,0)$  plane and (c) down the  $a$ -axis. Cyan, blue, red, and gray spheres represent Co, N, O, and C atoms, respectively.

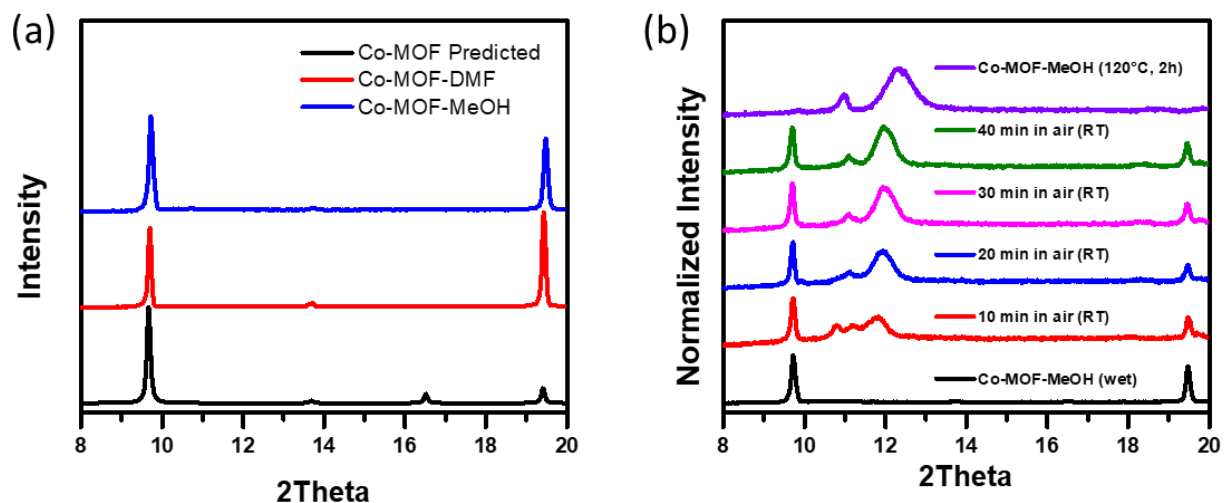
The Co atoms in the framework form 1D chains running down the  $c$ -axis, forming the rod secondary building blocks (SBUs) linked together by the alternating carboxy and hydroxy groups on the linker. The amino group of the ligand was found to be equally disordered over 2 positions, resulting in Co being 5-coordinate on average but also making it impossible to determine the exact coordination number and geometry of Co. Assuming, however, that only one amino group is present, the 4 O atoms and 1 N atom coordinated to Co would form a distorted square pyramidal geometry, with an OMS available for guest binding, although only small guests would fit into the binding pocket which is partially blocked by a H atom on the phenyl ring.

In order to further elucidate the structure of **Co-MOF**, a solvent exchange from DMF to methanol (MeOH) was conducted overnight at room temperature to give **Co-MOF-MeOH**. The single crystal structure was again measured at 100 K to reveal **Co-MOF-MeOH** crystallizes in a different space group  $P4_1/P4_3$  (no. 76/78) of the tetragonal system with the lattice parameters  $a = b = 9.1008(4)$  Å,  $c = 13.1449(9)$  Å,  $V = 1088.72(10)$  Å<sup>3</sup> (Figure 7). Contrary to **Co-MOF-DMF**, **Co-MOF-MeOH** displays near complete ordering of the amino groups (>85%), suggesting that the linker **L** can freely rotate and reorder in methanol. All Co atoms appear 5-coordinate, with square pyramidal geometry.



**Figure 7.** Single-crystal structure of **Co-MOF-MeOH** viewed (a) down the  $c$ -axis, (b) along the  $(1,1,0)$  plane and (c) down the  $a$ -axis. Cyan, blue, red, and gray spheres represent Co, N, O, and C atoms, respectively.

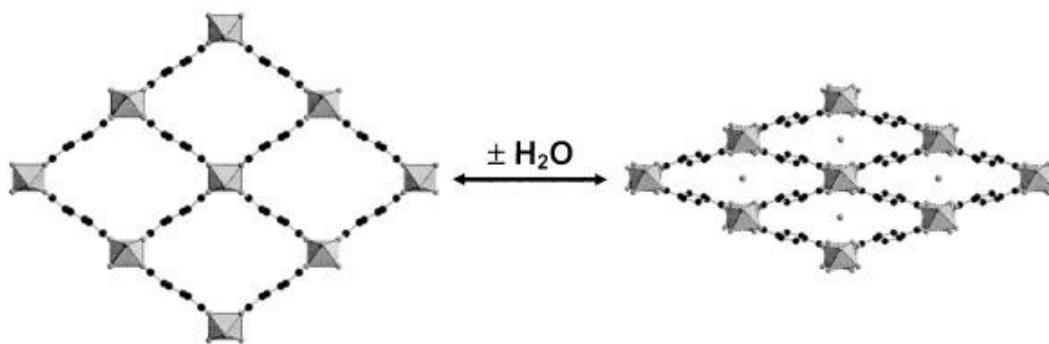
Upon solvent exchange of MeOH for **Co-MOF-MeOH** back to DMF, it was observed that **Co-MOF-DMF** was again obtained via sc-XRD, demonstrating the reversibility of this guest (i.e., solvent) induced phase-transformation. This solvent exchange was repeated a total of 3 times, and **Co-MOF** was characterized using sc-XRD after every exchange to confirm the phase change. Powder X-ray diffraction (PXRD) was also conducted to confirm the bulk crystallinity of the samples before and after the phase changes, although the PXRD spectra of both phases are identical (Figure 8).



**Figure 8.** (a) XRD patterns of **Co-MOF-DMF** and **Co-MOF-MeOH**. (b) XRD patterns of **Co-MOF-MeOH** over time as it is dried in air and heated in the oven.

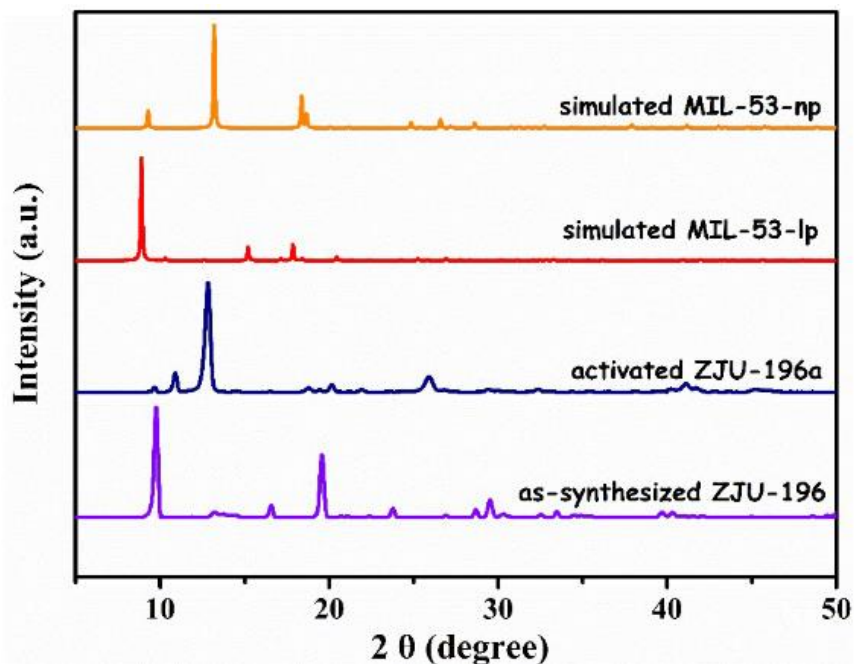
During the XRD measurement though, we noticed that as the **Co-MOF-MeOH** was dried in air, new peaks appeared that did not correspond to any peak in the predicted spectrum (Figure 8b). Furthermore, when **Co-MOF-MeOH** was placed in the oven at 120 °C for 2h, all the initial peaks disappeared and were replaced by new broad peaks that were shifted to higher angles, indicating a significant decrease in the lattice parameters and likely a change in crystal symmetry.

By comparing these XRD data to reported MOFs, we noticed a striking similarity between **Co-MOF** and the **MIL-53** series reported by Férey and co-workers<sup>75-76</sup> that display “breathing” upon hydration and dehydration (Figure 9). A combination of <sup>27</sup>Al, <sup>13</sup>C, and <sup>1</sup>H nuclear magnetic resonance (NMR) spectrometry revealed that this dynamic phase change of the **MIL-53(Al)** structure is related to the hydrogen-bonding interactions between water molecules trapped within the channels and the carboxylate groups of the organic terephthalate linkers.<sup>75</sup>



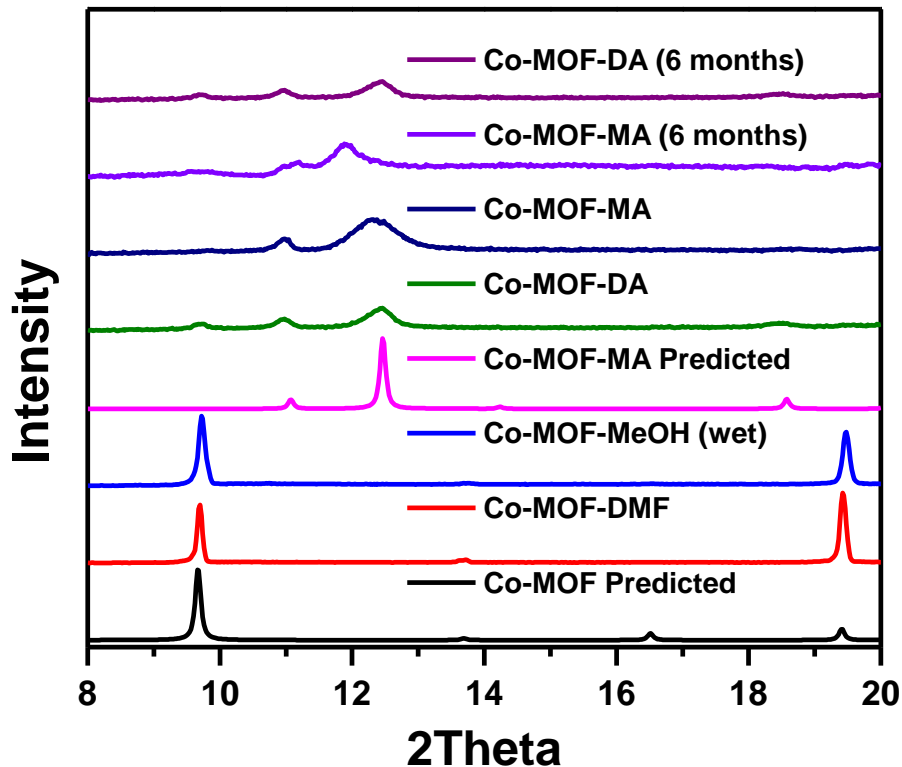
**Figure 9.** Phase-switching of MIL-53(Al) upon hydration and dehydration, showing the open phase with empty pores (left) and closed phase with water (right). Copyright 2004 Chemistry–A European Journal.

The Zn analog of **Co-MOF**, **ZJU-196**, reported by the Chen group,<sup>77</sup> also displayed similar structural changes upon heating under vacuum, although the collapsed phase of **ZJU-196** is extremely unstable under atmospheric pressure (both air and N<sub>2</sub> gas) and proved challenging to characterize except for a powder diffraction pattern (Figure 10). One key difference between **Co-MOF**, **ZJU-196** and **MIL-53** though, is that while **MIL-53** changes from the closed to the open phase upon guest removal, **Co-MOF** and **ZJU-196** change from the open to the closed phase.



**Figure 10.** A comparison of the changes in the PXR D patterns between **ZJU-196** and **MIL-53**, indicating that **ZJU-196** should possess a similar breathing property. Copyright 2018 Chemical Communications.

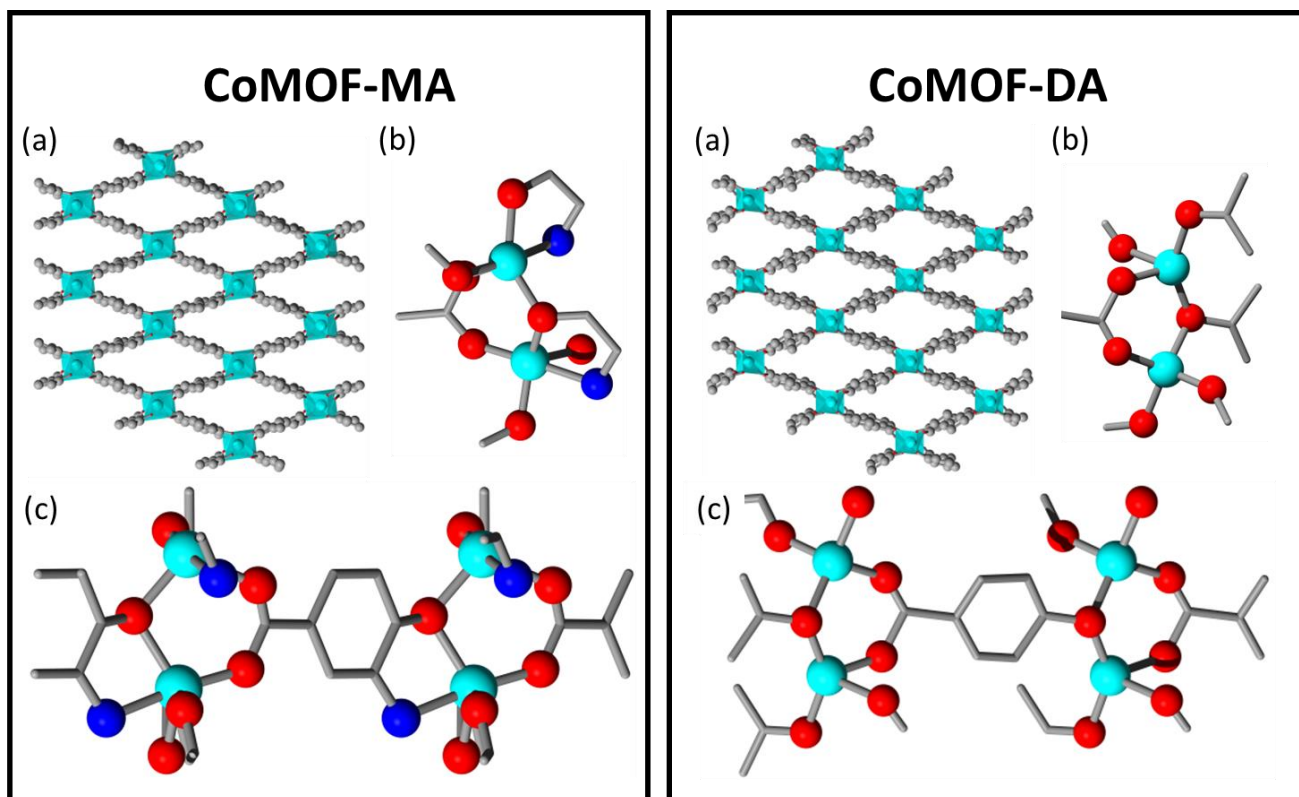
To characterize the closed-phase structure of **Co-MOF**, we thus heated **Co-MOF-MeOH** and **Co-MOF-DMF** with evacuation under high vacuum until PXR D showed that the bulk MOFs were collapsed to their corresponding activated forms, labeled **Co-MOF-MA** and **Co-MOF-DA** respectively (Figure 11). **Co-MOF-MA** was easily fully collapsed as indicated by the disappearance of the (1,0,0) peak at 9.7°, whereas the bulk **Co-MOF-DA** never fully collapsed even when heated at 200°C under high vacuum for 3 d. Contrary to the unstable **ZJU-196a** which is restored to the open phase after 5 min in air,<sup>77</sup> **Co-MOF-MA** and **Co-MOF-DA** proved to be extremely air-stable, remaining predominantly in their closed phases even 6 months after activation.



**Figure 11.** PXRD patterns of the open and closed phases of **Co-MOF** from both DMF and MeOH solvated phases.

sc-XRD was then used to characterize the activated forms of **Co-MOF-MeOH** and **Co-MOF-DMF**, labeled **Co-MOF-MA** and **Co-MOF-DA** (Figure 12). The optimal condition to preserve the highest crystallinity for both phases turned out to be 300 °C with high vacuum for 1 h, although much milder conditions were sufficient to activate the bulk MOF (see Materials and Methods for details). Unfortunately, due to the twinning of the structures generated during the structural collapse, a complete structure was only obtained and solved for **Co-MOF-MA**, while **Co-MOF-DA** shows a partial structure where the amino groups could not be located. From the distortion of the linker phenyl ring and diffuse electron densities, however, it is likely that the ring is slightly rotated such that the amino groups are either weakly coordinated or not coordinated to Co at all, resulting in an OMS with a slightly larger binding pocket than **Co-MOF-MA**.

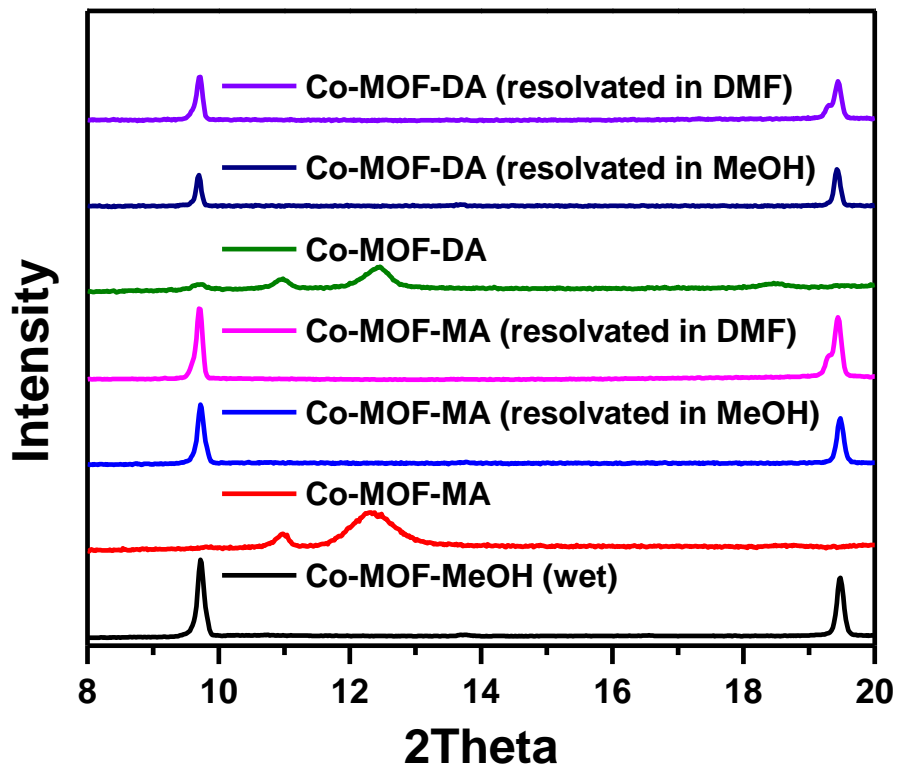




**Figure 12.** Crystal structures of **Co-MOF-MA** and **Co-MOF-DA** viewed from different angles. The amino groups could not be located in the **Co-MOF-DA**. Cyan, blue, red, and gray spheres represent Co, N, O, and C atoms, respectively.

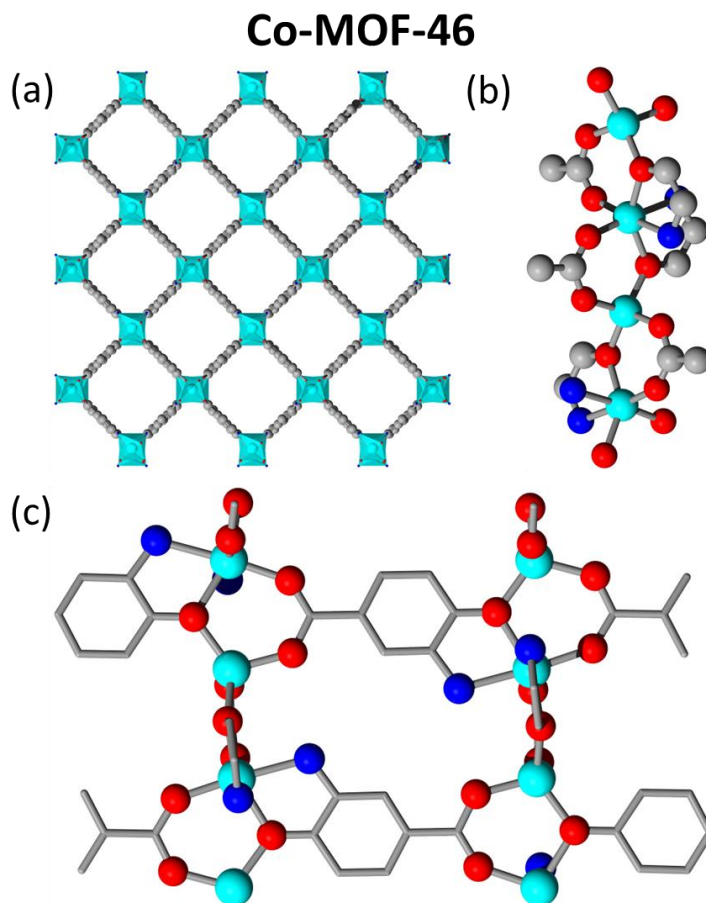
Both activated crystal structures were solved in the  $P2_1$  space group (no. 4) of the monoclinic system with the lattice parameters  $a = 7.92(3) \text{ \AA}$ ,  $b = 8.91(3) \text{ \AA}$ ,  $c = 12.90(3) \text{ \AA}$ ,  $\gamma = 116.35(4)^\circ$ ,  $V = 815.734 \text{ \AA}^3$  for **Co-MOF-MA** and a slightly larger  $a = 8.117(4) \text{ \AA}$ ,  $b = 8.936(5) \text{ \AA}$ ,  $c = 12.949(5) \text{ \AA}$ ,  $\gamma = 116.778(17)^\circ$ ,  $V = 838.512 \text{ \AA}^3$  for **Co-MOF-DA**. As predicted, the structure collapses in a similar manner as **MIL-53**, losing the tetragonal 4-fold symmetry to result in a 2-fold symmetry monoclinic space group. The coordination number of Co in **Co-MOF-MA** is preserved as 5-coordinate, the same as the open-phase, although the square pyramidal geometry distorts to form a distorted geometry in-between a square pyramid and trigonal bipyramid, decreasing the size of the binding pocket for the OMS.

The activated **Co-MOFs** were then placed back in solvents to confirm the reversibility of the phase transformation. When **Co-MOF-MA** and **Co-MOF-DA** were re-solvated in MeOH, the **Co-MOF-MeOH** structure was obtained as confirmed by sc-XRD at least 3 times, and PXRD was used to check the bulk crystallinity (Figure 13, blue and navy spectra). However, when **Co-MOF-MA** and **Co-MOF-DA** were re-solvated in DMF, yet another new phase was obtained as seen from Figure 13 (pink and purple spectra), with the appearance of shoulder peaks to the left of the main peak at  $9.7^\circ$  and  $19.4^\circ$ .



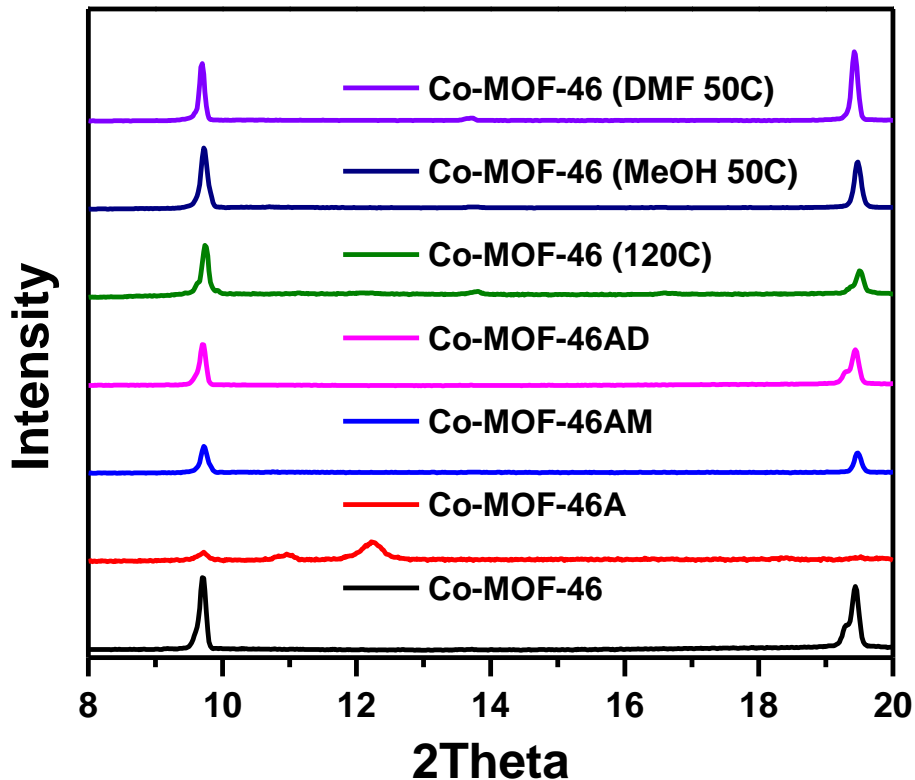
**Figure 13.** PXRD spectra of activated **Co-MOFs** before and after re-solvation.

sc-XRD was again used to study the new phase obtained after re-solvation of the activated **Co-MOFs** in DMF, labeled **Co-MOF-46**. Measurements at 100 K revealed that it crystallizes in space group  $P4_122/P4_322$  (no. 91/95) of the tetragonal system with the lattice parameters  $a = b = 12.90(2) \text{ \AA}$ ,  $c = 13.15(3) \text{ \AA}$ ,  $V = 2188.29 \text{ \AA}^3$  (Figure 14), indicating that the unit cell is twice as large as that of **Co-MOF-MA** and **Co-MOF-DA** and is rotated by  $45^\circ$ . Upon closer inspection, the reason for the larger unit cell is a loss in symmetry along the  $c$ -axis, where the coordination of Co is now perfectly alternating between 4-coordinate tetrahedral and 6-coordinate octahedral geometry, making it a structural analog of the reported Zn-MOF, **ZJU-196**.<sup>77</sup>



**Figure 14.** Single-crystal structure of **Co-MOF-46 MeOH** viewed (a) down the  $c$ -axis, (b) down the  $b$ -axis and (c) along the  $(1, -1, 0)$  plane. Cyan, blue, red, and gray spheres represent Co, N, O, and C atoms, respectively.

Interestingly, placing **Co-MOF-46** in MeOH or DMF at 50 °C restores it to **Co-MOF-MA** and **Co-MOF-DA** respectively, suggesting that **Co-MOF-46** is a metastable phase. **Co-MOF-46** was then heated under vacuum to activate the MOF (**Co-MOF-46A**) followed by re-solvation in MeOH and DMF, which gave the **Co-MOF-MA** and **Co-MOF-46** structures respectively as seen by PXRD (Figure 15, samples **Co-MOF-46AM**, **Co-MOF-46AD**) and re-confirmed by sc-XRD (Supporting Information). Unfortunately, the **Co-MOF-46A** single crystals were too physically damaged at this point due to the repeated phase changes to diffract well on sc-XRD, but assuming the structure collapses in a similar manner as **Co-MOF-MA**, the alternating 4, 6-coordination of Co should be preserved.



**Figure 15.** PXRD patterns of **Co-MOF-46**, **Co-MOF-46A**, as well as solvent-exchanged (**Co-MOF-46 (DMF 50C)** and **Co-MOF-46 (MeOH 50C)**), de-solvated open phase **Co-MOF-46 (120C)**, and re-solvated samples (**Co-MOF-46AM**, **Co-MOF-46AD**).

According to Fourier-transform infrared spectroscopy (FTIR) (Figure 16) and PXRD studies (Figure 15 **Co-MOF-46 (120C)**, green plot), it was possible to remove all the guests (i.e., free DMF) from **Co-MOF-46** without collapsing the structure by using mild drying conditions (120 °C, 3 h, high vacuum). This is in contrast to **Co-MOF-MA** and **Co-MOF-DA**, which gradually transform into the closed phase as solvents are removed (e.g., Figure 8b)). This is evident by the disappearance of the DMF C=O peak at 1660  $\text{cm}^{-1}$  in the FTIR spectrum, while the PXRD patterns show that the open phase MOF structure is retained. This would enable us to compare the gas adsorption between the completely desolvated closed and open phases of the MOF, which to our knowledge, has not been accomplished before for other flexible MOFs.

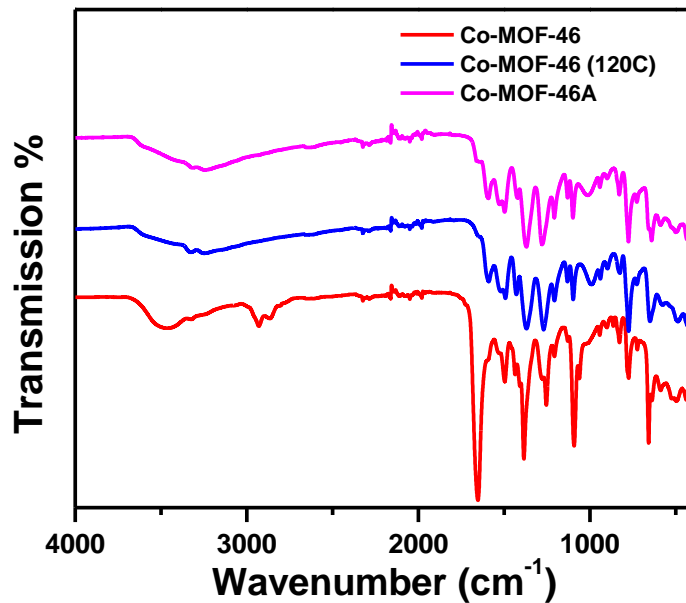


Figure 16. FTIR spectra of Co-MOF-46, Co-MOF-46 (120C), and Co-MOF-46A.

Given that ethylene cracking feed streams typically contain not only water, but some acidic gases, the chemical and thermal stability of Co-MOF were investigated. Chemical stability was evaluated using PXRD at different pH values and showed that Co-MOF remains intact from pH = 1 to 11 (Figure 17).

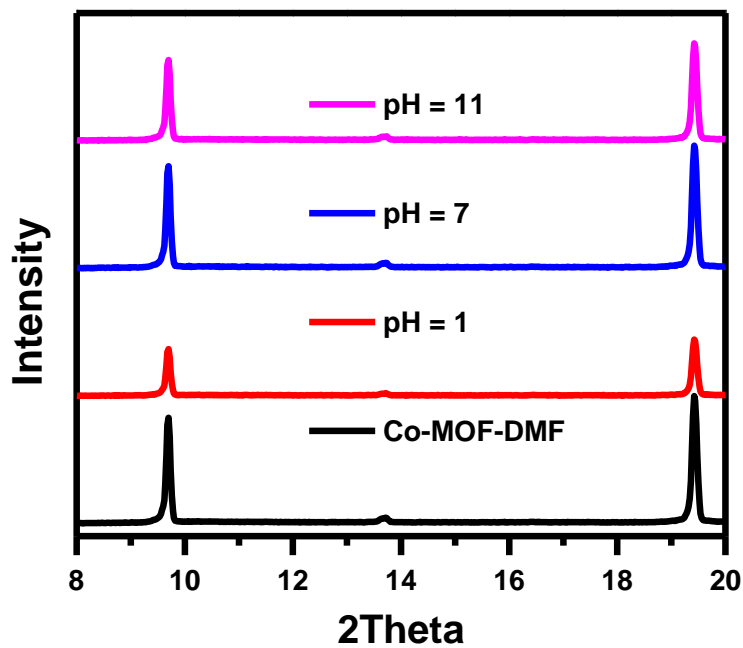
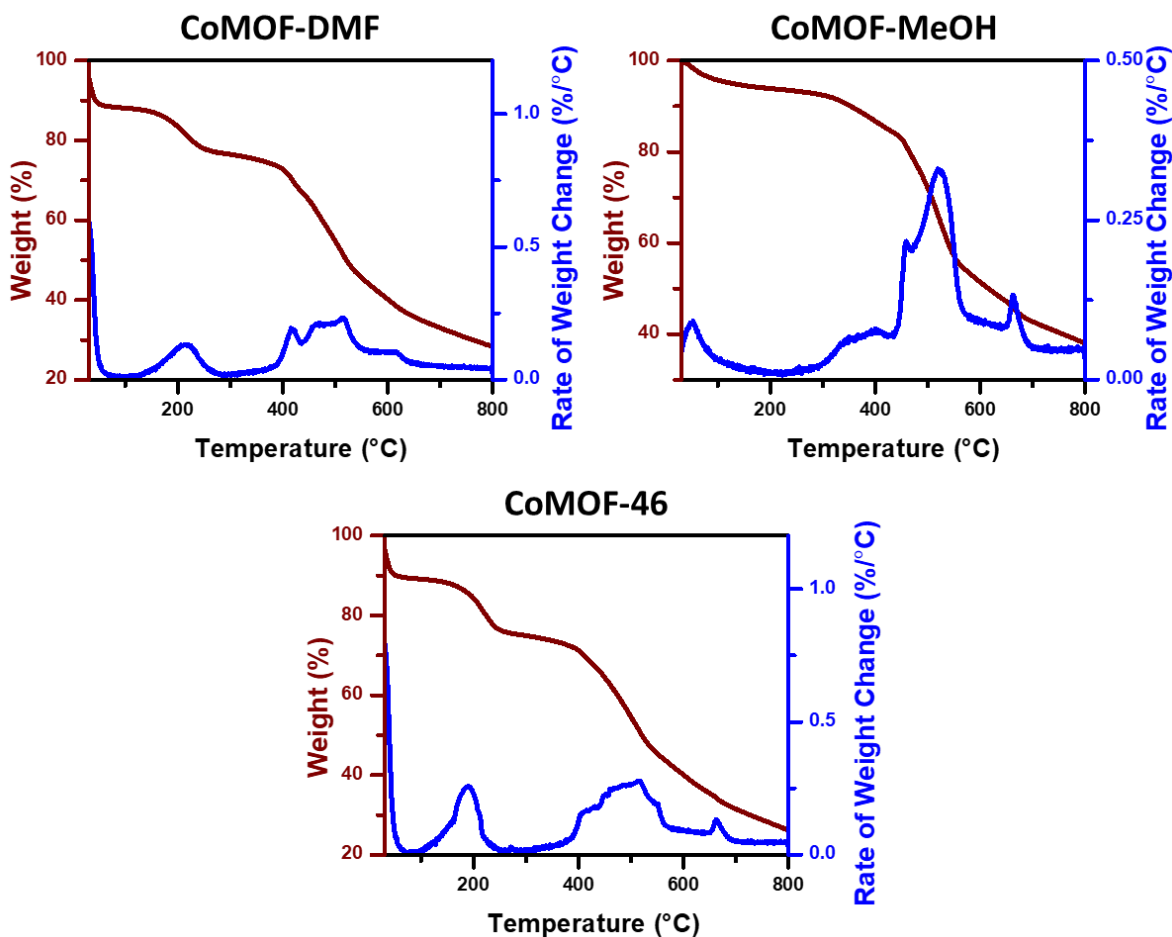


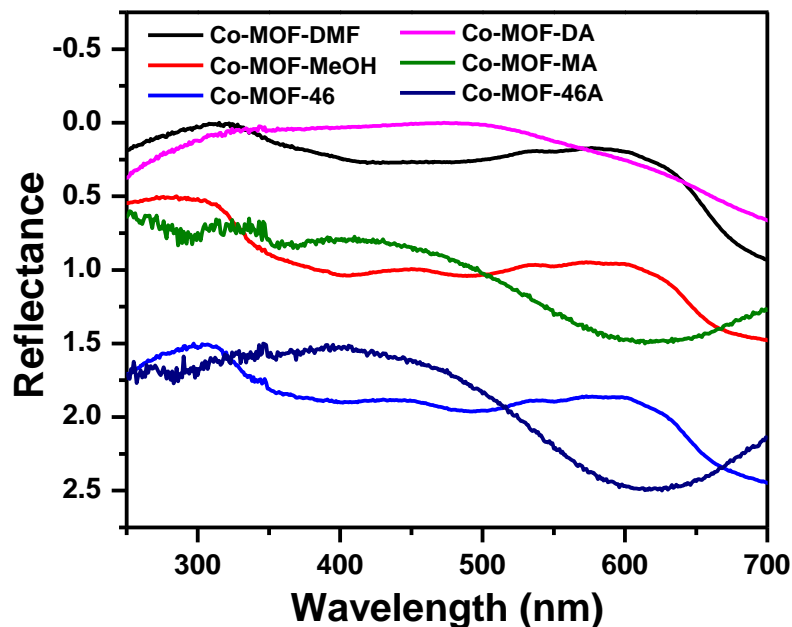
Figure 17. Chemical stability of Co-MOF-DMF at different pH (PXRD).

The thermal stability of **Co-MOF** was studied via thermogravimetric analysis (TGA) on the 3 open phases, namely, **Co-MOF-DMF**, **Co-MOF-MeOH**, and **Co-MOF-46** (Figure 18). As expected, **Co-MOF-DMF** and **Co-MOF-46** show a slight weight loss at 220 °C and 180 °C respectively corresponding to loss of adsorbed and free DMF, whereas **Co-MOF-MeOH** shows a weight loss at 50 °C corresponding to loss of MeOH. Decomposition for all the **Co-MOFs** corresponds to the weight loss above 400 °C.



**Figure 18.** TGA of **Co-MOF-DMF**, **Co-MOF-MeOH**, and **Co-MOF-46**, with weight loss and rate of weight change (1<sup>st</sup> derivative of weight loss).

UV-visible reflectance spectroscopy was also conducted to characterize the **Co-MOF** phases. Due to the dark color of the **Co-MOFs**, the samples had to be ground very finely before approximately 0.1-0.2 mg of sample was placed on the holder. Although there was little difference between **Co-MOF-DMF**, **Co-MOF-MeOH**, and **Co-MOF-46** as well as between their respective activated phases, there was a clear shift of the visible-range absorption peak from 600 nm to 400 nm upon activation from the open phase to the closed phase (Figure 19). This matches up well with the observed color change of the **Co-MOFs** from purple to brown.



**Figure 19.** UV-visible spectra of **Co-MOF-DMF**, **Co-MOF-DA**, **Co-MOF-MeOH**, **Co-MOF-MA**, **Co-MOF-46**, and **Co-MOF-46A**.

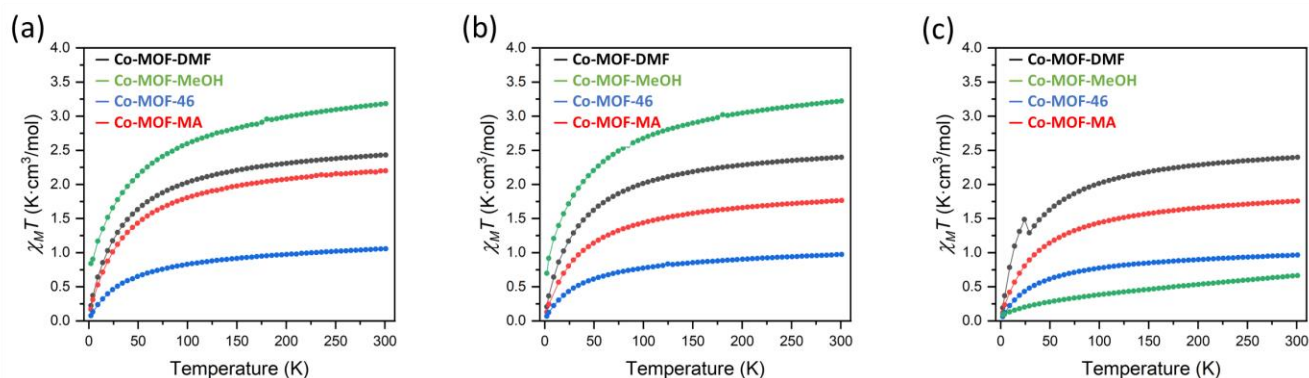
Finally, a dc magnetic susceptibility measurement was conducted to provide further support for the presence of 4 different **Co-MOF** phases (Figure 20 and Table 2). All 4 samples can be distinguished from each other based on their Curie-Weiss parameters, indicating that the structural changes associated with activation/solvent exchange in the sc-XRD studies translate into changes in magnetic properties.

The Curie constant of 2.6 for **Co-MOF-DMF** is consistent with mixture of weak-field octahedral  $\text{Co}^{\text{II}}$  and square pyramidal  $\text{Co}^{\text{II}}$  engaging in antiferromagnetic interactions. No change in ground state was noted across the three measured fields, however, a field induced ordering event was observed under 1 T applied field at 29 K, consistent with weak ferrimagnetic order indicating that there are two distinct  $\text{Co}^{\text{II}}$  sites present engaging with one another. From this data, it is likely that DMF solvent molecules are coordinating to alternate OMS sites, blocking half of the available sites in the open phase.

The Curie constant of 3.5 for **Co-MOF-MeOH** is consistent with the 5-coordinate  $\text{Co}^{\text{II}}$  in the crystal structure. The Curie constant of 1.1 for **Co-MOF-46** and lack of any field dependent behavior is also consistent with a coupled tetrahedral  $\text{Co}^{\text{II}}$  and octahedral  $\text{Co}^{\text{II}}$ , a perfect match with the observed single crystal structure. Lastly, the Curie constant of 2.0 for **Co-MOF-MA** is in line with  $\text{Co}^{\text{II}}$  in a tetrahedral geometry, suggesting that the amino group is weakly coordinated or non-coordinated to Co in the activated MOF under an external magnetic field.

To summarize, magnetic susceptibility measurements have allowed us to confirm the bulk differences in **Co-MOF** phases that were challenging to observe using other techniques such as PXRD, FTIR, or UV-VIS

spectroscopy. The sc-XRD structures are also highly influenced by symmetry and 3 measured crystals may not truly be representative of the whole.



**Figure 20.** Variable-temperature magnetic susceptibility ( $\chi_M T$ ) for Co-MOF-DMF, Co-MOF-MeOH, Co-MOF-46, and Co-MOF-MA under applied magnetic fields of 0.1 T (a), 0.5 T (b), and 1 T (c).

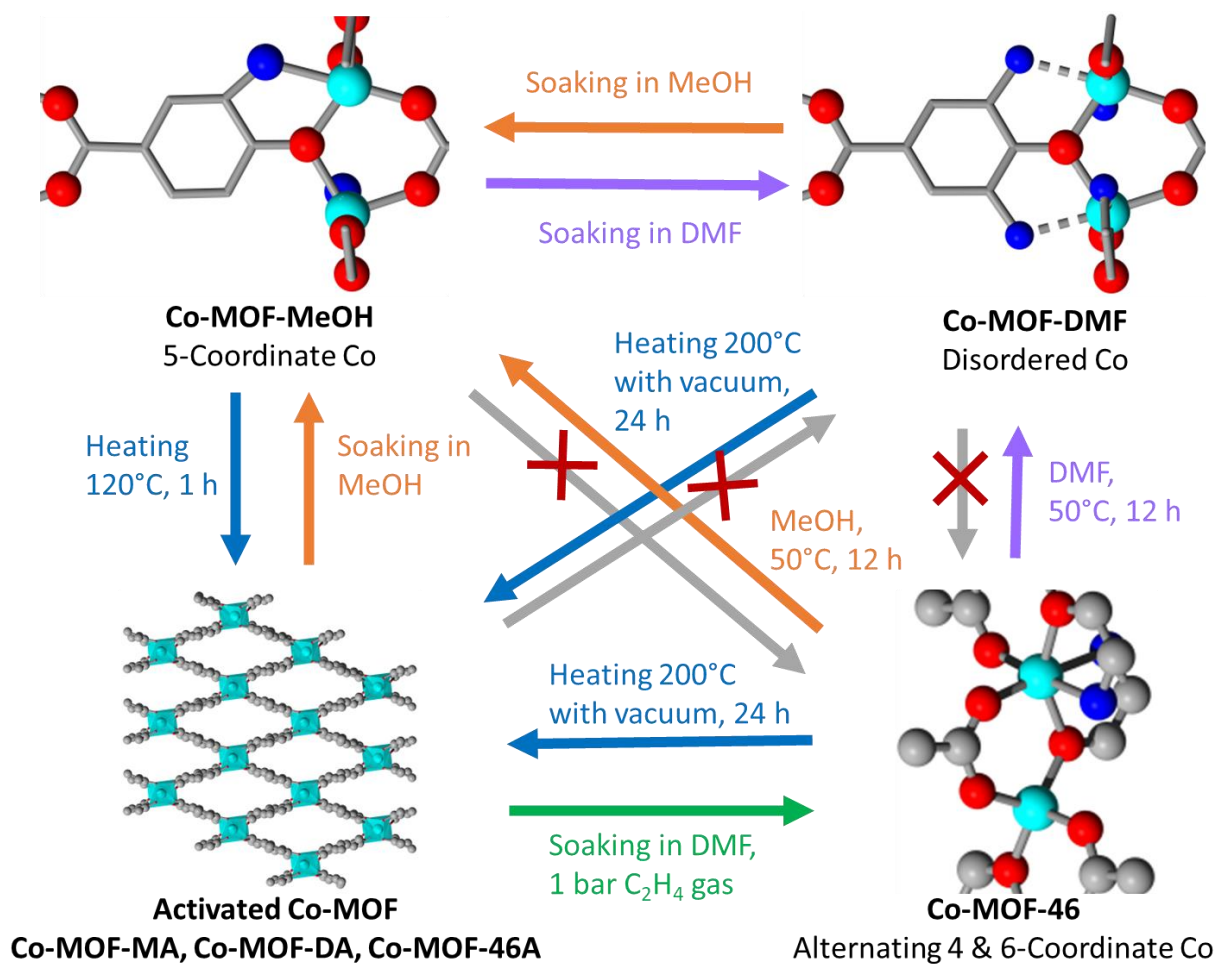
**Table 2.** Curie-Weiss fit parameters for Co-MOF-DMF, Co-MOF-MeOH, Co-MOF-46, and Co-MOF-MA.<sup>a</sup>

Sample	0.1 T		0.5 T		1 T	
	C ( $\text{K}\cdot\text{cm}^3/\text{mol}$ )	$\Theta$ (K)	C ( $\text{K}\cdot\text{cm}^3/\text{mol}$ )	$\Theta$ (K)	C ( $\text{K}\cdot\text{cm}^3/\text{mol}$ )	$\Theta$ (K)
Co-MOF-DMF	2.682(2)	-31.97(14)	2.640(10)	-31.04(8)	2.64326(97)	-31.39(9)
Co-MOF-MeOH	3.50(1)	-33.49(73)	3.521(9)	-30.55(53)	1.08(2)	-197(7)
Co-MOF-46	1.193(4)	-43.18(77)	1.089(3)	-39.96(59)	1.100(2)	-44.17(60)
Co-MOF-MA	2.451(3)	-35.55(21)	1.967(2)	-36.53(26)	1.973(2)	-38.26(27)

<sup>a</sup>Standard uncertainties are parenthesized.  $R^2$  values are all > 0.999.

In summary, Figure 21 shows a schematic diagram of all the phase changes as a result of the various conditions that were just discussed. Every phase change was accompanied by sc-XRD (at least 3 crystals) and PXRD analysis to check the individual structures and bulk phase purity, except for the phase changes that result in the closed-phase structure, as many of these crystals were heavily twinned or otherwise too poorly diffracting for sc-XRD analyses. It is also worth noting that soaking any of the Co-MOFs, regardless of phase, in non-coordinating solvents e.g. hexane and dichloromethane, or bulky ether solvents e.g. tetrahydrofuran and dioxane, does not trigger any phase change even under heating.





**Figure 21.** Schematic diagram of phase changes associated with **Co-MOF** and the relevant conditions that trigger the phase changes.

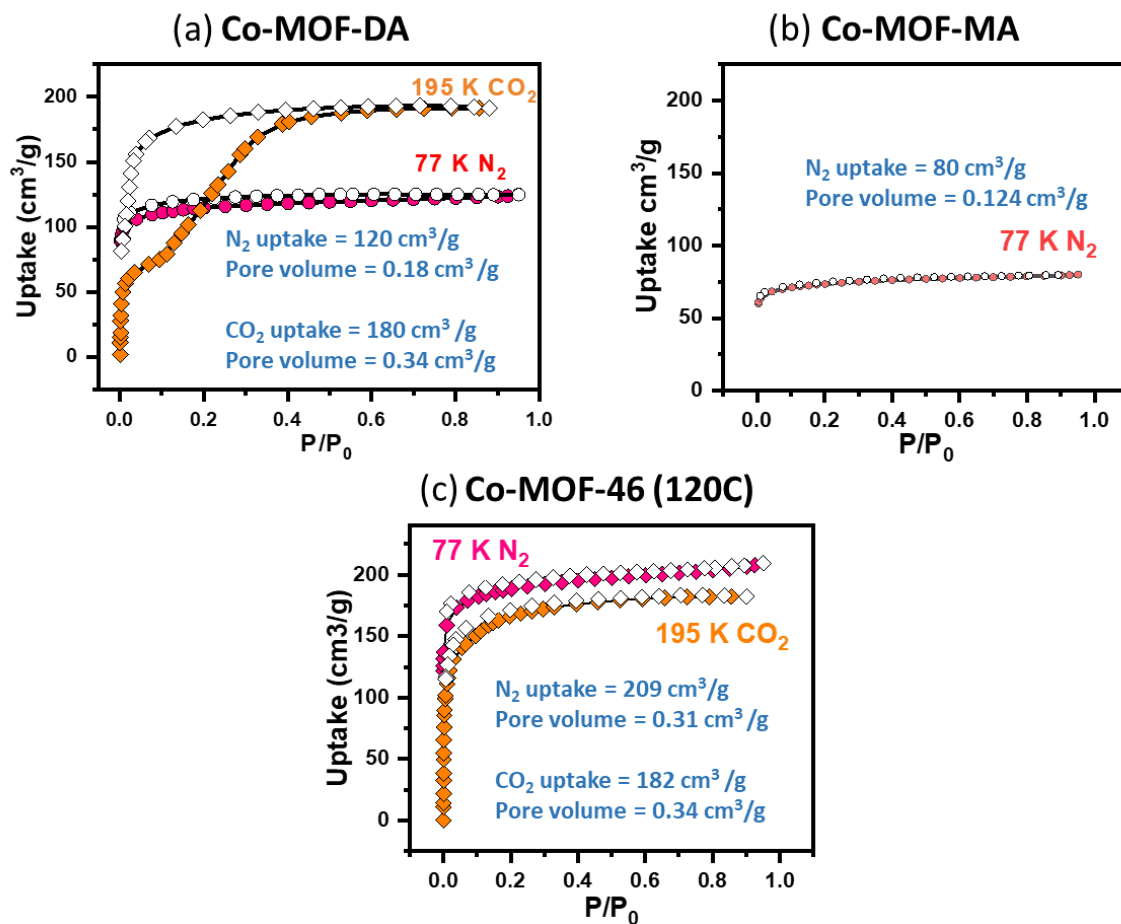
### 4.3 Ethylene/Ethane/Acetylene Gas Adsorption by Co-MOF

First, we investigated the permanent porosity and the closed-to-open phase change properties of the various desolvated **Co-MOF** phases using N<sub>2</sub> and CO<sub>2</sub> adsorption isotherms. Interestingly, even high pressures of N<sub>2</sub> do not trigger the opening of the closed phase **Co-MOF-DA** and **Co-MOF-MA**, allowing us to measure the porosity of the closed phases.

Although sc-XRD data showed that the unit cell of **Co-MOF-DA** was approximately 5% larger than **Co-MOF-MA**, the measured N<sub>2</sub> uptake and pore volume was a whopping 50% higher, suggesting that the slight difference in Co coordination and unit cell were sufficient to increase the adsorption of N<sub>2</sub> significantly. One possibility for this observation is that a C-H group on the phenyl ring of the linker is sterically restricting access to the space next to the Co OMS as seen in Figure 12a, whereas for **Co-MOF-DA**, the phenyl ring is rotated slightly so as to accommodate gases within that binding pocket (Figure 12b).

On the other hand, the desolvated open phase **Co-MOF-46 (120C)** displayed an N<sub>2</sub> uptake of 209 cm<sup>3</sup> g<sup>-1</sup> and pore volume of 0.31 cm<sup>3</sup> g<sup>-1</sup>, consistent with the predicted pore volume calculated from the crystal structure of **Co-MOF-46**.

When the **Co-MOFs** are exposed to CO<sub>2</sub> instead of N<sub>2</sub>, **Co-MOF-DA** showed a 2-step Type IV isotherm characteristic of the phase change from a closed to open phase structure, whereas the already open phase **Co-MOF-46 (120C)** had a typical Type I shaped isotherm. Unfortunately, partial degradation of the **Co-MOF-MA** sample after multiple activation-resolution cycles resulted in physical damage that made it impossible to measure the CO<sub>2</sub> uptake, and the sample is currently scheduled for a re-measurement within the next few months. However, we expect the adsorption behavior of **Co-MOF-MA** to strongly resemble **Co-MOF-DA**. The total CO<sub>2</sub> uptake and pore volumes of the final open-phase **Co-MOF-DA** and **Co-MOF-46 (120C)** correspond perfectly with the predicted value and with each other, confirming that they are indeed all the same open phase structure, albeit with differences in Co coordination.



**Figure 22.** 77 K N<sub>2</sub> and 195 K CO<sub>2</sub> uptake of (a) **Co-MOF-DA**, (b) **Co-MOF-MA**, and (c) de-solvated open phase **Co-MOF-46 (120C)**.

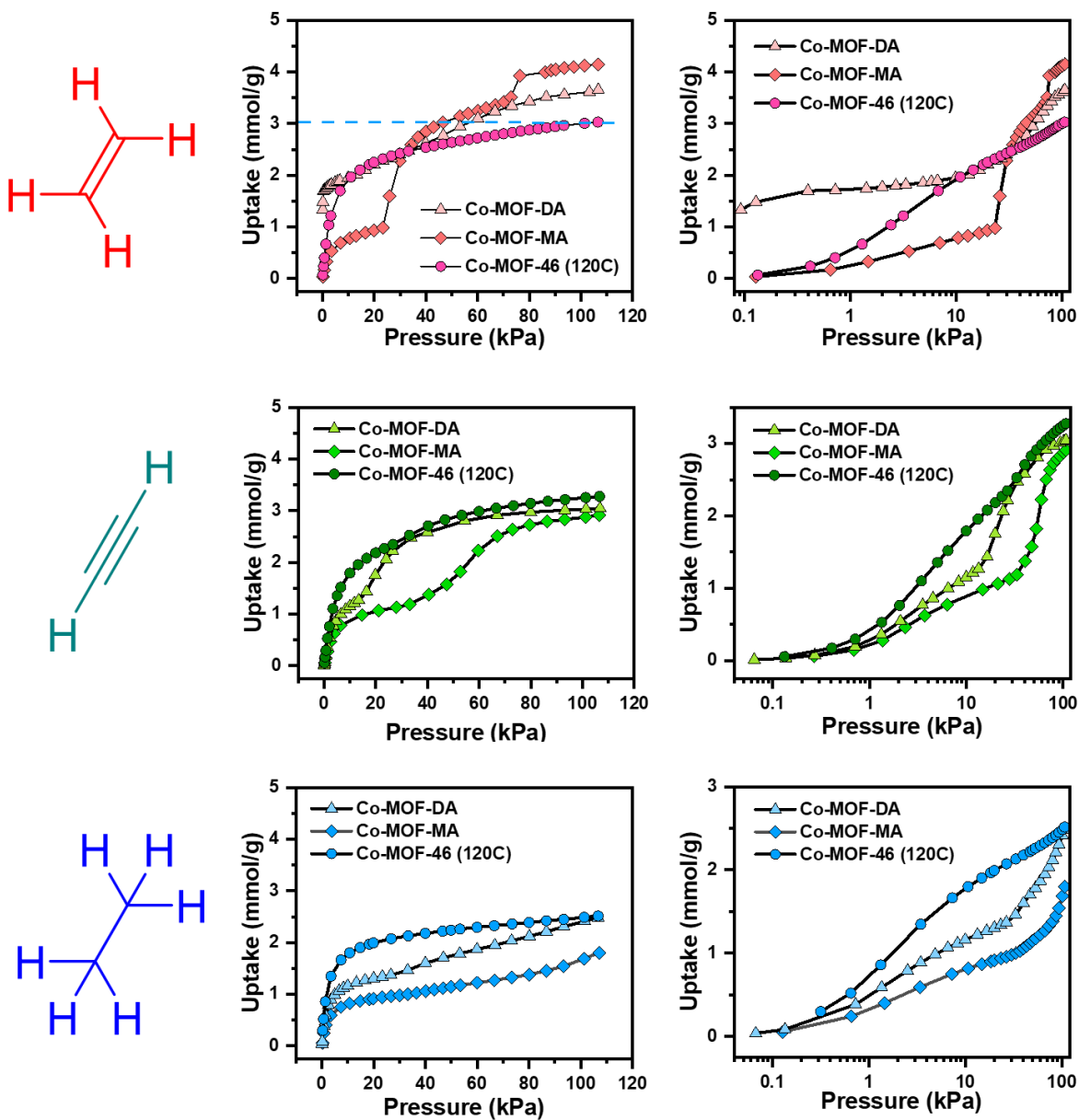
The C<sub>2</sub> gas adsorption properties of the **Co-MOFs** were then studied (Figure 23). To our delight, **Co-MOF-DA** displayed a large ethylene uptake of 1.8 mmol/g at extremely low pressures of 0.1-1 kPa, comparable to the M<sub>2</sub>(*m*-dobdc) series reported by the Long group over the same pressure range.<sup>74</sup> This further supports our hypothesis that **Co-MOF-DA** contains OMS that can effectively bind ethylene. Moreover, the maximal uptake of 2.3 mmol/g right before the phase opening matches up perfectly with the predicted 2.38 mmol/g that would come from exactly half of the Co sites being bound to ethylene, which coincides with the magnetic susceptibility data that there are two distinct Co<sup>II</sup> sites. It is also highly likely that the binding of an ethylene molecule to one Co<sup>II</sup> site results in a structural distortion that blocks its neighboring Co sites, such that only half of the Co(OMS) can be effectively utilized.

Unfortunately, **Co-MOF-MA** did not display a similar low pressure ethylene adsorption, likely due to the absence of a suitably-sized Co(OMS)-ethylene binding pocket from steric hindrance of the linker phenyl C-H, consistent with the low N<sub>2</sub> uptake at 77 K.

To our surprise, the maximum ethylene uptake at 100 kPa was 25-30% higher for **Co-MOF-DA** and **Co-MOF-MA** compared to the open-phase **Co-MOF-46 (120C)**, such that repeated adsorption measurements were conducted to confirm this unusual phenomenon. We found this unprecedented as the maximum CO<sub>2</sub> uptake and pore volumes of **Co-MOF-DA** and **Co-MOF-46 (120C)** were identical. We surmise that a possible reason for this is that the adsorption of ethylene into the closed phase **Co-MOFs** helps enhance cooperative, ordered packing of the ethylene molecules such that more molecules are fit into the pores after the phase change, but more precise modeling and/or structural studies of activated **Co-MOF** under low ethylene pressures are necessary to properly elucidate the adsorption mechanism.

Another exciting observation is that unlike with ethylene gas, **Co-MOF-DA** does not adsorb acetylene strongly at low pressures (< 0.3 mmol/g from 0.1-1 kPa). This is contrary to most OMS-type adsorptions as metals bind more strongly to alkynes than alkenes. It is likely that the Co(OMS) binding pocket of **Co-MOF-DA** fits only the geometry and size of ethylene but not the linear acetylene, resulting in selectivity for ethylene over acetylene.

Finally, the ethane uptake of the **Co-MOFs** was measured. Unlike ethylene and acetylene, the rate of phase opening for the **Co-MOFs** as seen by the gradient of the inflection point is far slower, and **Co-MOF-MA** did not seem to fully open even at 100 kPa. Maximum ethane uptake was also the lowest of the C<sub>2</sub> gases, consistent with the fact that ethane is the bulkiest C<sub>2</sub> gas and has little interaction with the MOF.



**Figure 23.** Uptake of ethylene (red), acetylene (green), and ethane (blue) for **Co-MOF-DA**, **Co-MOF-MA**, and **Co-MOF-46 (120C)** at 298 K. The graphs on the left are linearly scaled and the ones on the right are log-scaled to compare the isotherms more clearly at low pressures.

#### 4.4 Conclusions

**Co-MOF** remarkably displays a reversible, guest-assisted phase change between disordered, 5-coordinated, and 4,6-coordinated, as well as a flexible-robust structure where both the de-solvated open and closed phases can be obtained. Each phase and phase change were characterized by sc-XRD, PXRD, and several other analytic methods to provide evidence of all the different phases to the best of our ability.

Furthermore, tuning of the phases allows modification of the OMS site on Co and thus optimization of the uptake of C<sub>2</sub> gases, in particular ethylene, which displayed unusual uptake properties both at low and high pressures, which has rarely been reported in the literature. At low ethylene pressures, **Co-MOF-DA** displayed ethylene uptake characteristic of OMS, with exactly half of the Co sites being occupied before phase opening. At high pressures, the activated **Co-MOF-DA** and **Co-MOF-MA** showed higher ethylene uptakes than the open phase **Co-MOF-46 (120C)**, leading us to postulate that there is enhanced cooperativity in the adsorption of ethylene when a phase opening is involved.

Moving on, further modeling and measurements to obtain conclusive evidence for the unusual ethylene adsorption isotherms will be conducted to elucidate the mechanism behind these properties. Breakthrough experiments are also scheduled to investigate the application of **Co-MOF** in C<sub>2</sub> gas separations. Further magnetometry experiments have also been scheduled to elucidate the difference between the activated phases **Co-MOF-DA**, **Co-MOF-MA**, and **Co-MOF-46A**.

## 4.5 Materials and Methods

**Starting Materials.** All reactions and manipulations were carried out in air. All starting materials were purchased from Sigma-Aldrich, Combi-Blocks, and TCI (USA) and used without further purification.

**Single Crystal X-ray Diffraction.** Data was collected using synchrotron radiation at the Advanced Light Source, beamline 12.2.1, at Lawrence Berkeley National Laboratory, Berkeley, CA, USA. Indexing was performed using APEX3 (Difference Vectors method). Data integration and reduction were performed using SaintPlus 6.0. Absorption correction was performed by multi-scan method implemented in SADABS. Space groups were determined using XPREP implemented in APEX3. The structure was solved using SHELXT 2018/2 and refined using SHELXL 2018/3 within Olex 2 (full-matrix least-squares on  $F^2$ ). Zr, Cu, C, O, and N atoms were refined with anisotropic displacement parameters and H atoms were placed in geometrically calculated positions and included in the refinement process using riding model with isotropic thermal parameters:  $U_{\text{iso}}(\text{H}) = 1.2U_{\text{eq}}(-\text{CH})$ . The disordered solvent molecules were treated as diffuse using the SQUEEZE procedure implemented in PLATON. Crystal data and refinement details are shown in Table SX. This data can be obtained free of charge from The Cambridge Crystallographic Data Centre via [www.ccdc.cam.ac.uk/data\\_request/cif](http://www.ccdc.cam.ac.uk/data_request/cif).

**Powder X-Ray Diffraction (PXRD) Measurements.** PXRD data were collected by using a Rigaku X-ray diffractometer with Cu  $K\alpha$  radiation at 40 kV and 20 mA.

**$^1\text{H}$  NMR Spectra.**  $^1\text{H}$  spectra were recorded on an AVANCE II 500 (Bruker, Germany).

**Gas Sorption Measurements.** Gas adsorption isotherms were performed on the surface area analyzer ASAP-2020.  $\text{N}_2$  gas adsorption isotherms were measured at 77 K using a liquid  $\text{N}_2$  bath.

**Scanning Electron Microscope.** SEM images and EDS data were collected on a tabletop Phenom ProX equipped with the Element Identification (EID) software package and a specially designed and fully integrated Energy Dispersive Spectrometer (EDS).

**Fourier transform infrared (FTIR) Spectra.** FTIR spectra were recorded on the Nicolet iS50 FT-IR system (Thermo Fisher, USA).

**UV-visible Spectroscopy.** UV-visible diffuse reflectance data were taken using a Cary 5000 spectrometer with an internal diffuse reflectance accessory. **Co-MOF** samples were ground using a mortar and pestle for 10-15 min before mounting on the sample holder.

**Magnetic Susceptibility.** All magnetic measurements were carried out on a Quantum Design MPMS-XL equipped with RSO transport option. Sample tubes were immobilized within plastic drinking straws and mounted onto graphite sample rods prior to being loaded into the instrument. Diamagnetic corrections were applied for sample, eicosane, quartz wool, and methanol using Pascals constants. Curie-Weiss fits were made using the linear regions of the inverse susceptibility data.  $C$  and  $\theta$  defined using equation 1.

$$\chi = C/(T - \theta) \quad \text{Eq 1}$$

## MOF Syntheses.

**Co-MOF-DMF.**  $\text{Co}(\text{NO}_3)_2 \cdot 6\text{H}_2\text{O}$  (3.4 mmol, 2 g), 3-amino-4-hydroxybenzoic acid (**H<sub>4</sub>L**, 3.25 mmol, 1 g), 200 mL DMF and 10 mL water were added to a 500 mL bottle, sonicated until all the solids were dissolved, and then heated at 125°C for 48 hours to give a yield of **Co-MOF-DMF** of 73% based on **H<sub>4</sub>L**.

**Co-MOF-MeOH.** 500 mg of **Co-MOF-DMF** was soaked in 10 mL of methanol overnight at room temperature.

**Co-MOF-DA.** 50 mg of **Co-MOF-DMF** was activated under high vacuum while heating on a hotplate at 200°C for 24 h.

**Co-MOF-DA (single crystal).** 5 mg of **Co-MOF-DMF** was activated under high vacuum while heating on a hotplate at 300°C for 3 h.

**Co-MOF-MA.** 50 mg of **Co-MOF-MeOH** was activated under high vacuum while heating on a hotplate at 120°C for 1 h.

**Co-MOF-MA (single crystal).** 5 mg of **Co-MOF-MeOH** was activated under high vacuum while heating on a hotplate at 300°C for 1 h.

**Co-MOF-46.** 50 mg of **Co-MOF-MA** or **Co-MOF-DA** was re-solvated in DMF overnight at room temperature.

**Co-MOF-46A.** 50 mg of **Co-MOF-46** was activated under high vacuum while heating on a hotplate at 200°C for 24 h.

**Co-MOF-46 (120C).** 50 mg of **Co-MOF-46** was activated under high vacuum while heating on a hotplate at 120°C for 3 h.



## 4.6 References

1. Global Ethylene Market 2019-2023. (accessed retrieved Aug).
2. Matar, S.; Hatch, L. F., *Chemistry of Petrochemical Processes*. Second Edition ed.; Gulf Professional Publishing: 2001.
3. Khan, N. A.; Khan, M. I. R.; Ferrante, A.; Poor, P., Editorial: Ethylene: A Key Regulatory Molecule in Plants. *Front Plant Sci* **2017**, *8*, 1782.
4. Sadrameli, S. M., Thermal/catalytic cracking of hydrocarbons for the production of olefins: A state-of-the-art review I: Thermal cracking review. *Fuel* **2015**, *140*, 102-115.
5. Sholl, D. S.; Lively, R. P., Seven chemical separations to change the world. *Nature* **2016**, *532* (7600), 435-7.
6. Amghizar, I.; Vandewalle, L. A.; Van Geem, K. M.; Marin, G. B., New Trends in Olefin Production. *Engineering* **2017**, *3* (2), 171-178.
7. Eldridge, R. B., Olefin/paraffin separation technology: a review. *Ind. Eng. Chem. Res.* **1993**, *32* (10), 2208-2212.
8. Bander, F. Separation Technologies. (accessed Aug).
9. Worrell, E.; Phylipsen, D.; Einstein, D.; Martin, N. *Energy use and energy intensity of the U.S. chemical industry.*; Lawrence Berkeley National Laboratory: Berkeley, CA: 2000.
10. Pires, J.; Fernandes, J.; Fernandes, A. C.; Pinto, M., Reverse selectivity of zeolites and metal-organic frameworks in the ethane/ethylene separation by adsorption. *Sep. Sci. Technol.* **2016**, *52* (1), 51-57.
11. Chu, S.; Cui, Y.; Liu, N., The path towards sustainable energy. *Nat Mater* **2016**, *16* (1), 16-22.
12. Yang, R. T., *Adsorbents: Fundamentals and Applications*. John Wiley & Sons, Inc: Hoboken, NJ, 2003.
13. Kitagawa, S.; Kitaura, R.; Noro, S., Functional porous coordination polymers. *Angew Chem Int Ed Engl* **2004**, *43* (18), 2334-75.
14. Furukawa, H.; Cordova, K. E.; O'Keeffe, M.; Yaghi, O. M., The chemistry and applications of metal-organic frameworks. *Science* **2013**, *341* (6149), 1230444.
15. Martins, V. F. D.; Ribeiro, A. M.; Santos, J. C.; Loureiro, J. M.; Gleichmann, K.; Ferreira, A.; Rodrigues, A. E., Development of gas-phase SMB technology for light olefin/paraffin separations. *AIChE Journal* **2016**, *62* (7), 2490-2500.
16. Yang, Y.; Burke, N.; Ali, S.; Huang, S.; Lim, S.; Zhu, Y., Experimental studies of hydrocarbon separation on zeolites, activated carbons and MOFs for applications in natural gas processing. *RSC Advances* **2017**, *7* (21), 12629-12638.
17. Maurin, G.; Serre, C.; Cooper, A.; Ferey, G., The new age of MOFs and of their porous-related solids. *Chem. Soc. Rev.* **2017**, *46* (11), 3104-3107.
18. Wang, H.; Zhu, Q.-L.; Zou, R.; Xu, Q., Metal-Organic Frameworks for Energy Applications. *Chem* **2017**, *2* (1), 52-80.
19. Hendon, C. H.; Rieth, A. J.; Korzynski, M. D.; Dinca, M., Grand Challenges and Future Opportunities for Metal-Organic Frameworks. *ACS Cent Sci* **2017**, *3* (6), 554-563.
20. Yuan, S.; Feng, L.; Wang, K.; Pang, J.; Bosch, M.; Lollar, C.; Sun, Y.; Qin, J.; Yang, X.; Zhang, P.; Wang, Q.; Zou, L.; Zhang, Y.; Zhang, L.; Fang, Y.; Li, J.; Zhou, H. C., Stable Metal-Organic Frameworks: Design, Synthesis, and Applications. *Adv. Mater.* **2018**, 1704303.
21. Yaghi, O. M.; Kalmutzki, M. J.; Diercks, C. S., *Introduction to Reticular Chemistry*. Wiley-VCH: Weinheim, 2019.

22. Wu, Y.; Weckhuysen, B. M., Separation and Purification of Hydrocarbons with Porous Materials. *Angew Chem Int Ed Engl* **2021**, *60* (35), 18930-18949.
23. Kim, J.; Lin, L. C.; Martin, R. L.; Swisher, J. A.; Haranczyk, M.; Smit, B., Large-scale computational screening of zeolites for ethane/ethene separation. *Langmuir* **2012**, *28* (32), 11914-9.
24. Bereciartua, P. J.; Cantin, A.; Corma, A.; Jorda, J. L.; Palomino, M.; Rey, F.; Valencia, S.; Corcoran, E. W., Jr.; Kortunov, P.; Ravikovitch, P. I.; Burton, A.; Yoon, C.; Wang, Y.; Paur, C.; Guzman, J.; Bishop, A. R.; Casty, G. L., Control of zeolite framework flexibility and pore topology for separation of ethane and ethylene. *Science* **2017**, *358* (6366), 1068-1071.
25. Golipour, H.; Mokhtarani, B.; Mafi, M.; Moradi, A.; Godini, H. R., Experimental Measurement for Adsorption of Ethylene and Ethane Gases on Copper-Exchanged Zeolites 13X and 5A. *J. Chem. Eng. Data* **2020**, *65* (8), 3920-3932.
26. Narin, G.; Martins, V. F. D.; Campo, M.; Ribeiro, A. M.; Ferreira, A.; Santos, J. C.; Schumann, K.; Rodrigues, A. E., Light olefins/paraffins separation with 13X zeolite binderless beads. *Sep. Purif. Technol.* **2014**, *133*, 452-475.
27. Wu, C.; Wang, J.; Fang, Y.; Wang, Z.; Fei, D.; Han, X.; Dang, Y., Comparative Study of Ag<sup>+</sup>-Based Adsorbents Performance in Ethylene/Ethane Separation. *J. Chem. Eng. Data* **2019**, *64* (2), 611-618.
28. Choi, B.-U.; Choi, D.-K.; Lee, Y.-W.; Lee, B.-K.; Kim, S.-H., Adsorption Equilibria of Methane, Ethane, Ethylene, Nitrogen, and Hydrogen onto Activated Carbon. *J. Chem. Eng. Data* **2003**, *48* (3), 603-607.
29. Rungta, M.; Xu, L.; Koros, W. J., Carbon molecular sieve dense film membranes derived from Matrimid<sup>®</sup> for ethylene/ethane separation. *Carbon* **2012**, *50* (4), 1488-1502.
30. Gao, F.; Wang, Y.; Wang, X.; Wang, S., Ethylene/ethane separation by CuCl/AC adsorbent prepared using CuCl<sub>2</sub> as a precursor. *Adsorption* **2016**, *22* (7), 1013-1022.
31. Saha, D.; Toof, B.; Krishna, R.; Orkoulas, G.; Gismondi, P.; Thorpe, R.; Comroe, M. L., Separation of ethane-ethylene and propane-propylene by Ag(I) doped and sulfurized microporous carbon. *Microporous Mesoporous Mater.* **2020**, *299*, 110099.
32. Ren, Y.; Liang, X.; Dou, H.; Ye, C.; Guo, Z.; Wang, J.; Pan, Y.; Wu, H.; Guiver, M. D.; Jiang, Z., Membrane-Based Olefin/Paraffin Separations. *Advanced Science* **2020**, *7* (19), 2001398.
33. Aguado, S.; Bergeret, G.; Daniel, C.; Farrusseng, D., Absolute molecular sieve separation of ethylene/ethane mixtures with silver zeolite A. *J. Am. Chem. Soc.* **2012**, *134* (36), 14635-7.
34. Eldridge, R. B., Olefin/paraffin separation technology: a review. *Ind. Eng. Chem. Res.* **2002**, *32* (10), 2208-2212.
35. Li, J. R.; Sculley, J.; Zhou, H. C., Metal-organic frameworks for separations. *Chem. Rev.* **2012**, *112* (2), 869-932.
36. Kitagawa, S., Porous Materials and the Age of Gas. *Angew Chem Int Ed Engl* **2015**, *54* (37), 10686-7.
37. Bao, Z.; Chang, G.; Xing, H.; Krishna, R.; Ren, Q.; Chen, B., Potential of microporous metal-organic frameworks for separation of hydrocarbon mixtures. *Energy Environ. Sci.* **2016**, *9* (12), 3612-3641.
38. Adil, K.; Belmabkhout, Y.; Pillai, R. S.; Cadiau, A.; Bhatt, P. M.; Assen, A. H.; Maurin, G.; Eddaoudi, M., Gas/vapour separation using ultra-microporous metal-organic frameworks: insights into the structure/separation relationship. *Chem. Soc. Rev.* **2017**, *46* (11), 3402-3430.
39. Li, H.; Wang, K.; Sun, Y.; Lollar, C. T.; Li, J.; Zhou, H.-C., Recent advances in gas storage and separation using metal-organic frameworks. *Mater. Today* **2018**, *21* (2), 108-121.
40. Zhao, X.; Wang, Y.; Li, D. S.; Bu, X.; Feng, P., Metal-Organic Frameworks for Separation. *Adv. Mater.* **2018**, *30* (37), 1705189.

41. Li, H.; Li, L. B.; Lin, R. B.; Zhou, W.; Zhang, Z. J.; Xiang, S. C.; Chen, B. L., Porous metal-organic frameworks for gas storage and separation: Status and challenges. *Energychem* **2019**, *1* (1), 100006.
42. Lin, R.-B.; Xiang, S.; Xing, H.; Zhou, W.; Chen, B., Exploration of porous metal-organic frameworks for gas separation and purification. *Coord. Chem. Rev.* **2019**, *378*, 87-103.
43. He, Y. B.; Krishna, R.; Chen, B. L., Metal-organic frameworks with potential for energy-efficient adsorptive separation of light hydrocarbons. *Energy Environ. Sci.* **2012**, *5* (10), 9107-9120.
44. Liao, P. Q.; Zhang, W. X.; Zhang, J. P.; Chen, X. M., Efficient purification of ethene by an ethane-trapping metal-organic framework. *Nat Commun* **2015**, *6*, 8697.
45. Sen, S.; Hosono, N.; Zheng, J. J.; Kusaka, S.; Matsuda, R.; Sakaki, S.; Kitagawa, S., Cooperative Bond Scission in a Soft Porous Crystal Enables Discriminatory Gate Opening for Ethylene over Ethane. *J. Am. Chem. Soc.* **2017**, *139* (50), 18313-18321.
46. Chen, Y.; Qiao, Z.; Wu, H.; Lv, D.; Shi, R.; Xia, Q.; Zhou, J.; Li, Z., An ethane-trapping MOF PCN-250 for highly selective adsorption of ethane over ethylene. *Chem. Eng. Sci.* **2018**, *175*, 110-117.
47. Li, L.; Lin, R. B.; Krishna, R.; Li, H.; Xiang, S.; Wu, H.; Li, J.; Zhou, W.; Chen, B., Ethane/ethylene separation in a metal-organic framework with iron-peroxo sites. *Science* **2018**, *362* (6413), 443-446.
48. Lin, R. B.; Wu, H.; Li, L.; Tang, X. L.; Li, Z.; Gao, J.; Cui, H.; Zhou, W.; Chen, B., Boosting Ethane/Ethylene Separation within Isoreticular Ultramicroporous Metal-Organic Frameworks. *J. Am. Chem. Soc.* **2018**, *140* (40), 12940-12946.
49. Wang, X.; Niu, Z.; Al-Enizi, A. M.; Nafady, A.; Wu, Y.; Aguila, B.; Verma, G.; Wojtas, L.; Chen, Y.-S.; Li, Z.; Ma, S., Pore environment engineering in metal-organic frameworks for efficient ethane/ethylene separation. *Journal of Materials Chemistry A* **2019**, *7* (22), 13585-13590.
50. Qazvini, O. T.; Babarao, R.; Shi, Z. L.; Zhang, Y. B.; Telfer, S. G., A Robust Ethane-Trapping Metal-Organic Framework with a High Capacity for Ethylene Purification. *J. Am. Chem. Soc.* **2019**, *141* (12), 5014-5020.
51. Zeng, H.; Xie, X. J.; Xie, M.; Huang, Y. L.; Luo, D.; Wang, T.; Zhao, Y.; Lu, W.; Li, D., Cage-Interconnected Metal-Organic Framework with Tailored Apertures for Efficient C<sub>2</sub>H<sub>6</sub>/C<sub>2</sub>H<sub>4</sub> Separation under Humid Conditions. *J. Am. Chem. Soc.* **2019**, *141* (51), 20390-20396.
52. Zhang, X.; Li, L.; Wang, J. X.; Wen, H. M.; Krishna, R.; Wu, H.; Zhou, W.; Chen, Z. N.; Li, B.; Qian, G.; Chen, B., Selective Ethane/Ethylene Separation in a Robust Microporous Hydrogen-Bonded Organic Framework. *J. Am. Chem. Soc.* **2020**, *142* (1), 633-640.
53. Lee, S. K.; Lee, Y. J.; Cho, K.; Lee, U. H.; Chang, J. S., A Fluorinated Metal-Organic Framework, FMOF-2, for Preferential Adsorption of Ethane over Ethylene. *Bull. Korean Chem. Soc.* **2021**, *42* (2), 286-289.
54. Wang, H.; Luo, D.; Velasco, E.; Yu, L.; Li, J., Separation of alkane and alkene mixtures by metal-organic frameworks. *Journal of Materials Chemistry A* **2021**, *9* (37), 20874-20896.
55. Bao, Z.; Wang, J.; Zhang, Z.; Xing, H.; Yang, Q.; Yang, Y.; Wu, H.; Krishna, R.; Zhou, W.; Chen, B.; Ren, Q., Molecular Sieving of Ethane from Ethylene through the Molecular Cross-Section Size Differentiation in Gallate-based Metal-Organic Frameworks. *Angew Chem Int Ed Engl* **2018**, *57* (49), 16020-16025.
56. Bloch, E. D.; Queen, W. L.; Krishna, R.; Zadrozny, J. M.; Brown, C. M.; Long, J. R., Hydrocarbon separations in a metal-organic framework with open iron(II) coordination sites. *Science* **2012**, *335* (6076), 1606-10.
57. Yang, S.; Ramirez-Cuesta, A. J.; Newby, R.; Garcia-Sakai, V.; Manuel, P.; Callear, S. K.; Campbell, S. I.; Tang, C. C.; Schroder, M., Supramolecular binding and separation of hydrocarbons within a functionalized porous metal-organic framework. *Nat. Chem.* **2014**, *7* (2), 121-9.

58. Wang, S.; Yang, Q.; Zhong, C., Adsorption and separation of binary mixtures in a metal-organic framework Cu-BTC: A computational study. *Sep. Purif. Technol.* **2008**, *60* (1), 30-35.
59. Bao, Z.; Alnemrat, S.; Yu, L.; Vasiliev, I.; Ren, Q.; Lu, X.; Deng, S., Adsorption of ethane, ethylene, propane, and propylene on a magnesium-based metal-organic framework. *Langmuir* **2011**, *27* (22), 13554-62.
60. Bae, Y. S.; Lee, C. Y.; Kim, K. C.; Farha, O. K.; Nickias, P.; Hupp, J. T.; Nguyen, S. T.; Snurr, R. Q., High propene/propane selectivity in isostructural metal-organic frameworks with high densities of open metal sites. *Angew Chem Int Ed Engl* **2012**, *51* (8), 1857-60.
61. Geier, S. J.; Mason, J. A.; Bloch, E. D.; Queen, W. L.; Hudson, M. R.; Brown, C. M.; Long, J. R., Selective adsorption of ethylene over ethane and propylene over propane in the metal-organic frameworks M<sub>2</sub>(dobdc) (M = Mg, Mn, Fe, Co, Ni, Zn). *Chemical Science* **2013**, *4* (5), 2054-61.
62. Zhang, Y.; Li, B.; Krishna, R.; Wu, Z.; Ma, D.; Shi, Z.; Pham, T.; Forrest, K.; Space, B.; Ma, S., Highly selective adsorption of ethylene over ethane in a MOF featuring the combination of open metal site and  $\pi$ -complexation. *Chem. Commun.* **2015**, *51* (13), 2714-7.
63. Martins, V. F. D.; Ribeiro, A. M.; Ferreira, A.; Lee, U. H.; Hwang, Y. K.; Chang, J.-S.; Loureiro, J. M.; Rodrigues, A. E., Ethane/ethylene separation on a copper benzene-1,3,5-tricarboxylate MOF. *Sep. Purif. Technol.* **2015**, *149*, 445-456.
64. Kulkarni, A. R.; Sholl, D. S., Screening of Copper Open Metal Site MOFs for Olefin/Paraffin Separations Using DFT-Derived Force Fields. *Journal of Physical Chemistry C* **2016**, *120* (40), 23044-23054.
65. Bachman, J. E.; Kapelewski, M. T.; Reed, D. A.; Gonzalez, M. I.; Long, J. R., M<sub>2</sub>(m-dobdc) (M = Mn, Fe, Co, Ni) Metal-Organic Frameworks as Highly Selective, High-Capacity Adsorbents for Olefin/Paraffin Separations. *J. Am. Chem. Soc.* **2017**, *139* (43), 15363-15370.
66. Luna-Triguero, A.; Vicent-Luna, J. M.; Gómez-Álvarez, P.; Calero, S., Olefin/Paraffin Separation in Open Metal Site Cu-BTC Metal-Organic Framework. *Journal of Physical Chemistry C* **2017**, *121* (5), 3126-3132.
67. Kokcam-Demir, U.; Goldman, A.; Esrafilı, L.; Gharib, M.; Morsali, A.; Weingart, O.; Janiak, C., Coordinatively unsaturated metal sites (open metal sites) in metal-organic frameworks: design and applications. *Chem. Soc. Rev.* **2020**, *49* (9), 2751-2798.
68. Li, B.; Zhang, Y.; Krishna, R.; Yao, K.; Han, Y.; Wu, Z.; Ma, D.; Shi, Z.; Pham, T.; Space, B.; Liu, J.; Thallapally, P. K.; Liu, J.; Chrzanowski, M.; Ma, S., Introduction of  $\pi$ -complexation into porous aromatic framework for highly selective adsorption of ethylene over ethane. *J. Am. Chem. Soc.* **2014**, *136* (24), 8654-60.
69. Wang, Y.; Hu, Z.; Cheng, Y.; Zhao, D., Silver-Decorated Hafnium Metal-Organic Framework for Ethylene/Ethane Separation. *Ind. Eng. Chem. Res.* **2017**, *56* (15), 4508-4516.
70. Zhang, L.; Li, L.; Hu, E.; Yang, L.; Shao, K.; Yao, L.; Jiang, K.; Cui, Y.; Yang, Y.; Li, B.; Chen, B.; Qian, G., Boosting Ethylene/Ethane Separation within Copper(I)-Chelated Metal-Organic Frameworks through Tailor-Made Aperture and Specific  $\pi$ -Complexation. *Advanced Science* **2020**, *7* (2), 1901918.
71. Zeise, W. C., Von der Wirkung zwischen Platinchlorid und Alkohol, und von den dabei entstehenden neuen Substanzen. *Annalen der Physik* **1831**, *97* (4), 497-541.
72. Li, J. R.; Kuppler, R. J.; Zhou, H. C., Selective gas adsorption and separation in metal-organic frameworks. *Chem. Soc. Rev.* **2009**, *38* (5), 1477-504.
73. Bloch, E. D.; Queen, W. L.; Krishna, R.; Zadrozny, J. M.; Brown, C. M.; Long, J. R., Hydrocarbon separations in a metal-organic framework with open iron(II) coordination sites. *Science* **2012**, *335* (6076), 1606-1610.

74. Bachman, J. E.; Kapelewski, M. T.; Reed, D. A.; Gonzalez, M. I.; Long, J. R., M2(m-dobdc) (M = Mn, Fe, Co, Ni) Metal-Organic Frameworks as Highly Selective, High-Capacity Adsorbents for Olefin/Paraffin Separations. *J. Am. Chem. Soc.* **2017**, *139* (43), 15363-15370.
75. Loiseau, T.; Serre, C.; Huguenard, C.; Fink, G.; Taulelle, F.; Henry, M.; Bataille, T.; Férey, G., A Rationale for the Large Breathing of the Porous Aluminum Terephthalate (MIL-53) Upon Hydration. *Chemistry – A European Journal* **2004**, *10* (6), 1373-1382.
76. Millange, F.; Serre, C.; Férey, G., Synthesis, structure determination and properties of MIL-53as and MIL-53ht: the first C<sub>3</sub> hybrid inorganic–organic microporous solids: C<sub>3</sub>(OH)·{O<sub>2</sub>C–C<sub>6</sub>H<sub>4</sub>–CO<sub>2</sub>}·{HO<sub>2</sub>C–C<sub>6</sub>H<sub>4</sub>–CO<sub>2</sub>H}<sub>x</sub>. *Chem. Commun.* **2002**, (8), 822-823.
77. Zhang, L.; Jiang, K.; Li, L.; Xia, Y. P.; Hu, T. L.; Yang, Y.; Cui, Y.; Li, B.; Chen, B.; Qian, G., Efficient separation of C<sub>2</sub>H<sub>2</sub> from C<sub>2</sub>H<sub>2</sub>/CO<sub>2</sub> mixtures in an acid-base resistant metal-organic framework. *Chem. Commun.* **2018**, *54* (38), 4846-4849.

## 4.7 Supporting Information

**Table S1. Crystal data and structural refinement of Co-MOF-DMF, Co-MOF-MeOH, and Co-MOF-46.**

Compound name	Co-MOF-DMF	Co-MOF-MeOH	Co-MOF-46 (MAD)
Empirical formula	C <sub>7</sub> H <sub>4</sub> CoNO <sub>3</sub>	C <sub>7</sub> H <sub>5</sub> CoNO <sub>3</sub>	C <sub>14</sub> H <sub>10</sub> Co <sub>2</sub> N <sub>2</sub> O <sub>6</sub>
Formula weight (g mol <sup>-1</sup> )	205.84	224.06	420.10
Temperature (K)	265	100	100
Wavelength (Å)	synchrotron ( $\lambda = 0.7288$ )	synchrotron ( $\lambda = 0.7288$ )	tetragonal
Crystal system	tetragonal	tetragonal	P4 <sub>3</sub> 22
Space group	P4 <sub>3</sub> 22	P4 <sub>1</sub>	12.90(2)
a (Å)	9.107(4)	9.1008(4)	12.90(2)
b (Å)	9.107(4)	9.1008(4)	13.15(3)
c (Å)	13.290(8)	13.1449(9)	90
$\alpha$ (deg)	90	90	90
$\beta$ (deg)	90	90	90
$\gamma$ (deg)	90	90	2187(9)
Volume (Å <sup>3</sup> )	1102.2(11)	1088.72(12)	8
Z	4	4	1.264
Density (calculated) (g/cm <sup>3</sup> )	1.24	1.367	1.638
Absorption Coefficient (mm <sup>-1</sup> )	1.526	1.554	824
F(000)	409	448	3003
Crystal size (mm <sup>3</sup> )	0.5 × 0.1 × 0.1 mm	0.6 × 0.1 × 0.1 mm	0.1 × 0.05 × 0.05 mm
2 $\theta$ range for data collection (deg)	5.422 to 46.474	4.476 to 62.992	3.238 to 61.83
Index ranges	-10 ≤ h ≤ 10, -10 ≤ k ≤ 8, -14 ≤ l ≤ 14	-12 ≤ h ≤ 13, -13 ≤ k ≤ 11, -19 ≤ l ≤ 19	-18 ≤ h ≤ 18, -18 ≤ k ≤ 18, -18 ≤ l ≤ 18
Reflections collected	4700	21858	93578
Independent reflections	785 [Rint = 0.0617, Rsigma = 0.0468]	3618 [Rint = 0.1394, Rsigma = 0.1394]	3224 [Rint = 0.0943, Rsigma = 0.0620]
Completeness to $\theta$ (%)	100	100	100
Data/restraints/parameters	785/0/59	3618/1/97	3224/0/113
Goodness-of-fit on F <sup>2</sup>	1.26	1.075	1.595
Final R indexes [ $I \geq 2\sigma(I)$ ]	R1 = 0.1003, wR2 = 0.2787	R1 = 0.1196, wR2 = 0.2916	R1 = 0.1330, wR2 = 0.3514
Final R indexes [all data]	R1 = 0.1114, wR2 = 0.2940	R1 = 0.2062, wR2 = 0.3437	R1 = 0.1565, wR2 = 0.3872
Largest diff. peak/hole / e Å <sup>-3</sup>	2.46/-0.92	2.48/-0.88	6.25/-1.81

**Table S2. Crystal data and structural refinement of Co-MOF-DA and Co-MOF-MA.**

Compound name	Co-MOF-DA	Co-MOF-MA
Empirical formula	C <sub>72</sub> H <sub>56</sub> O <sub>32</sub> Zr <sub>6</sub>	C <sub>72</sub> H <sub>44</sub> Cu <sub>3.53</sub> N <sub>0.37</sub> O <sub>32</sub> Zr <sub>6</sub>
Formula weight (g mol <sup>-1</sup> )	120.24	183.86
Temperature (K)	100	100
Wavelength (Å)	synchrotron ( $\lambda = 0.7288$ )	synchrotron ( $\lambda = 0.7288$ )
Crystal system	hexagonal	hexagonal
Space group	P6/mmm	P6/mmm
a (Å)	40.212(2)	40.065(2)
b (Å)	40.212(2)	40.065(2)
c (Å)	11.5264(7)	11.6530(12)
$\alpha$ (deg)	90	90
$\beta$ (deg)	90	90
$\gamma$ (deg)	120	120
Volume (Å <sup>3</sup> )	16141(2)	16199(2)
Z	3	3
Density (calculated) (g/cm <sup>3</sup> )	3.031	3.185
Absorption Coefficient (mm <sup>-1</sup> )	4.092	8.553
F(000)	13475	14203
Crystal size (mm <sup>3</sup> )	0.8 × 0.02 × 0.02 mm	0.5 × 0.02 × 0.02 mm
2 $\theta$ range for data collection (deg)	3.172 to 55.798	1.204 to 58.138
Index ranges	-51 ≤ h ≤ 51, -51 ≤ k ≤ 51, -14 ≤ l ≤ 14	-53 ≤ h ≤ 53, -53 ≤ k ≤ 53, -15 ≤ l ≤ 15
Reflections collected	238734	353314
Independent reflections	6696 [R <sub>int</sub> = 0.0758, R <sub>sigma</sub> = 0.0256]	7489 [R <sub>int</sub> = 0.2501, R <sub>sigma</sub> = 0.0746]
Completeness to $\theta$ (%)	100	100
Data/restraints/parameters	6696/0/140	7489/0/149
Goodness-of-fit on F <sup>2</sup>	1.112	1.032
Final R indexes [ $I \geq 2\sigma(I)$ ]	R <sub>1</sub> = 0.0370, wR <sub>2</sub> = 0.1164	R <sub>1</sub> = 0.0730, wR <sub>2</sub> = 0.2167
Final R indexes [all data]	R <sub>1</sub> = 0.0435, wR <sub>2</sub> = 0.1223	R <sub>1</sub> = 0.0907, wR <sub>2</sub> = 0.2371
Largest diff. peak/hole / e Å <sup>-3</sup>	0.69/-0.60	1.86/-1.29